GEOTECHNICAL SPECIAL PUBLICATION NO. 192

Recent Advancement in Soil Behavior, In Situ Test Methods, Pile Foundations, and Tunneling

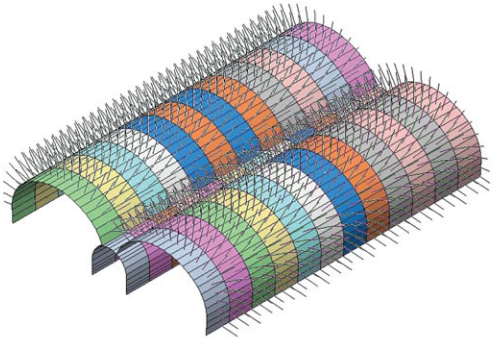

Edited by
Liaqat Ali, Ph.D.
António Gomes Correia, Ph.D.
Junsheng Yang, Ph.D.
Mingjiang Tao, Ph.D.

ASCE
GEO INSTITUTE

GEOTECHNICAL SPECIAL PUBLICATION NO. 192

RECENT ADVANCEMENT IN SOIL BEHAVIOR, IN SITU TEST METHODS, PILE FOUNDATIONS, AND TUNNELING

SELECTED PAPERS FROM THE 2009 GEOHUNAN INTERNATIONAL CONFERENCE

August 3–6, 2009
Changsha, Hunan, China

HOSTED BY
Changsha University of Science and Technology, China

CO-SPONSORED BY
ASCE Geo-Institute, USA
Asphalt Institute, USA
Central South University, China
Chinese Society of Pavement Engineering, Taiwan
Chongqing Jiaotong University, China
Deep Foundation Institute, USA
Federal Highway Administration, USA
Hunan University, China
International Society for Asphalt Pavements, USA
Jiangsu Transportation Research Institute, China
Korea Institute of Construction Technology, Korea
Korean Society of Road Engineers, Korea
Texas Department of Transportation, USA
Texas Transportation Institute, USA
Transportation Research Board (TRB), USA

EDITED BY
Liaqat Ali, Ph.D.
António Gomes Correia, Ph.D.
Junsheng Yang, Ph.D.
Mingjiang Tao, Ph.D.

Published by the American Society of Civil Engineers

Library of Congress Cataloging-in-Publication Data

Recent advancement in soil behavior, in situ test methods, pile foundations, and tunneling : selected papers from the 2009 GeoHunan International Conference, August 3-6, 2009, Changsha, Hunan, China / hosted by Changsha University of Science and Technology, China ; co-sponsored by ASCE Geo-Institute, USA … [et al.] ; edited by Liaqat Ali … [et al.].

p. cm. -- (Geotechnical special publication ; no. 192)
Includes bibliographical references and indexes.
ISBN 978-0-7844-1044-8
1. Roads--Foundations--Congresses. 2. Soil stabilization--Congresses. 3. Soils--Testing--Congresses. 4. Piling (Civil engineering)--Congresses. 5. Tunneling--Congresses. I. Ali, Liaqat. II. Changsha li gong da xue. III. American Society of Civil Engineers. Geo-Institute. IV. GeoHunan International Conference on Challenges and Recent Advances in Pavement Technologies and Transportation Geotechnics (2009 : Changsha, Hunan Sheng, China)

TE210.R43 2009
625.7'3--dc22 2009022726

American Society of Civil Engineers
1801 Alexander Bell Drive
Reston, Virginia, 20191-4400

www.pubs.asce.org

ISBN 978-0-7844-1044-8 Manufactured in the United States of America.

Geotechnical Special Publications

1 *Terzaghi Lectures*
2 *Geotechnical Aspects of Stiff and Hard Clays*
3 *Landslide Dams: Processes, Risk, and Mitigation*
7 *Timber Bulkheads*
9 *Foundations & Excavations in Decomposed Rock of the Piedmont Province*
11 *Dynamic Response of Pile Foundations - Experiment, Analysis and Observation*
14 *Geotechnical Aspects of Karst Terrains*
15 *Measured Performance Shallow Foundations*
16 *Special Topics in Foundations*
17 *Soil Properties Evaluation from Centrifugal Models*
18 *Geosynthetics for Soil Improvement*
19 *Mine Induced Subsidence: Effects on Engineered Structures*
21 *Hydraulic Fill Structures*
22 *Foundation Engineering*
23 *Predicted and Observed Axial Behavior of Piles*
24 *Resilient Moduli of Soils: Laboratory Conditions*
25 *Design and Performance of Earth Retaining Structures*
27 *Geotechnical Engineering Congress*
28 *Detection of and Construction at the Soil/Rock Interface*
29 *Recent Advances in Instrumentation, Data Acquisition and Testing in Soil Dynamics*
32 *Embankment of Dams - James L. Sherard Contributions*
33 *Excavation and Support for the Urban Infrastructure*
34 *Piles Under Dynamic Loads*
35 *Geotechnical Practice in Dam Rehabilitation*
37 *Advances in Site Characterization: Data Acquisition, Data Management and Data Interpretation*
39 *Unsaturated Soils*
40 *Vertical and Horizontal Deformations of Foundations and Embankments*
41 *Predicted and Measured Behavior of Five Spread Footings on Sand*
42 *Serviceability of Earth Retaining Structures*
43 *Fracture Mechanics Applied to Geotechnical Engineering*
44 *Ground Failures Under Seismic Conditions*
45 *In Situ Deep Soil Improvement*
46 *Geoenvironment 2000*
47 *Geo-Environmental Issues Facing the Americas*
48 *Soil Suction Applications in Geotechnical Engineering*
49 *Soil Improvement for Earthquake Hazard Mitigation*
50 *Foundation Upgrading and Repair for Infrastructure Improvement*
51 *Performance of Deep Foundations Under Seismic Loading*
52 *Landslides Under Static and Dynamic Conditions - Analysis, Monitoring, and Mitigation*
53 *Landfill Closures - Environmental Protection and Land Recovery*
54 *Earthquake Design and Performance of Solid Waste Landfills*
55 *Earthquake-Induced Movements and Seismic Remediation of Existing Foundations and Abutments*
56 *Static and Dynamic Properties of Gravelly Soils*
57 *Verification of Geotechnical Grouting*
58 *Uncertainty in the Geologic Environment*
59 *Engineered Contaminated Soils and Interaction of Soil Geomembranes*
60 *Analysis and Design of Retaining Structures Against Earthquakes*
61 *Measuring and Modeling Time Dependent Soil Behavior*
62 *Case Histories of Geophysics Applied to Civil Engineering and Public Policy*
63 *Design with Residual Materials: Geotechnical and Construction Considerations*
64 *Observation and Modeling in Numerical Analysis and Model Tests in Dynamic Soil-Structure Interaction Problems*
65 *Dredging and Management of Dredged Material*
66 *Grouting: Compaction, Remediation and Testing*
67 *Spatial Analysis in Soil Dynamics and Earthquake Engineering*
68 *Unsaturated Soil Engineering Practice*
69 *Ground Improvement, Ground Reinforcement, Ground Treatment: Developments 1987-1997*
70 *Seismic Analysis and Design for Soil-Pile-Structure Interactions*
71 *In Situ Remediation of the Geoenvironment*
72 *Degradation of Natural Building Stone*
73 *Innovative Design and Construction for Foundations and Substructures Subject to Freezing and Frost*

74 *Guidelines of Engineering Practice for Braced and Tied-Back Excavations*
75 *Geotechnical Earthquake Engineering and Soil Dynamics III*
76 *Geosynthetics in Foundation Reinforcement and Erosion Control Systems*
77 *Stability of Natural Slopes in the Coastal Plain*
78 *Filtration and Drainage in Geotechnical/Geoenvironmental Engineering*
79 *Recycled Materials in Geotechnical Applications*
80 *Grouts and Grouting: A Potpourri of Projects*
81 *Soil Improvement for Big Digs*
82 *Risk-Based Corrective Action and Brownfields Restorations*
83 *Design and Construction of Earth Retaining Systems*
84 *Effects of Construction on Structures*
85 *Application of Geotechnical Principles in Pavement Engineering*
86 *Big Digs Around the World*
87 *Jacked Tunnel Design and Construction*
88 *Analysis, Design, Construction, and Testing of Deep Foundations*
89 *Recent Advances in the Characterization of Transportation Geo-Materials*
90 *Geo-Engineering for Underground Facilities*
91 *Special Geotechnical Testing: Central Artery/Tunnel Project in Boston, Massachusetts*
94 *Performance Confirmation of Constructed Geotechnical Facilities*
95 *Soil-Cement and Other Construction Practices in Geotechnical Engineering*
96 *Numerical Methods in Geotechnical Engineering: Recent Developments*
97 *Innovations and Applications in Geotechnical Site Characterization*
98 *Pavement Subgrade, Unbound Materials, and Nondestructive Testing*
99 *Advances in Unsaturated Geotechnics*
100 *New Technological and Design Developments in Deep Foundations*
101 *Slope Stability 2000*
102 *Trends in Rock Mechanics*
103 *Advances in Transportation and Geoenvironmental Systems Using Geosynthetics*
104 *Advances in Grouting and Ground Modification*
105 *Environmental Geotechnics*
106 *Geotechnical Measurements: Lab & Field*
107 *Soil Dynamics and Liquefaction 2000*
108 *Use of Geophysical Methods in Construction*
109 *Educational Issues in Geotechnical Engineering*
110 *Computer Simulation of Earthquake Effects*
111 *Judgment and Innovation: The Heritage and Future of the Geotechnical Engineering Profession*
112 *Soft Ground Technology*
113 *Foundations and Ground Improvement*
114 *Soils Magic*
115 *Expansive Clay Soils and Vegetative Influence on Shallow Foundations*
116 *Deep Foundations 2002: An International Perspective on Theory, Design, Construction, and Performance*
117 *Discrete Element Methods: Numerical Modeling of Discontinua*
118 *A History of Progress: Selected U.S. Papers in Geotechnical Engineering*
119 *Soil Behavior and Soft Ground Construction*
120 *Grouting and Ground Treatment*
121 *Probabilistic Site Characterization at the National Geotechnical Experimentation Sites*
122 *Sinkholes and the Engineering and Environmental Impacts of Karst*
123 *Recent Advances in Materials Characterization and Modeling of Pavement Systems*
124 *GeoSupport 2004: Drilled Shafts, Micropiling, Deep Mixing, Remedial and Specialty Foundation Systems*
125 *Current Practices and Future Trends in Deep Foundations*
126 *Geotechnical Engineering for Transportation Projects*
127 *Recycled Materials in Geotechnics*
128 *Soil Constitutive Models: Evaluation, Selection, and Calibration*
129 *Advances in Designing and Testing Deep Foundations*
130 *Advances in Pavement Engineering*
131 *Contemporary Issues in Foundation Engineering*
132 *Advances in Deep Foundations: In Memory of Michael W. O'Neill*
133 *Earthquake Engineering and Soil Dynamics*
134 *Soil Dynamics Symposium in Honor of Professor Richard D. Woods*
135 *Erosion of Soils and Scour of Foundations*

136 *Innovations in Grouting and Soil Improvement*
137 *Legal and Liability Issues in Geotechnical Engineering*
138 *Site Characterization and Modeling*
139 *Calibration of Constitutive Models*
140 *Slopes and Retaining Structures under Seismic and Static Conditions*
141 *International Perspectives on Soil Reinforcement Applications*
142 *Waste Containment and Remediation*
143 *Geomechanics: Testing, Modeling, and Simulation*
144 *Sinkholes and the Engineering and Environmental Impacts of Karst*
145 *Seismic Performance and Simulation of Pile Foundations in Liquefied and Laterally Spreading Ground*
146 *Asphalt Concrete: Simulation, Modeling and Experimental Characterization*
147 *Unsaturated Soils 2006*
148 *Advances in Unsaturated Soil, Seepage, and Environmental Geotechnics*
149 *Site and Geomaterial Characterization*
150 *Soil and Rock Behavior and Modeling*
151 *Advances in Earth Structures: Research to Practice*
152 *Ground Modification and Seismic Mitigation*
153 *Foundation Analysis and Design: Innovative Methods*
154 *Pavement Mechanics and Performance*
155 *Underground Construction and Ground Movement*
156 *Geomechanics II: Testing, Modeling, and Simulation*
157 *Computer Applications in Geotechnical Engineering*
158 *Contemporary Issues in Deep Foundations*
159 *Case Studies in Earth Retaining Structures*
160 *Dynamic Response and Soil Properties*
161 *Embankments, Dams, and Slopes: Lessons from the New Orleans Levee Failures and Other Issues*
162 *Problematic Soils and Rocks and In Situ Characterization*
163 *Geoenvironmental Engineering*
164 *Innovative Applications of Geophysics in Civil Engineering*
165 *Geosynthetics in Reinforcement and Hydraulic Applications*
166 *Educational Activities in Geotechnical Engineering*
167 *Geotechnics of Soil Erosion*
168 *Grouting for Ground Improvement: Innovative Concepts and Applications*
169 *Soil and Material Inputs for Mechanistic-Empirical Pavement Design*
170 *Probabilistic Applications in Geotechnical Engineering*
171 *Advances in Shallow Foundations*
172 *Soil Improvement*
173 *Advances in Measurement and Modeling of Soil Behavior*
174 *Designing Our Underground Space*
175 *Field Measurements in Geomechanics 2007*
176 *Analysis of Asphalt Pavement Materials and Systems: Emerging Methods*
177 *GeoCongress 2008: Geotechnics of Waste Management and Remediation*
178 *GeoCongress 2008: Geosustainability and Geohazard Mitigation*
179 *GeoCongress 2008: Characterization, Monitoring, and Modeling of GeoSystems*
180 *From Research to Practice in Geotechnical Engineering*
181 *Geotechnical Earthquake Engineering and Soil Dynamics IV*
182 *Pavements and Materials: Characterization, Modeling, and Simulation*
183 *Sinkholes and the Engineering and Environmental Impacts of Karst*
184 *Pavements and Materials: Modeling, Testing, and Performance*
185 *Contemporary Topics in Deep Foundations*
186 *Contemporary Topics in In-Situ Testing, Analysis, and Reliability of Foundations*
187 *Contemporary Topics in Ground Modification, Problem Soils, and Geo-Support*
188 *Advances in Ground Improvement: Research to Practice in USA and China*
189 *Characterization, Modeling, and Performance of Geomaterials*
190 *Asphalt Material Characterization, Accelerated Testing, and Highway Management*
191 *Road Pavement Material Characterization and Rehabilitation*

This page intentionally left blank

Foreword

An international conference titled, *"Challenges and Recent Advances in Pavement Technologies and Transportation Geotechnics"* was held in China during 3 – 6 August 2009. The conference was hosted by Changsha University of Science and Technology, China and co-sponsored by ASCE Geo-Institute, Asphalt Institute, Central South University, Chinese Society of Pavement Engineering, Deep Foundation Institute, Federal Highway Administration, US Department of Transportation, Hunan University, China, International Society for Asphalt Pavements, Jiangsu Transportation Research Institute (JSTRI), China, Korea Institute of Construction Technology, Korean Society of Road Engineers, Shanghai Highway & Transportation Society, Texas DOT, Texas Transportation Institute, and Transportation Research Board (TRB).

This geotechnical special publication constitutes the proceedings of the four sessions of the conference: Soil Behavior and Laboratory Testing, In-situ Test Methods for Site Characterization, Design and Quality Control of Earth Structures and Subgrades, Pile Foundations in Subgrade, and Tunnel Engineering.

Whilst soil has been used as construction material since ancient times, technological advances continue to be made in the means of exploring, testing and in the geotechnical methods for planning and designing. The knowledge and awareness of soil behavior is fundamental to all aspects of geotechnical engineering. The objective of this publication is to provide the reader with information and foster the data on recent advances in the in-situ and laboratory testing, pile foundation systems, tunneling and design procedures for earth structures. The collection of peer-reviewed papers accumulated here synthesizes the current and future progression in respective geotechnical fields.

Papers in this volume were reviewed by professional geotechnical engineers with expertise in the subject area. Each paper included in this publication has received at least two positive examine reviews. Authors were given the opportunity to modify their papers based on reviewer's suggestions prior to final submittal of the papers. The ideas in the papers are those of authors and do not necessarily represent the views of reviewers, editors and ASCE. All papers are eligible for discussion in the Journal of Geotechnical and Geo-environmental Engineering and are eligible for ASCE awards.

The editors of this publication express appreciation to all the reviewers and authors who made this publication possible. We are grateful to Donna Dickert, of ASCE, for her prompt and willing support.

The Editors

Dr. Liaqat Ali
School of Civil and Environmental Engineering, National University of Science and Technology
Sector H-12, Islamabad, Pakistan
liaqatnust@yahoo.com

Dr. A. Gomes Correia
Head of Geotechnical Group
University of Minho/DEC
Campus de Azurem
4800 – 058 GUIMARAES, Portugal
agc@civil.uminho.pt

Dr. Mingjiang Tao
Department of Civil and Environmental Engineering Worcester Polytechnic Institute
100 Institute Road, Worcester, MA 01609, USA
taomj@wpi.edu

Dr. Junsheng Yang
School of Civil Engineering and Architecture, Central South University, 22 Shaoshan South Road, Changsha City, Hunan Province, 410075, China
jsyang@mail.csu.edu.cn

Contents

Indexes

Swelling Behavior of Compacted Expansive Soils

Yan Kezhen[1] and Wu Luocheng[2]

[1]Hunan University, Changsha 410082, China; email: yankz2004@163.com.
[2]Hunan University ,Changsha 410082, China; email: wlcwillcg2006@yahoo.com.cn.

ABSTRACT. In this paper, swell pressures of the compacted expansive soil of Guangxi Province are investigated by a series of swelling laboratory tests with different initial moisture contents and dry density. The relationships of swell pressure with initial moisture content and dry density are established. The method to calculate the expansive characteristics is obtained when the water contents and total stress levels are changed. These relationships can be used in practical expansive soils engineering.

INTRODUCTION

Expansive soil is mainly made of hydrophilic mineral such as montmorillonite, illte and so on. Expansive soils will cause relatively large volumetric change when it absorbs water or when it dries. The expansive force will damage engineer structures when the volume of expansive soils changes. Hence it is of great significance to study the swelling behavior of expansive soil to engineering projects in expansive soil areas.

Many factors have an effect on the characteristics of expansive and the magnitude of expansive force including component of soil, water content, dry density and upper load. In recent years, a number of researchers have studied the problem of expansive soils and obtain a new calculation method which takes different factors into account. According to the swelling experiment of compacted expansive soils, Xu et al. (1997,1998) summarized the formula of capacity of compacted expansive soils due to the change of water content and different total stress levels. Scott et al. (2004) obtained the formula of capacity of compacted expansive soils due to the variation in water content. By one-dimensional and three-dimensional swelling experiments, Mosleh and Abdulmohsin (2003) obtained the method of estimating swelling characteristics of compacted expansive soils due to the changes of matrix suction, total stress levels and water content. However, only the single factor on swelling deformation was considered in the above methods. In fact, there are a lot of variables which affect expansive soils; furthermore, these factors are always coupled. So, it can not reflect the coupling of multi-factor very well above formulas. Based on the different factors, Zhang et al. (2005) obtained the swelling deformation mode of artificial compacted expansive soils with different initial water content, initial dry

density and total stress levels. However, the swelling deformation of expansive soils is mainly caused by the change of water content, the approach can only calculate the swelling deformation of saturated expansive soils, while expansive soils are normally in the unsaturated state in the practical engineering. Therefore, it is necessary to study the model of swelling deformation due to the change of water content.

EXPANSIVE FORCE CHARACTERISTICS OF COMPACTED EXPANSIVE SOILS

The Relationships of Dry Density and Expansive Force

The expansive soil specimens are taken from the highway of someone areas in Guangxi province. The physical properties of the expansive soils are shown in Table 1. With different moisture contents and dry density in soil specimen, a series of expansibility tests are tested according to the criterion. Fig.1, 2 and 3 show the relationship of dry density and expansive force with the same water content. From the three figures, it can clearly be seen that the expansive force increases rapidly with the increase of dry density and there is an exponential relationship between them. When the water content of soils is same, the expansive force of soil sample no. 1 is the largest and the sample no. 3 is the smallest. The main cause is that the free expansibility of soil sample no. 1 is 60% which is the largest and the free expansibility of soil sample no. 3 is 33% which is the smallest. So, the results show that the expansive force of expansive soils has a relationship with the free expansibility. In other words, the free expansibility is higher, the expansive force will be larger too.

Table 1. The Physical Properties of the Three Soil Samples

Soil Samples	Liquid Limit (%)	Plasticity Limit (%)	Plasticity Index (%)	Moisture Content (%)	Specific Gravity	Dry Density (KN/m^3)
1	77.2	34.7	42.5	18	2.73	17.2
2	56	30.0	26	20	2.69	16.5
3	55.4	31.5	23.9	22	2.70	16.8

The Relationship of Water Content and Expansive Force

Fig. 4, 5 and 6 show the relationships of water content and expansive force with the same dry density. From the experiment results, it can clearly be seen that when the dry density of soil samples is same, the expansive force decreases with the increase of water content and there is a fine exponential relationship between of them.

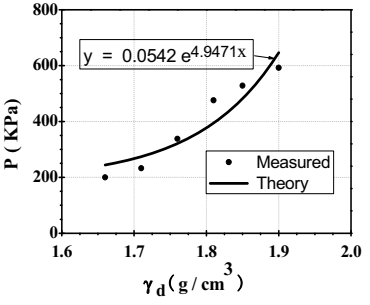

FIG. 1. Relations between expansive force and dry density of sample 1.

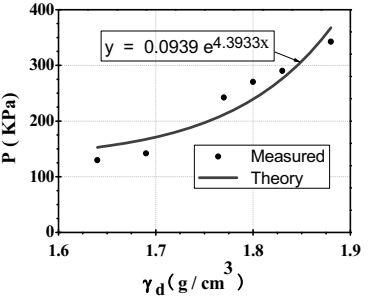

FIG. 2. Relations between expansive force and dry density of sample 2.

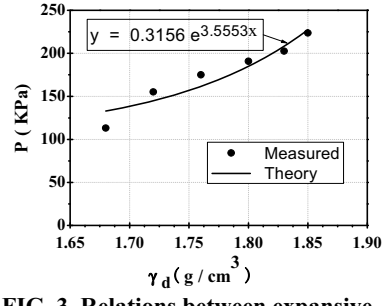

FIG. 3. Relations between expansive force and dry density of sample 3.

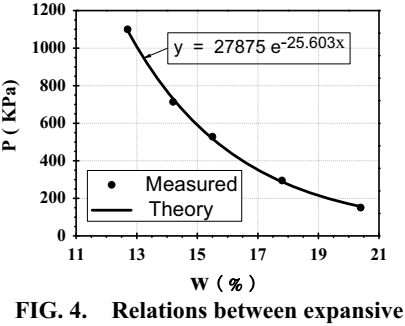

FIG. 4. Relations between expansive force and water content of sample 1.

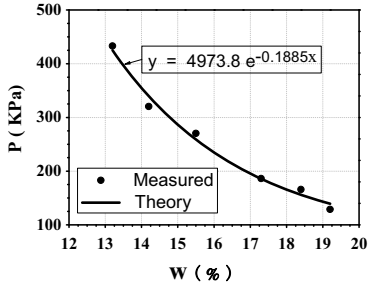

FIG. 5. Relations between expansive force and water content of sample 2.

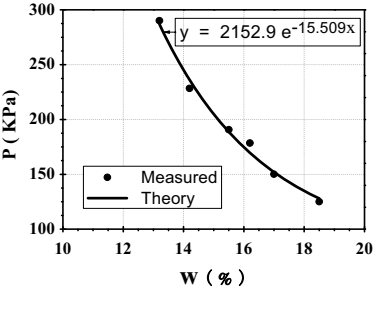

FIG. 6. Relations between expansive force and water content of sample 3.

THE SWELLING DEFORMATION CHARACTERISTIC OF COMPACTED EXPANSIVE SOILS

The Relationship of Swelling Deformation and Water Content

Figs. 7-9 show the relationship of swelling deformation and water content. It can clearly be seen that the swelling deformation of expansive soils decreases with the increasing of initial water content and there is a fine linear relationship between them. Therefore, the relationship between the swelling ratio and water content can be written as:

$$d_h = a - c_{wp} w_0 \quad (1)$$

Where d_p is the swelling ratio, w_0 is initial water content, a and c_{wp} are the parameters.

Fig.10 indicates that the relationship of the change value of water content and expansive deformation at different level of upper loads. Therefore, the relationship of the change value of water content and expansive deformation can be written as:

$$d_p = c_{e,wp}(w - w_0) \quad (2)$$

Where w is the final water content, $c_{e,wp}$ is the swelling coefficient which means the expansion ratio of expansive soils under the unit change of water content.

Scott et al. (2004) studied the swelling coefficient by the one-dimensional and three-dimensional swelling experiments for natural expansive soils and compacted expansive soils, and thought the level of upper load had important influence on the swelling coefficient of expansive soils. Thus, it is necessary to take into account the influence of upper load when the expansive deformation is calculated.

The Relationship of Swelling Deformation with the Change Value of Upper Load

Fig.11 shows the relationship between the swelling deformation and the change value of upper load under different water content. From fig.11, it can be seen that the swelling deformation decreases with the increase of upper load. So the relationship of

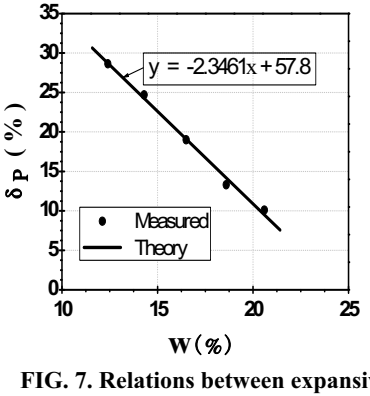

FIG. 7. Relations between expansive swelling deformation and initial water content of sample 1.

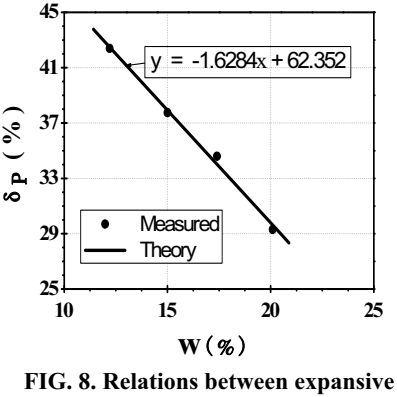

FIG. 8. Relations between expansive swelling deformation and initial water content of sample 2.

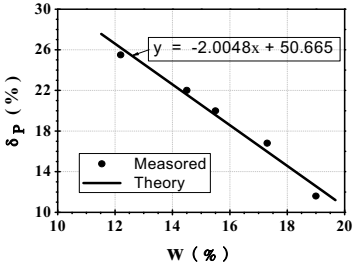

FIG. 9. Relations between swelling swelling deformation and initial water content of sample 3.

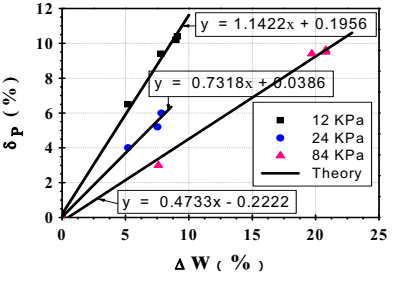

FIG. 10. Variation of swelling coefficient with different upper load.

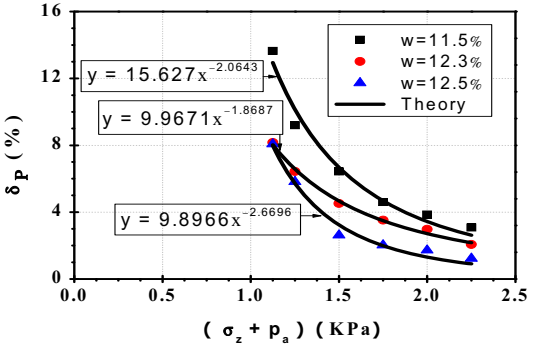

FIG. 11. Relationship between the swelling quality and upper load under the different water content.

the swelling deformation and the change value of upper load can be written as:

$$d_p = A(\frac{s_z + p_a}{p_a})^{-B} \quad (3)$$

Where A and B are parameters, p_a is the atmospheric pressure. When the upper pressure is equivalent to zero in equation (3), the swelling deformation is equal to the value of A. The parameter B is influenced by the types of soils and the variations of water content.

The Method to Calculate Swelling Deformation

From equation (4) we can see that A is the value of swelling deformation when the upper pressure is zero. So substituting equation (2) into (3) yields the following:

$$d_p = c_{e,w0}(w - w_0)(\frac{s_z + p_a}{p_a})^{-B} \quad (4)$$

Where the $c_{e,wo}$ is the swelling coefficient when the upper pressure is zero.

The magnitude of swelling deformation is affected not only by the change of water content and upper load pressure, but also by initial dry density. The equation (4) does not take the initial dry density into account. According to the different compaction conditions, the swelling coefficient $c_{e,w0}$ can be obtained through a series of swelling laboratory tests by soil samples with different compaction degree. Thus, the swelling values can be calculated as following:

$$\Delta H = \sum_{i=1}^{n} h_i c_{ei,wo} (w_i - w_{oi}) (\frac{\sigma_{zi} + P_a}{P_a})^{-B} \quad (5)$$

Where h_i is the thickness of soil layer, $c_{ei,w0}$ is the swelling coefficient of soil layer. there is no difference in other parameters. When the three-dimensional advancing effects of swelling deformation is taken into account, the calculation formula of swelling quality of expansive soils can be written as:

$$\Delta H = \sum_{i=1}^{n} h_i f_w c_{ei,wo} (w_i - w_{oi}) (\frac{\sigma_{zi} + P_a}{P_a})^{-B} \quad (6)$$

Where f_w is the modify coefficient and can be obtained in Scott et al. (2004).

CONCLUSIONS

The swelling force and swelling deformation are investigated by a series of swelling experiment of compacted expansive soil in the highway of some areas in GuangXi province. The study show that the relationships of swelling force with initial water content and dry density are exponential relationship. The swelling deformation is proportional to the change of water content and is the negative exponential relationship with upper pressure. Based on the experimental results of compacted expensive soils, a method to calculate swelling deformation is obtained under the condition of changed water content and changed upper loads simultaneity. In this paper, the results provide a simple and effective method to calculate the deformation of expansive soil subgrade. However, due to the lack of field experimental results, the computational model needs to be validated in the future.

REFERENCES

Xu, Y.f. and Shi, C.L. (1997). "Swelling Law of Expansive Soil In NingXia." *Chinese Journal of Geotechnical Engineering*, Vol. 19 (3): 95-98.

Xu, Y.f. (1998). "Calculation Method of The Settlement of Expansive Soil Foundation." *Journal of Hohai University.,* Vol. 26 (4): 4548.

Scott, A.M., Robert, B.G., and Alan, F.R. (2004). "A practical method for prediction expansive soil behavior"., *GeoTrans*, 1144-1152.

Mosleh A.A. and Abdulmohsin, W.D. (2003). "Experimental study of lateral restraint effects on the potential heave of expansive soils." *Engineering Geology.,* Vol. 69 : 63-81.

Zhang, A.J., Ha, A.Y., and Luo, Y.S. (2005). "Swelling Law And Calculation Mode of Compacted Expansive Soil." *Chinese Journal of Rock Mechanics and Engineering.*, Vol. 24 (7): 1236-1241.

Research on Applying Glass Fiber Cement Soil to Strengthen Soft Soil Subgrade

YIN Yong[1] and YU Xiao-jun[2]

[1]Lecturer, Department of Civil Engineering, Yancheng Institute of Technology, 0515-88298672; yyvalor@126.com

[2]Associate Professor, Department of Civil Engineering, Yancheng Institute of Technology, Post Doctor, Institute of Geotechnical Engineering, Hohai University, Xikang road, Nanjing City, 025-83787216; flyingfish7101@126.com

ABSTRACT: Soft soil is widely distributed in the world. With the increase in construction of highways and railways on soft soil, the treatment of soft soil subgrade is becoming more and more extensive. Based on the reinforcement effects of glass fiber, the possibility of applying glass fiber to strengthen soft soil subgrade is discussed in this paper. More than 100 groups of cement soil samples' laboratory testing results are presented and compared. The analysis of test results indicates that glass fiber mixed in cement soil can improve the strength and deformation characteristic of cement soil in a certain degree. It could also be used as a possible replacement of soft soil subgrade. The findings are a new contribution to the soft soil subgrade treatment techniques.

INTRODUCTION

Soft soils are extensively distributed in coastal and inland areas in China. This kind of soils is considered problematic due to their poor mechanical properties, such as small bearing capacity and long-term settlement under surcharge load. With the rapid development of the economy of China, lots of infrastructures are being constructed in soft soil areas. Therefore, soft soils often need to be treated by soft ground improvement techniques, among which, cement deep mixing method is widely used (GAO Guo-rui and LI Jun-cai, 1996). The soft soils mechanical properties such as compression strength and tensile strength can be improved to a certain extent after foundation treatment. However, the increase in compression resistance is always associated with brittle failure of cement soil under compression and tension and this will result in project failure. To overcome this undesired problem and get a higher strength, many researchers apply additional additives in the cement soil (Kaniraj and

Havanagi, 2001). These additives include fly ash, silica fume, slag powder, lime, industrial waste gypsum, and various fibers, etc. Each of them has achieved certain success.

Discrete randomly distributed fiber as a new reinforcement material has also been used to strengthen cement soil in soft ground (Shbib and Okumura, 2002), as the high tensile strength of the fiber can solve the problem of brittle failure of cement soil. In this paper, glass fiber is mixed in cement soil as a reinforcement material to improve the strength and deformation behavior of the soft subgrade through indoor test. The tests conducted on glass fiber cement soil include the compression tests, the tensile tests and the triaxial tests under a certain confining pressure. Results of the experimental work are therefore analyzed.

MATERIAL AND METHODOLOGY

Materials of Test

Index properties of the soft clay from Yancheng express highway are summarized in table1.

Table 1. Physical and Mechanical Properties of Soil Samples

w (%)	γ (kN/m^3)	w_L (%)	w_P (%)	I_L	I_P	C (kPa)	ϕ(°)
39.2	18	40.4	12.6	0.96	27.8	14	12

where:

w water content, γ unit weight, w_L liquid limit, w_P plastic limit, I_L liquidity index, I_P plasticity index, C cohesion, ϕangle of internal friction.

The cement type was P.C32.5, its compressive strength of cubic sample with 3 days was 21.0 MPa, and its tensile strength of cubic sample with 28 days was 42.7 MPa. The chopped and discrete strands of glass fiber were taken as the reinforcement material. For the convenience of sampling, the length of glass fiber was taken as 10mm. Its basic physical and mechanical properties are shown in Table 2.

Table 2. Physical and Mechanical Properties of Glass Fiber

Type	Monofil Dia.(μm)	Tensile Strength (MPa)	Contents of Inflammable Matter (%)	Water Content (%)	Linear Density (tex)
AR	7	2.24×10^3	≤1.5	4.0	200-235

where: AR Alkali-proof glass fiber.

Test Method

The cubic size of specimens in unconfined compression test and splitting tensile test was 7.07 cm × 7.07 cm × 7.07 cm. The diameter of cylinder specimens of triaxial test was 3.91 cm, and its height was 8 cm. The mixture ratio of materials in each group is shown in table 3. Materials in each group were mixed uniformly before being placed into a mold. The specimens were placed in the mold and covered with a plastic membrane for two days, and they were cured in the water to the desired age after demoulding.

Table 3. The Amount and Matched Groups of Specimens

Group	Cement Dosage(%, Accounts for the Weight of Soil)	Water Cement Ratio	Glass Fiber Content(%, Accounts for the Weight of Soil)	Parallel Specimens Amount		
				7 Days	30 Days	90 Days
A	12	0.5	0	3	3	3
B	15	0.5	0	3	3	3
C	12	0.5	1	3	3	3
D	12	0.5	2	3	3	3
E	12	0.5	3	3	3	3

In the tests of compression strength and tensile strength, the load was applied continuously and uniformly with the rate of 8 mm/min until the specimens breaking (Xiao ling et al, 1985). Triaxial tests took the form of unconsolidated-undrained test under the confining pressure of 100 kPa with three different ages of the specimens. The speed rate of axial strain was controlled as 1% / min (0.8 mm/min), and the data of stress were recorded every 0.2 mm of the axial strain until peak value was reached. The triaxial tests should not be stopped until the strain increase to 3%~5% continuously after the peak value (Nanjing Hydraulic Research Institute, 2003).

RESULTS AND DISCUSSIONS

Unconfined Compressive Strength of Cement-soil Mixed Glass Fiber

Compression test results of the cement-soil mixed glass fiber are shown in Fig. 1. where: q_u Unconfined compressive strength of the specimens; and T Ages of the specimens, with 7 days, 30 days and 90 days respectively.

The results illustrate that cement soil mixed with glass fiber contributes well to the effects of the strength of soft soil with three kinds of ages, and the extent of the strength increase is proportional to the glass fiber content. In three kinds of ages, the specimen mixed with 12% cement and 3% glass fiber has a larger compressive

strength than the specimen mixed merely with 15% cement.

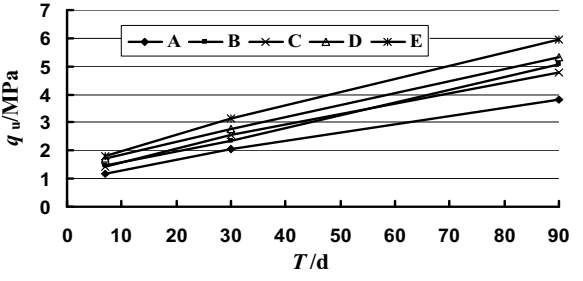

FIG. 1. Relationship of unconfined compressive strength.

In the aspect of failure modes, the crack width and quantity of the specimens with glass fiber are distinctly smaller than those without glass fiber. Few cracks were found as the specimens of glass fiber cement soil broke, while the specimens mixed with cement only peeled off the surface besides more cracks. Therefore, the glass fiber cement soil obviously helps in reducing brittleness than original cement soil.

Tensile Strength of Cement-soil Mixed Glass Fiber

From the results of tensile test shown on Fig. 2, the mixture of glass fiber also helps in improving the tensile strength of soft soil treated by cement soil with three kinds of ages. The tensile strength of specimens mixed with glass fiber and cement is obviously higher than those mixed with cement only, which can be seen from curves in Fig. 2. The increase of the tensile strength in short time seems larger than those in long time. It is found that the glass fiber mixed in cement soil for soft soil treatment can improve tensile properties of soft soil in a short period.

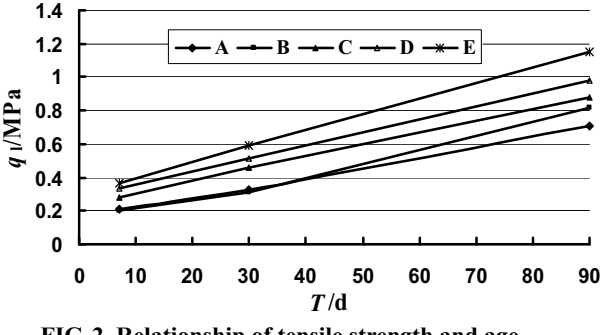

FIG. 2. Relationship of tensile strength and age.

Where: q_l Tensile strength of the specimens; and T Ages of the specimens, with 7 days, 30 days and 90 days respectively.

As for the failure mode, specimens of 90d without glass fiber present the character of brittle failure obviously in split tensile test. The fracture plane penetrates the entire specimen. While the specimens mixed with glass fiber show cracks on its surface when breaking, but they are not ruptured, which is attributed to the tensile strength of glass fiber. The crack width and depth of specimens with glass fiber are all smaller than specimens with cement only. Therefore, the mixture of glass fiber plays an important role to improve crack resistance of soft soil treated by cement.

Stress-strain Relationship of Cement-soil Mixed Glass Fiber

To investigate the deformation character of the specimens, triaxial test with three different kinds of ages are carried out under the confining pressure of 100 kPa. Stress and strain relationships of the specimens are illustrated in Figs. 3-5.

Where: ε - Axial strain; and $(\sigma_1-\sigma_3)$ - Deviatoric stress.

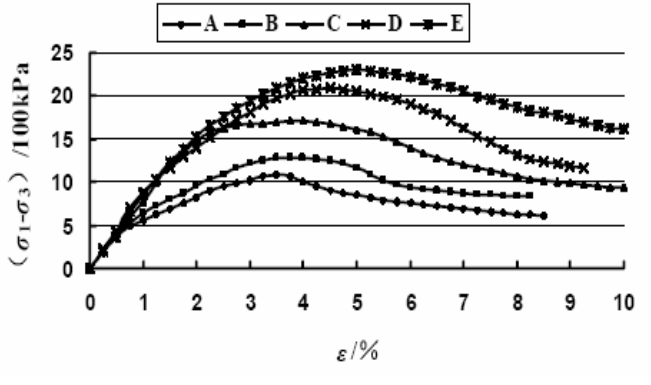

F IG. 3. Stress-strain relationship of 7d ages.

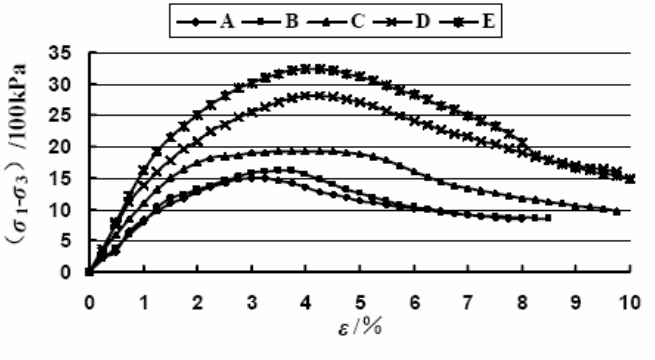

FIG. 4. Stress-strain relationship of 30d ages.

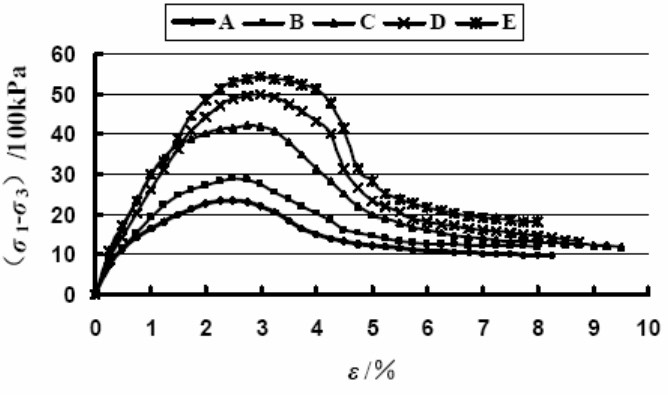

FIG. 5. Stress – strain relationship of 90d ages.

In three kinds of ages, the stress-strain curves of all cement soil specimens exhibit nonlinear features, which are similar to the deformation characteristics of the over-consolidated clayey soils. The difference of peak deviatoric stress and axial strain between specimens mixed merely with 12% or 15% cement is not obvious in the short term of 7d ages and 30d ages. However, the peak deviatoric stress of specimens mixed with glass fiber is obviously higher than those without glass fiber under the same condition of cement dosage. The peak deviatoric stress and axial strain of specimens mixed with glass fiber are directly proportional to the content of glass fiber. At the same time, the strength enhancement effect of glass fiber is verified with three kinds of ages. For the axial strain at failure, glass fiber cement soil specimens are also higher than those without glass fiber under the same conditions, especially when failed in the short term. The difference of peak axial strain between them decreases with the increase in age.

As for the failure mode, the short age specimens, such as 7d and 30d aged specimens, present plastic shear failure mode, with a distinct inclined crack penetrating the entire specimen. The fracture plane intersects major principal stress plane with an angle of about 60° . With the increase in age, glass fiber cement soil of 90d have compression fractures at the specimen ends when breaking, its failure mode is similar to brittle failure. Specimens mixed with cement only have vertical cracks which penetrate the two ends of the specimens when breaking, and it shows characteristics of brittleness failure.

CONCLUSIONS

(1) Glass fiber has a better effect in strengthening soft soil subgrade than with cement

only.
(2) Mixing with glass fiber, soft soil is modified as strong as over-consolidated soils. The compressive strength and tensile strength of cement soil have a great improvement with the increase of glass fiber content and specimen ages.
(3) Glass fiber has a good effect to improve crack resistance of cement soil. The peak axial strain of glass fiber cement soil is smaller than those specimens mixed with cement only, and the difference decreases with age.

Glass fiber as a new additive to cement soil is expected to play a positive role as cost-save factor and may open a new era of soft soil subgrade improvement by cement soil technique. And the work described in this paper is a preliminary research of glass fiber reinforced material, other more researches need to be carried out for more detailed properties of glass fiber strengthened cement soil in soft soil ground treatment field.

REFERENCES

GAO Guo-rui and LI Jun-cai (1996). "Study of Effect of Reinforcing Soft Cohesive Ground with Portland Cement." *Journal of Engineering Geology*,Vol.4(1):45-52.

Kaniraj, S. and Havanagi, V. (2001). "Behavior of Cement-stabilized Fiber-reinforced Fly Ash-soil Mixtures." *Journal of Geotechnical and Geoenvironmental Engineering*,Vol.127(7): 574-584.

Shbib, R. and Okumura, T. (2002). "Quantitative Analysis of Fiber Reinforced Cement Deep Mixing Soil Composite (FR-CDM)." *The 15th Engineering Mechanics Conference*, *Columbia University*, June 2-5, 2002, New York: 1-8.

Xiao ling et al (1985). "Construction material-cement soil." *China Water Power Press*, Beijing: 257-259.

Nanjing Hydraulic Research Institute (2003). "Model Specification for Soil Testing." *China Communications Press*, Beijing: 86-95.

Study on the Strength Mechanism of Coarse-Grained Soil Influenced by Clay Content Based on Laboratory Test

WANG Hong-gui, XU Lin-rong, CHEN Jie-jin and LV Da-wei

School of Civil Engineering & Architecture, Central South University, Changsha, Hunan 410075, China
email: guihonglong@163.com

ABSTRACT: Featured by its high strength and good water stability, coarse-grained soil can be mixed with clay and used as fine-property filler in embankment construction. However, the mixing ratio is usually difficult to determine. If the coarse-grained soil content is excessively high, the embankment is prone to crack or damage because of cohesion deficiency. On the contrary, if the coarse-grained soil content is too low, its high strength can not be utilized effectively, which may result in strength deficiency and excessive settlement. Based on field survey and laboratory test results, this paper has made deep analysis on the strength mechanism of glacial sediment coarse-grained soil, and the reasonable mixing ratio of coarse-grained soil and clay soil has been discussed.

INTRODUCTION

The scope of this paper is to show some field survey and laboratory test results obtained in the framework of a more comprehensive research project aimed at the research of the "Highway roadbed construction technology in glacial sediment areas". Such a project (2006A24-611 – coordinated by XU Lin-rong of Central South University) is supported by the Sichuan Provincial Communications Department.

Glacial sediment is widely distributed in areas in western China. It is made up of sediments transported by glacier, whose main components are gravel, sand pebble, etc. Therefore it has good strength and can be used as the filling material in embankment construction. Glacial sediment is typical coarse-grained soil with low adhesive force and poor integrity. Accordingly clay soil should be mixed together to obtain better compaction results, and enhance the overall strength of the embankment (Rahardjo et al. 2008; Indrawan et al. 2006). Based on the field survey (Wakatsukia et al. 2005) and laboratory large scale coarse-grained soil triaxial shear test (Pallara et al. 2006; Watson et al. 2002), the strength mechanism of glacial sediment coarse-grained soil has been studied, and the reasonable mixing ratio of coarse-grained soil and clay soil has been discussed (Loupasakis et al. 2008).

BACKGROUND

YaLu (Yaan - Lugu) highway is located in the transition zone between the

southwest edge of Sichuan basin and the plateau area, where complex topography, active seismic motion and geological disasters are very common. Consequently, sophisticated technology is demanded to overcome the great difficulty during construction. Therefore, it has been selected as the high technology demonstration project of science and technology in the Ministry of Transport of the P.R.China.

According to the field investigation and sampling study results in 2007, we have found massive glacial sediment (Q_{2+3}^{fgl}) along the YaLu highway. In consideration of its engineering properties and economic benefits, glacial sediment can be used as embankment filling material. But as a completely new filling material, there is no engineering experience and related research literature which could be consulted. Therefore, it is necessary to make further research, especially on the mixing ratio of coarse-grained soil and clay soil.

FIELD INVESTIGATION

The distribution range and formation reason has been ascertained through several months filed investigation (See FIG. 1). The typical gradation curves of glacial sediment used as filling material has also been obtained. Based on the proposed research scheme and in combination with the practical conditions, four roadbed sections have been selected to conduct long term field monitoring test. Meanwhile, 5 tons of soil samples has been obtained in Luba village (K178 + 200) to carry out laboratory test.

FIG. 1. Glacial sediment distribution field investigation and disturbed samples obtained on site.

EXPERIMENTAL SCHEME

According to the design and construction scheme, four factors have been considered in the experiment, including stone content, clay content, compaction degree and reinforced layer, and every factor has three levels. Comprehensive test is unpractical because of the experiment times (81 groups). Therefore, orthogonal test method has been adopted. The experiment grouping scheme has been formulated in the orthogonal design table $L_9(3^4)$ based on orthogonal design principles (FANG and MA 2001). Nine groups have been arranged in total and the level difference is approximately equal (See Table 1). Three samples have been made and tested in each group (the confining pressure is respectively 100 kPa, 200 kPa and 300 kPa). Because the embankment is working in the condition of unsaturated, non-consolidation and non-drainage during construction and operation, the experiment has been performed under the same condition. The test samples of each group have been made according to the optimum water content obtained form heavy compaction test.

Table 1. Orthogonal Experimental Scheme

Group Number	Stone Content (%)	Clay Content (%)	Compaction Degree (%)	Reinforced Layer	Optimum Water Content (%)	Maximum Dry Density (g/cm^3)
1	30.7	9.5	93	0	7.20	2.08
2	30.7	5.9	90	2	7.14	2.09
3	30.7	2.3	96	1	6.84	2.12
4	40	9.5	93	0	6.86	2.14
5	40	5.9	90	2	6.80	2.14
6	40	2.3	96	1	6.49	2.17
7	50	9.5	93	0	6.43	2.19
8	50	5.9	90	2	6.38	2.19
9	50	2.3	96	1	6.12	2.20

LABORATORY APPARATUS AND EXPERIMENTAL PROCEDURE

The experiment has been carried out on the SZ304 large scale triaxial test machine, whose sample size is 30 cm × 60 cm (D × H).The maximum permissible particle size is 6 cm. The sample has been made by artificial method with a heavy hammer (approximately 30 kg) and a charging cylinder (see FIG. 2).

The glacial sediment samples obtained from field have been sun dried and then sieved to the following seven groups: 40~60 mm, 20~40 mm, 10~20 mm, 5~10 mm, 2~5 mm, 0.075~2 mm and 0~0.075 mm (See FIG. 3) (Founie et al. 2007). Based on the experiment scheme and the gradation curves of the filling material, the sieved soil samples have been mixed together. The water is then added in according to the optimum water content of each group.

FIG.2. SZ304 triaxial test apparatus and sampling devices.

FIG. 3. Several groups of soil sample after sieving.

For better compaction effect, each sample has been divided into ten layers during sampling process, namely the thickness of each layer is 6cm. The well-mixed soil sample have been added into the charge cylinder and compacted layer by layer. Each interface has been pounded by a steel rebar to ensure closely junction. In the process of compaction the total height of each sample should be measured frequently to control the thickness of each layer. By this way, the soil sample can be compacted

evenly and scheduled compaction degree can be reached (see FIG. 5).

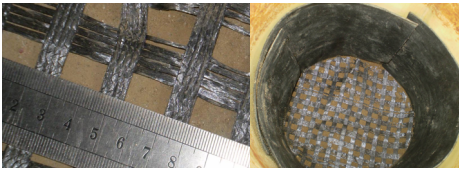

FIG. 4. Geotechnical grille is used as reinforce material in test sample.

FIG. 5. Compaction degree control and sampling process.

EXPERIMENTAL RESULTS

The results of cohesion force (c) and internal friction angle (ϕ) of soil samples in different groups were shown in Table 2.

Table 2. Results of the Orthogonal Experiment

Group Number	Clay Content (%)	Cohesion Force (kPa)	Internal Friction Angle (°)
1	9.5	42	41. 8
2	5.9	123	43. 7
3	2.3	66	43. 5
4	9.5	71	40. 8
5	5.9	75	42. 8
6	2.3	199	38. 0
7	9.5	315	29. 2
8	5.9	162	40. 1
9	2.3	55	42. 6

Due to the limited space, it is impossible to analyze all the experiment results in detail. Therefore, only the influence of the clay content on the strength of glacial sediment was discussed in this paper. Through visual analysis method (FANG and MA 2001), the relation between the clay content and strength parameters (cohesion force and internal friction angle) has been obtained and shown in Table 3. The cohesion force and internal friction angle values in Table 3 are obtained by averaging all the test results of the same clay content. For example, 106.7=average {66, 199, 55}. The curves of strength parameters' variation along with the clay content can be seen in FIG. 6.

From Table 3 and Fig. 6, it is shown that the cohesion force (c) increases obviously along with the increase of clay content and the clay content-c curve is approximately a straight line. The cohesion force value increases by 34% (from 1.067 to 1.427) while the clay content changes from 2.3% to 9.5%, which indicates that cohesion force is significantly influenced by the change of clay content.

Table 3. Cohesion Force and Internal Friction Angle with Different Clay Content

Clay Content (%)	Cohesion Force (kPa)	Internal Friction Angle (%)
2.3	106.7	41.4
5.9	120.0	42.2
9.5	142.7	37.3

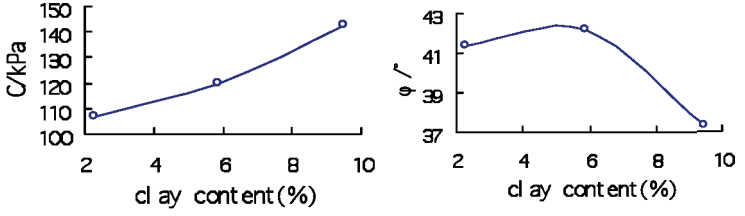

FIG. 6. Clay content-c curve and clay content- ϕ curve.

From the clay content- ϕ curve, it can be seen that the internal friction angle increases slightly with the clay content increasing at first. When the clay content is about 5%, the internal friction angle reaches its maximum value. Thereafter, it decreases rapidly. Trough analysis on the experimental data and the failure mode of test samples, the authors consider that when the clay content is relative low in test samples, there are a lot of tiny voids among coarse particles. Hence it is helpful for the soil compaction when the clay content increases, as a result the internal friction value increases with it. But when the clay content increases to a certain value, the lubrication action of clay destroys the bite force among coarse particles. Consequently, the internal friction value decreases.

DISCUSSION

Based on coarse-grained soil laboratory test results, the infection law of clay content on cohesion force and internal friction angle has been ascertained. We can simulate the infection law respectively with a function, such as $c=c(x)$ and $\phi=\phi(x)$,where x represents clay content. Substituting the above functions to coulomb law, we can get the following function: $\tau_f = \sigma \tan[\phi(x)] + c(x)$, where τ_f represents the shear strength of soil and σ represents the normal stress on shear plane. This function interprets the relationship between strength mechanism of coarse-grained soil and clay content. The reasonable mixing ratio can be got by seeking the maximum value of shear strength. Due to limited space, the authors will discuss this in another paper.

CONCLUSIONS

Through the analysis of the large scale triaxial test results of glacial sediment, the following conclusion can be drawn:

(1) The clay content has significant effect on the cohesion force of coarse-grained soil, which increases significantly with the clay content.

(2) As for the friction angle, the influence law is quite different. The friction angle increases slightly with the clay content and reaches to a peak value, then decreases rapidly.
(3) Considering above conclusions comprehensively, it can be concluded that the relationship between the strength of coarse-grained soil and clay content is not linear. For a particular soil, there should be an optimal clay content which makes the maximum overall strength of coarse-grained soil. The test results of this paper can be used as reference for further research to determine the reasonable mixing ratio of glacial sediment.
(4) The clay content also has important influence on ultimate bearing capacity and stability of coarse-grained soil, which needs further research.

ACKNOWLEDGMENTS

The research project was supported by the Sichuan Provincial Communications Department. The assistance of Mr. Liu Ming-yu, Mr. Hu Li-ming, Mr. Yu Hui and MS. SHAN Li-ping in carrying out this research is gratefully acknowledged.

REFERENCES

FANG Kai-tai, MA Chang-xing. (2001). “Orthogonal and uniform experimental design" *Beijing: Science Press.*

Fourie Walter J., Barnes David L. and Shur Yuri. (2006). "The formation of ice from the infiltration of water into a frozen coarse grained soil." *Cold Regions Science and Technology*, 48 (2007) 118–128.

Indrawan I.G.B., Rahardjo H., Leong E.C. (2006). "Effects of coarse-grained materials on properties of residual soil." *Engineering Geology,* 82 (2006) 154– 164.

Loupasakis C. J., Christaras B. G., Dimopoulos G. Ch., et al. (2008). "Evaluation of Plasticity Models’ Ability to Analyze Typical Earth Dams’ Soil Materials." *Geotech Geol Eng.,* DOI 10.1007/s10706-008-9212-5.

Pallara O., Froio F., Rinolfi A. and Presti D. Lo. (2006). "Assessment of strength and deformation of coarse grained soils by means of penetration tests and laboratory tests on undisturbed samples." *Soil Stress-Strain Behavior: Measurement, Modeling and Analysis,* 201–213.

Rahardjo H., Indrawan I.G.B., Leong E.C., et al. (2008). "Effects of coarse-grained material on hydraulic properties and shear strength of top soil." *Engineering Geology,* ENGEO-02811.

Wakatsuki Tsuyoshi, Tanaka Yukiya and Matsukura Yukinori. (2005). "Soil slips on weathering-limited slopes underlain by coarse-grained granite or fine-grained gneiss near Seoul, Republic of Korea." *Catena,* 60 (2005) 181–203.

Watson S.J., Barry D.A., Schotting R.J., et al. (2002) "Validation of classical density-dependent solute transport theory for stable, high-concentration-gradient brine displacements in coarse and medium sands." *Advances in Water Resources*, 25 (2002) 611–635.

SEM Microstructure and Chemical Foamed-Soil Modification Tests for Swelling Red Strata in Subway Shield Tunneling Engineering

Bo Liu[1], Tao Li[2], and Guogang Qiao[3]

[1]Professor, Department of Civil Engineering, China University of Mining and Technology, Beijing, P. R. China; Beijing 100083, dr_boliu@163.com
[2] Assistant Professor, [3] Ph. D student

ABSTRACT: A difficult problem for tunneling in red strata soils in Guangzhou subway is that the mud cakes are easily formed in the cut face of shield machine. It has frequently induced ground failures and collapse accidents. The microstructures of red soil are studied using SEM (scanning electron microscope). The SEM tests disclose the important microstructures of red strata minerals such as micro-lamina tactoid, petal-shape and micro-porosity. The mechanism of water-induced red strata swelling damage and high-viscosity characteristics are then investigated. The disclosed microstructure and micro-porous properties provide the evidences for understanding the mechanical behavior of Guangzhou swelling red strata soils. Furthermore, the chemical foamed-soil modification tests for red soils are presented. Experiments on foam modified red soils disclose the relationship between permeability and fluidity for foamed red soils and sandy soils in subway engineering. This research is helpful for applying foamed soil to stabilize the tunneling face and to prevent ground seepage damage in shield tunneling construction.

INTRODUCTION

Red sandstone strata, heavily weathered granite residual soils extensively distributed in South China, have imposed very serious threat to the construction safety of Guangzhou subway projects. When shield tunneling in these complex red sandstone strata, the soil-cake phenomenon, strata damages and collapse accidents such as the soil spewing, slurry extruding happen frequently. The strata damage is a long-standing problem troubling the shield construction (Wang 2004). Once the large volume hard cake is formed, it will drop the torque of shield head cutter and reduce the tunneling advance speed greatly (Yan 2005, Hou & Liu 2006, Chen 2006).

MINERAL COMPOSITIONS AND MICROSTRUCTURE TESTS

Sampling and Mineral Composition Tests

In order to study the microstructure, the mineral compositions and the swelling mechanism of Guangzhou red strata, samples are taken from all the typical sites. The sampling sites include 5 subway stations and 4 tunnel sites. The samples include the

main complex red strata, i.e., red soil, whole, strong weathered sandstone soils; sandy clay, red sandstone and so on. Microcosmic tests mainly include SEM analysis tests and X-ray diffraction analysis tests (XRD) (Hou & Liu 2006, Zhang & Wang 1978). The quantitative analyses of clay minerals and total minerals of red strata samples show that the content of clay minerals in Guangzhou red strata is up to 40% (see Table 1). The relative content of illite-smectite is reached to 47%. It shows that Guangzhou red strata are abundant with clay minerals.

Table 1. Mineral Composition of Red Strata in Guangzhou Subway with XRD Tests

Site	Soil / Rock	Relative Composition of Mineral in the Rock and Soil / %					Ratio of Mixolimnion / %		Clay Amount in Total Mineral /%
		S	I/S	I	Kao	C	C/S	I/S	
1	Red clay	54	/	46	/	/	/	/	35.5
2	Red sandy clay	64	/	36	/	/	/	/	39.9
3	Red argillaceous siltstone	/	47	44	3	6	/	15	40.1
4	Weathered sandstone	2	46	42	4	6	/	15	36.6
5	Red argillaceous sandstone	3	75	20	1	1	/	40/25	33.0
6	Slag soil-red clay	/	/	56	38	6	/	/	45.0

Note: 1. Tiyu west road station, 2 and 3 Zhujiangxincheng station, 4. Wushan road station, 5. Kecun station, 6. Tianhekeyun station. S-smectite, I-illite, C-chlorite, Kao-kaolinite, I/S-mixolimnion of illite-smectite, C/S- mixolimnion of chlorite-smectite.

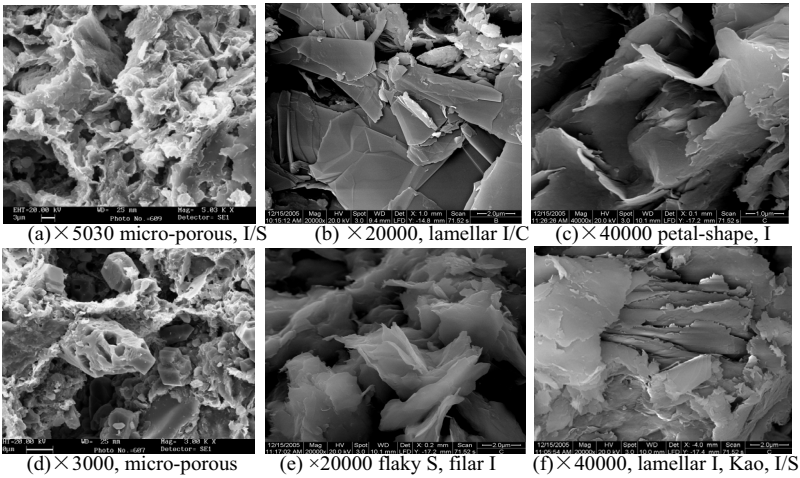

(a)×5030 micro-porous, I/S (b) ×20000, lamellar I/C (c)×40000 petal-shape, I

(d)×3000, micro-porous (e) ×20000 flaky S, filar I (f)×40000, lamellar I, Kao, I/S

FIG. 1. SEM photomicrograph of Guangzhou red soil under high amplification resolution (a, b, c and d, e, f sampled from two subway stations respectively).

SEM Microstructure Analysis

The SEM photos of red soil samples are presented as Fig.1. The micro appearance shows some characteristics: the inter-granular pore is between 30~100μm (Fig.1a, 1d); large quantity of foliated-flocculent mixolimnion of illite-smectite (Fig.1a, 1f), lamellar and petal-shape illite (Fig.1b, 1c), flaky smectite (Fig.1e), chlorite, foliated kaolinite and granular-corroded albite are contented. The results show that the red soil at this area is composed mainly of lamellar mini-group (or stacking group, Fig.1b) formed by plenty of foliated and flat clay groupings. The thickness of single flake is about $10\,^{A^{\circ}}$ (1nm), the length of single stacking group is 1~2 μm, and the width is different depending on the weathered degree of the sandstone: the more severe weathered the narrower the single stacking group, and generally, it is between 2~5μm. The typical interval (crack width) between the lamina is 0.1~0.5 μm.

Characteristics of Water-Induced Swelling Behavior of Guangzhou Red Strata

The microstructures of red clay benefit the formation of smectite, and the formation of smectite induces the hydration and swelling. The microstructure of red sandstone is prone to the penetration of water, and it creates the necessary condition for water migrating and contraction of the micro grouping.

The swelling and expansion behavior of the micro stacking group influences the water movement, water-induced damage and rheology properties. Two factors contribute the main function during the hydration of the clay minerals in soils: One is the arrangement state of the microstructure of stacking group under certain water content, and the other is the distance between two relative independent flakes. All the testing results show that the internal friction angle φ of Guangzhou red clay samples decreases as exponentially the increase of water content increases; the cohesive strength c first increases then decreases as water content increases by following a Gaussian-type relation; the maximum of cohesive strength c occurs at the water content w of 21.9 % (Yan 2005, Hou & Liu 2006, Chen 2006).

CHEMICAL FOAMED-SOIL MODIFICATION TESTS

All the testing samples are manipulated soils, the densities of soil samples with a water content of 23%, 20%, and 26% are 2.05g/m^3, 2.03g/m^3, and 2.07g/m^3, respectively.

Permeability Tests for Foamed Red Soils

Fig.2 shows the relationship between permeability coefficient of foamed clay soils and the consistency of foam agent (the water content of testing sample is 23%). Conclusion can be drawn as follows: for the soil mixed with foam under the same foam injecting ratio (FIR, the ratio between the obtained volume of foam and the volume of soil with defined water content), the permeability coefficient of foamed clay soil decreases significantly as the increasing of consistency. Fig.3 demonstrates the relationship between soil permeability coefficient and FIR at a water content of 20%. It shows that with the same consistency of foam agent solution, the permeability coefficient of foamed clay soil is the lowest when FIR is 40%. At the same time, Fig.3 expresses that there is an optimum FIR value for soils. The permeability coefficient of the strata for EPB shield tunneling should be less than 10^{-6}m/s, and the test results

show that they match it quite well.

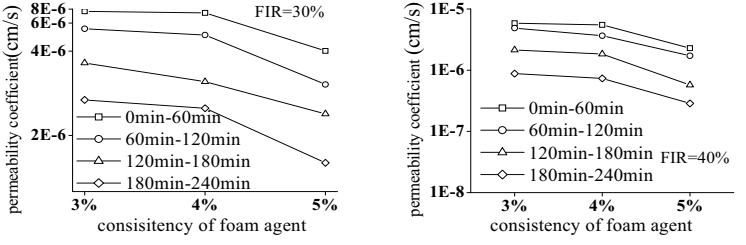

(a) FIR=30% (b) FIR=40%

FIG. 2. Permeability coefficients of foamed soils vs. the consistency of foam agent.

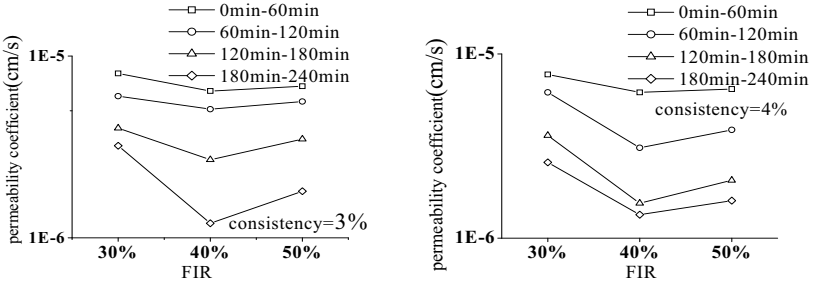

(a) Consistency=3% (b) Consistency=4%

FIG. 3. Curve of permeability coefficient of foamed clay soils vs. FIR.

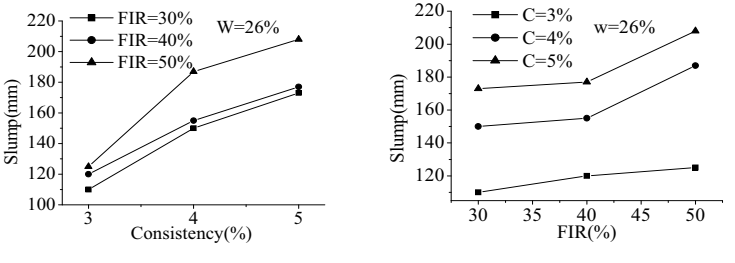

(a) Consistency vs. slump cone fall (b) FIR vs. slump cone fall

FIG. 4. The results of slump cone fall of the foamed soils.

Fluidity Tests for Foamed Red Soils

The adopted FIR is 30%, 40% and 50%, and the consistency of foam agent solution

is 3%, 4% and 5% respectively. The moisture content influences the slump significantly. For example, the adopted water content of soil sample is 26% and the corresponding slump cone fall is 58mm. When the FIR is 40%, the water content of the foamed soil is 27.7%, the plasticity Ip is 20.5, and the liquidity index IL is 0.75. The test results are illustrated in Fig.4. Fig.4 (a) indicates that for a certain quantity of FIR the slump cone fall of the conditioned soils and the fluidity of conditioned soils increase as the consistency of foam agent solution increases. Fig.4 (b) shows that for certain consistency of foam agent solution the slump cone fall of the conditioned soils increases with the increase of FIR, and for certain FIR, as the increasing of the concentration of the foam agent, the change amplitude of the slump cone fall is greater.

MECHANISM ANALYSIS OF FOAM MODIFIED RED CLAY SOIL

Mechanism Analysis of Foam Modifying Permeability Property of Red Clay Soil

The foam modifies the permeability of soils by injecting plenty of bubbles (with the size of 5~400μm) into the pore space. Double layer theory of solid-liquid interface adsorption can be employed for analyzing the mechanism of foam modification. According to the above-mentioned SEM microstructures of the red clay soils, the microstructures of red strata minerals are micro-lamina tactoid, petal-shape and micro-porosity, and so on. When foam is injected into the pores of red clay soils, part of the ions and molecules in the surfactant solution enter the micro-lamina and micro-porosity structure of the red clay soils. When the charge density of particles surface is changed, for example, some ions are injected into the soils; the double layer structure also will be changed. Equation (1) (James K. 1993) shows that the thickness of the double layer varies inversely with the valence and the square root of the concentration and directly with the dielectric constant and temperature, with other factors remaining constant.

$$\frac{1}{K} = \left(\frac{\varepsilon_0 DkT}{2n_o e^2 \upsilon^2} \right)^{1/2} \tag{1}$$

Where $1/K$ is the "thickness" of the double layer, n_0 is the electrolyte concentration, υ represents the cation valence, D is the dielectric constant of the medium, T is the temperature, e is the electronic charge, k is the Boltzman constant, and ε_0 is the permittivity of vacuum.

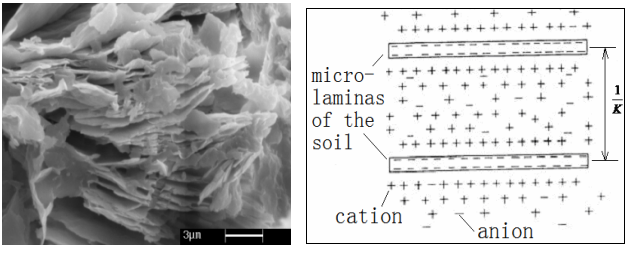

FIG.5. SEM photomicrograph of lamina structures of red clay soil (amplification 9400 times) and the diagram of diffuse double layer structure.

Fig.5 shows the diffuse double layer structure of soil granule surface. Because of the surfactant ion and molecule in the foamed soil, the electrolyte concentration is increased, so the "thickness" of the double layer is decreased. Consequently the separation between the micro-laminas of the soil is decreased. It is even difficult for fluid flowing through the micro-lamina, and the bubbles in the pore space of the soil block the passage of fluid, so the permeability of the soil is decreased greatly.

Mechanism of Foam Modifying the Fluidity of Red Clay Soils

After the foam is injected into clay soils, the pores are filled with micro-bubbles. The bubbles work as mechanical bearing by lubricating the soils, and the granules are surrounded by bubbles. The contact area among granules is reduced – it can be regarded as lubricating balls coating the granules. Therefore, the internal friction angle of the clay soils will be reduced greatly, as well as the external friction angle, so the fluidity of the clay soil and sand is enhanced accordingly. The shearing strength is then reduced with the decreasing of the internal friction angle. In the micro-structure of red clay soils, two solid-liquid interfaces exist between two arbitrary micro-laminas; correspondingly, two similar double layer structures exist. According to the double layer theory, two double layers overlap when they approach to each other, the repulsion forces prevent them from collapsing into each other, however, the repulsion force can't stop the relative lateral moving of two double layers, and the repulsion force will increase as the increasing of ions absorbed on the double layer, so the friction between two adjacent micro-laminas is reduced and the lubricating ability gets increased. Because of the contribution of surfactant ion and molecule injected in the soils, it will reduce the friction among granules and improve the fluidity effectively.

CONCLUSIONS

1) The clay minerals and total mineral compositions and SEM observation tests for Guangzhou red strata are determined quantitatively using the X-ray diffraction analysis. The clay minerals content is about 40 percent, which explains the causes of hydration-induced swelling for Guangzhou red strata. The minerals analyses unveiling the microstructure and micro-porous properties provide important evidences to explain the water-induced damage of the Guangzhou red soils.

2) The microstructure properties of the swelling-induced clay minerals cause the water-induced swelling, argillation and strong viscidity for Guangzhou red strata. The results are very helpful for studying the chemical foam agent modifying soils to control ground damage when shield tunneling in this complex strata.

3) The properties of foam modifying the permeability coefficient and fluidity of soils are achieved. The reasons for the permeability reduction of the foam modified soils are the prevention of water efficacy due to the bubbles in the pore space and the surfactant between micro-laminas of red clay soil.

ACKNOWLEDGMENTS

The research is supported by the National Natural Science Foundation of China (50674095, 50304012), the fund of Excellent Talent of Beijing Municipal Government (20071D1600700414), the New Century Excellent Talent Foundation from Education

Ministry of China, Doctoral funds of Education Ministry of China (20060290014), and Chinese National Key Project for Fundamental Researches (2009CB724601).

REFERENCES

Brown, D.Z. and Vinson, R.J. (2006). "Stiffness parameters for a strong and colorful aeolian soil." G*eomaterial Characterization* (GSP 199), ASCE, Reston/VA: 12-22.

Cimponella, G.R. and Rubertsen, K.P. (1999). "Common problems with conventional testing." *J. Geotechnical & Geoenv. Engrg.*, Vol. 181 (9): 1193-1199.

Raymond N. Y. (1999). "Overview of modeling of clay microstructure and interactions for waste isolation barrier performance." *J, Engineering Geology* 54: 83-91.

Wang D.C., Ke H.Y. (2004). "Reason analysis on Dayili interval tunnel shield construction induced ground settlement. " *J. West-china Exploration Engineering* (95): 94-95.

Hou G.Y., Liu B. (2006). "Numerical implementation and underground engineering application of Geothchnical reinforcement theory." *Coal Industrial Pres*s, Beijing

Yan J. H. (2005). "Property analysis and research on complex geotechnical of Guangzhou metro." *MS thesis, China University of Mining and Technology*, Beijing.

Chen J. (2006). "Macro-micro property analysis on complex red sandstone strata of Guangzhou metro" *MS thesis, China University of Mining and Technology*, Beijing.

Zhao X.Y., Zhang Y.Y. (1990). "Clay mineral and the analysis of clay mineral." *Ocean Press*, Beijing.

Markus Tuller, Dani Or. (2003). "Hydraulic functions for swelling soils: pore scale considerations." *J, Journal of Hydrology*, 272(1): 50-71.

Zhang T. L., Wang Z. L. (1978). "The electron microscope analysis on the minerals of China clay." *Geological Press*, Beijing.

Tan L. R. (2001). "The discussion on slaking, argillization mechanism of claystone." *J, rock mechanics*, 22 (1): 1-5.

Ohshima H. (1995). "Effective Surface Potential and Double layer Interaction of Colloidal Particles." *J, Colloid Interface Scien*ce.

James K., Mitchell. (1993). "Fundamentals of soil behavior." *John Wiley & Sons, Inc*.

Experimental Study on K_0 Consolidation Behavior of Recompacted Unsaturated Expansive Soil

Rui Zhang[1], Jian Long Zheng[2], and He Ping Yang[3]

[1]Lecturer, School of Communication and Transportation Engineering, Changsha University of Science and Technology, Chiling Road 45#, Changsha, Hunan, China, 410076; zr_csust@yahoo.com
[2]Professor, Changsha University of Science and Technology, Chiling Road 45#, Changsha, Hunan, China, 410076; zjl@csust.edu.cn
[3]Professor, School of Communication and Transportation Engineering, Changsha University of Science and Technology, Chiling Road 45#, Changsha, Hunan, China, 410076; cscuyang@163.com

ABSTRACT: To investigate the variation of K_0, the coefficient of lateral earth pressure at rest, with initial saturation degree (S_r) and constant radial stress (σ_{rc}), a series of K_0 consolidation tests were conducted on expansive soil samples under different saturation and stress conditions using a stress-path triaxial system equipped with Hall-effect transducer. The coefficient K_0 of every sample were obtained by strictly confining radial strain and evenly increasing radial stress to a given value with a slow and steady speed. The test results showed that the curve axial stress-radial stress exhibits nonlinear under small saturation degree; K_0 of samples in different saturation and stress state ranged from 0.22 to 0.72 and increased with increase of initial saturation degree and radial stress.

INTRODUCTION

K_0, the coefficient of earth pressure at rest under conditions of zero lateral strain, is important parameter for determining stress and deformations around retaining walls piles, tunnels, slopes, dams and excavations. When constitutive behavior is non-linear, predictions of deformations depend on stress history, so "starting stresses" must be known (Simpson, 1992; Vaughan, 1994; Shohet, 1995). Vertical stresses can be determined easily from depths, densities and groundwater information, but horizontal stresses are more difficult. They usually have to be estimated from empirical values of the coefficient K_0, which is the ratio of in situ horizontal stress, σ_h, to the vertical stress, σ_v. So far many researchers have developed different in-situ and laboratory methods to determine K_0 and proposed empirical relationships between K_0 and ϕ (frictional angle) or OCR (Over Consolidation Ratio) (Simpson, 1992; Sivakumar, 2001), and some studies also showed that K_0 was influenced by various factors, such as previous loading history, Poisson ratio, plastic limit, compressibility, and soil structure (Li, 1995; Schmidt, 1996). However, the classical earth pressure theory was established

basing on saturated soil and the influence of saturation degree on K_0 was not considered in previous studies. In engineering practice, soil is usually unsaturated, particularly such as expansive soils, loess and residual soils. Mechanical properties of saturated and unsaturated soils are obviously different (Fredlund, 2006). For example, earth pressure on a retaining wall increases with increase of saturation degree of back fill (Zu and Liu, 2001). Therefore, it is necessary to study K_0 consolidation behavior of unsaturated soils and the variation of K_0 with saturation degree and stress.

PREPARATION OF SPECIMENS AND TEST PROCEDURE

Specimen Preparation and Triaxial Testing System

The soil used in this study is dark-gray expansive clay taken from an excavated slope of the Expressway from Naning to Youyi Guan in Ningming, Guangxi Zhuangzu Autonomous Region of China. The basic physical and mineralogical properties are listed in Table 1. Swelling potential of the soil can be classified as medium according to the smectite content, free swelling ratio and plastic index (Zheng, 2008).

Table 1. The Basic Physical and Mineralogical Properties of Ningming Clay

Specific Gravity	Liquid Limit (%)	Plastic Limit (%)	Free swelling Ratio (%)	Composition of Grains (%)		Smectite Content (%)
				<0.005 mm	< 0.002 mm	
2.74	59.6	21.3	48	50.08	47.12	19.07

The specimens for triaxial K_0 consolidation tests, 50 mm in diameter and 100 mm in height, were prepared by statically compacting method. The initial saturation degree were 60%, 75%, 90%, and 100% respectively considering the variation in situ, corresponding to 16.2%, 20.1%, 24.1%, and 27.2% in water content. Static compacting pressure was 800 kPa and the initial dry density was 1580 kg/m^3. To produce uniform specimens, the compaction of 100 mm height triaxial specimen was conducted in 6 layers. As for every saturation degree, four “same” specimens were prepared for tests under four different radial stresses, i.e., 25 kPa, 50 kPa, 150 kpa and 200 kPa. Therefore, 16 specimens were totally used in the laboratory study.

An advanced computer-controlled triaxial stress-path testing systems, shown in Fig.1, was used in the tests. With three hydraulic pressure controllers, radial stress, axial stress, and pore-water pressure can be controlled independently. Four transducers consist of an internal load cell (measurement of axial force), a LVDT (measurement of axial displacement), pore pressure transducers and Hall Effect transducer (measurement of radial deformation, shown in Fig. 2). All the four transducers are connected to the digital transducer interface (DTI) for data acquisition. The three digital hydraulic pressure/ volume controllers are connected to the computer by an IEEE interface card for computer-control. All of these form a closed-loop controlling and feedback system.

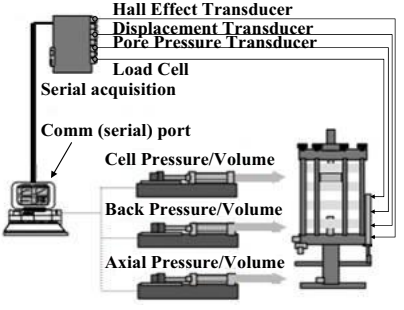

FIG. 1. Layout of triaxial stress-path testing system.

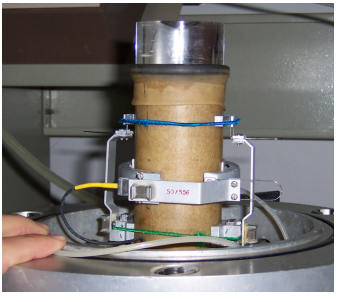

FIG. 2. Hall-effect transducer.

Test Procedure

K_0 is defined as the ratio of effective horizontal stress (σ'_r) to effective vertical stress (σ'_a). As for unsaturated soil, the equation of effective stress (Fredlund, 1993) is:

$$\sigma' = (\sigma - u_a) + \chi(u_a - u_w) \tag{1}$$

where u_a is air pressure and usually zero in value, $(u_a - u_w)$ is matric suction and χ is coefficient and related to saturation degree, $0 < \chi < 1$.

Therefore, the equation of K_0 of unsaturated soil can be given by:

$$K_0 = \frac{\sigma'_r}{\sigma'_a} = \frac{(\sigma_r - u_a) + \chi(u_a - u_w)}{(\sigma_a - u_a) + \chi(u_a - u_w)} \tag{2}$$

The triaxial K_0 consolidation tests were conducted on the recompacted unsaturated expansive soil, and the test procedure was similar to the traditional tests on saturated soil. At first, radial stress was slowly increased at the speed of 10 kPa/h by the computer-controlled system (stage OA shown in Fig. 3). Meanwhile, axial stress also increased to keep no radial deformation which was judged by Hall Effect Transducer. When radial stress reached the given stress it kept constant (σ_{rc}) and the specimen

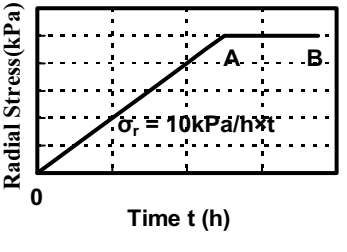

FIG. 3. Procedure of applying radial stress.

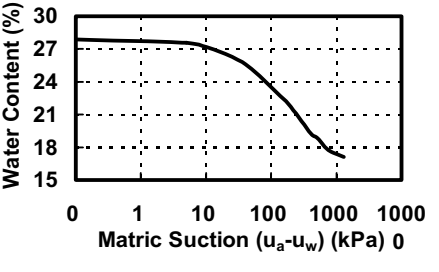

FIG. 4. SWCC of Ningming expansive soil.

was consolidated under σ_{rc} (stage AB shown in Fig. 3). The consolidation would end as long as the change of axial deformation was less than 0.01mm in one hour, and the axial stress at this time was named as σ_{ault}. Because $(u_a - u_w)$ can not be measured in the test, $(u_a - u_w)$ was indirectly obtained from soil-water characteristic curve (SWCC) of the expansive soil, a relationship curve between water content and matric suction (shown in Fig. 4). χ was determined according to the tests results on a similar clayey soil (Fredlund, 1993). Then K_0 was calculated by Equation (1).

RESULTS AND ANALYSIS

Fig. 4 shows variation of axial stress (σ_a) with radial stress (σ_r) of specimen with different saturated degree during the stage OA and AB shown in Fig. 3. The percentage closing to every curve in Fig. 4a to Fig. 4d stands for the saturation degree of corresponding specimen, and the bold number at the end of every curve and on the right side stands for the ultimate axial stress (σ_{ault}) at the end of K_0 consolidation. The Fig. 4 shows that in the stage of increasing σ_r, σ_a increases with σ_r. At the condition of high

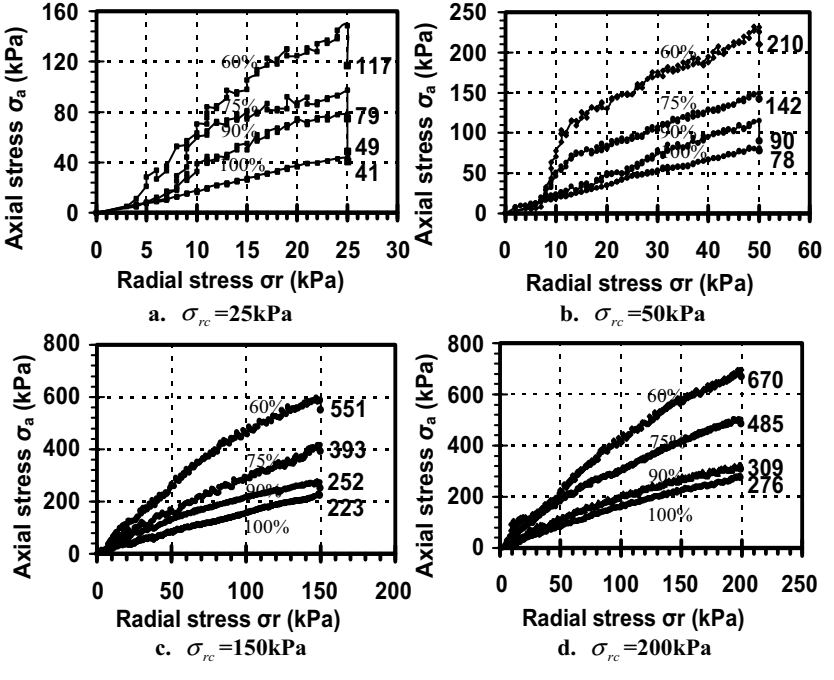

FIG. 4. Variation of axial stress with radial stress of specimen under different saturated degree.

saturation degree, σ_a increases with σ_r linearly. However, the σ_a-σ_r curve tends to be much more non-linear as the saturation degree of specimen decreases, and the curve at the condition of small saturation degree can be divided two parts: (1) σ_a sharply increases with increase of σ_r, and the slope of curve is big. At this stage, the strength of soil structure exhibits to resist the axial load and the strength is larger as the saturation degree specimen is lower. (2) With the increase of axial stress, specimen is compacted and the soil structure tends to collapsed. The slope of curve becomes moderate as σ_a increases slowly with the increase of σ_r. The two parts are shown obviously in Fig. 4b.

At the stage of constant radial stress σ_{rc}, axial stress decreases slowly with time elapsing and tends to be constant (σ_{ault}). After corresponding σ_{rc}, σ_{ault}, $(u_a - u_w)$, χ are submitted to Equation (2), the K_0 of different saturated degree and stress state can be calculated. Fig. 5 gives the variation of K_0 with saturation degree under different radial stress. It shows that (1) K_0 obviously increases with increase of saturation degree and the increasing tendency of K_0 under different radial stress is nearly same; (2) K_0 under small radial stress is smaller than the K_0 under big radial stress. The reason is that under small radial stress soil contains much big pore, the contact area among soil particles is small, soil easily deforms in radial, as a result a big axial stress applies on the top of soil to keep no radial deformation. Therefore, the K_0 is small under the small radial stress; (3) As for the Ningming recompacted expansive soil, K_0 ranges from 0.21 (Sr=60%, σ_{rc} = 25 kPa) to 0.72 (Sr=100%, σ_{rc} = 200 kPa). Therefore, it can be concluded that K_0 of expansive soil changes in big range and is influenced by saturation degree and the stress state.

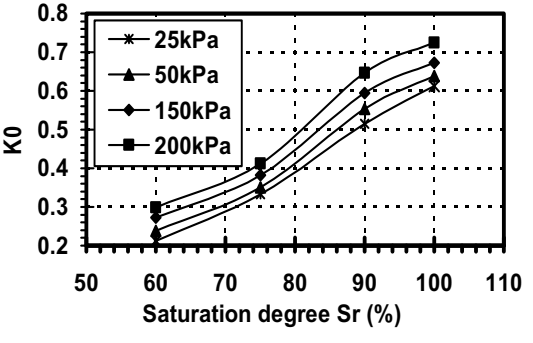

FIG. 5. Variation of K_0 with saturation degree under different radial stress.

CONCLUSIONS

K_0 consolidation tests on Ningming expansive soils under different saturated degree and stress state were conducted over an advanced computer-controlled triaxial stress-path testing systems. The variation of axial stress with radial stress during testing process and the variation of K_0 with saturation degree under different stress state were

obtained and analyzed. Some conclusions were drawn as follow:

(1) At the stage of increasing σ_r, σ_a increased with the increase of σ_r. At low saturation degree, the σ_a-σ_r curve tends to be more non-linear. Firstly, σ_a sharply increases with increase of σ_r. After the inflexion, σ_a increases slowly with the increase of σ_r and the slope of the curve becomes moderate.

(2) At high saturation degree, the σ_a- σ_r curve tends to be linear. At the stage of consolidation at constant σ_r, σ_a decreases slowly with time elapsing and tends to be an ultimate stress (σ_{ault}).

(3) K_0 obviously increases with increase of saturation degree. The K_0 under small radial stress is smaller than the K_0 under big radial stress. K_0 of expansive soil changes in big range and is obviously influenced by saturation degree and stress state.

REFERENCES

Fredlund, D. G., and Rahardjo, H. (1993). *Soil mechanics for unsaturated soils*. Wiley, New York:47-48.

Fredlund, D. G. (2006). "Unsaturated Soil Mechanics in Engineering Practice." *Journal of Geotechnical and Geoenvironmental engineering*, Vol. 132(3): 286–321.

Li, Z. Q. (1995). "Some Problems Affecting Lateral Earth Pressure at Rest in Clays." Rock and Soil Mechanics, Vol. 16(1): 9-16.

Schmidt B. (1996). Discussion "Earth pressure at Rest Related to Stress History". *Canadian Geotechnical Journal*. Vol. 3(4): 239-242.

Simpson, B. (1992). "Retaining structures: displacement and design." *Geotechnique*, Vol. 42(4): 541-576.

Sivakumar, V., Doran, I. G., Graham, J. and Navaneethan, T. (2001). "Relationship between K_0 and overconsolidation ratio: a theoretical approach." *Geotechnique*, Vol. 52(3): 225-230.

Shohet, D.C. (1995). "Prediction of in-situ horizontal stresses in clay soils from the measurement of undrained shear strength, plasticity index and vertical effective stress." *Proceedings - ICE: Geotechnical Engineering*, 113(4): 206-214.

Vaughan, P.R. (1994). "Assumption, prediction and reality in geotechnical engineering." *Geotechnique*, Vol. 44(4): 573-609.

Zheng. J. L., Zhang, R. and Yang, H. P. (2008) "Validation of a Swelling Potential Index for Expansive Soils." *Unsaturated soils: Advances in Geo-Engineering*, Toll D. G., Durham/U.K.: 397-404.

Zhu, Z. D., Liu, S. Y. (2001). "Analysis of Active Earth Pressure of Unsaturated Expansive Soil." *Journal of Highway and Transportation Engineering Research and Development*. Vol.18(5): 8-10.

Discrete Element Modeling of Aggregate Behavior in Fouled Railroad Ballast

Hai Huang[1], Erol Tutumluer[2], Youssef M.A. Hashash[3], and Jamshid Ghaboussi[4]

[1]Research Assistant, University of Illinois at Urbana Champaign, B142 NCEL, 205 N Mathews, Urbana 61801; hhuang14@illinois.edu
[2]Professor, University of Illinois at Urbana Champaign, 1205 NCEL, 205 N Mathews, Urbana 61801; tutumlue@illinois.edu
[3]Associate Professor, University of Illinois at Urbana Champaign, 2230c NCEL, 205 N Mathews, Urbana 61801; hashash@illinois.edu
[4]Professor Emeritus, University of Illinois at Urbana Champaign, 3118 NCEL, 205 N Mathews, Urbana 61801; jghabous@illinois.edu

ABSTRACT: This paper describes an aggregate imaging based Discrete Element Modeling (DEM) methodology successfully employed to model both clean and coal dust fouled railroad ballast behavior. Laboratory direct shear box tests were conducted on granite type clean and fouled ballast aggregate samples. The size, shape and angularity properties of the aggregate particles were obtained through image analysis. Accordingly, direct shear box DEM simulations were conducted for different aggregate contact friction conditions. Both the clean ballast behavior and the heavily fouled case of coal dust filling completely all the voids in ballast were adequately modeled using the DEM approach by assigning a lower contact friction angle as the controlling discrete element model parameter in the latter case. In accordance with the direct shear test results, much lower shear stress-shear deformation curves, i.e., lower shear strengths, were predicted the coal dust fouled case using the DEM simulations.

INTRODUCTION

Traditional modeling techniques such as Finite Element Method (FEM) can hardly simulate the behavior of a particulate assembly such as the ballast layer to properly address problems related to track fouling, lateral stability, and settlement. In a ballast layer, individual aggregate particles move independently and interact only at contact points. Such discrete nature results in a complex behavior of the granular assembly, which is very difficult to model by continuum theory used in the FEM. In addition, dilation, inter-particle sliding and nonlinear stress dependent behavior of granular materials with typical anisotropic stiffness and deformation properties under vertically induced load application are almost impossible to be adequately modeled using the continuum approach.

Discrete Element Modeling (DEM) of aggregate behavior in ballasted railroad track structure has been gaining increased attention. Recent research clearly demonstrates that DEM methodology has the potential to realistically model railway

ballast by accounting for individual aggregate particle movements and interactions within the granular assembly (Tutumluer et al., 2006 and 2007). With three-dimensional block shaped elements used to represent aggregate particles, the DEM model is created according to the sizes, shapes, and contact characteristics of the ballast aggregate used. Once the DEM model is calibrated based on laboratory test results of the aggregate assembly, the load carrying ability and the deformation behavior of the ballast layer can be predicted for various field loading conditions due to stationary and moving trains.

For a new railroad track, ballast is commonly constructed to serve its drainage function with clean aggregates used with uniform gradation. As the track usage or the traffic level increases, ballast gets fouled gradually when the unbound aggregate layer is progressively contaminated with fine-grained materials filling the void spaces. These fine-grained materials come from following sources: ballast aggregate breakdown under repeated train loading, subgrade soil intrusion, and foreign material. It is believed that fouling material lubricates the contacts and may eventually separate individual ballast aggregate particles thus causing movements and reorientations within the granular assembly to decrease the strength and stability of ballast layer. Different fouling materials, fouling percentages, and moisture levels in the ballast may individually or in combination impact the serviceability and proper functioning of the existing ballast layer.

This paper focuses on a successful application of the DEM approach for studying effects of fouled ballast behavior. In this DEM application, the ballast layer is modeled as an assembly of uniform sized angular aggregate particles with preferred cubical shapes and rough surface textures. The DEM model parameters are then calibrated using the results of direct shear tests conducted on a granite type ballast aggregate fouled with various fine materials at different stages of fouling, i.e., different percentages of fines accumulated in ballast under both dry and wet conditions. Using the laboratory measured strength characteristics under both clean and fouled conditions, the discrete element contact characteristics, i.e., surface friction angle or surface texture condition, are shown to primarily govern the behavior in the DEM predictions for each fouling condition. The DEM simulation approach in this paper is therefore demonstrated to be a realistic and powerful tool for better understanding the deterioration behavior of the railroad infrastructure ballast component and can be potentially used to schedule ballast maintenance and rehabilitation activities.

BALLAST FOULING AND ITS MECHANISM

Fouling materials in ballast have been traditionally considered not favorable for railroad ballast performance. Early research studies reported that around 70% of the fouling materials could be due to ballast breakdown (Selig et al., 1988; Collingwood, 1988; Selig et al., 1992). Railroad company internal studies also noted that almost all fouling fines in the railroad track were commonly from aggregate breakdown (CN, 1987). According to Selig and Waters (1994), ballast breakdown on the average accounts for up to 76% of the ballast fouling followed by 13% infiltration from subballast, 7% infiltration from ballast surface, 3% subgrade intrusion, and 1% due to tie wear.

In terms of the stability and load carrying ability of the fouled ballast layer, three distinct phases can be identified for the different conditions of fine materials filling the void space (see Figure 1). Phase I shows a clean ballast sample with almost all aggregates establishing contact with each other at the aggregate surface to carry the load (see Figure 1a). As shown in Figure 1b, partially to fully fouled ballast in phase II will have the voids in between contacting aggregates filled with fine particles, however, still maintaining aggregate to aggregate contact. Whereas, in a phase III fouled ballast condition, due to the excessive amount of fine particles, aggregate to aggregate contacts are mostly eliminated and the aggregate particle movements are then only constrained by the fine particles filling the matrix or voids between the particles (see Figure 1c). As ballast in phase III is no doubt unacceptable and needs immediate remedial action, ballast in phase II is particularly worth studying from the aspect of how different fouling agents at different stages in phase II would affect ballast strength and therefore impact track stability.

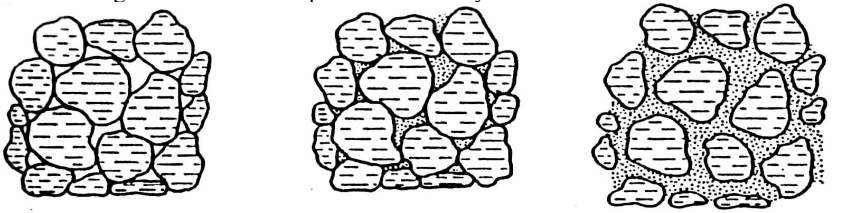

(a) Clean (Phase I) **(b) Partially fouled (Phase II)** **(c) Heavily fouled (Phase III)**

FIG. 1. Critical ballast fouling phases.

SHEAR STRENGTH TESTING OF CLEAN AND FOULED BALLAST

Materials Tested

The ballast material tested was a granite aggregate obtained from Gillette, Wyoming in the United States and commonly used as the ballast layer of the railroad track structures in the Powder River Basin (PRB) coal transportation line jointly used by two major railroad companies. Figure 2 shows the grain size distribution of the granite sample, with a specific gravity of 2.62, tested in compliance with ASTM C 117 test procedure. The granite aggregate size distribution conforms to the typical AREMA No. 24 ballast gradation having a maximum size (D_{max}) of 63.5 mm (2.5 in.), a minimum size (D_{min}) of 25.4 mm (1 in.), and an average particle size corresponding to 50 percent passing by weight (D_{50}) of approximately 45 mm (1.77 in.).

The coal dust sample tested in this study was also collected from the PRB Orin line milepost 62.4 and was sampled in March 2007. Figure 2 also shows the typical gradation coal dust and Table 1 lists the engineering properties of coal dust with the moisture-density information obtained from the standard Proctor ASTM D 698 test procedure**.**

Testing Apparatus

Direct shear strength tests were performed on the reconstituted clean and fouled granite aggregate samples at the University of Illinois. The test device is a square box

with side dimensions of 305 mm (12 in.) and a specimen height of 203 mm (8 in.). It has a total 102 mm (4 in.) travel of the bottom 152 mm (6 in.) high component which is large enough for ballast testing purposes to record peak shear stresses. The vertical (normal direction) and horizontal load cells are capable of applying and recording up to 50 kN load magnitudes. The device controls and the data collection are managed through an automated data acquisition system controlled by the operator through a build-in display and the test data are saved on to a personal computer.

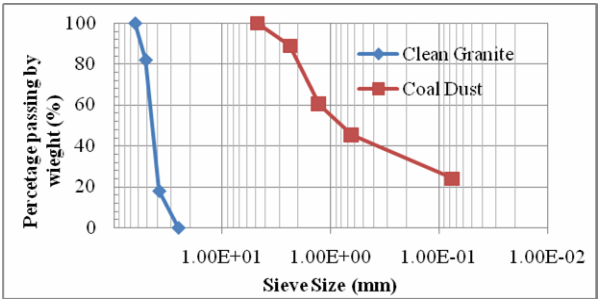

FIG. 2. Grain size distributions of the clean ballast and fouling materials.

Table 1. Engineering Properties of Coal Dust as the Fouling Material

	Specific Gravity	Liquid Limit (%)	Plastic Limit (%)	Optimum Moisture Content or OMC[1] (%)	Maximum Dry Density[1] (kg/m^3)	Passing 0.075 mm or No. 200 sieve (%)
Coal Dust	1.28	91	50	35	874	24

[1]: Obtained from standard Proctor ASTM D 698 test procedure.

Sample Preparation

Clean ballast samples were prepared in the lower shear box to the condition similar to the field according to the following steps:

1. Place aggregates in the lower box by lifts (usually two 76 mm lifts).
2. For each lift, use vibratory compactor on top of a flat Plexiglas compaction platform and compact until no noticeable movement of particles is observed.
3. Record the weight of aggregate used.
4. Place upper ring (76 mm high) on top of lower box. Align ring with sides and back edge of box (opposite of block) and fill with single lift of ballast and compact.

Coal dust fouled granite ballast samples were prepared similar to the clean sample procedure by spreading coal dust on the ballast surface and spraying water, if needed. The individual steps are as follows:

1. Obtain clean aggregates of the same weight as previously recorded.
2. Compact ballast sample into the lower box in two lifts.

3. Obtain prescribed weight of coal dust and water.
4. Spread coal dust over compacted ballast evenly in two lifts (half of material each lift). Shakedown material using vibratory compactor after each lift. If test is conducted with wet fouling material (for example, at the optimum moisture content or OMC), pour proportional amount of water over ballast after shakedown of each lift.
5. Step 4 in the clean sample preparation procedure.

Direct Shear Test Results

The ballast samples were sheared horizontally in the shear box under target normal pressures of 172, 241, 310 kPa (25, 35, 45 psi), typical ballast layer confining pressures, so that the relationships between the normal stress and shear stress could be established. The maximum shear stress at failure under each applied normal pressure was recorded from each test. This maximum shear stress typically occurred when approximately 10% shear strain was reached during testing. The shear strength $\tau_{max} = C + \sigma_i * \tan\Phi$ (where C is the cohesion intercept, σ_i is the applied normal stress, and Φ is the internal friction angle) expression was then developed for each ballast sample tested at a corresponding fouling fines content and moisture state.

Figure 3 shows the maximum shear stresses predicted under the applied normal stresses during shear box testing for coal dust fouling cases in comparison to the clean granite test results. As the applied normal stresses increased, the maximum shear stresses at failure or simply shear strength τ_{max} also increased primarily influenced by the ballast fouling percentage and the moisture condition of the coal dust, i.e., dry or wet at OMC = 35%. As expected, the highest shear strength values were obtained from the clean ballast at all applied normal stress levels. When ballast samples were fouled, the shear strengths typically decreased. For all the samples tested, wet coal dust fouling resulted in lower shear strengths when compared to those obtained from dry coal dust fouling. The lowest shear strength values were recorded for the fouling level of 25% by weight (at a dry density of 1873 kg/m^3) of ballast when wet coal dust was at 35% moisture content**.**

DISCRETE ELEMENT MODELING (DEM) OF FOULED RAILROAD BALLAST

Aggregate Imaging and Discrete Element Modeling

Imaging technology provides detailed measurements of aggregate shape, texture and angularity properties and has been successfully used in the last two decades for quantifying aggregate morphology. A variety of imaging based aggregate morphological indices have been developed and linked to material strength and deformation properties in the recent years (Masad and Button, 2000; Tutumluer et al., 2000). Among the various particle morphological indices, the flat and elongated (F&E) ratio, the angularity index (AI), and the surface texture (ST) index, all developed using University of Illinois Aggregate Image Analyzer (UIAIA), are key indices. They have been recently validated by measuring aggregate properties and successfully relating them to laboratory measured strength data and field rutting performances of both unbound aggregate and asphalt mixtures (Rao et al., 2001; Rao et al., 2002; Pan et al., 2004; Pan et al., 2005).

Railroad ballast behavior can be simulated using DEM methodology both realistically and reliably by considering actual irregular shaped aggregate particles in the analysis. BLOKS3D is a DEM program developed at the University of Illinois and used in this research study (Nezami et al., 2006). The BLOKS3D uses arbitrary polyhedrons to represent discrete elements with the capability of user defined particle shapes obtained from the digital image apparatus UIAIA (Tutumluer et al., 2006).

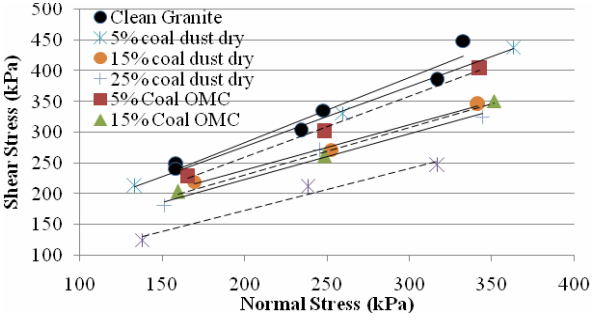

FIG. 3. Direct shear box test results of coal dust fouled ballast samples.

Direct Shear Box DEM Simulations of Clean and Coal Dust Fouled Ballast

For the shear box direct shear strength test DEM simulations, nearly 300 granite aggregate particles were first processed through the UIAIA and then representative DEM element shapes were created for an accurate modeling of the average shape properties in the granular assembly. In this particular case, all aggregate samples processed in UIAIA imaging equipment had an average AI of 550 (subangular to angular) and F&E ratio of 1.3 to 1 obtained (Rao et al., 2002). Discrete elements were created according to the actual AREMA No. 24 gradation of the granite ballast sample shown in Figure 2 and tested in the exact geometry of the virtual shear box created in the DEM simulation. Aggregate samples at similar void ratios achieved in the tests, around 43%, were then sheared at a constant speed of 0.15 mm/sec.

Figure 4 shows the recorded shear stresses against the shear displacements for both the laboratory and DEM simulation results. A stiffness combination of Kn = 20 MN/m and Ks = 10 MN/m for normal and shear, respectively, with a contact friction angle of 31 degrees were selected as the clean granite ballast DEM model parameters for all three normal stress levels, i.e., 172, 241, 310 kPa (25, 35, 45 psi). Figure 4 indicates for the clean ballast sample reasonably good DEM model predictions were achieved when compared to the laboratory results at all normal stresses levels.

In a fully fouled laboratory ballast sample, aggregate particles may separate due to excessive amounts of fine materials filling the voids. Aggregate particles can therefore be treated as “floating” in the fine matrix consisting of primarily coal dust in this study. This is in fact analogous to the case that aggregate surface is lubricated by this typically very low strength coal dust (Tutumluer et al., 2008). To simulate such a ballast fouling effect in DEM, surface friction angles of these non-contacting

aggregates or discrete elements had to be reduced down due to the presence of the lubricating coal dust.

Figure 5 compares the coal dust fouled ballast DEM model predictions to the laboratory test results. A lower contact friction angle of 27 degrees was used for the fully fouled condition with dry coal dust filling all the voids (43% by volume and 25% by weight of clean ballast). The DEM prediction curves in Figure 5 are in reasonably good agreement with the laboratory stress-strain curves thus capturing the shear strength increase with the increasing normal stress. The effect of coal dust fouling, i.e., decrease in strength, could be adequately simulated by using a lower friction angle for the aggregate to aggregate contact in the DEM simulations.

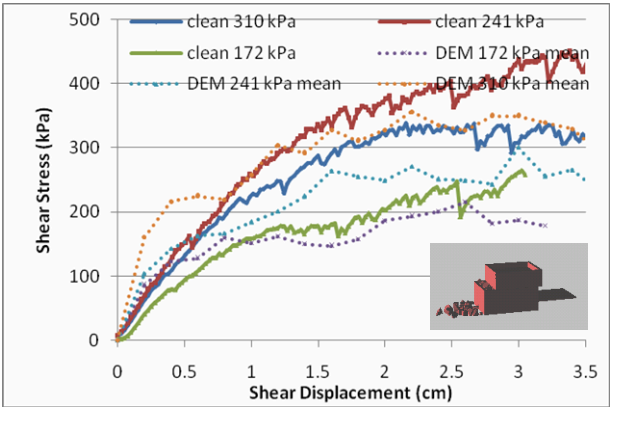

FIG. 4. Shear box laboratory test and DEM simulation results for clean ballast obtained under the application of 172, 241 and 310 kPa normal stresses.

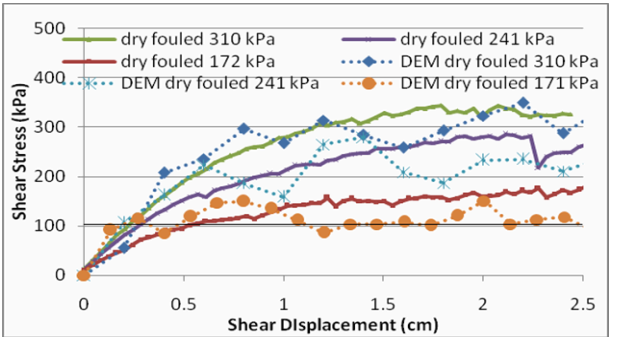

FIG. 5. Shear box laboratory test and DEM simulation results for fouled ballast (dry coal dust filling all the voids in ballast) obtained under the application of 172, 241 and 310 kPa normal stresses.

CONCLUSIONS

Large-sized shear box direct shear laboratory tests were conducted at the University of Illinois on granite ballast samples obtained from Powder River Basin (PRB) coal transportation joint line in Wyoming, United States to investigate the effect of coal dust fouling. From the direct shear tests, the highest shear strength values were obtained from the clean ballast samples at all applied normal stress levels, which were representative of typical stress states experienced in the ballast layer under train loading. When ballast samples were fouled, the shear strengths always decreased.

The direct shear box test results for the granite ballast samples were simulated using a special Discrete Element Modeling (DEM) approach, which considered determining size, shape and angularity properties of aggregate particles from image analyses and utilizing arbitrary polyhedrons, i.e., discrete elements, established realistically from the imaging based aggregate properties. Both clean and coal dust fouled ballast shear box test results were predicted using the DEM simulations by adequately changing contact friction angles of the discrete elements or aggregate particles adopted in the modeling approach. The shear stress–shear displacement curves predicted from the DEM simulations were in reasonably good agreement with the laboratory test results at all normal stress levels that shear box tests were conducted. A lower contact friction angle than the one used for the clean ballast sample was needed to simulate the coal dust fouled ballast shear deformation behavior and to predict the strength behavior accurately.

ACKNOWLEDGEMENTS

The authors would like to thank Association of American Railroads (AAR) and Burlington Northern Santa Fe (BNSF) Railroad Company for providing the financial support needed to carry out this research study. The assistance of William (Zach) Dombrow on the ballast shear box tests is greatly appreciated. The contents of this paper reflect the views of the authors who are responsible for the facts and the accuracy of the data presented herein. This paper does not constitute a standard, specification, or regulation.

REFERENCES

CN (Canadian National) Rail. (1987). “Ballast Performance in Concrete Tie Track.” Prairie Region. Edmonton. CN, Geotechnical Service. Internal Report.

Collingwood, B.I. (1988). “An Investigation of the Cause of Railroad Ballast Fouling.” *Master of Science Degree Project Report No. AAR88-350P*. University of Massachusetts.

Masad, E. and Button, J.W. (2000). “Unified Imaging Approach for Measuring Aggregate Angularity and Texture.” *The International Journal of Computer-Aided Civil and Infrastructure Engineering* – Advanced Computer Technologies in Transportation Engineering, Vol. 15, No. 4, pp. 273-280.

Nezami, E.G., Y.M.A. Hashash, D. Zhao, and J. Ghaboussi, (2006). “Shortest Link Method for Contact Detection in Discrete Element Method.” *International Journal for Numerical and Analytical Methods in Geomechanics*, Vol. 30(8), pp. 783-801.

Pan, T., Tutumluer, E., and Carpenter, S.H. (2004). "Imaging Based Evaluation of Coarse Aggregate used in the NCAT Pavement Test Track Asphalt Mixes." Proceedings of the 1st International Conference on Design and Construction of Long Lasting Asphalt Pavements. Auburn, Alabama.

Pan, T., Tutumluer, E., and Carpenter, S.H. (2005). "Effect of Coarse Aggregate Morphology on Resilient Modulus of Hot-mix Asphalt." *Transportation Research Record* No. 1929, Journal of the Transportation Research Board, National Research Council, Washington, D.C.

Rao, C., Tutumluer, E., and Stefanski, J.A. (2001). "Flat and Elongated Ratios and Gradation of Coarse Aggregates using a New Image Analyzer." *ASTM Journal of Testing and Standard*, Vol. 29, No. 5, pp. 79-89.

Rao, C., Tutumluer, E., and Kim, I.T. (2002). "Quantification of Coarse Aggregate Angularity Based on Image Analysis." *Transportation Research Record* No. 1787, Journal of the Transportation Research Board, National Research Council, Washington, D.C.

Selig, E.T., Collingwood, B.I., and S.W. Field. (1988). "Causes of Fouling in Track." *AREA Bulletin 717*.

Selig, E.T., DelloRusso, V., and K.J. Laine. (1992). "Sources and Causes of Ballast Fouling." *Report No.R-805*. Association of American Railroad (AAR), Technical Center, Chicago.

Selig, E.T. and J.M. Waters. (1994). "Track Geotechnology and Substructure Management." London, Thomas Telford Publications.

Tutumluer, E., Dombrow, W., and Huang, H., (2008). "Laboratory Characterization of Coal Dust Fouled Ballast Behavior." *In Proceedings of the AREMA 2008 Annual Conference*, Salt Lake City, Utah, September 21-24.

Tutumluer, E., Huang, H., Hashash, Y.M.A., and Ghaboussi, J., (2006). "Aggregate Shape Effects on Ballast Tamping and Railroad Track Lateral Stability." *In Proceedings of the 2006 AREMA Annual Conference*, Louisville, Kentucky September 17-20.

Tutumluer, E., Huang, H., Y.M.A. Hashash and Ghaboussi, J. (2007). "Discrete Element Modeling of Railroad Ballast Settlement," *In Proceedings of the 2007 AREMA Annual Conference*, Chicago, Illinois, September 9-12.

Tutumluer, E., Rao, C., and Stefanski, J.A. (2000). "Video Image Analysis of Aggregates." *Final Project Report, FHWA-IL-UI-278*, Civil Engineering Studies UILU-ENG-2000-2015, University of Illinois Urbana-Champaign, Urbana, Illinois.

Numerical Analysis of Critical Bearing Capacity of Subsoil with K_0 Unequal to 1

MEI Ling[1], MEI Guoxiong[2] and ZAI Jinmin[3]

[1]Ph.D College of Civil Engineering, Nanjing University of Technology, Nanjing 210009; mling530@163.com
[2]Professor, College of Civil Engineering, Nanjing University of Technology, Nanjing, 210009; meiguox@163.com
[3]Professor, College of Civil Engineering, Nanjing University of Technology, Nanjing, 210009, zjm@njut.edu.cn

ABSTRACT: Traditionally, the formulas of critical edge pressure p_{cr} and critical load $p_{1/4}$ are developed by assuming coefficient of earth pressure at rest K_0 equal 1. It means that the geostatic stress is treated as hydrostatic stress. This assumption leads to an increase in lateral load of subsoil and results in a higher bearing capacity of subsoil. In the paper, a MATLAB program is used to find the numerical solution of bearing capacity of soil for $K_0 \neq 1$. The proposed method overcomes some shortcomings of the methods available in the literature for $K_0 \neq 1$. The influence of shear strength parameters of soil on the critical load is investigated.

INTRODUCTION

The commonly used formulas of critical edge pressure and critical load are developed for vertical loads on strip foundation based on elastic theory. As shown in Figure 1, stresses at an arbitrary point M in foundation soil include two components: major and minor principal stresses induced by the strip load and geostatic stresses. Generally, these two components cannot be simply added together because the direction of stresses induced by external strip load and geostatic stresses is different. However, if coefficient of earth pressure at rest K_0 is assumed to be 1, i.e., the geostatic stress field is treated as hydrostatic pressure field and the geostatic stress is the same in every direction, the stresses induced by the strip load and geostatic stresses can be directly added together. The formulas for critical edge pressure and critical load are traditionally obtained based on this assumption. Many soil mechanics books present this method (Craig R.F., 1995). However, strictly speaking, K_0 is not equal to 1, i.e., the directions of the major and minor principal stresses induced by the strip load are different from the geostatic stresses at point M, so they cannot be simply added together.

Zhao (1995) and Xue (2005) proposed formulas for critical edge pressure and critical load without the assumption of K_0=1. The normal stress and shear stress generated by geostatic stress at point M along the direction of the major and minor principal stresses induced by the strip load are found and then added to the major and minor principal

stresses induced by the strip load. Now the direction of the total stress is not the direction of the principal stress at point M. Zhao (1995) and Xue (2005) obtained expressions for the vertical distance of point M to foundation base Z. Take partial derivatives of the expressions of Z with respect to α and δ, which is shown in Figure 1, and obtain approximate formulas for the critical load. Angles α and δ are related to each other based on geometric relation, as shown in Figure 1. It is therefore not reasonable to take partial derivatives of the expressions of Z with respect to α and δ. Additional principal stress is added to geostatic stress along the direction of X and Z to obtain total stress at point M by Cui (1998). The principal stresses at point M can then be calculated easily. However, only formulas of critical edge pressure and critical load for the points under the center of foundation are given because they are readily obtained. While it is hard to get an analytical solution, numerical solution is a good choice.

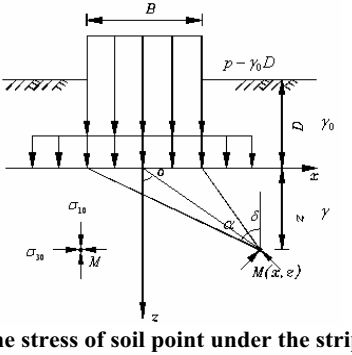

FIG. 1. The stress of soil point under the strip footing.

NUMERICAL METHOD

Basic Consideration

A strip foundation with a width of B and an embedment of D is shown in Figure 1. Uniform strip load p acts on the base of foundation. The unit weight of soil above the footing embedment depth is γ_0, and below the footing embedment depth is γ, which is equal to effective unit weight when soil is below the groundwater table. The shear strength parameters of soil are c and φ and the coefficient of earth pressure at rest is K_0.

A MATLAB program is used to calculate the bearing capacity of subsoil, and the basic considerations are:

Expressions of additional stress at point M along the directions X and Z are obtained using elastic theory (Poulos, H.G, 1990) as follows:

$$\sigma'_z = \frac{p_0}{\pi}\{\alpha + \sin\alpha\cos(\alpha + 2\delta)\} \tag{1}$$

$$\sigma'_x = \frac{p_0}{\pi}\{\alpha - \sin\alpha\cos(\alpha + 2\delta)\} \tag{2}$$

$$\tau'_{xz} = \frac{p_0}{\pi}\sin\alpha\sin(\alpha + 2\delta) \tag{3}$$

The geostatic stresses at point M are:

$$\sigma_{cz} = \gamma_0 D + \gamma z \tag{4}$$

$$\sigma_{cx} = K_0(\gamma_0 D + \gamma z) \tag{5}$$

$$\tau_{cxz} = 0 \tag{6}$$

The total stress expressions at point M can be obtained by adding additional stresses and geostatic stresses together:

$$\sigma_z = \frac{p_0}{\pi}\{\alpha + \sin\alpha\cos(\alpha + 2\delta)\} + \gamma_0 D + \gamma z \tag{7}$$

$$\sigma_x = \frac{p_0}{\pi}\{\alpha - \sin\alpha\cos(\alpha + 2\delta)\} + K_0(\gamma_0 D + \gamma z) \tag{8}$$

$$\tau_{xz} = \frac{p_0}{\pi}\sin\alpha\sin(\alpha + 2\delta) \tag{9}$$

Principal stress can then be obtained for point M as:

$$\sigma_3^1 = \frac{p_0}{\pi}\alpha + \frac{1+K_0}{2}(\gamma_0 D + \gamma z) \pm \sqrt{[\frac{p_0}{\pi}\sin\alpha\cos(\alpha+2\delta) + \frac{1-K_0}{2}(\gamma_0 D + \gamma z)]^2 + [\frac{p_0}{\pi}\sin\alpha\sin(\alpha+2\delta)]^2} \tag{10}$$

This process improves the methods proposed by Zhao (1995) and Xue (2005), which can't obtain principal stresses of point M. Moreover, equation of uniform strip load can be established when point M reaches the state of limit equilibrium based on Mohr-Coulomb failure criterion:

$$\sigma_1 = \sigma_3 \tan^2(45^\circ + \frac{\varphi}{2}) + 2c\tan(45^\circ + \frac{\varphi}{2}) \tag{11}$$

Then critical edge pressure p_{cr} or critical load $p_{1/4}$ can be calculated by assuming z equal 0 or $B/4$. Input the basic parameters of soil, and let the abscissa of point M vary in a certain range. The bearing capacities with different abscissas are obtained by solving the equation and choosing reasonable solutions. The minimum reasonable solution is critical edge pressure p_{cr} or critical load $p_{1/4}$ of the foundation soil.

Example

A 3 m wide strip foundation is embedded in clay at a depth of 1 m .The unit weight of clay is 19 kN/m^3. The shear strength parameters of soil are c=10 kPa, and $\varphi' = 10^\circ$. The influence of groundwater is ignored. Find bearing capacity of soil p_{cr} and $p_{1/4}$.

In this example, coefficient of earth pressure at rest is $K_0 = 1 - \sin\varphi' = 0.83$. Input known parameters to program in this paper, and let Z coordinate of point M equal to 0 and $B/4$ respectively. p_{cr} and $p_{1/4}$ can then be calculated. The comparison between solutions obtained by program and those by other methods are shown in Table 1.

Table 1. Comparison of Results with Different Methods

Result	Method in this Paper When K_0=0.83	Method in this Paper When K_0=1	Method in Textbook
p_{cr}/kPa	55.7	74.6	75.0
$p_{1/4}$/kPa	61.3	85.1	84.8

Method in textbook in the table is the method mentioned in section 1. It is derived

with the assumption of $K_0 = 1$.

It is obviously, from Table 1, that, when the value of K_0 approaches 1, the solutions obtained by method in this paper are basically in agreement with results calculated by the method in textbook. The errors between them are induced by the accuracy of value. The validity of the method of this paper is then confirmed.

It is also shown that the solutions obtained by the program of this paper are 30% less than the solutions calculated by the method in textbook because $K_0 \neq 1$ is considered in program. Assumption of K_0=1 makes geostatic stress of soil just act like hydrostatic stress, and limits the lateral deformation of soil. Therefore, the bearing capacity must increase. This phenomenon is also pointed out by Poulos (2001) at the 15th International Conference on soil mechanics and foundation engineering. It is said that "some traditional theories are proved inaccurate with the progress in theory of soil mechanics including Terzaghi's bearing capacity theory. This theory often overestimates bearing capacity of shallow foundation." Furthermore, it can be found in some engineering practice that the critical load determined by bearing capacity formulas is higher than the results controlled by deformation of soil (Cui 1998). This is to say that K_0=1 is incorrect when developing bearing capacity formulas.

Solutions under the condition of $K_0 \neq 1$ are less than those under the condition of K_0=1, as shown in Table 1. It shows that depth of plastic zone in soil when $K_0 \neq 1$ is deeper than that when K_0=1. The depth of plastic zone in soil with different ultimate loads is calculated for $K_0 = 1 - \sin\varphi'$ and $K_0 = 1$ respectively. The corresponding results are presented in Table 2.

Table 2. Comparison of Development of Plastic Zones

p /kPa	100	150	200	250
$K_0 = 1 - \sin\varphi'$	0.43B	0.48B	0.52B	0.56B
K_0=1	0.35B	0.38B	0.40B	0.42B

It is shown in Table 2 that the depth of plastic zone under the condition of $K_0 = 1 - \sin\varphi'$ is deeper than that under the condition of $K_0 = 1$. The depth of plastic zone appears to be conservative when assuming $K_0 = 1$. Assuming the depth of plastic zone to be $B/4$ in the standard is therefore not reasonable, i.e., assuming $K_0 = 1$ is not reasonable.

PARAMETER SENSITIVITY ANALYSIS

In order to study the relationship between K_0 and c or φ, the sensitivity analysis of parameters is performed in the paragraphs below.

Influence of K_0 on Critical Load

In order to study the influence of K_0 on critical load when changing c, we can vary the value of c from 0 to 50 kPa. The friction angle is $\varphi = 10^\circ$ and all other parameters are

the same as those used in the example in section 2.2. The calculated results are shown in Figure 2.

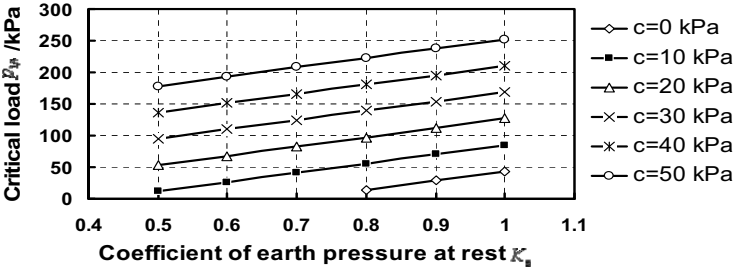

FIG. 2. Relationship between K_0 and $p_{1/4}$ ($\varphi = 10^\circ$).

Critical load $p_{1/4}$ linearly increases with increasing coefficient of earth pressure at rest K_0, as shown in Figure 2. Critical loads also increase with increasing cohesion c. When c changes from 0 kPa to 50 kPa, the relationship lines between critical loads and K_0 are almost parallel to each other. In other words, the increasing rate of critical load is nearly invariant with different cohesion. Therefore, regardless of the value of cohesion, the rate of increase in bearing capacity of soil is nearly constant when the value of φ is fixed.

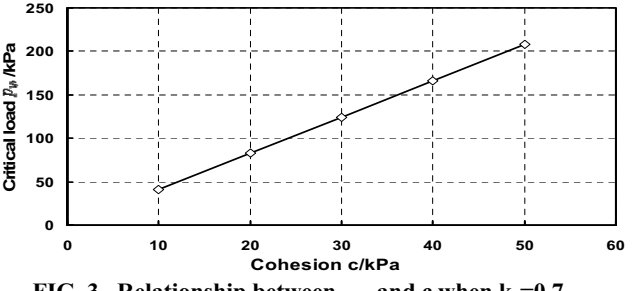

FIG. 3. Relationship between $p_{1/4}$ and c when k_0=0.7.

Figure 2 also shows that the distance between two adjacent parallel lines is almost constant, i.e., the relationship between $p_{1/4}$ and c is approximately linear. In order to verify this observation, the relationship between $p_{1/4}$ and c is plotted in Figure 3 for φ equal 10° and K_0 equal 0.7. It is obvious that the critical load and cohesion have linear relationship.

There is also a problem appeared from Figure 2. The critical load calculated by the program of this paper is obviously smaller when c is 0 kPa. Three negative values on the line of c=0 kPa are not plotted in Figure 2. Similar conclusion can be obtained by using formulas of textbook. Actually, bearing capacity of soils with c=0 kPa is quite high which is verified the field loading tests (Xue 2005). This suggests that the critical load

developed based on elastic theory and Mohr-Coulomb failure criterion is not suitable for medium sand and coarse sand.

Influence of K_0 on Critical Load

In order to study the influence of K_0 on critical load when changing φ, we can vary the value of φ from 10° to 35°. The cohesion intercept of soil is c=20 kPa and all other parameters are the same as those used in the example in section 2.2. The calculated results are shown in Figure 4.

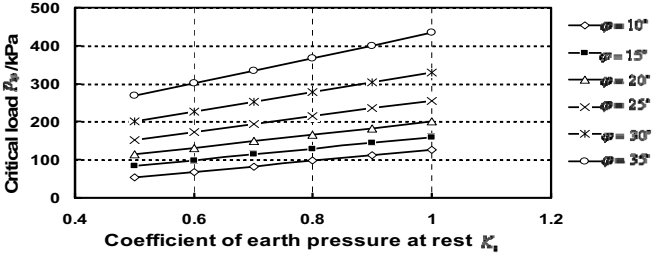

FIG. 4. Relationship between K_0 and $p_{1/4}$ (c=20 kPa).

Again, critical load $p_{1/4}$ and coefficient of earth pressure at rest K_0 have linear relationship, as shown in Figure 4. Critical loads increase with increasing friction angle φ. When φ changes from 10° to 20°, the relationship lines between critical load and K_0 are almost parallel to each other. As φ changes from 20° to 35°, the relationship line between $p_{1/4}$ and K_0 becomes steeper and steeper. In other words, the rate of change in critical load is nearly invariant when the soil has small friction angle (clayey soil). However, for the soil with large friction angle (sand), the rate of change in $p_{1/4}$

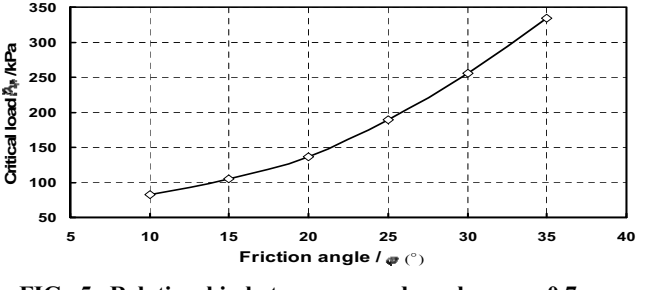

FIG. 5. Relationship between $p_{1/4}$ and φ when K_0 = 0.7.

gradually increases with increasing K_0. Therefore, the rate of change in critical load for soil with small friction angle is less than that for soil with large friction angle when value of c is fixed.

Figure 5 presents the relationship between $p_{1/4}$ and φ is for c equal 20 kPa and K_0 equal to 0.7. It is shown that $p_{1/4}$ gradually increases with increasing φ when φ varies from 10° to 20°. It is also shown that $p_{1/4}$ increases at a faster rate when φ is greater than 20°. As shown in Figure 5, the critical load approximately exponentially increases with increasing of the friction angle.

CONCLUSION

A MATLAB program is used to find the numerical solution of soil bearing capacity when $K_0 \neq 1$. This method overcomes some shortcomings of the methods available in the literature. Based on the results of numerical solution, the following conclusions can be drawn:

(1) Assumption of $K_0=1$ makes geostatic stress of soil just act like hydrostatic stress, and limits the lateral deformation of soil that bearing capacity must increase.

(2) K_0 and critical load have linear relationship when the value of either c or φ is fixed.

(3) When the value of φ is fixed, the rate of increase in $p_{1/4}$ is nearly constant regardless of the value of c. The rate of increase in critical load for soil with small φ is less than the soil with large friction angle when the value of c is fixed.

(4) The critical load approximately linearly increases with increasing cohesion and exponentially increases with increasing friction angle.

It should be mentioned that the bearing capacity of soils with c=0 kPa and the influence of K_0 on plastic zone depth need to be further investigated.

REFERENCES

Craig R.F. Soil mechanics. Chapman & Hall, 1995: 296-299.

Zhao Shude. Formulation of bearing capacity of subgrade with $K_0 \neq 1$[J]. J. Xi'an Univ. of Arch. & Tech, 1995, 27(3): 294-298.

Xue Hui, Liu Junyong. Study on critical edge pressure of foundation[J]. *Subgrade Engineering,* 2005(6): 47-50.

Cui Jiangyu, Song Jinfeng. The analysis of the critical edge pressure for subsoil[J]. *Engineering Mechanics*, 1998, 15(4): 96-100.

Poulos, H.G., Carter, J.P., Small, J.C., Proc. 15th International Conference on soil mechanics and foundation engineering, Foundations and retaining structures - research and practice, 2001, Istanbul, Turkey.

Zhang Zaiming, Zhou Honglei, Gao Wensheng. Review of some problems of theory and practice in foundation design [C]// Proc. of the 10th Conf. on soil mechanics & geotechnical engineering. Beijing: Science Press. 2007: 12-31.

H.G.Poulos., E.H.Davis, Elastic solutions for soil and rock mechanics [M]. Beijing: China University of Mining Technology Press, 1990: 43-44.

Study on the Determination of Residual Shear Strength for Expansive Soil

Heping Yang[1], Jie Xiao[2], Shu Wang[3], and Weiran Zuo[4]

[1]Professor, School of Communication and Transportation Engineering, Changsha University of Science and Technology; PH (86) 731-2309581; cscuyang@163.com
[2]Assistant, School of Communication and Transportation Engineering, Changsha University of Science and Technology; PH (86) 731-2309581; xiaojie324@sina.com
[3]Graduate student, School of Communication and Transportation Engineering, Changsha University of Science and Technology; PH (86) 731-2309581; daiias@qq.com
[4]Engineer, Roadway administration of Hunan; PH (86)731-2582626; nhw3344@sohu.com

ABSTRACT: Generally, it is very difficult to obtain the undisturbed soil and keep it in the undisturbed state in practice. In this paper the residual shear strength of Grey-white expansive soil of Ningming was studied based on the analysis of the influencing factors of residual shear strength of expansive soil. The test results of undisturbed samples, compacted samples and samples prepared by static compaction conducted by strain-controlled repeated direct shear test were compared, which show that the differences of the peak shear strengths are very large but the differences of the residual shear strengths are very small. By the comparison and analysis of the test results, it is more reasonable and practical to use the residual shear strength of static compaction sample to represent that of undisturbed sample. Therefore, the residual shear strength (c=10.53 kPa, φ=11.55°) of samples prepared by static compaction can be taken as that of Ningming Grey-white expansive soil.

INTRODUCTION

The shear strength of the soil decreases when the shearing displacement continues to increase after the peak shear strength and in the end reaches a constant (i.e., the residual shear strength of the soil) during the shear tests of the soil (Skempton 1985). The residual shear strength of the soil plays an important role in the evaluation of engineering properties of soils, analysis of slope stability and estimation of old landslide stability (Dai Fuchu 1998).

Factors that influence the residual shear strength of soils include the type of clay mineral (Lupini et al. 1981; Yamasaki et al. 2000, Tiwari and Marui 2003), the relative amounts of the soil constituents (Skempton 1985, Bao Chenggang 2007), index properties of the clay (Voight 1973), pore-water chemistry (Ramiah et al. 1970). Furthermore, the stress history and initial structure of the soil have a great influence on

the residual shear strength. So the correlation between the residual shear strength and plasticity index of soil or clay fraction under different effective normal stresses should be established (Hawkins 1986). In general, the greater plasticity indexes of the soil and the more the clay fraction, the smaller the residual shear strength. Skempton (1985) obtains that the residual shear strength is mainly determined by the friction between clay mineral (<0.002mm) when the clay fraction of the soil is more than 50%. In addition, mineral component of the soil and pore-water chemistry have certain influence on the residual shear strength. In addition, the residual shear strength of clay mineral particles with flat shape is smaller than that of clay mineral particles with needle shape.

The influence of shearing rate on the residual shear strength is very complex. Research show that it has little influence on the residual shear strength for shearing rates in a small range, but have a great influence on the residual shear strength for the shearing rate more than 100 mm/min. The relationship between the residual shear strength and effective normal stress is not a constant, which is nonlinear for the effective normal stress less than 150 kPa.

At present, there are three methods to determine the residual shear strength of soils: (1) in-situ shear method; (2) laboratory test method, including repeated direct shear method, ring-shear test method and triaxial test method; (3) back analysis evaluation method. Back analysis evaluation method as a theoretical method is very useful to evaluate the old landslide and slowly sliding slopes. However, some basic assumptions having uncertain properties must be given in the process of back analysis, which will result in uncertain analysis results. Compared to the other two laboratory test methods, the repeated direct shear method is a common method having some advantages of simple device, low price and simple operation.

Expansive soil as one type of special clays has such characteristics: swelling and softening when absorbing water and shrinkage and cracking when losing water. The shear strength of expansive soil is an important parameter to evaluate the slope stability of cut slopes, embankment, canal and earth dam and the earth pressure of retaining building. In practical engineering, many landslide slopes analyzed by the peak strength are stable. However, the average shear strength of sliding surface determined by back analysis method is much less than the peak strength because of the peak strength of expansive soil is higher than the residual shear strength (Liu Xiaoli 2004). Actually, the evolution of deformation failure of expansive soil slope is a process of the shear strength of expansive soil decaying from the peak strength to the residual shear strength. Therefore, it is necessary to apply the residual shear strength instead of the peak strength to analyze the stability of expansive soil slope.

It is very inconvenient for undisturbed soil's sampling, transportation and preservation. In this paper the residual shear strength of Ningming Grey-white expansive soil was conducted by the strain-controlled direct shear apparatus. Therefore, the feasibility of applying disturbed samples to determine the residual shear strength of expansive soil is discussed by comparison of the results of compacted samples, undisturbed samples and the samples prepared by static compaction. The analysis and comparison of the test results are performed.

RESIDUAL SHEAR STRENGTH TESTS ON NINGMING EXPANSIVE SOIL

Characteristics of Expansive Soil

Ningming expansive soil is a brown or gray residual expansive soil. Material composition and characteristics of the soil used in the test are shown in table 1 and table 2 respectively (Yang Heping 2005).

Table 1. Material Composition of Ningming Expansive Soil

Sampling Point	Particle Composition/%				Smectite Content (%)	Specific Surface Area ($m^2 \cdot g^{-1}$)
	>0.075 (mm)	0.075~0.005 (mm)	<0.005 (mm)	<0.002 (mm)		
K139+297.8	3.71	41.01	55.28	48.24	20.14	191.38

Table 2. Properties of Ningming Expansive Soil

Unit Weight ($kN \cdot m^{-3}$)	Water Content (%)	Dry Density ($g \cdot cm^{-3}$)	Liquid Limit (%)	Plastic Limit (%)	Plasticity Index	Free Swelling Ratio (%)	Specific Gravity
19.31	25.0	1.31	59.67	27.09	32.58	75	2.77

Repeat Direct Shear Testing

The repeat direct shear tests for this study are conducted by the strain-controlled direct shear apparatus produced by Nanjing geotechnical instrument factory. The drained shear tests on four samples in each group are performed at different effective normal stresses (50 kPa, 100 kPa, 150 kPa and 200 kPa), all of which are sheared at the shearing rate of 0.02 mm/min until the shearing displacement reaching the maximum. After the first shearing test finished reverse the motor and put the top and bottom box superposition, and then continue the next shearing test. Repeat until the relationship curve of shear stress and displacement is almost horizontal.

In this paper the residual shear strength tests on three kinds of samples (i.e., undisturbed samples, compacted samples and samples prepared by static compaction method) are carried out. The procedures of these samples preparation are in accordance with the procedure of the soil sampling and sample preparation (T0102-2007) in Tests Method of soils for Highway Engineering (JTG E40-2007). The water contents of the all samples are 25%. The samples prepared by static compaction method have the same dry density of 1.31 g/cm^3 as that of undisturbed samples.

TEST RESULTS AND ANALYSIS

The representative relationships between shear stress and displacement for undisturbed sample, compacted sample and static compaction sample at the effective normal stress of 100 kPa are shown in figure 1, 3 and 5 respectively.

For the test data, two envelopes can be plotted for the peak shear strength measured for the first shearing and the residual shear strength for the third shearing. The relationships between normal stress and shear strength for three kinds of samples are showed in figure 2, 4 and 6 respectively.

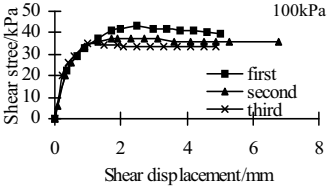

Fig. 1. Relationship between shear stress and shear displacement for undisturbed sample.

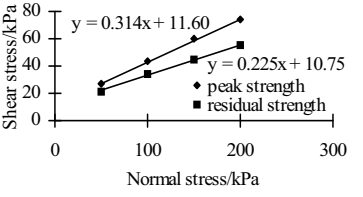

Fig. 2. Relationship between normal stress and shear stress for undisturbed sample.

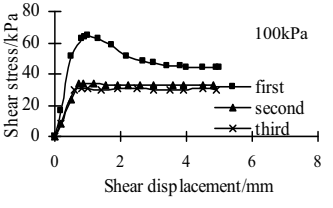

Fig. 3. Relationship between shear stress and shear displacement for compacted sample.

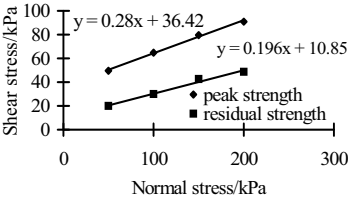

Fig. 4. Relationship between normal stress and shear stress for compacted sample.

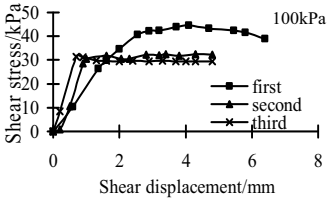

Fig. 5. Relationship between shear stress and shear displacement for static compaction sample.

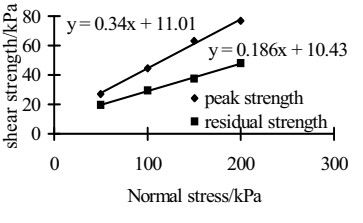

Fig. 6. Relationship between normal stress and shear stress for static compaction sample.

The corresponding shear strength parameters determined for the undisturbed, compacted and static compaction sample obtained from figure 2, 4 and 6 are summarized in table 3.

Table 3. Shear Strength Parameters of Ningming Expansive Soil

Soil Sample	Peak Shear Strength		Residual Shear Strength	
	c/kPa	*φ*/(°)	*c*/kPa	*φ*/(°)
Undisturbed sample	11. 60	17.41	10.75	12.70
Compacted sample	36.40	15.60	10.85	11.10
Static compaction sample	11.01	18.53	10.53	11.55

Figure 1, 3 and 5 shows that the residual shear strength tends to a constant after three times shearing. The peak shear strength of compacted sample exhibits obvious strain softening at the first shearing, but the peak shear strengths of undisturbed sample and static compaction sample exhibit no obvious strain softening at the first shearing. There is no obvious peak shear strength during the second shearing and the third shearing.

Table 3 shows that the peak shear strength parameter c of 36.40 kPa of compacted sample is very large as compared to 11.60 kPa of undisturbed sample and 11.01 kPa of static compaction sample. In contrary, the peak shear strength parameter φ of compacted sample is a bit less than those of undisturbed sample and static compaction sample. However, not only the peak shear strength but also the residual shear strength of the undisturbed sample and the static compaction sample are very close. In addition, comparing to compacted sample it is easier to control the dry density of static compaction sample to that of undisturbed sample. All of these indicate that it is more reasonable and useful to use the residual shear strength of static compaction sample compared to compacted samples to represent that of undisturbed sample. Meanwhile, the residual shear strength parameters (c=10.53 kPa, φ=11.55°) of static compaction sample are only a bit less than those of undisturbed sample. Utilizing these parameters to calculate the stability of expansive soil slope inclines to be safer. Therefore, it can be taken as the residual shear strength of Ningming expansive soil.

It should be noted that there is little decrease in c but larger decrease in φ for undisturbed sample and static sample, which is probably due to the water content increasing and the clay mineral particles rearranging along the shearing surface of samples. This is probably the main reason for the decrease of the peak shear strength to the residual shear strength.

CONCLUSIONS

The residual shear strength is an essential characteristic of expansive soil. The main reason for the failure of expansive soil slope is that the shear strength of the soil slowly decreases by cyclic wetting and drying, and slow sliding. Therefore, residual shear strength need to be used to calculate the stability of expansive soil slope.

It is very difficult to get the undisturbed expansive soil samples and especially

keep it in the undisturbed condition during sampling, transportation, presentation and sample preparation. In this paper, the test results of undisturbed samples, compacted samples and samples prepared by static compaction conducted by strain-controlled repeated direct shear test were compared and analyzed. It is more reasonable and useful to use the residual shear strength of static compaction sample to represent that of undisturbed sample. Therefore, the residual shear strength of expansive soil may be determined by repeated direct shear test performing on the static compaction sample.

REFERENCES

Bao Chenggang (2007). "Relationship between residual shear strength of soil and engineering problems." *Bao Chenggang selected papers on study of geotechnical engineering*. (in chinese).

Dai Fuchu., Wang Sijing., and Li Zhuofen (1998). "The drained residual shear strength of volcanics-derived soil sampled on Lantau island." *Journal of engineering geology*, Vol. 6(3):223-228. (in chinese).

Hawkins, A. B., and Privett, K. D (1986). Residual shear strength: Does Bs5930 help or hinder? *Geological Society*, Engineering Geology Special Publication, No. 2, 279-282.

Liu Xiaoli., Deng Jianhui., and Li Guangtao (2004). "Shear strength properties of slip soils of landslides: an overview." *Rock and Soil Mechanics*. Vol. 25(11): 1849-1854.

Ministry of Transport of the People's Republic of China. (2007). Test methods of soils for highway engineering, Beijing, China (in chinese).

Lupini, J. F., Skinner, A. E., and Vaughan, P. R. (1981). "The drained residual strength of the cohesive soils." Geotechnique, 31(2), 181-213.

Ramiah, B. K., Dayalu, N. K., and Purushothamaraj, P. (1970). Influence of chemicals on residual strength of silty clay." Soils Found., 10, 25-36.

Skempton A. W. (1985). "Residual shear strength of clays in landslides, folded strata and the laboratory." *Geotechnique*, Vol. 35 (1), 3-18.

Tiwari, B., and Marui, H. (2004). "Objective oriented multi-stage ring shear test for the shear strength of landslide soil." J. Geotech. Geoenviron. Eng., 130(2), 217–222.

Voight, B. (1973). "Correlation between Atterberg plasticity limits and residual shear strength of natural soils." Geotechnique, 23(2), 265-267.

Yang Heping., Qu Yongxin., and Zheng Jianglong (2005). "New development in studies on Ningming expansive soils." *Chinese journal of geotechnial engineering*, Vol. 27(9):981-987. (in chinese).

Yamasaki, T., and Mayumi, T. (2000). "Ring shear characteristics of high purity clay minerals-correlation with natural slip surface clay." J. Japan Landslide Society, 37(2), 30-39.

Modeling Stress-Strain Behavior of Sand-EPS Beads Lightweight Fills Based on Cam-Clay Models

An Deng[1] and Yang Xiao[2]

[1]Associate Professor, Key Laboratory of Ministry of Education for Geomechanics and Embankment Engineering, Hohai University, Nanjing 210098, China;
Geotechnical Research Institute, Hohai University, Nanjing 210098, China; a_deng@hhu.edu.cn
[2] ditto

ABSTRACT: A lightweight fill was produced by blending expanded polystyrene (EPS) beads and sands in proportions. Such formed granular geomaterials, known as sand-EPS lightweight fills, have potentials of being lightweight compared to traditional fills, thus are suitable for many infrastructure works where less overburdens are expected, e.g., utilities trench backfills. Consolidated drained triaxial compression (TC) tests were conducted on the lightweight fills to observe materials' stress-strain relationships, specifically, the stress-strain variations associated with the mixing ratios of EPS beads. EPS beads were incorporated into the mixtures based on their mass ratios over sands, i.e., 0.5%, 1.5% and 2.5%. It was found that confining pressures and mixing proportions played important roles in affecting the stress-strain behaviors of lightweight fills. The materials underwent shear contraction, which is related to the inclusion of EPS beads. The constitutive law of the lightweight fills was derived based on Cam-clay model and modified Cam-clay model, and verified by the test results.

INTRODUCTION

Lightweight fills possess an attractive advantage over general soil fills, i.e., low unit weight. Such property immediately offsets some overburdens, and thus mitigates the settlement or deformation of underlying stratums. Potential end applications of the materials include embankments over soft ground or being widened, slope and retaining works, and many backfilling works. Furthermore, many lightweight fills are able to isolate or mitigate vibrations. As such, more and more researches are drawn onto the lightweight fills. At the very beginning, Horvath (1994, 1997) and Duškov (1997) applied expanded polystyrene (EPS) block geofoams to embankments and bridge approach embankments to reduce overburdens, isolate vibrations and resist frost attacks. The Japanese researchers initiated laboratory and pilot scale studies on lightweight soils containing EPS scraps or beads, geofoam materials, or foaming agents (Tsuchida 2001). Recently, Chinese researchers investigated the strength and deformation behavior (Liu et al. 2006) and dynamic behavior (Wang and Gao 2007) of

lightweight fills containing silty soils, EPS beads and Portland cement. Sediment or dredge slurry was also used to form lightweight soils, which not only reclaims the slurry, but also stabilizes the pollutants in the slurry (Zhu et al. 2005). Besides the EPS materials and geofoams, rubber or tire scraps were also used to make lightweight geomaterials.

In this paper, EPS beads and construction sands were blended homogeneously to form nonstructural granular lightweight fills. The non-cementitious lightweight fills not only save the use of cement, but also are suitable for works where low strength and instant excavation are expected. The focus of the research is on the constitutive law reflecting the stress-strain behavior of the granular fills. Laboratory consolidation-drained triaxial compression (TC) tests were implemented on fills of different mixing proportions. The stress-strain relationships of the materials were observed and analyzed. Based on Cam-clay and modified Cam-clay models, a proportion-based constitutive model was derived and verified.

EXPERIMENTAL PROGRAM

Materials and Specimens

Materials included construction fine sands and EPS beads. The water content of sand was 5%. Its specific gravity was 2.62. The gradation curve of sands is shown in Fig. 1. It was classified as well-graded sand (SW) by ASTM D2487. EPS is a super light polymer, foamed from polystyrene resin and pre-puffed at 35-40 folds. The EPS beads were even and spherical, sizing around 2 mm (Fig. 2), with bulk density and specific gravity being 0.015 g/cm^3 and 0.03, respectively.

The specimens were formed by incoporating EPS beads into sands at a mass ratio η of EPS beads over sands. Selected ratios were 0.5%, 1.5% and 2.5%. Scaled materials were mixed completely through air-mixing methods. The specimens were prepared in accordance with Chinese Standard for Soil Test Method (GB/T50123-1999). Mixtures were loaded into the rubber membrane hooped by a splittable mold. The relative densities of mixtures were controlled at 0.5. Back-pressures were used to saturate the specimens.

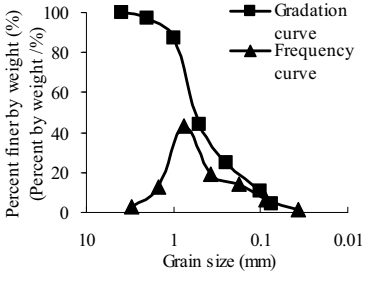

FIG. 1. Gradation curves of sands.

FIG. 2. Sand-EPS beads mixture.

Test Methods

Consolidation-drained TC tests were performed in accordance with Chinese Standard for Soil Test Method (GB/T50123-1999). The confining pressures σ_3 were 100, 200, 300 and 400 kPa. The compression rate was 0.015 mm/min (i.e., 0.018% strain per minute) to allow for drainage in shears. Observations include deviatoric stress q, axial strain ε_a and volumetric strain ε_v.

DISCUSSION OF CONSTITUTIVE LAW

Establishment of Constitutive Law

Many constitutive models were proposed with regards to the stress-strain behavior of soils (Huang 1980, Yin 1988, Shen 1989, Li 2006). These models are largely divided into two types: elastic models and elasto-plastic models. The latter is more robust than the former to represent the soil behavior, e.g., soil hardening or softening characteristics, shear dilation and stress paths, and thus is more prevailing (Qu 1987, Yin 1988, Qian and Yin 1996, Li 2006). One of the classical elasto-plastic model is Cam-clay model, which contains relatively less parameters, and is easy to be verified. Eqs. 1-2 present the strain differential eqs. of Cam-clay model (Qu 1987).

$$d\varepsilon_v = \frac{-de}{1+e} = \frac{1}{1+e}\left[\frac{\lambda-k}{mp}\left(dq - \frac{qdp}{p}\right) + \lambda\frac{dp}{p}\right] \tag{1}$$

$$d\varepsilon_s = \frac{\lambda-k}{(1+e)mp}\left(\frac{dq}{m-q/p} + dp\right) \tag{2}$$

$$d\varepsilon_a = d\varepsilon_s + \frac{1}{3}d\varepsilon_v \tag{3}$$

where, ε_v denoting volumetric strain, ε_a denoting axial strain, ε_s denoting shear strain, e denoting initial void ratio, λ denoting the slope of normal consolidation line $v - \ln p$, k denoting the slope of over-consolidation line $v - \ln p$, m denoting lateral confinement modulus, p denoting average normal stress, q denoting general stress.

Eqs. 1-3 were combined to produce Eq. 4:

$$d\varepsilon_a = \frac{\lambda-k}{(1+e)mp}\left(\frac{dq}{m-q/p} + dp\right) + \frac{1}{3(1+e)}\left[\frac{\lambda-k}{mp}\left(dq - \frac{qdp}{p}\right) + \lambda\frac{dp}{p}\right] \tag{4}$$

Similarly, Eqs. 5-7 can be derived in accordance with modified Cam-clay model (Qu 1987).

$$d\varepsilon_v = \frac{1}{1+e}\left[(\lambda-k)\frac{2\left(\frac{q}{p}\right)d\left(\frac{q}{p}\right)}{m^2+\left(\frac{q}{p}\right)^2}+\lambda\frac{dp}{p}\right] \tag{5}$$

$$d\varepsilon_s = \frac{\lambda-k}{1+e}\left[\frac{2\left(\frac{q}{p}\right)}{m^2-\left(\frac{q}{p}\right)^2}\right]\left[\frac{2\left(\frac{q}{p}\right)d\left(\frac{q}{p}\right)}{m^2+\left(\frac{q}{p}\right)^2}+\frac{dp}{p}\right] \tag{6}$$

$$d\varepsilon_a = \frac{\lambda-k}{1+e}\left[\frac{2\left(\frac{q}{p}\right)}{m^2-\left(\frac{q}{p}\right)^2}\right]\left[\frac{2\left(\frac{q}{p}\right)d\left(\frac{q}{p}\right)}{m^2+\left(\frac{q}{p}\right)^2}+\frac{dp}{p}\right]+\frac{1}{3(1+e)}\left[(\lambda-k)\frac{2\left(\frac{q}{p}\right)d\left(\frac{q}{p}\right)}{m^2+\left(\frac{q}{p}\right)^2}+\lambda\frac{dp}{p}\right] \tag{7}$$

Sand-EPS bead lightweight mixtures are more complex than soils, which complicates the constitutive law of the lightweight mixtures. The classical soil constitutive models may not suit the stress-strain behavior of sand-EPS mixtures. For instance, as shown in Fig. 3, neither Cam-clay model nor modified Cam-clay model is able to reflect the stress-strain relationship of a specimen. It is seen that the strain is either over-estimated or under-estimated for Cam-clay model and modified Cam-clay model respectively.

Nevertheless, it was noticed that the higher the EPS proportion η, the closer to the Cam-clay model the curve; the less the EPS proportion η, the closer to the modified Cam-clay model the curve. The stress-strain curve basically fluctuates within these two models depending upon the EPS proportions. It was thus conceived to derive a model comprising Cam-clay and modified Cam-clay models to simulate the observations in Fig. 3.

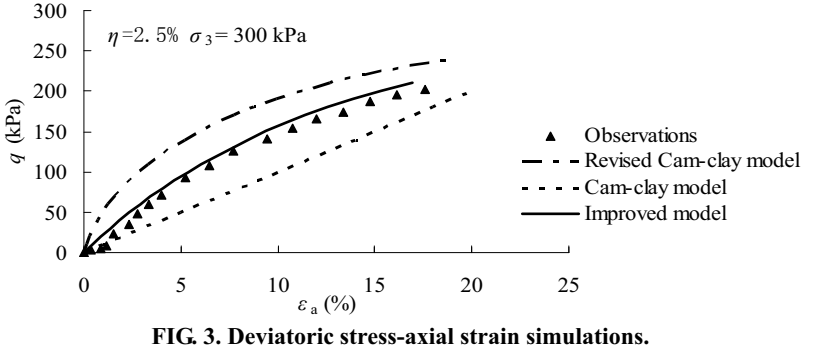

FIG. 3. Deviatoric stress-axial strain simulations.

A lightweight fill unit was divided into two parts, denoted by $\zeta(\eta)$ and $(1-\zeta(\eta))$. Stress-strain increments of the former part was depicted using modified Cam-clay

model, i.e., Eqs. 5-7; the latter part was depicted using Cam-clay model, i.e., Eqs. 1-2 and 4. It was assumed that the boundary conditions were stabilized in shears. Thus, the total strain increments ($d\varepsilon_v$, $d\varepsilon_s$, $d\varepsilon_a$) were equal to the sum of strain increments of two parts, i.e., $d\varepsilon_v^A$, $d\varepsilon_s^A$, $d\varepsilon_a^A$ for part (1-ζ(η)), and $d\varepsilon_v^B$, $d\varepsilon_s^B$, $d\varepsilon_a^B$ for part ζ(η), as described in Eqs. 8-10.

$$d\varepsilon_v = (1-\zeta(\eta))d\varepsilon_v^A + \zeta(\eta)d\varepsilon_v^B \tag{8}$$

$$d\varepsilon_s = (1-\zeta(\eta))d\varepsilon_s^A + \zeta(\eta)d\varepsilon_s^B \tag{9}$$

$$d\varepsilon_a = (1-\zeta(\eta))d\varepsilon_a^A + \zeta(\eta)d\varepsilon_a^B \tag{10}$$

The model described in Eqs. 8-10 comprises Cam-clay and modified Cam-clay models, and is able to depict the complex stress-strain behavior by taking into account the EPS proportions.

Merging Eqs. 1, 2 and 4 and Eqs. 5-7 into Eqs. 8-10, the following strain increments were obtained:

$$d\varepsilon_v = [1-\zeta(\eta)]\frac{1}{1+e}\left[\frac{\lambda-k}{mp}\left(dq-\frac{qdp}{p}\right)+\lambda\frac{dp}{p}\right]+\zeta(\eta)\frac{1}{1+e}\left[(\lambda-k)\frac{2\left(\frac{q}{p}\right)d\left(\frac{q}{p}\right)}{m^2+\left(\frac{q}{p}\right)^2}+\lambda\frac{dp}{p}\right] \tag{11}$$

$$d\varepsilon_s = [1-\zeta(\eta)]\frac{\lambda-k}{(1+e)mp}\left(\frac{dq}{m-q/p}+dp\right)+\zeta(\eta)\frac{\lambda-k}{1+e}\left[\frac{2\left(\frac{q}{p}\right)}{m^2-\left(\frac{q}{p}\right)^2}\right]\left[\frac{2\left(\frac{q}{p}\right)d\left(\frac{q}{p}\right)}{m^2+\left(\frac{q}{p}\right)^2}+\frac{dp}{p}\right] \tag{12}$$

$$d\varepsilon_a = [1-\zeta(\eta)]\left\{\frac{\lambda-k}{(1+e)mp}\left(\frac{dq}{m-q/p}+dp\right)+\frac{1}{3(1+e)}\left[\frac{\lambda-k}{mp}\left(dq-\frac{qdp}{p}\right)+\lambda\frac{dp}{p}\right]\right\}+$$

$$\zeta(\eta)\left\{\frac{\lambda-k}{1+e}\left[\frac{2\left(\frac{q}{p}\right)}{m^2-\left(\frac{q}{p}\right)^2}\right]\left[\frac{2\left(\frac{q}{p}\right)d\left(\frac{q}{p}\right)}{m^2+\left(\frac{q}{p}\right)^2}+\frac{dp}{p}\right]+\frac{1}{3(1+e)}\left[(\lambda-k)\frac{2\left(\frac{q}{p}\right)d\left(\frac{q}{p}\right)}{m^2+\left(\frac{q}{p}\right)^2}+\lambda\frac{dp}{p}\right]\right\} \tag{13}$$

where, ζ(η) denoting the ratio of material volume relying on modified Cam-clay model over the entire volume, which is associated with the EPS proportion η. The more the EPS contents, the less the ζ(η) value. According to the TC results, the model parameters are figured out in Table 1.

Table 1. Parameters of Constitutive Model.

$_1$ /%	m	k	λ	ζ(η)
0.5	1.4723	0.0353	0.0869	0.8100
1.5	1.1107	0.0918	0.2386	0.6500
2.5	0.9084	0.1399	0.3952	0.5200

The solid line in Fig. 3 represents a model curve plotted in terms of Eq. 13 and parameters in Table 1. It is seen that the solid line is superior to the Cam-clay models to simulate the observations.

Verification of Model

Deviatoric stress-axial strain relationship*s*

Verifications were implemented by plotting strain increments (Eqs. 11-13) and test observations in a chart, as shown in Figs. 4 and 5. The solid lines represent the model curves, which basically simulate the observations of specimens subjected to tested stress conditions. Under high confining pressures, the model curves deviate a bit from the observations, slightly under-estimating strains. Anyhow, the improved strain increments are suitable for simulating deviatoric stress-axial strain behavior of sand-EPS beads lightweight fills.

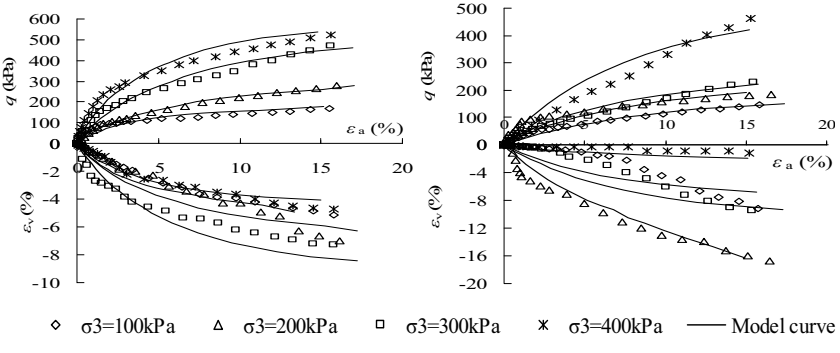

FIG. 4. q - ε_a - ε_v simulations (η=0.5%). **FIG. 5. q - ε_a - ε_v simulations (η=1.5%).**

Volumetric strain-axial strain relationships

A volumetric contraction is presumed to be negative. As shown in Figs. 4 and 5, sand-EPS beads lightweight fills underwent shear contraction throughout the TC tests. When the confining pressures σ_3 were 100 and 400 kPa, the model curves well simulated the observations. When the EPS proportions were relatively low, the model curves were also robust to simulate the observations. When the confining pressures σ_3 were 200 and 300 kPa, the volumetric strain simulations were weak. This may source from the bias occurred to the observation of volumetric strain of EPS beads. Anyhow, the simulations were superior to that directly given by Cam-clay models, and were basically acceptable for describing the volumetric strain-axial strain relationships.

Combine the above stress-strain simulations, the proposed model was verified suitable for depicting the constitutive laws of sand-EPS bead lightweight fills, and thus usable for estimating the stress, strain, settlement and strength of practical works.

CONCLUSIONS

Through consolidation-drained TC tests, sand-EPS bead lightweight fills of three mixing proportions were researched about their deviatoric stress-volumetric strain-axial strain relationships. Based on TC test results and analyses, a proportion-based model was derived depicting the constitutive laws of lightweight fills in terms of Cam-clay and modified Cam-clay models. The model was verified according to the TC observations.

ACKNOWLEDGEMENTS

The work was supported by National Natural Science Foundation of China (50708031) and Scientific Research Foundation for the Returned Overseas Chinese Scholars, SEM.

REFERENCES

Duškov, M. (1997). "Measurements on a flexible pavement structure with an EPS geofoam sub-base." *Geotext. Geomembranes*, Vol. 15 (1-3): 5–27.

Horvath, J.S. (1994). "Expanded polystyrene (EPS) geofoam: An introduction to material behavior." *Geotext. Geomembranes*, Vol.13 (4): 263–280.

Horvath, J.S. (1997). "The compressible inclusion function of EPS geofoams." *Geotext. Geomembranes*, Vol. 15 (1-3): 77–120.

Huang, W.X. (1980). "The influence of the hardening law on the formulation of the elasto-plastic model of soil." *Chinese J. Geotech. Eng.*, Vol. 2 (1): 1-11. (In Chinese)

Li, G.X. (2006). "Characteristics and development of Tsinghua Elasto-plastic Model for soil." *Chinese J. Geotech. Eng.*, Vol. 28 (1): 1-10. (In Chinese)

Liu, H.L., Deng, A., Chu, J. (2006). " Effect of different mixing ratios of polystyrene pre-puff beads and. cement on the mechanical behaviour of lightweight fill." *Geotext. Geomembranes*, Vol.24 (6): 339-348.

Qian, J.H., Yin, Z.Z. (1996). *Theory and Computation of Soil Engineering*.Water Resources and Hydro Power Press of China, Beijing, pp. 73-75. (In Chinese)

Qu, Z.J. (1987). *Soil Plasticity Mechanics*. Publishing House of Chengdu University of Science and Technology, Chengdu, 1987. (In Chinese)

Shen, Z.J. (1989). "Development of constitutive modelling of geological materials (1985-1988)." *Rock Soil Mech.*, Vol. 10 (2): 3-13. (In Chinese)

Tsuchida, T., Porbaha, A., Yamane, N. (2001). "Development of a geomaterial from dredged bay mud." *J. Mater. Civil Eng.*, Vol. 13(2): 152–160.

Wang, S.M., Gao, Y.F. (2007). "Study on degradation behavior of dynamic shear modulus for lightweight sand-EPS beads soil." *Rock Soil Mech.*, Vol. 28 (5): 1001-1004,1014. (In Chinese)

Yin, Z.Z. (1988). "A hyperbolic stress-strain model for soils." *Chinese J. Geotech. Eng.*, Vol. 10 (4): 64-71. (In Chinese)

Zhu, W., Ji, F.L., Ma, D.G., et al. (2005). "Shear strength properties of lightweight bead-treated soil made from dredged silt." *Chinese J. Rock Mech. Eng.*, Vol. 24 (S2): 5721-5726. (In Chinese)

Investigation of Ground Improvement Effects: Two Case Studies

Yong Tan[1], Ye Lu[2], and Fangle Peng[3]

[1]Department of Geotechnical Engineering, Tongji University, 1239 Siping Road, Shanghai, 200092, China; tanyong21th@hotmail.com
[2]School of Civil & Environmental Engineering, Georgia Institute of Technology, 210 Technology Circle, Savannah, GA 31407, USA; ylu31@mail.gatech.edu
[3]Department of Geotechnical Engineering, Tongji University, 1239 Siping Road, Shanghai, 200092, China; pengfangle@gmail.com

ABSTRACT: This paper investigated the densification effects of deep dynamic compaction (DDC) and vibratory compaction on loose saturated sands, which was based on two well-documented case histories. This investigation was carried out by examining pre- and post-compaction cone penetration testing (CPT) results. The CPT results indicated that under the same design earthquake excitation, the sands treated by DDC were densified to the level of resisting potential liquefaction, while, the sands were still liquefiable after vibratory compaction.

INTRODUCTION

In roadway, port, and coastal projects, granular materials are commonly placed in water to serve as foundation soils. Usually, these kinds of sites are required to be densified to mitigate potential liquefaction hazards, via deep dynamic compaction (DDC), vibratory compaction, or other ground improvement methods. Among these ground treatment methods, DDC and vibratory compaction are most frequently used due to their economical effectiveness.

DDC is carried out essentially by repeatedly dropping a very heavy tamper onto the soil surface from certain height. DDC can be used for both unsaturated and saturated granular soils. The densification process in unsaturated soils is the process of expelling air out from voids, thereby decreasing void volume and making soil denser. The mechanism of densification of saturated soils is based on dynamic consolidation. The energy generated in DDC destroys the soil structures and then causes the water trapped between soil particles to be expelled out. As a result, cracks are formed in the soils, allowing rapid dissipation of pore pressures. Then, the soils consolidate, and the soil particles are forced into a denser state. Vibratory compaction is performed using a vibratory probe. By means of its self-weight and vibration, usually accompanied with water jetting, the probe penetrates to the specified treatment depth. Then, the probe is withdrawn while maintaining vibration energy. Since the motion of probe is radial in the horizontal plane, the vibration energy is transmitted radially into the surrounding

soils and creates a dynamic force in the direction in which soils are weakest. Then, soils are densified by intense vibration during the process of progressively raising and lowering probe into soil deposits.

Many researchers (Menard and Broise 1975; David 1976; Leonards et al. 1980; Lukas 1980; Mayne et al 1984; Massarch 1991; Massarch and Fellenius 2002) have investigated the densification effects of DDC or vibratory compaction on granular soils via site-characterization testing methods. Mackiewicz and Camp (2007) investigated the influences of soil fine contents on densification effects of DDC, vibro-compaction, and vibro-replacements at five project sites in South Carolina, USA. However, no studies are known to compare the densification effects of DDC and vibratory compaction. The purpose of this study was to compare the densification effects of DDC and vibratory compaction on loose saturated sands, based on two ground-treatment projects, namely DDC at US Route 44 relocation project in Massachusetts and vibratory compaction during construction of Container Berth Eight (CB8) at Port of Savannah in Georgia, USA. This was achieved through comparisons in terms of mitigation of liquefaction susceptibilities. The investigation indicated that DDC was much more effective than the adopted vibratory compaction method in densifying the loose saturated sands.

TWO GROUND IMPROVEMENT PROJECTS

US Route 44 Relocation Project

Figure 1(a) presents the view of construction of US Route 44 relocation project in the peatlands. The site was located in Massachusetts, USA. A large portion of the proposed roadway embankments traversed across the bogs and ponds which feature deep peat deposits overlying medium dense to dense sands. Due to its extremely poor engineering properties, all the peat deposits within the footprint of the proposed embankments were replaced with sands, installing steel sheet pile walls on both sides of the proposed roadway as retaining structures. During the process of peat replacement, the site was not dewatered and the backfills were placed in a loose saturated state, susceptible to potential liquefaction hazards. Thus, two passes of DDC were adopted to densify the backfills, dropping a 14.4-ton tamper from a height of 18.3 m for the backfills beyond 6.9 m away from the sheet pile walls and from a height of 9.1 m for the backfills within 4.6 m to 6.9 m away from the retaining walls. Figure 2(a) presents the view of implementation of DDC at US Route 44 site. Figure 3(a) shows typical DDC grid-pattern. Each grid point was repeatedly impacted by nine drops. The second pass was conducted at the center spacing of the first pass. To ensure complete dissipation of excess pore pressures generated in DDC, the second pass was conducted six days later. During each pass, the distance between the adjacent tamping points was 4.6 m.

Construction of Container Berth Eight (CB8) in Port of Savannah

As the largest single-terminal container facility of its kind on the U.S. East and Gulf coasts, the Port of Savannah is located on the south bank of Savannah River in

Savannah, Georgia. In order to keep pace with the increasing trade volume, a new Container Berth Eight (CB8) was constructed, which included construction of approximately 518 m long pile-supported dock tied to the existing CB7 dock at the downstream end, and a sheet pile bulkhead and a container yard behind. Figure 1(b) presents the view of construction of CB8. Both the dock and sheet pile walls are located in Savannah River. The areas between the sheet pile bulkhead and the shoreline were filled with sandy soils to the existing ground surface and then served as loading and handling zones for trucks and storage areas for containers. The muddy soils at the riverbed behind the sheet pile walls were removed and then filled with averagely 6 meter thick loose saturated sands, which posed risks of liquefaction. Therefore, vibratory compaction was adopted to densify the fills. Figure 2(b) presents the view of implementation of vibratory compaction at the site. Vibratory compaction was carried out in a grid pattern with a center spacing of 1.8 m (see Fig. 3(b)). Different from conventional vibratory probe (vibroflot), the probe used at this site consisted of a vibratory hammer mounted on the top of a steel H beam supported by a crane and the H beam was in vibration during penetration and extraction.

(a) Construction of US Route 44 in bogs and ponds

(b) Construction of CB8 in Savannah River

FIG. 1. View of construction at two ground-treatment project sites.

(a) DDC at US Route 44

(b) Vibratory compaction at CB8 of Savannah Port

FIG. 2. View of ground-improvement at two project sites.

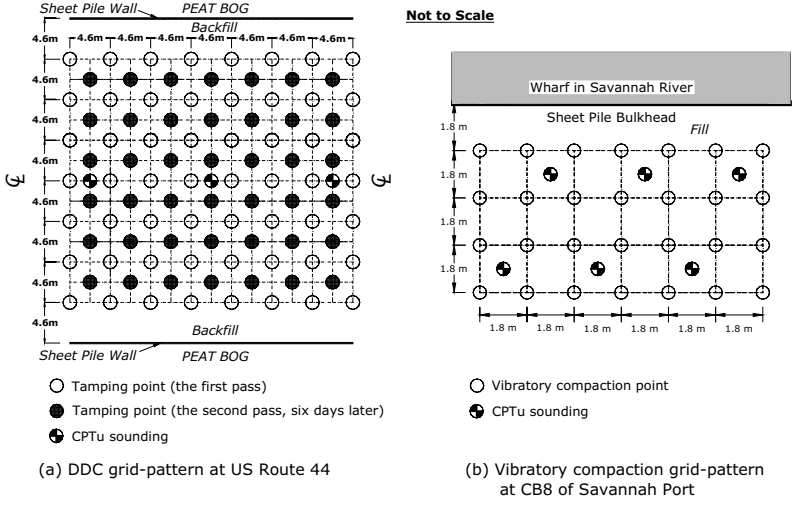

(a) DDC grid-pattern at US Route 44

(b) Vibratory compaction grid-pattern at CB8 of Savannah Port

FIG. 3. Typical grid-pattern along with the locations of CPT soundings.

SOIL CONDITIONS

Prior to compaction, a series of in-situ cone penetration tests (CPT) had been conducted at both sites. Figure 4 presents soil identification of the backfills at US Route 44 and the fills at CB8, using the CPT results. The soil classification in Figure 4 was based on the procedure developed by Robertson and Campanella (1983). The CPT sounding results indicated that the backfills and the fills mainly consist of clean sands and silty sands. At Route 44, the water table level was around 1 m below the surface, and it was around 1.5 m below the surface at CB8. Prior to compaction, it was very important to determine whether the soils could be improved by dynamic compaction or vibratory compaction methods. The compaction criterion developed by Massarch (1991) was adopted (see Fig. 4). At both sites, most of backfills and fills lied within the boundaries of compactable and marginally compactable. As a result, the backfills and fills were considered suitable for compaction.

CONE PENETRATION TESTS (CPT)

For quality assurance and control (QA/QC) purposes, a series of cone penetration tests (CPT) were carried before and after compaction at both project sites. At US Route 44, the CPT soundings were performed at the center spacing of the first and second pass of DDC and were spaced at 30.5 m along the central line of the proposed roadway. At the site of CB8, the CPT soundings were performed at the midway between vibratory compaction points. At both sites, the CPT soundings after compaction were located as close as possible to the CPT soundings prior to

compaction. Detailed locations of CPT soundings at these two project sites are presented in Figures 3(a) and 3(b).

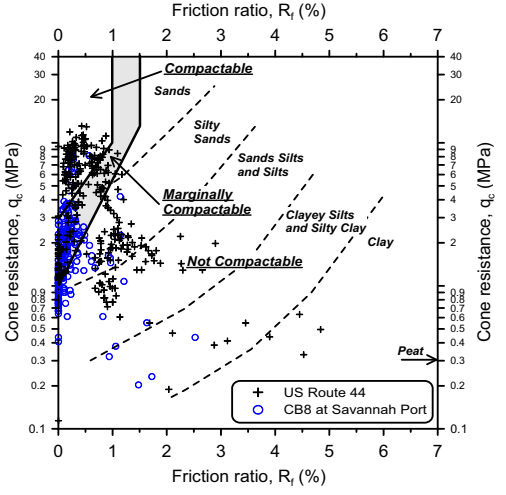

FIG. 4. Soil identification at two project sites (after Robertson and Campanella 1983; Massarch 1991).

COMPARISONS

In order to compare the capabilities of DDC and vibratory compaction on mitigation of potential liquefaction susceptibilities, it was assumed that both project sites were to withstand a maximum earthquake magnitude M_w of 5.5 with 2 percent probability of being exceeded in 50 years (this implies a mean recurrence interval around 2500 years). A maximum horizontal ground acceleration a_{max} equal to 0.136g was used in the following liquefaction analyses.

The method based on the CPT data developed by Robertson and Wride (1998) was adopted in the liquefaction evaluation. It assumes liquefaction to occur if F_S is less than 1.0 and no liquefaction occurs if F_S is greater than or equal to 1.0. The safety factor F_S is defined as the ratio of cyclic resistance ratio (*CRR*) to cyclic stress ratio (*CSR*):

$$F_S = CRR/CSR = MSF \times CRR_{7.5}/CSR \tag{1}$$

in which, *MSF* is magnitude scaling factor, $CRR_{7.5}$ is cyclic resistance ratio for magnitude 7.5 earthquake, and *CSR* is cyclic stress ratio. A magnitude scaling factor (*MSF*) value equal to 1.43, which was recommended by Seed and Idriss (1982) for the magnitude 5.5 earthquake, was used in equation (1). $CRR_{7.5}$ is calculated as (Robertson and Wride 1998):

$$\text{if } (q_{c1N})_{cs} < 50,\ CRR_{7.5} = 0.833[(q_{c1N})_{cs}/1000] + 0.05 \tag{2a}$$

$$\text{if } 50 \le (q_{c1N})_{cs} < 160,\ CRR_{7.5} = 93[(q_{c1N})_{cs}/1000]^3 + 0.08 \tag{2b}$$

where, $(q_{c1N})_{cs}$ is cone penetration resistance for clean sands normalized by approximately 100 kPa (1 atm). *CSR* is calculated as (Seed and Idriss 1971):

$$CSR = 0.65 \times (a_{\max}/g) \times (\sigma_{v0}/\sigma'_{vo}) \times r_d \tag{3}$$

where, $a_{\max}$ is peak horizontal acceleration at the ground surface generated by earthquake; g is acceleration of gravity; σ_{v0} and σ'_{v0} are total and effective vertical overburden stresses, respectively; and r_d is shear stress reduction coefficient. The value of r_d in equation (3) was estimated by the equations (Cetin et al. 2004) as follows:

For $d < 20$ m,

$$r_d(d, M_w, a_{\max}, V^*_{s,12m}) = \frac{[1 + \frac{-23.013 - 2.949 \cdot a_{\max} + 0.999 \cdot M_w + 0.0525 \cdot V^*_{s,12m}}{16.258 + 0.201 \cdot e^{0.341(-d + 0.0785 V^*_{s,12m} + 7.586)}}]}{[1 + \frac{-23.013 - 2.949 \cdot a_{\max} + 0.999 \cdot M_w + 0.0525 \cdot V^*_{s,12m}}{16.258 + 0.201 \cdot e^{0.341(0.0785 V^*_{s,12m} + 7.586)}}]} \pm \sigma_{\varepsilon_{rd}} \tag{4a}$$

For $d \geq 20$ m,

$$r_d(d, M_w, a_{\max}, V^*_{s,12m}) = \frac{[1 + \frac{-23.013 - 2.949 \cdot a_{\max} + 0.999 \cdot M_w + 0.0525 \cdot V^*_{s,12m}}{16.258 + 0.201 \cdot e^{0.341(-d + 0.0785 V^*_{s,12m} + 7.586)}}]}{[1 + \frac{-23.013 - 2.949 \cdot a_{\max} + 0.999 \cdot M_w + 0.0525 \cdot V^*_{s,12m}}{16.258 + 0.201 \cdot e^{0.341(0.0785 V^*_{s,12m} + 7.586)}}]} - 0.0046 \cdot (d - 20) \pm \sigma_{\varepsilon_{rd}} \tag{4b}$$

As $d < 12$ m,

$$\sigma_{\varepsilon_{rd}}(d) = d^{0.8500} \cdot 0.0198 \tag{5a}$$

As $d \geq 12$ m,

$$\sigma_{\varepsilon_{rd}}(d) = 12^{0.8500} \cdot 0.0198 \tag{5b}$$

Where, d is depth below the ground surface in meter, $a_{\max}$ is in gravitational acceleration (g/s), $V^*_{s,12m}$ is the representative site shear wave velocity over the top 12 m in m/s, M_w is earthquake magnitude. The measured $V^*_{s,12m}$ by seismic cone penetration tests (SCPT) was around 150 m/s before compaction, and was around 160 m/s after compaction at both project sites.

In reality, soils may liquefy even if the calculated safety factor $F_S > 1.0$ (Juang et al. 2002). There is a need to assess likelihood of liquefaction. Based on the calibration of Robertson and Wride method (1998) using large database of field observed cases, Juang and Jiang (2000) presented the following mapping function to relate the safety factor F_S to the probability of liquefaction P_L,

$$P_L = \frac{1}{1 + (F_S)^{3.3}} \tag{6}$$

Where, F_S is the safety factor calculated by equation (1).

Figures 5 and 6 present liquefaction analysis results at the sites of US Route 44 and CB8. Before DDC, the backfills at depths of 3.0 to 8.5 m at US Route 44 were liquefiable and had liquefaction probabilities around 60% to 70% under the design earthquake excitation. While, after two passes of DDC, the backfills along depths were densified to the state of unliquefiable with liquefaction probabilities less than 20%.

However, at the site of CB8 in Savannah Port, the fills were still liquefiable and had high liquefaction probabilities around 80 to 100 percent after vibratory compaction. Compared with DDC, the adopted vibratory compaction method imposed negligible effects in mitigating liquefaction susceptibilities.

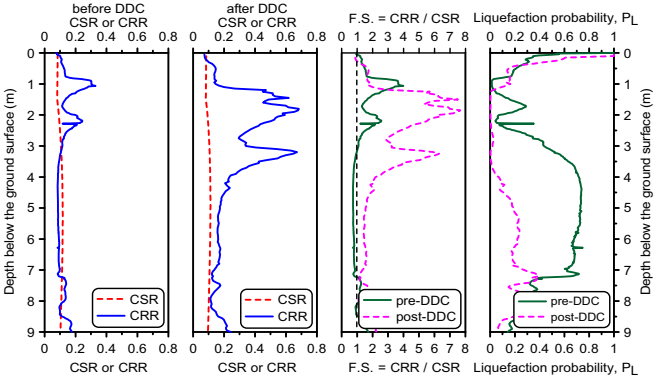

FIG. 5. The estimated liquefaction susceptibilities at US Route 44 site.

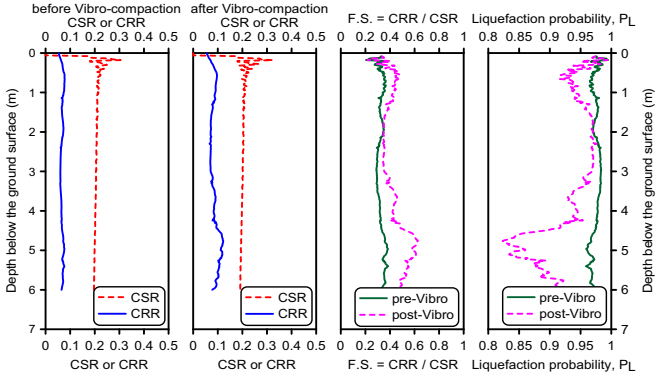

FIG. 6. The estimated liquefaction susceptibilities at CB8 in Savannah Port

CONCLUSIONS

Compared with the adopted vibratory compaction method, DDC was much more effective in mitigating potential liquefaction hazards. When subjected to the same earthquake shaking, the site treated by DDC was densified to the level of resisting potential liquefaction, while, the site treated by vibratory compaction was still liquefiable. The adopted vibratory compaction imposed negligible effects in mitigating liquefaction hazards of the loose saturated sands.

ACKNOWLEDGEMENTS

The funding support from NSFC (No.50679056), NCET (No.06-0378) and Shuguang Project (No.05SG25) is acknowledged.

REFERENCES

Cetin, K.O., Seed, R.B., Kiureghian, A.D., Tokimatsu, K., Harder, L.F., Kayen, R.E. and Moss, R.E.S. (2004). "Standard penetration test-based probabilistic and deterministic assessment of seismic soil liquefaction potential." *Journal of Geotechnical and Geoenvironmental Engineering*, ASCE, 130(12): 1314-1340.

David, D. (1976). Deep compaction. Bulletin, D. David Engineers Ltd, Ramat Aviv, Isreal.

Juang, C.H. and Jiang, T. (2000) "Assessing probabilistic methods for liquefaction potential evaluation." *Soil Dynamics and Liquefaction, Geotechnical Special Publication, GSP 107*, ASCE: 148-162.

Juang, C.H., Yuan, H., Lee, D.H. and Ku, C.S. (2002). "Assessing CPT-based methods for liquefaction evaluation with emphasis on the cases from the Chi-Chi, Taiwan, earthquake." *Soil Dynamics and Earthquake Engineering*, No.22: 241-258.

Leonards, G. A., Cutter, W. A. and Holtz, R. D. (1980). "Dynamic compaction of granular soils." *Journal of Geotechnical Engineering Division,* ASCE, 106(1): 35-44.

Lukas, R.G. (1980). "Densification of loose deposits by pounding." *Journal of the geotechnical engineering division,* ASCE, 106(4): 435-446.

Mackiewicz, S. M. and Camp, W.M. (2007). "Ground modification: how much improvement?" *Geotechnical Special Publication: Soil Improvement, GSP172*, ASCE: 1-9.

Massarsch, K.R. (1991). "Deep vibratory compaction of land fill using soil resonance." *Proceedings, "Infrastructure's 91", Intern. Workshop on Technology for Hong Kong's infrastructure Development:* 677-697.

Massarsch, K. R. and Fellenius, B. H. (2002). "Vibratory compaction of coarse-grained Soils." *Canadian Geotechnical Journal,* Vol.39: 695-709.

Mayne, P.W., Jones, J.S. and Dumas, J.C. (1984). "Ground response to dynamic compaction." *Journal of Geotechnical Engineering,* ASCE, 10(6): 757-774.

Menard, L. and Broise, Y. (1975). "Theoretical and practical aspects of dynamic consolidation." *Geotechnique*, Vol. 25: 3-18.

Robertson, P.K. and Campanella, R.G. (1983). "Interpretation of cone penetration tests. Part I: Sand." *Canadian Geotechnical Journal*, 20(4): 718-733.

Robertson, P.K. and Wride, C.E. (1998). "Evaluation cyclic liquefaction potential using the cone penetration test." *Canadian Geotechnical Journal,* 35(3): 442-459.

Seed, H.B. and Idriss, I.M. (1971). "Simplified procedure for evaluating soil liquefaction potential." *Journal of the Geotechnical Engineering Division,* ASCE, 97(9): 1249-1273.

Seed, H.B. and Idriss, I.M. (1982). "Ground motions and soil liquefaction during earthquakes." Earthquake Engineering Research Institute Monograph.

In Situ Determination of Layer Thickness and Elastic Moduli of Asphalt Pavement Systems by Spectral Analysis of Surface Waves (SASW) Method

M. A. Ismail[1], A. R. Samsudin[2], A.G. Rafek[2] and K. A. M. Nayan[3]

[1]Malaysian Nuclear Agency, 43000 Kajang, Selangor, Malaysia; azmi@nuclearmalaysia.gov.my
[2]Geology Programme, Universiti Kebangsaan Malaysia, 43600 Bangi, Selangor, Malaysia
[3]Dept. Civil Engineering, Universiti Kebangsaan Malaysia, 43600 Bangi, Selangor, Malaysia

ABSTRACT: Spectral Analysis of Surface Waves (SASW) is a non-destructive method for determining the stiffness profile of pavement sites. The method consists of generation, measurement, and processing of dispersive elastic waves in layered systems. The test is performed on the pavement surface at low strain level, where the elastic properties are considered independent of strain amplitude. During an SASW test, an impact source was used to generate energy at various frequencies. Two vertical acceleration transducers are set up to detect the energy transmitted through the testing media. By recording signals in digitised form using a data acquisition system and processing them, surface wave velocities can be determined by constructing a dispersion curve. Through forward modeling, the shear wave velocities can be obtained, which can be related to the variation of stiffness with depth. This paper presents the results of two case studies for near-surface profiling of two different asphalt pavement sites.

INTRODUCTION

There are more than 60,000 km of roads in Malaysia, of which more than one half are either flexible or rigid pavements. Most of the expressways, federal roads, state roads and council roads are more than 20 years old. Owing to aging roads and increasing traffic loads and volumes, the responsibility for maintenance, rehabilitation and management of pavement structures is becoming more critical. Therefore, the need for accurate, fast, cost effective and non-destructive evaluation of the pavement structure is becoming ever more important. Recent advancement and improvement of the well-known steady-state Rayleigh wave method (Richart *et al*. 1970) resulted in promising a new NDT method known as the Spectral Analysis of Surface Waves (SASW) method (Heisey *et al*. 1982; Nazarian & Stokoe 1984). The SASW technique successfully reduces the field-testing time and improves the accuracy of the original steady-state method.

The purpose of this paper is to describe the role of the SASW technique in assistance to pavement engineers in evaluation and management of highways. The first part of

the paper discusses the fundamentals of the SASW method and properties in pavement that can be detected by the method. The second section illustrates the results of the SASW tests in pavement investigations.

THE SASW METHODOLOGY

The SASW method is based on the phenomenon of Rayleigh wave dispersion in layered systems, i.e. the velocity of propagation is frequency dependent. The energy of Rayleigh waves propagates from the source along the surface of a media and their amplitude decrease exponentially with depth.

In homogenous, elastic half-space, Rayleigh wave velocity does not vary with frequency. However, in the layered medium, Rayleigh wave velocity is frequency dependent. This phenomenon is termed dispersion. The shorter wavelength of higher frequency penetrates the shallow zone and the longer wavelength (lower frequency) penetrates deeper into the medium. Rayleigh wave propagation technique may be used to determine the parameters of the elastic moduli of pavement and soil layers. Values of these parameters represent the material behaviour at small shearing strain. Nazarian and Stokoe (1984) have explained that the modulus parameter of material is constant below a strain of about 0.001 % and is equal to E_{max} and its corresponding G_{max}.

The objective of the SASW test is to determine the velocity-frequency relationship described by the dispersion curve. Through the process of inversion or forward modeling, the shear wave velocity profile is obtained. Elastic moduli profiles can then be obtained using relationships with the velocity of propagation and approximated values for mass density and Poisson's ratio, as follows,

$$G = \frac{\gamma}{g} V_s \tag{1}$$

$$E = \frac{2\gamma}{g} V_s^2 (1 + \mu) \tag{2}$$

$$E = 2(1 + \mu)\, G \tag{3}$$

where, G = dynamic shear modulus, E = dynamic Young's modulus, V_s = shear wave velocity, γ = total unit weight of the pavement or soil, g = gravitational acceleration, and μ = Poisson's ratio.

Elastic waves are generated on the surface of pavement and are detected by a pair or an array of receivers (Fig. 1). A dynamic spectrum analyser (OROS OR25 PC-Pack II) was utilized for recording and analysing the data. The common receiver midpoint (CRMP) array geometry was used (Nazarian 1984). The spacing between receivers was 0.1, 0.2, 0.4, 0.8, 1.6, and 3.2 m. Piezoelectric accelerometers were glued to the pavement surface to pick up the signal. The dynamic signal is generated in the pavement using a variety of impact sources. For small spacing, small steel ball bearings were used to sample shallow layers, and hammers were employed for larger spacing to sample deeper layers.

The spectrum analyser is used to capture the receiver outputs denoted by $x(t)$ and $y(t)$ for receivers 1 and 2. The outputs in the time domain were transformed through a Fast Fourier Transform (FFT) to $X(t)$ and $Y(t)$ in the frequency domain by the analyser. Two functions in frequency domain are utilized for analysing the averaged data

signals, i.e. the phase spectrum and coherence functions. The cross power spectrum, G_{XY}, between the two receivers is defined as

$$G_{XY} = X(f)^*.Y(f) \tag{4}$$

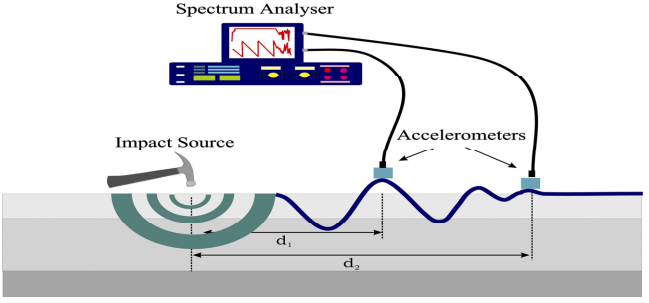

FIG. 1. Layout of the SASW method for pavement evaluation.

where $X(f)^*$ denotes the complex conjugate of $X(f)$. The phase shift, $\theta_{XY}(f)$, which represents physically the number of cycles that each frequency possesses in distance D between the two receivers, can be computed as

$$\theta_{XY} = \theta_X(f) - \theta_Y(f) = \tan^{-1}\left[\mathrm{Im}(G_{XY}) / \mathrm{Re}(G_{XY})\right] \tag{5}$$

where $\theta_{XY}(f)$ is the phase shift of the cross power spectrum at each frequency, $\mathrm{Im}(G_{XY})$ and $\mathrm{Re}(G_{XY})$ are the imaginary and real parts of the cross power spectrum at each frequency, and f is the frequency in cycles per seconds (or Hz).

The coherence function is the ratio of the output power caused by the measured input to the total measured output. The coherence function, $\gamma^2(f)$, is mathematically defined as

$$\gamma^2(f) = |G_{XY}|^2 / (G_{XX}.G_{YY}) \tag{6}$$

where $G_{XX} = X(f)^*.X(f)$ is the power spectrum of receiver 1, and $G_{YY} = Y(f)^*.Y(f)$ is the power spectrum of receiver 2. The value of coherence function in the range of frequencies being measured is between zero and one. A value of one indicates perfect correlation between the signals being picked up by the receivers, which is equivalent to a signal-to-noise ratio of infinity. A value of zero for the coherence function at a frequency represents no correlation between the detected signals.

When displaying the phase spectra, the analyser may not use full-scale display, instead it may display the phase in the range of ±180º and hence cause it to wrap. The step to find the actual phase of a frequency is to count the number of full 360º cycles preceding the frequency and to add that to the fraction of the last cycle or the frequency. The process is called unwrapping of the phase (Nazarian 1984). By using the principle of a rotating vector, a phase shift of 360º is equivalent to the travel time of one period. For a harmonic wave, the period, T, is the reciprocal of the frequency of the wave, (i.e. $T = 1/f$). Therefore, the travel time, $t(f)$, from receiver 1 to receiver 2, i.e. the time delay, can be computed by

$$t(f) = \theta_{XY}(f).T/360° = \theta_{XY}(f)/(360°.f) \quad (7)$$

Knowing the distance D between the receivers, the phase velocity, $V_R(f)$, and the corresponding wavelength, $\lambda_R(f)$, are calculated by

$$V_R(f) = D/t(f) \quad (8)$$

$$\lambda_R(f) = V_R(f)/f \quad (9)$$

By repeating the procedure outlined by Eq. (7) through (9) for every frequency, the Rayleigh wave velocity corresponding to each wavelength is evaluated and the experimental dispersion curve is generated. The process of converting the dispersion curve into the shear wave velocity profile is called inversion or forward modeling. There are several modeling approaches available for SASW applications. Among them are: (1) the transfer matrix method (Haskell, 1953; Thomson, 1950); (2) the dynamic stiffness matrix method (Kausel & Röesset 1981); and (3) the finite difference method (Hossain & Drnevich 1989). The transfer and stiffness matrix methods provide exact formulation as compared to the other methods (Ganji *et al*. 1998).

Joh (1996) has suggested two methodologies for the evaluation of a stiffness profile: the iterative forward modeling analysis and the inversion analysis. The iterative forward modeling analysis requires an initial guess (*priori*) of the stiffness profile. To each layer a thickness, a shear wave velocity, a Poisson's ratio (or compression wave velocity), a mass density and a damping ratio are assigned.

Based on these initial *priori* parameters of the initial profile, a theoretical dispersion curve is calculated using stress wave propagation theory. The theoretical dispersion curve is compared with the experimental dispersion curve. If the two dispersion curves do not match, the initial profile (number of layers, layer thickness, shear wave velocity, or any combination) is adjusted, and another theoretical dispersion curve is calculated. The trial-and-error procedure is repeated until the two curves match, and then the associated assumed profile is considered the real profile. Fig. 2 shows the comparison between the experimental and theoretical dispersion curves during inversion analysis. The accuracy of the theoretical dispersion curve is controlled by the RMS data error, which measures the difference of both the dispersion curves.

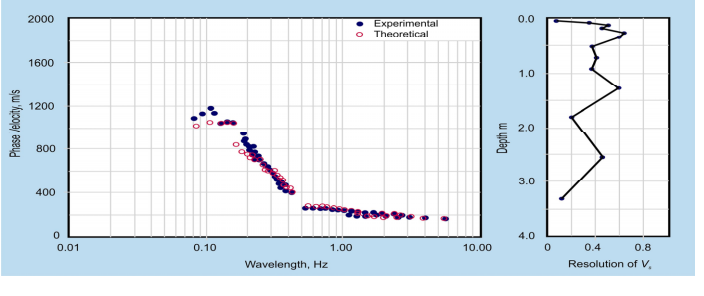

FIG. 2. Experimental and theoretical dispersion curves wave velocity.

CASE STUDIES

Case Study 1: Landed-Zone 4-B, Precint 11, Putrajaya

The SASW testing was carried out on a council road pavement surface at Landed-Zone 4-B, Precint 11, Putrajaya construction project (PREC11-JP1 line). The pavement profile consists of an asphalt layer (100 mm thick), a base of crushed aggregates (300 mm thick), and a sub base of sand (200 mm thick) over a metasediment sub grade. Material properties and thickness of the four layers are shown in Fig. 3(a). In this study, the receiver spacing of 10, 20, 40, 80, 160 and 320 cm were used.

The result of the inversion is as shown in Fig. 3(b). A total of 10 layers were used in this inversion analysis and the thickness of the layers was increased gradually as the properties of the near surface material are of most interest in a pavement system. By assuming reasonable values of Poisson's ratio and mass density of each layers, the dynamic Young's modulus profile is calculated using Eq. (2) and (3) and is plotted in Figure 3(c). The modulus and depths determined by the SASW measurements from the inversion are in good agreement with each layer of the pavement profile. A zone with higher modulus is interpreted from 0 to 10 cm for the asphalt concrete layer that has the highest stiffness properties (100 – 1000 MPa). An abrupt decrease of the modulus then occurs at the transition layer of the base followed by a gradual increase of the modulus for the sub base and sub grade with elastic modulus of around 10 MPa.

Case Study 2: Km 296, North – South Expressway

The SASW testing was carried out on a pavement surface at Km 296 of the North–South Expressway during rehabilitation works (LRSB-ApJ line). The pavement structure consists of an asphalt layer (180 - 200 mm thick), a sub base of crushed aggregates and fine sand (2000 - 2500 mm thick), over a metasediment sub grade. Material properties and thickness of the four layers are shown in Fig. 4(a). In this study, the receiver spacing of 10, 25, 50, 100, and 200 cm were used. The sources for the Rayleigh wave employed were slightly different from those in the case study 1. For high frequency signals, 2-inch nail and small hammers were used, geological hammer was used for receiver spacing higher than 100 cm.

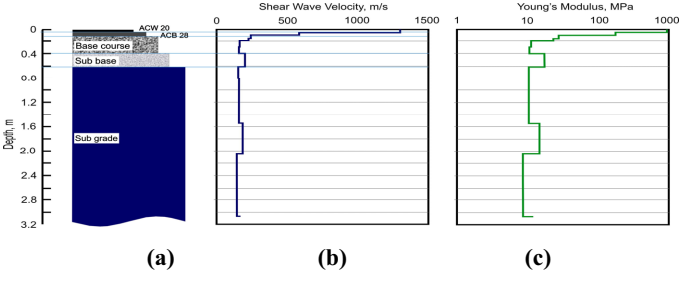

FIG. 3. (a) The designed pavement profile, (b) the final shear wave profile, and (c) the calculated dynamic Young modulus profile for PREC11-JP1 line.

The shear wave velocity profile along with the layering use in this inversion is shown in Fig. 4(b). RMS data error obtained for this inversion analysis is 20.75 %. The dynamic Young's modulus profile is calculated and is plotted in Figure 4(c). The profiles determined by the SASW measurements show good agreement with the pavement profile. A zone with higher modulus is interpreted from 0 to 20 cm for the asphalt concrete surface layer that has the highest stiffness properties (100 – 1500 MPa).

Concluding Remarks

The thickness of layering obtained from the inversion analysis compared well with the existing profile obtained from the construction record. This surface layer of LRSB-ApJ line line is slightly stiffer than the PREC11-JP1 line as a more stringent specification was applied to the former. The shear wave velocities and dynamic Young's modulus profiles from this study were compared with SASW testing that had been carried out by other workers, such as Nazarian (1984) and Al Hunaidi (1998) (Table 1). In general, there is a reasonable agreement between the results from these studies.

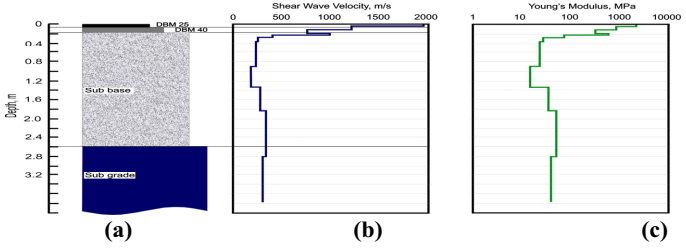

FIG. 4. (a) The pavement structure profile, (b) The final shear wave profile, and (c) the calculated dynamic Young modulus profile for LRSB-ApJ line.

Table 1. Comparison of Shear Wave Velocities

Profile	Shear Wave Velocity (m/s)		
	This study	Nazarian (1984)	Al Hunaidi (1998)
Surface course	900 – 2000	2425	1000 – 2500
Sub base course	195 – 270	301.95	100 – 500
Sub grade	200 – 400	271.45	80 – 300

CONCLUSION

The SASW method has managed to characterise all the layers of the pavement profile in terms of shear wave velocity and dynamic shear and elastic modulus satisfactory. The method can be useful to be applied in the early stages of pavement evaluation for detecting the dynamic properties and thickness of the profile. This method has been also found to be able to detect sandwiched low modulus layers

reasonably accurate, unlike the drawbacks from the other seismic methods for this case.

ACKNOWLEDGEMENTS

The study was supported by IRPA grant 02-02-02-0010. The authors would like to give our sincere appreciations to Geology Programme, Universiti Kebangsaan Malaysia, Mr. Nordin of Africon Asia and Ms. Raja Azizah Raja Yeop of Perembajaya Engineering for the permission of using their sites. We would also like to thank Prof. Dr. Sung Ho Joh of Chung-Ang University, Korea for his input during the data processing work.

REFERENCES

Al-Hunaidi, M.O. (1998). "Evaluation-based genetic algorithms for analysis of non-destructive surface waves test on pavements" *NDT &E International*, Vol.31, No.4, pp.273-280.

Ganji, V., Gucunski and Nazarian, S. (1998). "Automated Inversion Procedure For Spectral Analysis of Surface Wave." *Journal of Geotechnical and Geoenvironmental Engineering*, August 1998, pp.757-770.

Haskell, N.A. (1953). "The Dispersion of surface waves in multi-layered media." *Bull. Seismol. Soc. Am.*, Vol. 43, No. 1, pp 17-34.

Hossain, M.M. and Drnevich, V.P. (1989). "Numerical and optimisation techniques applied to surface waves for back-calculation of layer moduli." *Non-destructive testing of pavements dan back-calculation of moduli.* Edited by Bush, A.J., III, dan Baladi, G.Y. American Society for Testing dan Materials, Special Technical Publication 1026, pp. 649-669.

Heisey, J.S., Stokoe II, K.H. and Meyer, A.H. (1982). "Moduli of pavement systems from Spectral Analysis of Surface Waves." *Transportation Research Record 852*, TRB, National Research Council, Washington, D.C., pp 22-31.

Joh, S.-H. (1996). "Advances in data interpretation technique for Spectral Analysis-of-Surface-Waves (SASW) measurements." Ph.D. Dissertation, the University of Texas at Austin, Austin, Texas, U.S.A., 240 pp.

Kausel, E. and Röesset, J.M. (1981). "Stiffness matrices for layered soils." *Bull. Seismol. Soc. Am.*, 72, pp 1743-1761.

Nazarian, S. (1984). "In-situ determination of elastic moduli of soil deposits and pavement systems by Spectral-Analysis-Of-Surface-Wave Method." Ph.D. Dissertation, University of Texas at Austin, 452 pp.

Nazarian, S. and Stokoe II, K. H. (1984). "In-situ shear wave velocity from spectral analysis of surface waves." *Proc. 8th World Conf. On Earthquake Engineering*, 3, pp 31-38.

Richart, F.E.Jr., Hall, J.R., Jr. and Woods, R.D. (1970). "Vibrations of soils and foundations." New Jersey: Prentice-Hall.

Thomson, W.T. (1950). "Transmission of elastic waves through a stratified solid medium." *Jour. of Appl. Phys.*, Vol. 21, Feb. 1950, pp 89-93.

Logging for Diametric Variation of Stone Columns Using Crosshole Seismic Tests

Hak Sung Kim[1], In Beom Park[1], Chul Soo Park[2], and Young Jin Mok[3], P.E.

[1]Research Assistant, Dept. of Civil Eng. , Kyunghee University , Korea; azacplus@khu.ac.kr
[2]Post-Doctoral Researcher, Railroad Structure Research Dept., Korea Railroad Research Institute, Korea; cspark77@krri.re.kr
[3]Professor, Dept. of Civil Eng. , Kyunghee University , Korea ; yjmok@khu.ac.kr, corresponding author

ABSTRACT: An integrity testing for stone columns was attempted using crosshole S-wave logging. The method is conceptionally quite similar to the crosshole sonic logging (CSL) for drilled piers. The critical difference in the logging is the use of s-wave rather than p-wave, which is used in CSL, because s-wave is the only wave sensing the stiffness of slower unbounded materials than water. An electro-mechanical source, which can generate reversed S-wave signals, was utilized in the logging. The stone column was delineated from the S-wave travel times across the stone column, and taking S-wave velocities of the crushed stone and surrounding soil into account. The volume calculated from the diametrical variance delineated is very close to the actual quantity of the stone filled.

INTRODUCTION

Stone columns, locally called “GCP (granular compaction pile)” or “RAP (rammed aggregate piers)” are used to improve strength and resistance against lateral movement of a foundation soil with the same efficiency as rigid piles and piers. Moreover, these discrete columns facilitate drainage, and densify and reinforce the soil in the sense of ground improvement. The installation procedure of a stone column is driving a casing (ID 400mm) with a conic shoe hinged at the tip (the tip of the casing is closed with the shoe) to the desired depth, filling one batch of crushed stone (diameter of 400mm, height of 3m) into the casing, pulling up the casing 3 meters with keeping tip open, compacting the 3 meter column down to 1 meter height using the casing with closing the shoe so that the diameter of the column expands from 400 mm to 700 mm, and repeating the above steps for each batch up to ground surface.

The integrity of the stone column has been indirectly controlled with the records of each batch including depth and the quantity of stone filled. However, this indirect control can not guarantee the continuity of the column with consistent diameter or detect, if any, anomalies of the shaft. In the paper, a methodology to delineate stone

columns after installation was developed using crosshole S-wave logging.

METHODOLOGY

The method is conceptionally quite similar to the crosshole sonic logging (CSL) for drilled piers (Hellema and Olson, 2003). But there are two key differences between stone column logging and CSL. The first critical difference is the wave type adopted. The CSL uses P-wave, which is very effective for materials faster than water, such as concrete. Often, the stone column is installed under the ground water table and its P-wave velocity is less than that of ground water. Thus, the CSL logger, if adopted, will measure P-wave velocity of water rather than that of the skeleton of crushed stone. In the S-wave logging, an electro-mechanical source was used to generate S-waves. This key point will be explained in depth in the following field application. Second, the concrete is a bonded material and its stiffness is not affected by the confinement. Thus, the confinement does not count in CSL. However, the stone column composes of unbounded granular material, which is significantly affected by the confinement of the surrounding soil. The stiffness of a stone column, that is, even if installed with the same density through out the shaft, will increases with depth because of increasing confinement. Thus the stiffness increment should be taken into account in the stone column logging.

EQUIPMENT

The crosshole source consists of a spring-loaded impact pestle, a gear-servomotor triggering gadget, and a mechanical coupler as shown in FIG. 1. The triggering gadget and the coupler are controlled by the servomotors. The impact pestle strikes on the impact anvil, which is pushed against borehole wall by the coupler. The source is operated by the control unit at the ground surface. The companion receiver houses a horizontal geophone with the same mechanical coupler. In shear wave measurements, a pair of reversed shear wave signals is recorded by reversing impacts and its "butterfly" pattern is utilized in picking the first arrival of shear wave. The details of the source and measurement can be referred to Park et al. (2008).

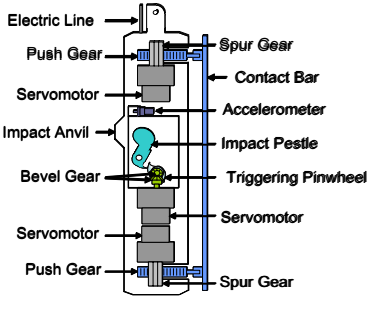

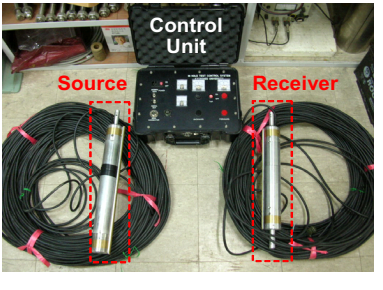

(a) Schematic diagram of source **(b) Logger set**

FIG. 1. Crosshole logger for stone column logging(Park et al., 2008).

IMPLEMENTATION

The stone column was installed with the target diameter of 700 mm. However, in the firm fill, placed for the access of the installation equipment, the column was expanded only to about 510mm in diameter as shown in FIG. 2. Five cased boreholes (ID 76mm) were installed for 3 sets of crosshole tests. The borehole pairs of 1 and 2, and 2 and 3, were for S-wave measurements across stone column and across soil only, respectively. To evaluate the S-wave velocity of crushed stone itself, boreholes 4 and 5 were installed in the immediate vicinity of the column to the depth of 1 meter.

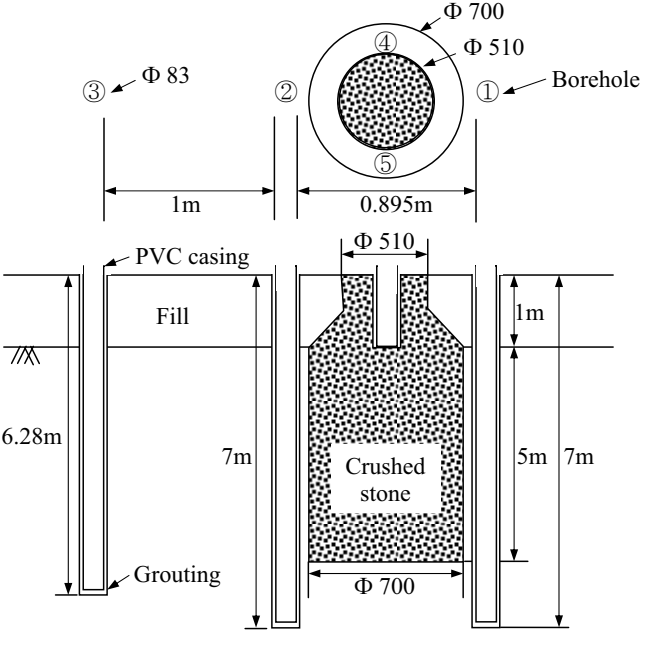

FIG. 2. Borehole for crosshole logging.

S-Wave Velocity of Crushed Stone

The stiffness of an unbounded material, such as crushed stone, is significantly affected with confinement and in turn with buried depth. Thus the variance of S-wave velocity with depth should be evaluated. The S-wave velocities were measured to the depth of 0.8 m using boreholes 4 and 5. From the increment of S-wave velocity, due to the increasing confinement with depth, coefficient of confining pressure (n_G ; the slope of the linear relationship between S-wave velocity and mean effective stress in log-log scale) was calculated as the value of 0.2866 and the S-wave velocities for deeper depth were extrapolated with n_G of 0.2866 as shown in FIG. 4.

S-Wave Velocity of Surrounding Soil

To measure the S-wave velocities of soil surrounding the stone column, a crosshole test was performed across soil between borehole 2 and 3. The reversed signals were stacked and shaded as shown in FIG. 3. The dark traces show the overall stiffness profile of soft clay overlain at the depth of 4m over sand layer. The first arrival time of S-wave at each depth was picked with the help of distinct butterfly pattern of the reversed signals. The S-wave velocity profile is shown in FIG. 4 along with the S-wave velocity profile of crushed stone.

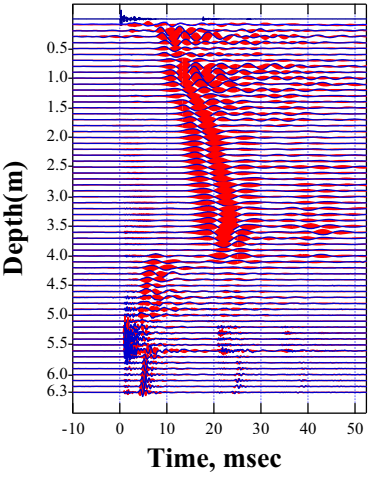

FIG. 3. Stacked S-wave signals of surrounding soil.

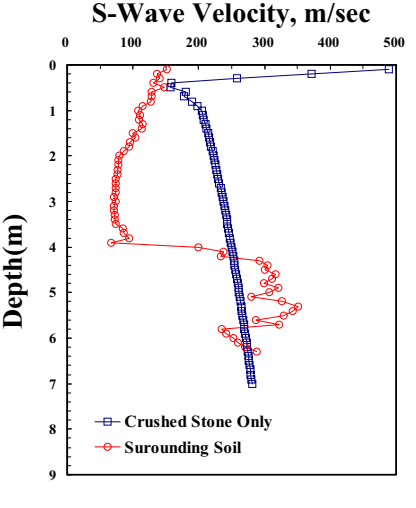

FIG. 4. S-wave velocity profiles of crushed stone and surrounding soil.

S-Wave Travel Times across Stone Column

To measure the S-wave travel times across the stone column, S-wave measurements were carried out across the stone column between borehole 1 and 2. FIG. 5 shows the typical P- and S-wave signals measured at the depth of 5.6 m under the water table. The fast P-wave transmitted through pore water is ringing for a while and overrides the slower P-wave propagated through the skeleton of crushed stone, whose initial arrival time is hardly indentified because of blending of two waves. In the other hand, the reversed signals show distinct polarity reversal and butterfly pattern of S-wavelet, while there is no polarity reversal of P-wave afore-arrived. Thus, S-wave is only wave type to sense stiffness of the unbounded material under the ground water table. The reversed S-wave signals were stacked and shaded for visual distinction of S-wave arrival as shown in FIG. 6. However each S-wave arrival time was picked as shown in FIG. 5 and plotted in FIG. 7.

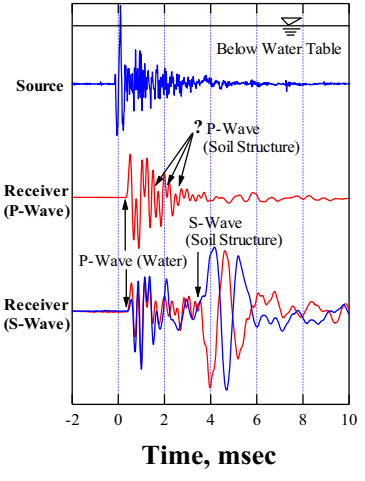

FIG. 5. Typical P- and S-wave signals.

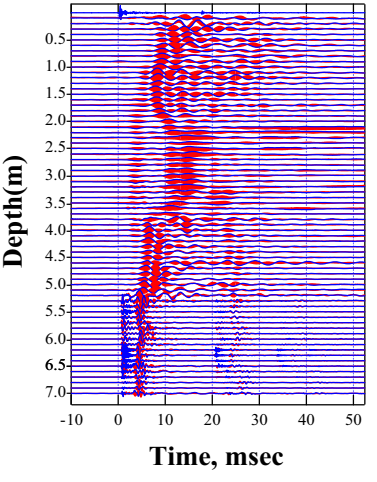

FIG. 6. S-wave signals of stone column.

Back-calculating Diameter

The diameter of the stone column (D) was calculated with travel path (L), the S-wave travel time across the stone column (t_r), the shear wave velocity of crushed stone (V_{cs}) and that of surrounding soil (V_s) at each depth using Eq. 1

$$D = ((L - V_s \cdot t_r)/(V_{cs} - V_s)) \cdot V_{cs} \quad (1)$$

where, L is distance between two boreholes across the stone column, t_r is S-wave travel time over ray path L shown in FIG. 7, V_{cs} and V_s are shear wave velocity of crushed stone and surrounding soil, respectively as shown in FIG. 4. The stone column was delineated with the diametric variance with the assumption of symmetry of the column as shown in FIG. 8. The column was expanded slightly more than the target diameter of 700mm in soft clay layer to the depth of 4 m and less in the underlain sand layer. The volume integrated with the diametric variance was 2.40 m^3, compared to actual filled quantity of 2.70 m^3. The difference was due to the quantity spilt over surface and densification of crushed stone during compaction.

CONCLUSIONS

Crosshole S-wave logging can successfully delineate and confirm the integrity of the stone column. In the logging, S-wave should be used and the stiffness increment of filling material of column, due to increasing confinement with depth, also should be taken into account. The electro-mechanical source can be effectively utilized in generating reversed S-wave signals and in turn accurate measurements of S-wave travel times.

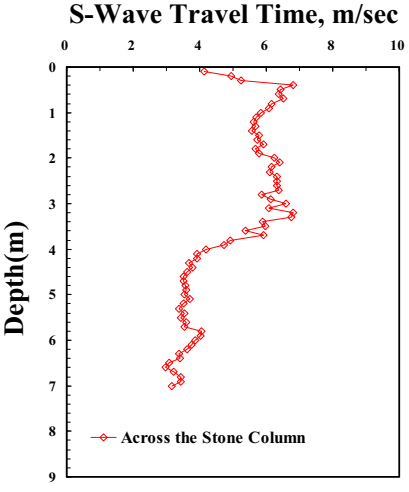

FIG. 7. S-wave travel times across stone column.

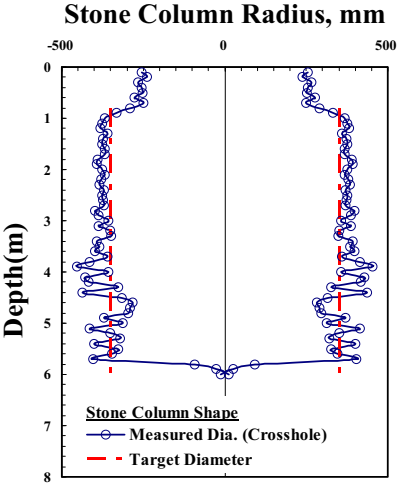

FIG. 8. Diametric variance of stone column.

ACKNOWLEDGMENTS

The research was partly supported by a grant (No., C105B000008-07B010000612) funded by Ministry of Land, Transport and Maritime Affairs of Korean government. The authors also thank June Construction Co. for the field collaboration.

REFERENCES

Hellema, D.A. and Olson, L.D. (2003). "Crosshole Sonic Logging and Velocity Tomography Imaging of Drilled Shaft Foundations," International Simposium(NDT-CE2003)

June Construction Co., Ltd. (2008). "Construction of Stone Columns for Soil Improvement for Cho-Jie Bridge," JUNE-08-01 (G) (in Korean).

Park, C.S., Jung, J.W. and Mok, Y.J. (2008). "Development and Applications of In-Hole Seismic Method to Measure Shear Wave Velocity of Subsurface Materials," *Geotechnical Earthquake Engineering and Soil Dynamics IV,* ASCE GSP 181 (CD-ROM), Sacramento, CA.

Estimating Field Properties of Soft Soil Using Penetration–type S-Wave Probe

Hak Sung Kim[1], Jae Woo Jung[1], Tae Hee Lee[1] and Young Jin Mok[2]

[1]Research Assistant, Dept. of Civil Eng., Kyunghee Univ., Korea;jujawo@khu.ac.kr
[2]Professor, Dept. of Civil Eng., Kyunghee Univ., Korea; yjmok@khu.ac.kr, corresponding author

ABSTRACT: A new s-wave probe, called "MudFork", has been recently developed and is used in accurate measurements of shear wave velocities of soft soils. The probe is composed of two bender elements mounted on a “fork” having two blades, one element perturbing ground and the other one monitoring seismic waves, and can be penetrated using SPT(standard penetration test) rods pushed with a routine boring machine. To expand its use to estimate undrained shear strength and density, an attempt to correlate shear wave velocity to those properties was made at normally consolidated silt near Incheon, Korea. A simple linear relationship between shear strength and shear wave velocity was obtained, and a tentative relationship between density and shear wave velocity was also defined.

INTRODUCTION

Much effort has been made to evaluate stiffness of soft soil accurately and to correlate with other properties such as strength and density. Such correlations would be very beneficial in soil exploration. Recently, a new s-wave probe, called "MudFork", has been developed and is used for accurate and easy measurements of shear wave velocities of soft soils (Jung et al., 2008). To expand its use to estimate other properties such as undrained shear strength and density, an attempt to correlate shear wave velocity to those properties was made at a normally consolidated soft ground near Incheon, Korea. In the paper, the new s-wave probe, MudFork and the correlations developed herein are described.

BACKGROUND

Mud Fork

The probe is composed of two bender elements mounted on a “fork” having two blades, one element acting as a seismic source perturbing ground and the other one as a receiver monitoring seismic waves as shown in FIG. 1. The probe is penetrated using SPT(standard penetration test)rods pushed with a routine boring machine and shear waves signals are recorded at each measurement depth. The details of the probe can be referred to Jung et al.(2008).

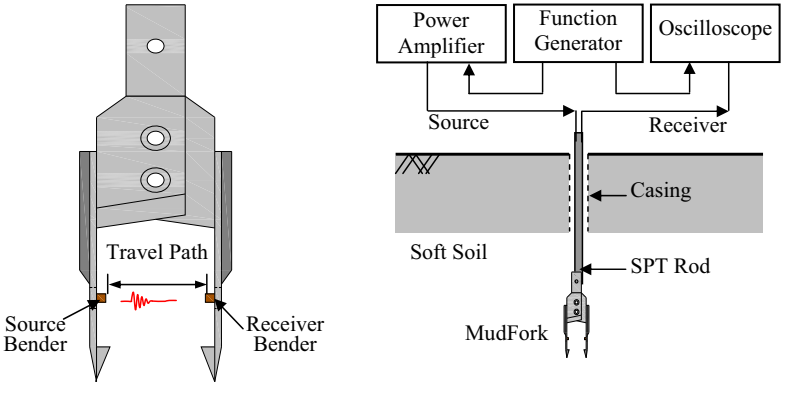

FIG. 1. Schematic diagram of Mud Fork and S-wave measurement (Jung et al., 2008).

Stiffness vs. Strength

The shear deformation of a normally consolidated soil can be characterized by the hyperbolic model, in which stiffer materials exhibit higher shearing resistance (Kondner, 1963; Hardin & Drenevich, 1972) as shown in FIG. 2. That is, shear strength (C_u) is proportional to shear modulus (G_{max}) or s-wave velocity. In this context, cone tip resistance (q_c), which is an indirect measure of shear strength, was correlated with shear modulus by many researchers (Mayne & Rix, 1993; Tanaka & Nishida, 1994, Simonini & Cola, 2000). This is the key motivation to correlate s-wave velocity to shear strength of a normally consolidated material.

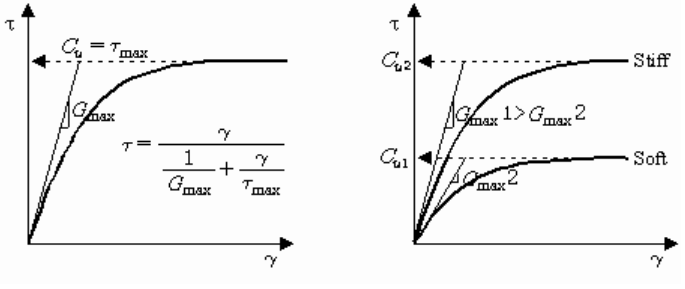

FIG. 2. Shear stress-strain relationship.

TESTING

Laboratory Testing

Three borings were drilled and undisturbed samples were taken at the depths of 3, 5, and 8 meters to measure undrained shear strength (C_u) and shear wave velocity (V_s) as well in the laboratory. Before shearing the specimens in the triaxial cell, shear wave velocities were measured using bender elements installed at the top cap and base pedestal of the cell as shown in FIG. 3(Oh et al. 2008). To mitigate disturbance effects, the specimens were recompressed with the isotropic confining pressure equivalent to in-situ effective stress. The typical shear wave signals are shown in FIG. 4. The middle and lower signals are shear waves recorded before and after recompression, respectively. The increment of shear wave velocity denotes the mitigation of disturbance effects. Laboratory testing results were plotted with field values later on.

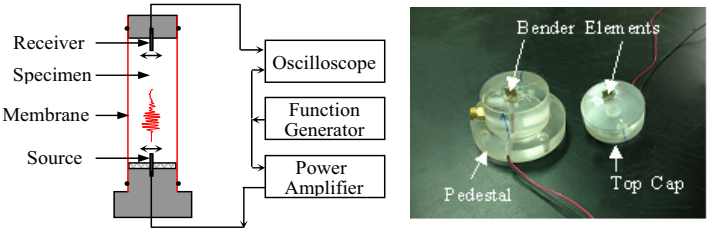

FIG. 3. Test set-up for laboratory shear wave measurements (Oh et al., 2008).

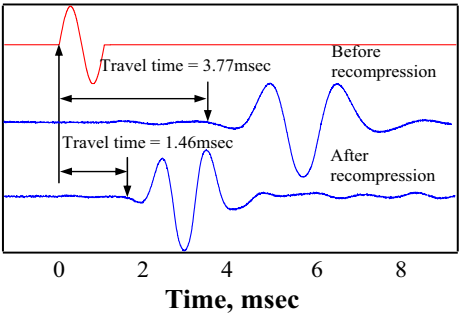

FIG. 4. Typical shear wave signals in laboratory (Jung et al., 2008).

Field Testing

S-wave measurements were carried out at every half meters up to 7.5 meters by penetrating the s-wave probe using a boring machine at a construction site near Incheon, Korea, whose ground water level was close to the surface. The shear wave

signals measured at each measurement depth are shown in FIG. 5. The signals are decent enough to identify first arrival times of shear wave. The first arrival times of shear wave, indicated by a black dot, are in the range of 0.5-1.0 msec. The net travel distance between the source and receiver is 59mm. The shear wave velocities, obtained by dividing the travel path with the first shear wave arrival times, are plotted with the laboratory values as shown in FIG. 6. The laboratory values are less than the field values partly because of disturbance effect and/or partly because of locality of specimens. The driving voltage and frequency of the source was 30 volts and in the range of 2.4-4.5 kHz, respectively. The driving frequency is high enough to maintain more than two wave lengths of the shear wave within the ray path (59mm), which is to eliminate the near field effect on the first arrival of shear wave. The shear wave velocities are linearly increased with depth and overall profile can be represented by a straight line shown in FIG. 6, except abrupt change at the sand seam near the depth of 5 meters.

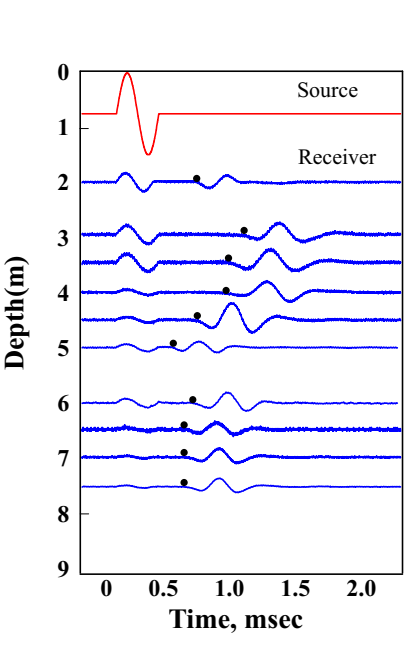

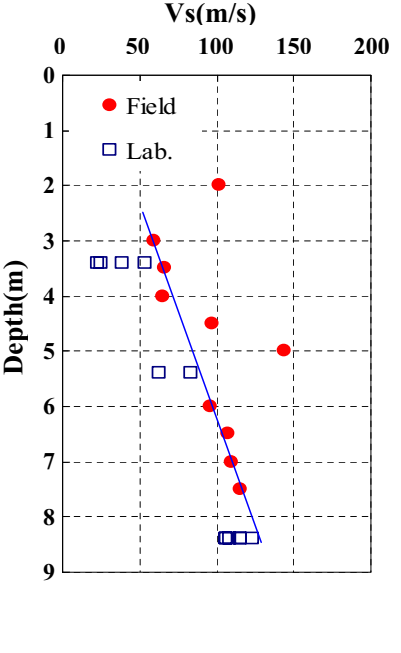

FIG. 5. S-wave signals (Jung et al., 2008). FIG. 6. Shear wave velocity profile.

Three cone penetration tests (CPT) were performed. The CPT tip resistance also increases linearly with depth, except for the values of the sand seam near the depth of 5 meters. The undrained strength was calculated from the tip resistance (q_c) with the value of cone factor, N_k =15, as suggested by Robertson and Campanella (1998), and also taken the laboratory values in account as shown in FIG. 7. The values of undrained strength, C_u from recompressed specimens are very close to the field values.

CORRELATION

The interpreted shear strength and shear wave velocity profiles were plotted in the same plane as shown in Figure 7. These interpreted profiles may resolve data scatter caused by the disturbance effect and local variability of individual specimen. The linear relationship between undrained shear strength (C_u, in the unit of kPa) and shear wave velocity (V_s, m/sec.) was obtained as Eq.1 for the normally consolidated silt, whose plasticity index was in the range of 2-7 %.

$$C_u = 0.38\ V_s - 6.65 \qquad (1)$$

The empirical relationships between void ratio (e) and shear modulus(G_{max}) for clay and sand were proposed by Hardin and Black(1969), and Richart(1977), respectively. The silt site seems to behave more like fine sand rather than clay in terms of strength and density. Accordingly, the relationship between stiffness and void ratio was evaluated by modifying the correlation of sand proposed by Richart rather than the one for clay, as shown by Eq.2.

$$G_{max} = 3786\frac{(2.17-e)^2}{1+e}\sqrt{\bar{\sigma}_o} \qquad (2)$$

where G_{max} and $\bar{\sigma}_o$ are shear modulus and mean effective stress in kPa, respectively and e is void ratio.

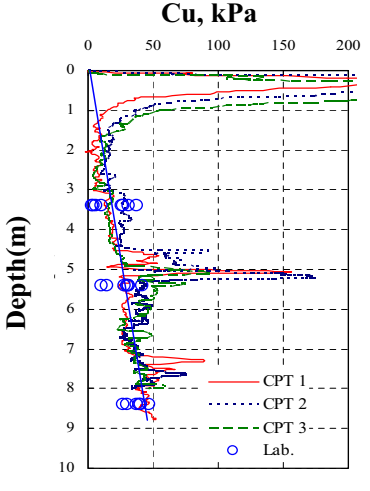

FIG. 7. Undrained shear strength profile.

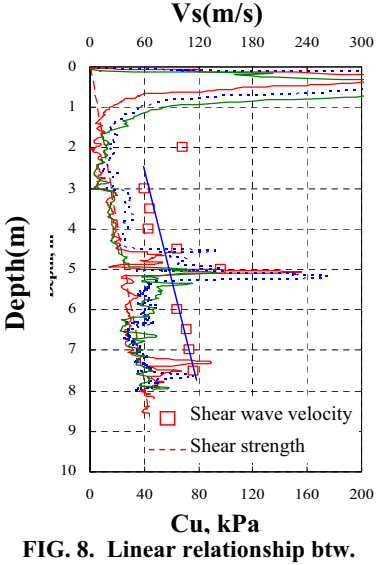

FIG. 8. Linear relationship btw. C_u and V_s.

CONCLUSIONS

A new s-wave probe, called "MudFork", has been recently developed and is used in accurate measurements of shear wave velocities of soft soils. To expand its use to estimate undrained shear strength and density, an attempt to correlate shear wave velocity to those properties was made at normally consolidated silt. A simple linear C_u-V_s relationship is obtained from interpreted profiles by combining laboratory and field data. e-G_{max} relationship of silt can be modified from the same equation of sand by changing the coefficient.

ACKNOWLEDGEMENTS

The research was partly supported by a grant (Code No.; C105A1000013-06A030001220) funded by Ministry of Construction & Transportation of Korean government.

REFERENCES

Hardin, B.O. and Black, W.L. (1969). "Closure to Vibration Modulus of Normally Consolidated Clays." *J. Soil Mech. Found Div*., ASCE, Vol.95(SM6):1531-1537.

Hardin, B.O. and Drnevich, V.P. (1972). "Shear Modulus and Damping in Soils : Design Equations and Curves." *J. Soil Mech. Found. Div*., ASCE, Vol.98(SM7):667-692.

Jung, J. W., Kim, H. S., Park, C. S. and Mok, Y. J. (2008). "Development of Penetration-type Bender Element Probe for Stiffness Measurements of Soft Soils." *Journal of Geotechnical and Geoenviromental Engineering*, ASCE(submitted)

Kondner, R. L. (1963). "Hyperbolic Stress-Strain Response : Cohesive Soils." *Journal of the Soil Mechanics and Foundations Division*, ASCE, Vol.89(SMI):115-143.

Mayne, P. W. and Rix, G. J. (1993). "Relationships for clay." *Geotech. Testing J.*, Vol.16(1): 54-60.

Oh, S. H., Park, D. S., Kim, B. J., Kim, E. J. and Mok, Y. J. (2008). "Laboratory Measurements of Stiffness of Soft Clay using Bender Elements" *The 14th World Conference on Earthquake Engineering*(CD-ROM), Beijing, China.

Richart, F. E. Jr. (1977). "Dynamic Stress-Strain Relations for Soils." State of the Art Report, *Proc. Ninth International Conference on Soil Mechanics and Foundation Engineering, Tokyo*, Vol. 2:605-612.

Robertson,P. K., and Campanella, R. G.(1998). "Guidelines for using the CPT, CPTU and Marchetti DMT for geotechnical design." U.S. Department of Transportation. Report No. FHWA-PA-87-022+84-24. Vol. 2.

Simonini, P. and Cola, S. (2000). "Use of piezocone to predict maximum stiffness of Venetian soils." *Journal of Geotechnical and Geoenviromental Engineering,* ASCE, Vol.126(4): 378-382.

Tanaka, H., Tanaka, M., Iguchi, H. and Nishida, K. (1994). "Shear modulus of soft clay measured by various kinds of tests." *Proc., Int. Symp. On Pre-Failure Deformation of Geomaterials.* Rotterdam, The Netherlands, Vol.1:235-240.

An Automatic Portable Near Surface Soil Characterization System

Ronald W. Gamache[1], Ehsan Kianirad[2] and Akram N. Alshawabkeh[3], PhD, ASCE, P.E.,

[1]Director of R&D Programs, TransTech Systems, 1594 State St., Schenectady, NY 12304; rgamache@transtechsys.com
[2]PhD Candidate, Northeastern University, Department of Civil and Environmental Engineering, 400 Snell Engineering Center, Northeastern University, 360 Huntington Avenue, Boston, MA 02115; kianirad.e@neu.edu
[3]Professor, Department of Civil and Environmental Engineering, 400 Snell Engineering Center, Northeastern University, 360 Huntington Avenue, Boston, MA 02115; aalsha@neu.edu

ABSTRACT: Soil strength, type, and moisture content are needed for site characterization applications and to assess the load carrying capacity of soil in construction control applications. Currently, no portable, automatic, easy-to-use field methods exist to measure the required soil parameters. In this paper, we describe a new instrument that integrates and extends two proven technologies, the cone penetrometer (CPT) and dynamic cone penetrometer (DCP). A portable Rapid Soil Characterization System is under development to perform near surface assessments to determine trafficability for heavy vehicles and aircraft. In the construction control context, the new device has the potential to eliminate errors in the measurement of soil strength due to soil type and moisture effects. A fully automatic prototype system has undergone limited field demonstration at the USACE facility in Vicksburg, MS. Preliminary laboratory and field test results indicate that the required soil geotechnical parameters can be extracted from dynamic penetration data, providing a near surface instrument that can provide accurate soil strength assessment to a depth of one meter.

INTRODUCTION

Examples of devices used in practice for construction control are the nuclear density gauge, stiffness devices (Soil Stiffness Gauge, Clegg hammer, and portable falling weight deflectometer), and the dynamic cone penetrometer (DCP). Several significant issues exist with devices used in the field for construction control: they only measure an average property in the volume and do not provide a profile, or they do not correct for the influence of soil type and moisture content (Edil 2005).

For site characterization applications, such as providing information to assess pollutant flow or validate a pavement drainage system, soil strength, soil type, and soil moisture content are all required to determine parameters such as degree of saturation and hydraulic conductivity. While Cone Penetrometers (CPT) may be used for deep site characterization applications where accessibility, portability, and survey cost are not issues, a significant need exists for a portable near surface capability.

CPT devices operate in a constant-push mode and consist of an instrumented tip that contains sensors to measure cone resistance, sleeve resistance, and in the CPTu configuration, pore pressure. For the CPT configuration, it has been shown in the literature that the ratio of sleeve friction to cone resistance is correlated to soil type (Robertson 1990).

In its standard form, the DCP consists of a rod fitted with a conical tip that is driven into the soil by energy provided by a slide hammer. The hammer is dropped a fixed distance onto an anvil attached to the rod thereby transferring the kinetic energy to a cone shaped tip. If the energy is great enough, the soil fails in shear and the tip advances. The penetration of the rod into the soil as a result of the imparted energy is related to the strength of the soil. As the hammer mass and drop height are known, the kinetic energy is known. For coarse materials, the dynamic cone resistance (q_d) can be related to the test conditions and instrument geometry according to the commonly used Dutch formula (Cassan 1988).

$$q_d = (1/A) \times \left(\frac{KE}{X} \right) \times \left(\frac{M}{M+P} \right) \tag{1}$$

where A is the cross sectional area of the cone, KE is the imparted kinetic energy, X is the incremental penetration stated in mm/blow, M is the mass of the hammer and P is the mass of the penetrometer. The penetration X is also a function of the angle of the cone. Cone angles of 60° and 90° are typically used.

Research (Webster 1992) has correlated the DCP index with the established measure of soil strength (CBR). The general equation is

$$Log(CBR) = K1 - K2(\log(DCPI)) \tag{2}$$

where the K1 and K2 are constants that, for the simple penetrometer described, are dependent on soil type and moisture level. CBR can range from >100 for crushed coarse soils to <1 for fine grained materials containing high organic and moisture content. To address the wide dynamic range, a dual mass hammer is utilized.

Some of the known issues with the standard DCP include: dependency of CBR correlations on soil type, inability to measure near the surface in cohesionless materials, errors due to adhesion at depths greater than ~12 in. (30 cm) in highly plastic materials, sensitivity of the results to moisture level, and lack of control over spatial resolution necessary for accurate determination of layer boundaries. The new device described in this work was developed to address these issues. The new device extends the widely used DCP functionality to provide a fully automatic portable capability that integrates the measurement of soil strength, soil type, and moisture content into a single field instrument. The device is called the Rapid Soil Characterization System (RapSochs).

SYSTEM DESCRIPTION

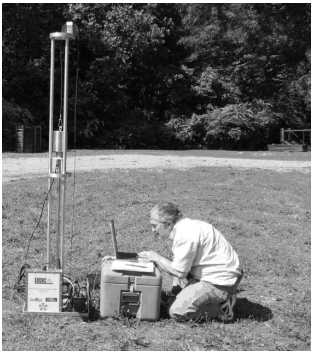

Fig. 1. Prototype RapSochs.

The RapSochs (shown in Figure 1) provides for characterization of unbound layers to a depth of one meter. Automation of the DCP drop hammer approach (ASTM D6951) provides the requisite ease of use, portability and cost effectiveness. Incorporation of an extended and miniaturized version of the CPT sensing strategy provides the required measurement capability. The sensing approach combines cone resistance and sleeve friction sensing from proven CPT technology with additional new sensing technologies. The cone resistance and sleeve friction data are used to develop soil strength and soil type. Moisture measurement is provided by an electrical impedance spectroscopy (EIS) sensor that has been recently developed to measure soil moisture and density in construction control applications (Pluta 2008). The RapSochs system is comprised of a penetrometer whose configuration (cone area, hammer mass, and drop height) is similar to the ASTM D6951 standard DCP. Strain gauges and a friction sleeve are arranged in the standard CPT subtraction cone configuration. An accelerometer is placed in contact with the tip to record the dynamic response to the hammer impact and trigger the acquisition of the sensor data. The EIS moisture sensor consists of an electrode to inject radio frequency electromagnetic radiation into the soil and a second electrode to sense the resultant signal that has been modified by the dielectric properties of the soil.

LABORATORY TESTING

The objective of the laboratory testing was to validate the CBR measuring capability of the RapSochs by comparison with the performance of a standard dual mass DCP in prepared materials. The DCP was used as the benchmark for soil strength profiles as considerable Army experience exists using this device.

Soil Samples

A total of 18 samples were prepared using five different soil types that covered the main diagonal of the Robertson soil type curve (SW, SP, ML, SC, CH). The individual samples varied in soil density or moisture. Standard laboratory tests were used to determine the geotechnical properties of the soils tested and determine the optimum density and moisture level for sample preparation. Tested soil strength spanned the range from loose to CBR 50. Moisture content varied from very dry to saturate.

Effect of Variable Hammer Drop

As a consequence of variable drop height of the RapSochs, the strain rate in the soil will also vary. The effect of variable hammer drop height was studied by applying different drop heights and observing the resultant penetration per blow in a region of the sample where the penetration per blow was nominally constant. After several blows of the maximum drop height of 559 mm, the drop height was decreased to 254 mm and 381 mm, and then back to 559 mm for the remainder of the test. The penetration per blow, corrected for drop height, is presented along with drop height in Figure 2 for different soil samples.

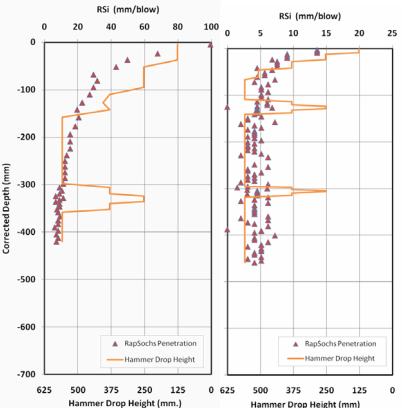

Fig. 2. Strain Rate Effects in CH and ML.

In this graph the penetration per blow is normalized to the DCP standard of 575 mm. Comparison of corrected penetration data around the drop height change shows no observable trend or shift in data.

Soil Behavior Classification

Soil type measurements using the sleeve and cone resistance are widely used in fixed rate pushing through homogeneous material. Complicating the extraction of the soil type information from the dynamic data is the presence in the signals of high frequency information due to the compression wave propagation and its interaction with the hammer, impedance discontinuities in the penetrometer, and the soil. To extract the similar features from the RapSochs data, the tip force and sleeve (total - tip) force signals are filtered and the maximum peak of the pulse is extracted. The tip force is then normalized for the mass of the hammer and drop height and plotted versus friction ratio (sleeve/tip expressed as a percentage). One data set for each soil sample was used for the soil classification analysis. Results are shown in Figure 3. Distinctive classification of soil behavior is clearly observed in this graph.

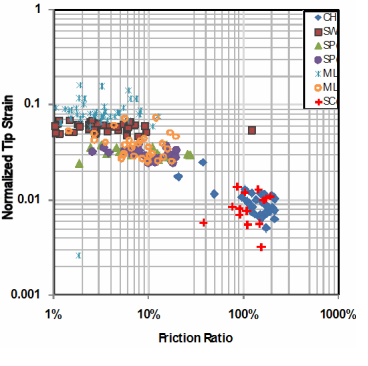

Fig. 3. Soil Classification.

PRELIMINARY FIELD TEST RESULTS

The first field testing of the fully automatic prototype was conducted at the Army's Waterways Experiment Station in Vicksburg, MS. Side by side testing was conducted using a DCP as the standard for soil strength. Full depth penetrations were conducted in three on-site locations; buckshot clay (CH), a well compacted silt, and a layered deposit of 0.5 m sand over clay. One of the goals of the adaptive hammer drop system is to achieve an average penetration per blow no greater than 12-25 mm. There are several geometry and other factors that could influence the response compared to a standard DCP. There are several implicit assumptions in Cassan's formula that have been questioned in the literature. Cassan's formula states that only the kinetic energy, cone area, and penetrometer mass distribution influence the penetration. Tsai et al., (2004) have shown that the ratio of the hammer area to the anvil area and the specific hammer shape influence the energy transfer. In CPT, much has been written on strain rate effects and in some cases additional understanding about soil behavior is obtained by deviating from the standard rate of penetration (Lunne 1997). The authors have derived analytical results that predict that the cone angle influences the penetration. In order to implement the friction sleeve and moisture sensor, the Rapsochs penetrometer diameter is the same as the tip, not smaller as in the DCP. Finally, an elastomer is installed on top of the anvil to reduce peak impact acceleration and the acoustic signature. However, as shown in the previously described testing, no significant strain rate effects have been observed in RapSochs data for the materials tested to date.

In order to assess the influence of the explicit factors in Cassan's equation, the raw RapSochs penetration data is converted to an equivalent DCP penetration by the following relation:

$$X_D = X_R(M_R + P_R)M_D^2 h_D \big/ (M_D + P_D)M_R^2 h_R = 16.45 X_R / h_R \qquad (3)$$

where the R subscripts apply to the RapSochs terms, the D subscripts the DCP terms in Cassan's equation, and the h's are the drop heights in mm. Figure 4 shows the DCP and RapSochs results (converted as described) expressed in CBR using the ASTM D6951 conversion equation for the SP over CH layered test location. In the Rapsochs data, all points are shown. In the DCP data, as many as three drops were taken to produce a single point. The DCP hammer mass was changed at 515 mm from 8 kg to 4.6 kg. The drop height of the Rapsochs was automatically controlled to produce penetrations of 25 mm or less. For the SP portion of the penetration, there is good agreement with the DCP, with both methods indicating a peak CBR in the 20-30 range. Deviation is visible in the lower (clay) portion of the penetration. As shown in the DCP record, the clay may be over-consolidated and drier in the region just below the sand, with decreasing strength with depth. The RapSochs record shows a relatively constant indication after an initial drop in the clay

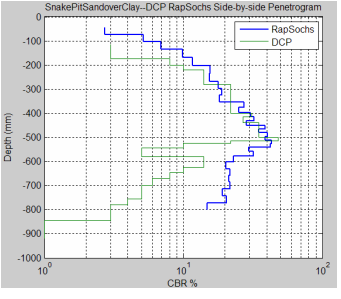

Fig. 4. Rapsochs correlation with DCP.

region. This behavior may be due to the fact that the penetrometer is the same size as the tip instead of smaller as in the DCP. This may result in significantly more adhesion during penetration in the clay.

CONCLUSIONS

1. The program results to date have established that a portable, automatic DCP type device for accurate soil characterization is feasible.
2. The penetrometer resident sensors and electronics are able to withstand the shock and vibration induced by the hammer impacts in hard materials.
3. The adaptive control drop height produces increased and uniform spatial resolution through the measuring range and does not appear to degrade the correlation with the DCP. Additional data must be taken in fine materials to determine if the variable strain rate affects the penetration. This capability may also result in improved capability to localize layer transitions.
4. Preliminary data suggests that information equivalent to CPT sleeve and tip strain data may be obtained from the dynamic data with appropriate signal processing to facilitate assessment of soil type.
5. A correction for measured strength must be developed to compensate for the apparent depth related adhesion effects in plastic clays. This correction could make use of the measured soil type and moisture along with the known penetration depth.

ACKNOWLEDGEMENTS

The work has been supported by US Army Engineer Research and Development Center. The authors convey their appreciation to Northeastern University's Gordon CenSSIS (an NSF Engineering Research Center for Subsurface Sensing and Imaging Systems) for their technical support and use of their SoilBed test facility.

REFERENCES

Webster, S. L., Grau, R. H., and Williams, T. P. (1992). "Description and Application of Dual Mass Dynamic Cone Penetrometer", *Report GL-92-3*, Department of the Army, Washington, DC, pp 48.

Edil, Tuncer B. and Benson, Craig H. (2005). "Investigation of the DCP and SSG as Alternative Methods to Determine Subgrade Stability", *Wisconsin highway Research Program*, SPR# 0092-01-05.

Robertson, P.K. (1990). "Soil classification using cone penetration test", *Canadian Geotechnical Journal*, V. 27, pp. 151-158.

Cassan, M. (1988). "Les essays in situ en mechanique des sols Volume 1 realization et interpretation", *Eyrolles*, pp146-151.

Pluta, S. (2009). "Non-Destructive Impedance Spectroscopy Measurement of Soil Characteristics", to be presented at GeoHunan.

Tsai, J-S, Liou, Y-J, Liu, F-J and Chen, C-H, 2004. (2004). "Effect of Hammer Shape on Energy Transfer Measurement in the Standard Penetration Test", *Soils and Foundations*, Volume 44, Issue 3, pp 103-114.

Lunne, T, Robertson, P. K. and Powell J. J. M. (1997). "Cone Penetration Testing in Geotechnical Practice", *Blackie Academic and Professional*, an imprint of Chapman and Hall, London, UK, ISBN 0751403938.

Study on the Ultimate Pullout Capacity and Shape Modification Factors of Horizontal Plate Anchors based on Nonlinear Mohr-Coulomb Failure Criterion

Zhao L. H.[1], Li L.[2], Yang F.[3], Dan H. C.[4] and Yang X. L.[5]

[1]Doctoral candidate, School of Civil and Architectural Engineering, Central South University, Changsha, Hunan Province, People's Republic of China, +86(137)5513-9425; zlh8076@163.com
[2] Professor, School of Civil and Architectural Engineering, Central South University, Changsha, Hunan Province, People's Republic of China, +86(731)887-6678; liliang_csu@163.com
[3]Doctoral candidate, School of Civil and Architectural Engineering, Central South University, Changsha, Hunan Province, People's Republic of China, +86(135)4964-1242; yf5754@126.com
[4]Doctoral candidate, School of Civil and Architectural Engineering, Central South University, Changsha, Hunan Province, People's Republic of China, +86(138)7493-4466; danhancheng@163.com
[5] Professor, School of Civil and Architectural Engineering, Central South University, Changsha, Hunan Province, People's Republic of China, +86 (731)265-6248; yangxl@mail.csu.edu.cn

ABSTRACT: Based on the limit analysis and nonlinear Mohr-Coulomb failure criterion, the ultimate pull-out capacity of horizontal plate anchors is calculated, in which the type of anchors and the corresponding failure mechanism are taken into consideration. The ultimate pullout capacity is obtained by a nonlinear sequential quadratic programming algorithm, and the theoretical results are compared with the available results presented in the existing literatures. The relationship between the nonlinear parameter and the ultimate pullout capacity is analyzed. The shape modification factors for different kind of anchors are given through a multiple nonlinear regression method.

INTRODUCTION

As the range of applications for plate anchors expands, a greater understanding of their behaviors including the ultimate pullout capacity (UPC) is required, the main research methods are as follows. (1) studies of full scale and/or scaled model tests (Meyerhof and Adams (1968), Murray and Geddes (1987), Ilamparuthi, et al. (2002), Dickin and Laman (2007)); (2) the numerical simulation techniques (Merifield, et al. (2006), Dickin and Laman (2007)); (3) the limit equilibrium method (Meyerhof and Adams (1968), Ghaly and Hanna (1994)); (4) the lower-bound and upper-bound theorem of limit analysis (Murray and Geddes (1987), Merifield, et al. (2006)).

The linear Mohr-Coulomb failure criteria are widely used in the ultimate pullout capacity calculation by the researcher mentioned above. However, the experimental results show that the strength envelopes of almost all geo-materials possess the nature

of nonlinearity, and that linear failure criterion is a special case of nonlinear failure criteria (Yang 2006). Therefore, the ultimate pull-out capacity analysis of plate anchors with a nonlinear M-C failure criterion and the shape factors for different kind of anchors are the main purposes of this paper.

THE NON-LINEAR MOHR-COULOMB FAILURE CRITERION

The experimental results show that the strength envelopes of almost all geo-materials have the nature of nonlinearity in the σ_n–τ stress space. In general, a nonlinear yield criterion can be expressed as

$$\tau = c_0 \cdot \left(1 + \sigma_n / \sigma_t\right)^{1/m} \tag{1}$$

where c_0 ,σ_t and m are test parameters and can be obtained by the triaxial test.

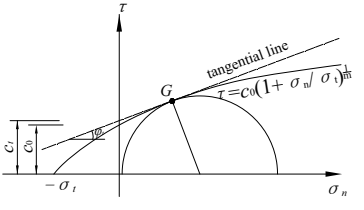

FIG. 1. Curve for a nonlinear failure criterion.

The sketch map of nonlinear yield criterion is shown in FIG.1, where σ_n and τ are the normal and shear stresses on the failure envelope, respectively. When the nonlinear parameter m = 1, Equation (1) reduces to the well-known linear MC yield criterion.

A limit load computed from a convex failure surface, which always circumscribes the actual failure surface, will be an upper bound on the actual limit load. Thus, the linear MC failure criterion represented by the tangential line will give an upper bound on the actual load for the material, whose failure is governed by the nonlinear failure criterion. By using this idea, a tangential line to the nonlinear yield criterion, is employed by Yang (2006) to calculate the energy dissipation of geo-materials to avoid the calculating difficulty under the nonlinear failure criterion. And this paper extends the work for calculation of the UPC of anchor plates by using a nonlinear MC yield criterion by applying this tangential technique.

The tangential line to the curve at the location of tangency point G, as shown in FIG.1, can be pressed as

$$\tau = c_t + \sigma_n \tan\varphi_t \tag{2}$$

where φ_t is the mobilized internal friction angle as an intermediate variable and can be introduced as $\tan\varphi_t = d\tau/d\sigma_n$; c_t is the intercept of the tangential line on the τ-axis. The c_t is determined by the following expression

$$c_t = \left(m-1\right)/m \cdot c_0 \cdot \left[\left(m \cdot \sigma_t \cdot \tan\varphi_t\right)/c_0\right]^{\frac{1}{1-m}} + \sigma_t \cdot \tan\varphi_t \tag{3}$$

A more comprehensive description of this method can be found in Yang (2006).

THE FAILURE MECHANISM OF ANCHOR PLATES

Many researchers are interested in the failure type and the failure mechanism of different soils. Large numbers of study supposed that those type of anchors as shallow anchors when $H/B \leq 8$, and integral damage occurrence in the soil mass above the anchor (Murray (1987), Ilamparuthi (2002), Dickin (2007)). Where H/B is called as the critical embedment ratio, H is depth of embedment and B is width or diameter of anchor plate.

A possible straight-line failure mechanism for strip anchor has been constructed by Murray (1987) to define the failure mode under the effect of a vertical force. The failure surfaces are shown in FIG. 2. And for the general failure mechanism in a nonlinear yield criterion soil, equating the work done by external forces to the dissipation of energy, the upper bound solution of the *UPC* of strip anchor plate in the soil (including the sand soil and cohesive soil) could be obtained.

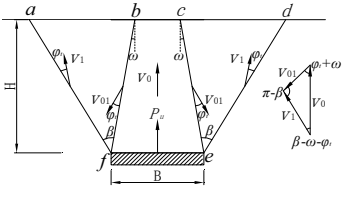

FIG. 2. The failure mechanism and velocity hodograph of strip anchors (Murray. 1987).

$$P_u = \left(G_z - W_{soil}\right)/V_0 \qquad (4)$$

where P_u is the ultimate pullout capacity of strip anchor plate, V_0 is velocity of strip anchor plate under the effect of the *UPC*, B is the width of anchor, H is the embedment depth of the anchor plates, φ_t, ω, β are angle parameters, G_z is the dissipation of energy alone the velocity discontinuity lines, W_{soil} is the work done by the soil's weight above the anchor plates.

With the same process, the failure mechanisms for the circle anchor plates and rectangular anchor plates could be constructed, as shown in FIG. 3.

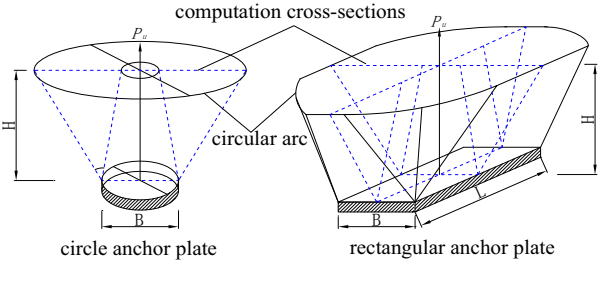

FIG. 3. The failure mechanism of 3-D horizontal anchor plates.

Equating the work done by external forces to the dissipation of energy, the upper bound solutions of the *UPC* of circle and rectangular anchor plates could be obtained as well.

THE SOLUTIONS AND CALCULATION ANALYSIS

Equation (4) provides an upper-bound solution for the upper bound solution of the *UPC* for the different kind of anchor plates. In order to find the best estimation of P_u, an optimization procedure needs to be used to minimize P_u with respect to ω , β and φ_t. This means taking the first derivatives of P_u and equating them to zero, i.e.

$$\partial P_u/\partial\omega = 0 \quad , \quad \partial P_u/\partial\beta = 0 \quad \text{and} \quad \partial P_u/\partial\varphi_t = 0 \tag{5}$$

An optimization procedure with sequential quadratic programming algorithm is employed to get a least upper bound for the *UPC* for the anchor plates.

Comparing Calculation

Generally, the *UPC* of anchor plate is measured with the dimensionless anti-pulling coefficient N_{qu}, as given by $N_{qu}=P_u/A\gamma H$, where γ is the soil's weight above the anchor plates and A is area of the anchor plates. The comparison result between the present method and other solutions is shown in Table 1. In the process of calculation, the geo-materials obey the linear Mohr-Coulomb failure criterion and the nonlinear parameter $m = 1$.

Table 1. Comparison of N_{qu} by this Paper and other Solutions in Sand

Strip Anchor Plates (φ = 45°)									
N_{qu}	***H/B***	**1**	**2**	**3**	**4**	**5**	**6**	**7**	**8**
	Meyerhof	1.95	2.90	3.85	4.80	5.75	6.70	7.65	8.60
	Murry	2.00	3.00	4.00	5.00	6.00	7.00	8.00	9.00
	This paper	2.00	3.00	4.00	5.00	6.00	7.00	8.00	9.00
Circular Anchor Plates (φ = 40°)									
N_{qu}	Merifield	4.38	9.05	16.30	23.75	36.25	48.75	64.95	81.90
	Merifield	3.75	8.13	14.38	21.72	32.2	44.4	57.55	70.60
	Murray	3.61	7.75	13.05	19.00	27.05	36.65	46.65	57.85
	Ghaly	3.50	10.05	15.01	26.00	37.00	47.55	61.75	75.56
	This paper	3.62	8.12	14.48	22.73	32.86	44.87	58.75	74.51
Square Anchor Plates (φ = 40°)									
N_{qu}	Merifield	3.35	7.00	12.05	18.45	26.45	35.35	48.50	60.25
	Murray	3.42	7.31	12.67	19.51	27.82	37.61	48.88	61.61
	This paper	3.00	6.59	11.65	18.19	26.20	35.68	46.64	59.07

As can be seen from Table 1 that the calculation values for N_{qu} in this paper are agreement in close with those obtained form the previous studies. Therefore, when the nonlinear parameter m = 1, Equation (1) reduces to the well-known linear *MC* yield criterion, the comparison shows that the proposed method is an effective method for evaluating the ultimate pullout capacity of the anchor plates.

Nonlinear Parameters Analysis

How the anchor break-out factor (N_{qu}) being influenced has been investigated when the modified nonlinear Mohr–Coulomb failure criterion is considered, FIG. 4 shows N_{qu} of five different kinds of anchor plates corresponding B=1.0 m, γ=18 kN/m^3, c_0=20 kPa and σ_t = 32 kPa. The nonlinear coefficient m varies from 1.0 to 3.0 and two different embedment ratio (H/B=1 and H/B=4) have been considered. In the calculations it has been assumed as well: for all kind of anchor plates, B=1.0 m and for the rectangular anchor plates, L/B=4 or L/B=8.

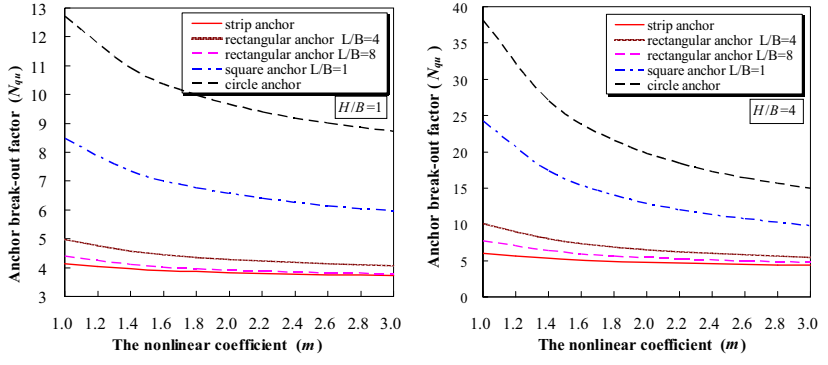

(a) The embedment ratio H/B=1 **(b) The embedment ratio H/B =4**

FIG. 5. The anchor break-out factor N_{qu} of different kinds of anchor plates for the embedment ratio (H/B): (a) H/B =1 and (b) H/B =4.

It can be observed from FIG.4 that the nonlinear coefficient m have significant influences on the anchor break-out factor (N_{qu}), and the anchor break-out factor of different kind of anchor plates presents a non-linear decrease relationship with the nonlinear coefficient m increase when parameters B, c_0 and σ_t are constant. Therefore, the linearity simplification of the nonlinear geo-materials takes disadvantageous influence on evaluating the real pull-out characteristics of the anchor plates.

Several further conclusions from Table 1 and FIG.4 are outlined as follows:

(1). For the rectangular anchor plates, with the length-width ratio (L/B) increasing,

the value of N_{qu} tends to close the N_{qu} of strip anchor plate gradually. Therefore, when L/B is bigger than a certain value, the rectangular anchor plate can be analyzed as the strip anchor plate. (2). The anchor types take significant influences on the N_{qu} when other parameters are constant. The N_{qu} for strip anchor is the smallest, and the value of N_{qu} for circular anchor is the biggest on the same conditions.

Dimensionless Shape Factor Analysis

The effect of anchor shape on N_{qu} can be expressed as a dimensionless factor

$$F_{shape} = N_{qu\_3\text{-}D} / N_{qu\_strip} \tag{6}$$

where and $N_{qu\_3\text{-}D}$ and N_{qu_strip} are obtained from Figure 5 respectively. Though a multiple nonlinear regression method, we expect the shape factor to be expressed as the function of the L/B, H/B and m in the following approximate form

$$F_{Cir} = 1.1 \cdot \frac{(H/B)}{m} + 2.0 \quad \text{and} \quad F_{Rect} = \frac{0.66}{(L/B)} \cdot \frac{(H/B)}{m} + \frac{1.34}{(L/B)^{0.15}} \tag{7}$$

where the diameter of circular anchor is equal to the strip anchor width, and if $F_{Rect} <$ 1.0, let be F_{Rect} =1.0, which means the rectangular anchor can be analyzed as a strip anchor. FIG. 6 shows F_{shape} of different kinds of anchor plates corresponding the embedment ratio H/B=1.0 and H/B=4.0.

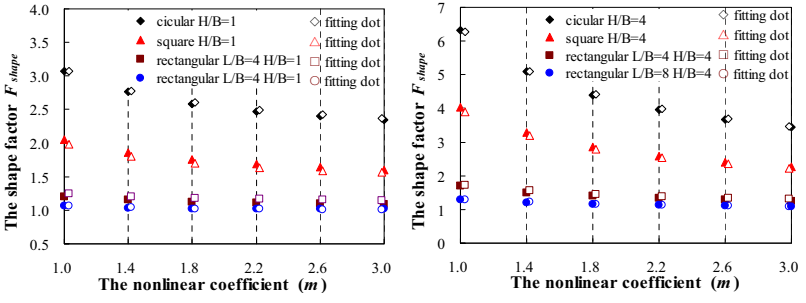

FIG. 6. The shape factor F_{shape} of different kinds of anchor plates for the embedment ratio (H/B): (a) H/B =1 and (b) H/B =4.

It can be observed from Equation (7) and FIG.6 that all of L/B, H/B and m have a certain influences on the shape factor (F_{shape}). The shape factor (F_{shape}) is inversely linear proportional to the nonlinear coefficient m and is linear proportional to the embedment ratio (H/B), but it is inversely nonlinear proportional to the length-width ratio (L/B). The approximate functions of shape factor compare reasonably well with

the upper bound calculation results.

CONCLUSIONS

(1) When the nonlinear parameter m = 1, nonlinear MC yield criterion reduces to the well-known linear MC yield criterion and the comparison of results between present results and existing researches shows good agreement.

(2) The nonlinear coefficient m has significant influences on the anchor break-out factor (N_{qu}), and the anchor break-out factor of different kind of anchor plates presents a non-linear decrease relationship with the nonlinear coefficient m increase when other parameters are constant.

(3) The anchor type, the embedment ratio (H/B) and the material characteristics have significant influences on the pullout behavior of anchor plates. Though a multiple nonlinear regression method, the shape factor can be expressed as the function of the shape parameter L/B or D/B, H/B and m.

ACKNOWLEDGMENTS

The author is grateful to T. Zhang for her assistance. The present work was sponsored by the Nation West Traffic Construction Science and Technology Item of China (No. 2006318802111). The financial support is greatly appreciated.

REFERENCES

Dickin E.A. and Laman M. (2007). “Uplift response of strip anchors in cohesionless soil.” *Advances in Engineering Software*, Vol. 38: 618-625.

Ghaly, A. and Hanna, A. (1994). “Ultimate pullout resistance of single vertical anchors.” *J. Can. Geotech.*, Vol. 31: 661-672.

Ilamparuthi K., Dickin E.A. and Muthukrishnaiah K. (2002). “Experimental investigation of the uplift capacity of circular plate anchors in sand.” *J Can. Geotech.*, Vol. 39: 648-664.

Meyerhof G.G. and Adams J.I. (1968). “Ultimate uplift capacity of foundation.” *J Can. Geotech.*, Vol. 5 (4): 225-244.

Murray E.J. and Geddes J.D. (1987). “Uplift of anchor plates in sand.” *Journal of Geotechnical Engineering*, ASCE., Vol. 113 (3): 202-215.

Merifield R.S., Lyamin A.V. and Sloan S.W. (2006). “Three-dimensional lower bound solutions for the stability of plate anchors in sand.” *Géotechnique*, 56(2): 123-132.

Yang X.L. and Yin J.H. (2006). “Estimation of seismic passive earth pressure with non- linear failure criterion.” *Engineering Structures*. Vol. 28(3): 342-348.

Evaluation of Pavement Layers and Foundation Sites with Seismic Surface Wave Method

Deren Yuan[1], Manuel Celaya[2] and Soheil Nazarian[3], M. ASCE

[1]Research Specialist, Center for Transportation Infrastructure Systems, the Univ. of Texas at El Paso, 500 W. University Ave, TX 79968; dyuan@utep.edu
[2]Research Specialist, Center for Transportation Infrastructure Systems, the Univ. of Texas at El Paso, 500 W. University Ave, TX 79968; mcelaya@utep.edu
[3]Professor, Dept. of Civil Engineering , the Univ. of Texas at El Paso, 500 W. University Ave, TX 79968; nazarian@utep.edu

ABSTRACT: This paper provides the fundamentals, capabilities and limitations of the seismic surface-wave method as applied to in-situ testing of pavement and foundation and represents the results obtained from its recent applications in a number of projects. These applications include characterization of flexible pavement layers during construction, monitoring of early-age strength development of Portland cement concrete and evaluation of soil foundations. The issues on understanding the results from surface-wave tests and how to incorporate them in those requirements adopted in most existing specifications or common practices are discussed.

INTRODUCTION

Stiffness or modulus is one of the major parameters to qualify pavement layers and shallow foundation soils and has been used in flexible pavement design and foundation evaluation. For rigid pavements or other concrete structures, concrete strength is another major parameter being concerned. In-situ determination of these parameters has been an essential and challenging task for quality control during pavement construction and for soil foundation evaluation and improvement.

The systematic introduction of seismic surface-wave method, named the spectral analysis of surface wave (SASW) method, to engineering applications (Nazarian and Stokoe, 1985) has resulted in an increasing use of this nondestructive testing technology in these aspects.

This paper represents the results from the recent applications of surface-wave method. These applications include characterization of flexible pavement layers during construction, monitoring of early-age strength development of Portland cement concrete and evaluation of shallow foundation soils. Attention is also paid to understanding of the results from surface-wave tests and how to incorporate them in those requirements adopted in most existing specifications or common practices.

PRINCIPLE OF SURFACE-WAVE TECHNOLOGY

Seismic surface waves are a type of stress waves traveling along the free surface of a medium and usually are the predominant portion (over body waves: compressive and shear waves) in a wave train. Surface waves propagating in a heterogeneous medium are dispersive; that is, waves of different wavelengths or frequencies travel with different speeds. The dispersive characteristic is dependent on the elastic properties of the affected medium and thus the information of the subsurface can be obtained through the generation and detection of surface waves.

Normally, a complete test with surface-wave method consists of three steps: 1) field measurement to obtain time domain signals, 2) reduction of the time signals to obtain a dispersion curve (phase velocity vs. frequency or wavelength), and 3) inversion of the dispersion data for a shear-wave velocity profile that best represent the data. Dynamic Young's (or seismic) modulus can be directly calculated from the shear-wave velocity through measured or assumed mass density and Poisson's ratio.

An offshoot of the SASW method is the ultrasonic-surface-wave (USW) method. The major distinction between the two methods is that with the USW method the velocity or modulus of the top pavement layer can be directly estimated without involving any complicated inversion algorithm. This method is particularly useful for quality assurance/quality control in a layer-by-layer manner during pavement construction. Actually, at wavelengths less than or equal to the thickness of the uppermost layer, the velocity of propagation is more or less independent of wavelength if the uppermost layer is uniform. Therefore, the modulus of the layer can be determined from surface wave velocity of the layer, V_R, by

$$E_{USW} = 2\,\rho\,[(1.13 - 0.16\nu)\,V_R]^2\,(1+\nu) \qquad (1)$$

where ρ and ν are the mass density and Poisson's ratio, respectively.

TESTING DEVICES

Tests for individual pavement layers were carried out with a **portable seismic property analyzer (PSPA, see Figure 1) for its testing speed,** repeatability and instant results in terms of velocity and modulus. The waveforms or time records saved can be used for further analysis.

Tests for soil foundation evaluation were carried out with a package consisting of a Tektronix Fourier Analyzer for recording, two 4.5-Hz geophones as the receivers and a sledge-hammer as the impact source. The procedures used for data collection, reduction and analysis can be found in the papers of Nazarian and Desai (1993) and Yuan and Nazarian (1993).

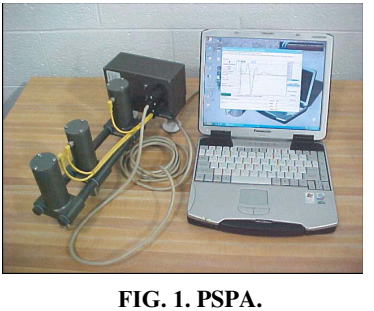

FIG. 1. PSPA.

REPRESENTATION OF RESULTS

To relate the modulus values obtained from USW tests on pavement layers in the field to those from laboratory tests on the specimens of the same mixes used in constructions, two simple nondestructive laboratory tests were performed. They are the free-free resonant column (FFRC) test (for base and subgrade materials as well as concrete) and the ultrasonic test for hot-mixed asphalt (HMA) materials.

If a material is compacted and cured equally, the moduli from USW and FFRC tests are analytically related through:

$$E_{USW} / E_{FFRC} = (1 + \nu)(1 - 2\nu) / (1 - \nu) \quad (2)$$

Details for the procedure that relate the modulus from the USW test to that form the ultrasonic test with a V-meter for HMA can be found in Celaya and Nazarian (2006).

Flexible Pavement Layers

Currently, the mix design and structural design for a flexible pavement project are based on the engineering parameters such as strength or modulus. However, the construction acceptance for a pavement layer, besides the thickness, is typically based on the density of the compacted material in that layer measured with a nuclear density gauge (NDG); that is, the percentage of the maximum dry density (MDD) obtained from laboratory tests. The following examples show that the density-based acceptance criteria may not work well for the chemical-treated base and subgrade.

Subgrade

A subgrade was constructed with 6% lime (slurry) to improve its plasticity index (PI) and strength of the original soil. Figure 2 shows the results from modulus tests with a PSPA and density tests with a NDG at ten stations.

The average modulus of the subgrade is about 65 ksi. Based on our experience on subgrade tests, this low-strain modulus corresponds to a modulus of about 30 ksi obtained from the Falling Weight Deflectometer (FWD) tests, which indicates a good quality subgrade.

On the other hand, the NDG tests did not provide meaningful results as no percentage of MDD reached the required value 95%.

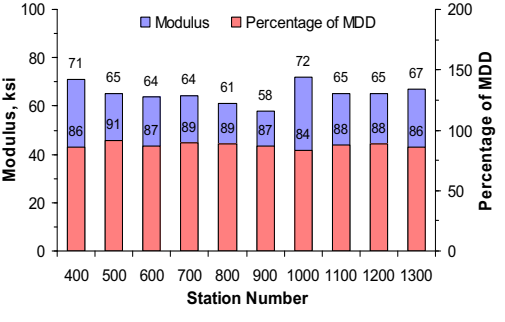

FIG. 2. Test results from a treated subgrade.

Base Layer

The base layer under study was constructed with reclaimed pavement materials, about 2/3 of RAP (reclaimed asphalt pavement) and 1/3 of the existing base, and treated with 1% cement and 4% of asphalt emulsion. Since the traditional quality control tool, nuclear density gauge, could not provide reasonable readings for the emulsion-treated base, the moisture content and percentage of MDD on lab-compacted specimens prepared from field-retrieved materials had to be used. Almost all specimens exhibited a density of at least 97% of MDD.

The in-situ tests with a PSPA were performed on top of the base layer at its three ages after construction. The laboratory tests on specimens were performed with a FFRC device and a MTS system (for resilient modulus or RM). Figure 3 shows the results from these different tests.

A commonly accepted modulus value is not currently specified for mix design of asphalt emulsion-treated bases. Once such values and curing regimes are specified, the field-measured modulus can be related to the specified value through Equation 2 for FFRC tests or statistical correlation for RM tests.

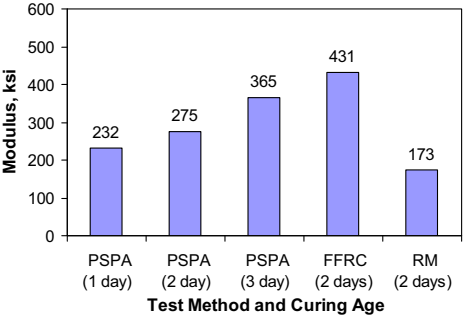

FIG. 3. Moduli from different tests on a treated base.

HMA Layer

This study is related to a 4-inch thick HMA layer. The main goal of field tests on the HMA layer was to evaluate its variation in modulus. Tests with a PSPA were performed at 34 stations. To verify the results from PSPA tests, eight cores were retrieved from the HMA layer and tested with a V-mater in the laboratory. Results from these tests are shown in Figures 4 and 5.

The global average of moduli measured on the HMA layer is 1400 ksi with a coefficient of variation (CV) of 6.8 %. The average modulus of eight cores is 1540 ksi with a CV value of 10%. The average modulus from PSPA tests at the spots close to the core locations was 1393 ksi with a CV of 6.4 %. These numbers are similar to the global average modulus and CV value.

It should be mentioned that the modulus of a HMA material is highly dependent on the frequency of impact load and the temperature of the material when it is tested. The modulus values reflected in Figures 4 and 5 have been adjusted for a temperature of 77^{o} F (25^{o} C) (see Li and Nazarian, 1995). To adjust the HMA modulus for a frequency similar to one used with a FWD, the modulus values in the two figures should be divided by a factor of about 3 (Aouad et al., 1993).

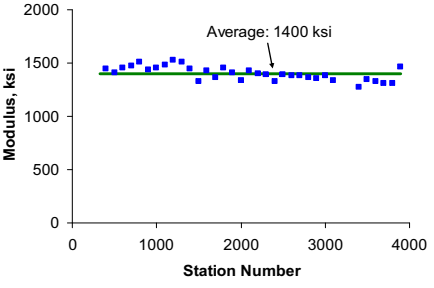

FIG. 4. Variation of HMA modulus.

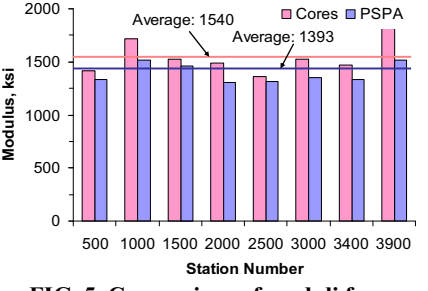

FIG. 5. Comparison of moduli from cores and HMA layer.

Concrete Slab

Strength is the primary parameter considered as the basis for mix design, quality assurance and acceptance of the placed Portland cement concrete (PCC). The strength parameters of concrete have been measured through conventional tests on cast specimens (cylinders or beams) that are cured under ideal conditions. Cores retrieved from a PCC slab can be tested for the compressive strength of in-place concrete. However, coring is costly, destructive and time-consuming.

In conjunction with the construction of a taxiway at a municipal airport, an integrated laboratory-field experiment was conducted to evaluate the feasibility of using seismic nondestructive technology to estimate the early-age strength development of in-place concrete. The representative results from this experiment are summarized in Figure 6.

All tests took place at (concrete) ages of 1, 4, 7, and 28 days except for cores. In general, a power function can best describe the strength-modulus relationship that can be used to estimate the in-place strength of concrete. Such a relationship is mainly affected by the nature of coarse aggregate and much less by other factors such as water-cement ratio and curing temperature.

It should be pointed out that the modulus values measured on the slab must be adjusted through Equation 2 for a given a Poisson's ratio before they were used for estimating the in-place strengths

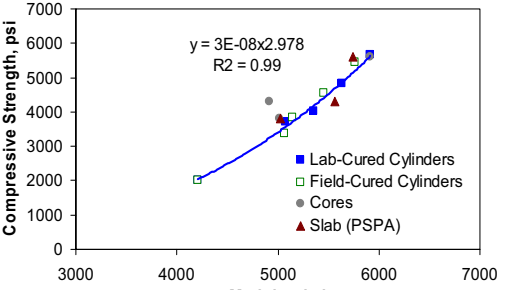

FIG. 6. A strength-modulus relationship.

Soil Foundation

Figure 7 shows an example using the surface-wave method in evaluation of a natural soil site prepared for building foundation. The variation of shear-wave velocity with depth, which is approached by a number of thin layers, is the final result from this

application.

The obtained shear-wave velocity of the soil is very low as it is less than 600 ft/s down to a depth of about 25 ft.

The standard penetration resistances (N-values) from the standard penetration tests (SPT) at this site are also shown Figure 7. The results from the two different tests are consistent even though there is no quantitative relation available for the two tests.

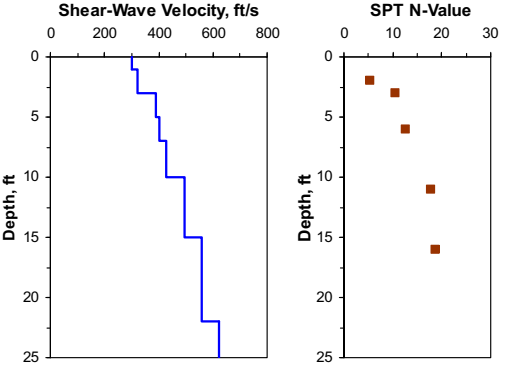

FIG. 7. Variations of shear-wave velocity and SPT N-value with depth.

CONCLUSIONS

Seismic surface wave method is a rapid, economic and relatively accurate means for characterization of pavement layers and evaluation of soil foundations. Great potentials exist by using this method in quality control and quality assurance.

ACKNOWLEDGMENTS

Most of the work presented in this paper was supported by the Texas Department of Transportation and the Innovative Pavement Research Foundation.

REFERENCES

Aouad, M. F., Stokoe II, K. H. and Briggs, R. C. (1993). "Stiffness of Asphalt Concrete Surface Layer from Stress Wave Measurements" *Transportation Research Record,* No.1384, 29-35.

Celaya, M. and Nazarian, S. (2005). "Seismic Testing to Determine Quality of Hot Mix Asphalt" *Transportation Research Record,* No 1946, 113-122.

Li, Y. and Nazarian, S. (1995). "Evaluation of Aging of Hot-Mix Asphalt Using Wave Propagation Techniques" STP 1265, ASTM, Philadelphia, PA, 166-179.

Nazarian, S. and Desai, M. R. (1993). "Automated Surface Wave Method: Field Testing" *Journal of Geotechnical Engineering*, ASCE, 119, 7, 1094-1111.

Nazarian, S. and Stokoe II, K. H. (1985). "In situ Determination of Elastic Moduli of Pavement Systems by Spectral-Analysis-of-Surface-Waves method (Practical aspects)" *Research Report 368-1F*, CTR, University of Texas at Austin.

Yuan, D. and Nazarian, S. (1993). "Automated surface wave method: Inversion Technique" *Journal of Geotechnical Engineering*, ASCE, 119, 7, 1112-1126.

Research and Practice of Roadbed and Pavement Disease Treatment with Cement-Emulsified Bitumen Composite Grouting Material

Ming Liu [1], Hang Yuan [2] and Wei Wang [3]

[1]Master, Civil &Architecture School, Central South University, Changsha, Hunan, 410075, China
[2] Professor, Hunan Tengda Geotechnical Engineering Ltd., Changsha, Hunan, 410075, China
[3]Vice-professor, Civil &Architecture School, Central South University, Changsha, Hunan, 410075, China

ABSTRACT: Through the analysis of the common roadbed and pavement diseases such as cavity beneath slab and pumping, and their current treatment situation, the author proposed the idea of improving and resuming the loading capacity and waterproof performance of highway through intercalating a waterproof bonding layer between base and slab. The author has developed a new composite grouting material composed of an environmentally friendly powdery inorganic component and an emulsified bitumen component to solve the technical issue of the pressure grouting of emulsified bitumen. Their practices show that the material can combine the excellent waterproofing behavior of bitumen and the high-strength of cement and adjust its rigidity to be suitable for different road structures. Through the grouting treatment by the new material, the stress state of roadbed and slab can be significantly improved and the carrying capacity can be resumed at reasonable cost/performance ratio.

INTRODUCTION

Cavity beneath slab and pavement pumping are the most common diseases on highway, the repeated exposures to free water and heavy load are the two fundamental reasons to cause them. According to the survey (Qiling, 2000), after used for more than one year, no matter semi-rigid slab, composite rigid slab or rigid road slab can be damaged to various degrees by water. The detailed reasons appear as the following forms:

(1) After opened to traffic, the highway starts to bear the repeated actions of traffic load. The continuous decrease of the load transfer capacity of joints can give rise to the failure of their filling materials finally.

(2) Under the gradual erosion of both underground capillary water and rainfall, the inner structure of highway is gradually hollowed.

(3) In rainy and/or severe cold areas, the roadbed experiences continuously the cycles of consolidation-softening, and its strength is reduced as the water content of roadbed increases by absorbing water vapour during spring thawing period (Fanhong et al, 2003).

(4) The base and road slab do not completely contact with each other. Due to the existence of cavities between them, rainwater can continually erode roadbed.

APPROACHES OF DISEASE TREATMEMT

The practice shows that the diseases, such as pavement pumping and cavity beneath slab, are directly related to the interlayer treatment process, good interlayer treated measures can effectively prevent roadbed from reflective cracking, the surface water from precipitating and the roadbed water from arising, thus improving significantly the performances and service life of road. So, the effective interlayer treatment is necessary when the damage of road structure occurs.

Grouting has been considered as an effective method to solve the roadbed and pavement diseases for a long time (Jinyou, 2004). At present, cement based grouting materials are mainly adopted for the treatment of these diseases as only compressive strength is paid attention to. However, the imcompatibility issue between base and road slab may occur when it is used. Since a hardened cement paste is a rigid material, it cannot match with the rigidity of road slab and will negatively affect the stress state of road structure, and the hardened cement paste has poor waterproofing capability, whose functions cannot completely fulfill the original requirements for prime, tack and seal layers. This type of passive treatment has poor durability and shorter maintenance period, only about one year. Therefore, it is urgent to develop a new grouting material with adjustable rigidity, excellent waterproofing performance and high durability. Through grouting treatment, a waterproof bonding layer is reset to prevent effectively the interlayer from shear sliding damage and water damage and achieve the functions of prime, tack and seal layers, thus improving the stress state of roadbed and road slab and resuming the loading capacity of road structure (Yuchun, 2004 and Ronghua et al, 2007) .

DEVELOPMENT OF NEW GROUTING MATERIAL

The new grouting material should enable us to reset a waterproof bonding layer between base and road slab. Therefore, it must have two fundamental characteristics: a) good mechanical properties such as bonding strength and impermeability and durability as a waterproof bonding layer and b) appropriate stability, fluidity, setting time and viscosity as a grouting slurry.

Components of the Formulation

The grouting material is composed of three components: inorganic dry mix, modified emulsified bitumen and protective agent. The inorganic dry mix can be one or mixtures of cement, ground slag, fly ash, bentonite, diatomite and quartz sand. The emulsified bitumen is modified by cationic ions with the solid content of 30-70% by weight. The protective agent is a liquid solution consisting of cationic redispersible polymer powder, latex emulsion, polyethylene glycol, bentonite, defoamer, amphoteric surfactant and calcium chloride (Hang and Xianhong, 2008).

Mechanism

As a commonly used rigid grouting material, cement can form an ideal framework.

Emulsified bitumen is an ideal waterproof bonding material due to its good bonding behavior, impermeability and chemical stability, the cation emulsified bitumen is usually used for grouting as its strong permeability and absorbability allow it to penetrate almost all the cracks into which water can do and fill cavities effectively. Therefore, the composite material of cement and emulsified bitumen is an ideal waterproof bonding material. However, in order to realize the stability of slurry and the durability of the paste, we have to solve two issues: a) controllability of the demusification of emulsified bitumen during operation and b) further modification of the brittleness at low temperatures, melting at high temperatures and waterproofing performance of bitumen.

Considering the requirement for the stability of slurry during grouting operation, we have synthesized an amphiphilic polymer containing betaine, this polymer can maintain the balance of the slurry system under the conditions of the temperatures 5-45ºC, low pressures 0.1-0.5 MPa and positive charges (cement: weakly alkali) or negative charges (fly ash: weakly acid) after mixed for 30-40 min. In addition, we also used cationic acrylic to modify emulsified bitumen and enlarge the range of the high temperature melting and the low temperature brittleness of bitumen by use of its swelling action. The natural inorganic nano bentonite is also adopted to modify the comprehensive properties of the slurry, which has excellent compatibility with cement and partially emulsified action to bitumen. Therefore, under a given technical condition, the composite material can form a uniform dispersed system, which can significantly improve the total performances such as compactness, durability, impermeability, bonding and expansion of the grouting material (Zhenguo et al, 2004).

Characteristics of the Material

The slurry of the grouting material has good fluidity and stability and its hardened paste can form a network with polymer film and inorganic cement hydrates interlaced to achieve good mechanical properties and waterproofing behavior. This material has the following characteristics:

(1) Protective agent can control the breaking time of emulsified bitumen through maintaining the stability of slurry.

(2) The grouting material combines the high strength of cement and the excellent waterproofing behavior of bitumen.

(3) Through the comprehensive modification of emulsified bitumen, its temperature range between melting and brittling is enlarged to -20-80ºC. In addition, the composite system can achieve high durability due to the significant improvement of aging resistance by its uniformity and compactness.

(4) The contradictory between the hydrophobicity of bitumen and the water demand of cement hydration have been solved, thus preventing the formation of cavities from the evaporation of free water of cement slurry.

(5) The rigidity of the composite material is changeable through adjusting the content of bitumen to be adapted to various road structures.

(6) The grouting material is nontoxic, environmentally friendly and easy to operate, and has short curing time.

APPLICATIONS

The cement based emulsified bitumen composite grouting material was massively used to treat the diseases of cavities under slab and pavement pumping on Jing-Zhu Highway for the first time in July 2006, after the remediation, this section of highway has been put into use for more than 2 years and no pumping damages have been founded. Up to June 2008, we have used the material to treat the road diseases for about 160,000 m^2 highway in various projects, including cement concrete pavement and asphalt pavement, and achieved satisfactory results.

Engineering Example 1

In October 2007, we carried out the task to treat the diseases on Chang-Yong Highway in China. This highway is semi-rigid asphalt pavement. Large amount of cracks were observed on the surface. The widest cracks were as large as 2 cm. Part of the road were severely hollowed under slabs. Pits occurred locally and road surface was covered by yellow mud, as shown in Fig.1 (a). According to the manual jobsite survey and testing by Falling Weight Deflectometer, the degrees of diseases were divided into slight and sever types for being treated separately.

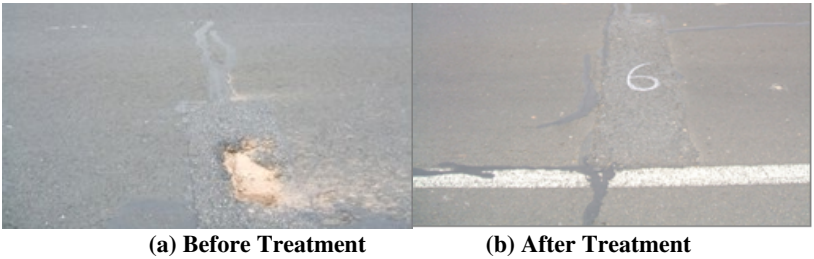

(a) Before Treatment **(b) After Treatment**

FIG. 1. Comparison before and after treatment.

For the slight cavities, we used directly the composite material to treat the disease with steel flower tube grouting. The grouting pressure is normally 0.2-0.4 MPa. The distances between holes are normally 2.5×2.5 m, which can be adjusted according to the specific construction conditions. The holes are arranged as quincunx. The depth of the holes is the same as the thickness of road slab. The grouting material consists of A component and B component with the mass ratio of A:B=6:4, in which A component is cement slurry with w/c=1:0.8 and B component emulsified bitumen with the mass ratio of emulsified bitumen : protective agent=10:1. For the severe cavities, we had to grout cement slurry to strengthen roadbed at first, and subsequently to grout the composite material to squeeze out the diluted cement slurry from cracks on road surface and fully fill the interlayer cavities.

After finishing the grouting, we observed the job sites for many times to check the treatment effect. No mud pumping occurs up to now as shown in Fig. 1 (b). The stress state of roadbed and road slab is also significantly improved from the testing results of deflection values as shown in Table 1.

Table 1. Deflection Values of Road Slab Before and After Treatment

Measuring Point		1	2	3	4	5	6	7	8	9	10
Deflection Value ($\times 10^{-2}$ mm)	Before Treatment	28	120	14	22	14	53	72	38	16	18
	After Treatment	14	22	12	16	10	15	18	16	10	12
	Difference	14	98	2	6	4	38	54	16	6	5

The cores drilled from jobsite show clearly the network of the hardened paste of the grouting material formed in roadbed. After the emulsified bitumen is demulsified and hardened, it can form a compact waterproofing layer in the cavities under road slab. The testing results of compressive and tensile strengths and impermeability in Table 2 made by the Engineering Testing Center under Changsha Polytechnic University show that the hardened slurry has good mechanical properties and impermeability.

Table 2. Specific Test Data of Coring Test Block

Compressive Strength (MPa)		Tensile Strength (MPa)		Impermeability (MPa)	
8h	24h	8h	24h	8h	24h
11.4	16.2	2.3	3.4	1.0	1.2

Engineering Example 2

From June to September 2008, the composite grouting material was used for road diseases treatment on Da-Xin Highway with concrete slab in Shanxi Province of China, the same treatment process above-mentioned was used for the project. However, the formulation of the slurry should be adjusted accordingly so that the rigidity of the hardened slurry matches with the road structure.

After finishing the project, we checked the construction quality with Falling Weight Deflectometer. From the results shown in Table 3, the deflection values are generally below 0.05 mm for the sections in good service condition.

Table 3. Deflection Values of Disease/Non-Disease Sections and Before/After Treatment

Stake Number	Lane	Number of Testing Points	Maximum Value ($\times 10^{-2}$ mm)	Average Value ($\times 10^{-2}$ mm)	Representative Value ($\times 10^{-2}$ mm)	Note
K484+720 ~ K485+000	Left slow	20	5.0	1.8	3.1	Non-disease, untreated
K483+000 ~ K486+000	Left fast	150	20.0	5.5	9.1	Disease, before treated
K483+000 ~ K486+000	Left fast	150	5.0	2.7	4.7	Disease, after treated

After the treatment by grouting, the deflection values were significantly reduced showing that the working condition of road slabs have been greatly improved.

CONCLUSIONS

(1). The cement based emulsified bitumen grouting material overcomes the shortcomings of pure bitumen or pure cement paste by combining their advantages together. Since its rigidity is adjustable, it is applicable to various road structures. Through grouting treatment, a waterproofing bonding layer can be reset between roadbed and slab to act as penetration, bonding and seal layers. This treatment can well solve the trouble of water erosion, improve the stress state of roadbed and road slab and prolong their service life. It is an ideal method to treat the diseases of highway and has wide developing prospect.

(2). Currently the grouting technology is still in the situation that the theories are behind the practices. The effect of grouting is still influenced by human factors to a big extent. It is necessary to select the experienced applicators and determine the right grouting factors including mix proportion, depth of holes, distance of holes and grouting pressure etc. If having conditions, one should make experiments to optimize grouting factors. In addition, we still need to improve the properties of the composite material such as durability, penetrability and high pressure grouting etc.

ACKNOWLEDGMENTS

We would like to thank the Department of Communications,Hunan Province for sponsoring and supporting the research.

REFERENCES

Fanhong, M., Zengke, Z. and Sumin C. (2003). “Research on Cause of Road Longitudinal Crack.” *Highway and Transportation Research and Development*, 20(6):35~38(in Chinese).

Hang, Y. and Xianhong, C. (2008). “The environmentally friendly inorganic dry mix and polymer modified emulsified bitumen grouting material.” Chinese patent, CN101148338.2008-03-26 (in Chinese).

Jinyou, L. (2004). “Application of grouting in Settle down Plat Bottom Escape of Cement Surface. *Communications Standardization,* 2004, 7:46~48(in Chinese).

Qingling, S. (2000). “Water Damage and Prevention Measures of Expressway Asphalt Pavement.” *Foreign Highway*, 20(30): 1~4(in Chinese).

Ronghua, Y., Zhiyong, Z. and Hui, Y. (2007). “Performance Analysis on Waterproof and Cohesive Layer of Asphalt Pavement.” *Changsha University of Science and Technology:Natural Science*, 4(4):21~24(in Chinese).

Yuchun, Y. (2004). “Research on Sealing Material Structure and Mechanical Performance.” *Petroleum Asphalt*, 18(2):22-26 (in Chinese).

Zhenguo, Z., Guoting, W. and Zhong, S. (2004) "Colloid and Surface Chemistry." Beijing Chemical Industry Press, (in Chinese).

Research on Meshless Method using Uniform Design and its Application in Piles Engineering

Wang You[1], Huang Liang[2], Wang Xing-hua[3] and Zhao Ming-hua[4]

[1]Lecturer, Postdoctoral, School of Civil Engineering and Architecture, Central South University, Changsha, P. R. of China, 410075; ywang1920@hotmail.com
[2]Lecturer, College of Civil Engineering, Hunan University, Changsha, P. R. of China, 410082; lhuang1178@hnu.cn
[3]Professor, School of Civil Engineering and Architecture, Central South University, Changsha, P. R. of China, 410075; xhwang@mail.csu.edu.cn
[4]Professor, College of Civil Engineering, Hunan University, Changsha, P. R. of China, 410082; mhzhaohd@21cn.com

ABSTRACT: In order to ensure that the nodes are distributed uniformly in the definition domain of calculation points, the uniform experiment design is introduced in the meshless method, which can make the nodes distribution uniform in the domain. Using uniform designs table, distributes these nodes, the interpolation function is built by those nodes, and dispersant equations are founded by the Galerkin Method. According to this concept, a programme based on uniform design is made. In order to verify the theory and programme, a load test of pile foundation is chosen to provide calculation data. The calculated results accord with survey data on-the-spot and show that it's possible that the uniform design may be applied in the nodes distribution in meshless method. And the calculation result obtained by less nodes is precise, based on the meshless method using uniform design. Because the radius of influence domain is decreased, the computer workload is greatly reduced.

INTRODUCTION

Traditional finite element methods have encountered many difficulties in addressing many technical problems in the areas of the large deformation (molding, high speed collision and liquid-solid coupling), singularity and dynamic crack expansion. The meshless method, created in 1970's, need only node information, but not element information. Unlike traditional finite element methods, it does not use the concept of element and grid. However, when using the meshless method to compute the physique functions, the problem of solving the reversible of matrix $A(x)$ can not be avoided. To ensure that (1) on one hand the matrix is reversible, the radius of node strut domain should be large enough, so that each computation point within the definition domain has sufficient number of nodes; and (2) on the other hand, the nodes within the definition

domain should be made uniformly distributed, so that it guarantees that the matrix will not cause singularity. In order to solve the problem of uniform distribution, the uniform design method was proposed by Academician Wang Y. and Fang K.T. in 1978, and its mathematical principle is based on the identical distribution theory of the number theory. In addition, the changes of the models have steady nature, thus it is suitable for multi-factor, multi-level experiments, and achieves better approximation for non-linear models. All the above characteristics make it a suitable choice in the field of geotechnical engineering (Fang, 2004 & Gu, 2001).

In this paper, the principle of uniform design was applied and the uniform design table was utilized to make the nodes uniformly distributed in the solution domain. Then by utilizing these uniformly distributed nodes, an interpolation function was established. Subsequently by applying the Galerkin Method, a discrepancy equation was founded and the meshless method based on uniform design was derived. Lastly, a sample analysis of pile foundation was carried out for the validity and effectiveness of this method.

PRINCIPLE OF THE MESHLESS METHOD BASED ON UNIFORM DESIGN

The uniform design method is classified as pseudo-Monte Carlo Method. From statistical point of view, the pseudo-random number is a sampling of uniform distribution, and the uniform design is to find small samples out of the uniform distribution sampling. Because these samples are more uniformly distributed than that of the orthogonal design, a better result can be achieved by using it in the experiment, at the same time, the workload can be significantly reduced, and all possible combinations of experiments can be controlled effectively.

The uniform design uses the standard deviation as its uniformity appraisal target, and the size of deviation is correlated with the effectiveness of uniformity. The commonly used uniform design may be obtained by looking up the value in the uniform design table [Fang, 2001]. Each uniform design table has a representation code $U_n^*(n^m)$ or $U_n(n^m)$, where U is the uniform design, n is the horizontal number and the number of experiments, m is the maximum number of factors used. The presence or absence of the "*" to the right upper corner of U represents two different types of uniform design tables. The uniform design table with the "*" has better uniformity and is recommended to be used first. Each row in the uniform design table is not equal, and the selected row for each experiment is closely tied to the number of experiment factors. Therefore, each uniform design table has a usage table for reference. Moreover, there is often more than one uniform design table that meets the same experiment factor requirement, thus researchers need to select the appropriate uniform design table so as to meet the requirements of the experiment, has good uniformity, i.e, have small deviation, and at the same time requires relatively smaller number of experiments.

Different from the finite element method, which uses interpolation to establish approximate function, the meshless method obtains superior localized approximation through the computation points in the neighbor domain, and then utilizes the superior localized approximation to solve the overall approximate functions in the solution domain.

The control formulas of elastic mechanics are equilibrium formula: $\sigma_{ij,j} + \bar{f}_i = 0$ within Ω, geometry formula: $\varepsilon_{ij} = 0.5(u_{i,j} + u_{j,i})$ within Ω, physics formula: $\sigma_{ij} = D_{ijkl}\varepsilon_{kl}$ within Ω, stress boundary condition: $\sigma_{ij}n_j - \bar{t}_i = 0$ within Γ_t, displacement boundary condition: $u_i = \bar{u}_i$ within Γ_u (Zhang, 2004).

In the formulae, $\bar{f}_i$ is the given physical strength of domain Ω; Γ_t is boundary of the given surface strength; $\bar{t}_i$ is the given surface strength; n_j is the outer normal direction cosine of the boundary of Γ_t; Γ_u is the given displacement boundary; $\bar{u}_i$ is the given displacement; D_{ijkl} is the constitutive tensor.

For example, for a two dimensional problem, in order to get the distribution of approximate function $\boldsymbol{u}$ within the sub-domain Ω_x, use the finite random distributed nodes $x_i (i = 1,2,\cdots,n)$, the approximate value $u^h(x)$ of function $\boldsymbol{u}$, $\forall x \in \Omega_x$, can be defined as:

$$u(x) \approx u^h(x) = \sum_{j=1}^{m} p_j(x)a_j(x) = p^T(x)a(x) \tag{1}$$

Where: $p^T(x) = [p_1(x) \quad p_2(x) \quad \cdots \quad p_n(x)]$ is m times the base of complete monomial formula, $a(x)$ is the vector of the coefficient $a_j(x)(j = 1,2,\cdots,m)$. These coefficients are the function of the space coordinate $x = [x, y, z]$.

In the MLS, the selection of the coefficient $a(x)$ makes the solution to the function $u(x)$ the best approximation by some kind of least square principle, when solving the approximation function $u^h(x)$ within the neighbor domain Ω_x of computation point $\boldsymbol{x}$. The neighbor domain Ω_x of computation point $\boldsymbol{x}$ is called the definition domain of MLS approximate function in the computation point $\boldsymbol{x}$, abbreviated as the definition domain of computation point $\boldsymbol{x}$.

To discretize N nodes in solution domain, the weight function $w_I(x) = w(x - x_I)$, which is compact, is defined at every node x_I. In addition, define the approximate function at the node $\bar{x} = x_I$ as the weighted sum of squares:

$$J = \sum_{I=1}^{N} w_I(x)[u^h(x_I) - u(x_I)]^2 = \sum_{I=1}^{N} w_I(x)[\sum_{i=1}^{m} p_i(x_I)a_i(x) - u_I]^2 \tag{2}$$

In order to make the approximate solution very close to the actual solution, the weighted sum of squares should be extremely small, such that the coefficient vector $a(x)$ can be assured. Use $a(x)$ to derivative $\boldsymbol{J}$:

$$\frac{\partial J}{\partial a_j(x)} = 2\sum_{I=1}^{N} w_I(x)[\sum_{i=1}^{m} p_i(x_I)a_i(x) - u_I]p_j(x_I) = 0, \ j = 1,2,\cdots,m \tag{3}$$

Thus obtain:

$$\sum_{i=1}^{m}[\sum_{I=1}^{N} w_I(x)p_i(x_I)p_j(x_I)]a_i(x) = [\sum_{I=1}^{N} w_I(x)p_j(x_I)]u_I \tag{4}$$

Then $A(x)a(x) = B(x)u$ (5)

Where:

$A(x)=\sum w_I(x)p(x_I)p^T(x_I)$, $B(x)=[w_1(x)p(x_1) \quad w_2(x)p(x_2) \quad \cdots \quad w_N(x)p(x_N)]$.

Use equation (5) to solve the coefficient vector $a(x)$.

ANALYSIS OF CALCULATION EXAMPLE

A load test on pile foundation made by Hunan University is chosen to provide calculation data and provides engineering background to the meshless method using uniform design [Liu, 2004]. The test pile is borehole cast-in-place concrete pile, and the shaft wall is protected by drilling mud. The diameter of pile is 1.0 m, and the embedment depth is 60.0 m, and the bottom of pile reaches slightly weathered sedimentary rock layer. The strength of the concrete in the pile body is C30, the true measurement of the concrete's elastic modulus is 3.47×104 MPa, and Poisson's ratio μ=0.2.

A calculation programme, which adopts meshless method using uniform design, is written in Matlab. Simplify the pile as a geometric model shown in figure 1(a), that is, the pile underneath the ground is considered as clamped support, the top as free standing, The nodes of pile are distributed in the computation domain by two ways, i.e, usual design and uniform design as shown in the figure 1(b) and (c). The nodes distribution plan takes 36 nodes for example. The problem's computation domain can be divided into 55 (11×5) integral sub-domain, that is, background net, as shown in figure 1(d). The numerical integral all uses 4×4 Gauss integral; Utilize the linear function, the weight function is Gauss weighting function.

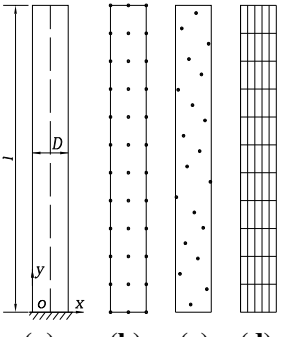

FIG. 1. Sketch map of embedded rock pile. (a) geometric model (b) usually node distribution plan (c) uniform design node distribution plan (d) background net.

For simulating the process of test, the load applied to the pile's top has been increased gradually using load increment method. When the horizontal displacement exceeds 6 mm, the scale coefficient of soil foundation should be reduced 0.4 times of original value (Zhao, 2001). And when the stress of pile reaches materials strength, the stiffness of pile should be discount proportionally. Computed and measured load-displacement curves are shown in figure 2.

In figure 2, the both computed load-displacement curves, i.e, which distribute nodes by meshless method using uniform design and normal way, accord with survey data on-the-spot. The calculated results may satisfy the engineering requirements and estimate the bearing capacity and displacement of piles. And we can observe that the horizontal displacement of pile on top increases with addition of horizontal load, and the soil surrounding pile deforms continuously. Which mean that the soil is pressed and bears the loads with pile. The soil failure is earlier than materials failure. The curve has characteristic of slow change and no inflexion. That shows that the strength and softening of soil may greatly influence the horizontal carrying capacity of pile.

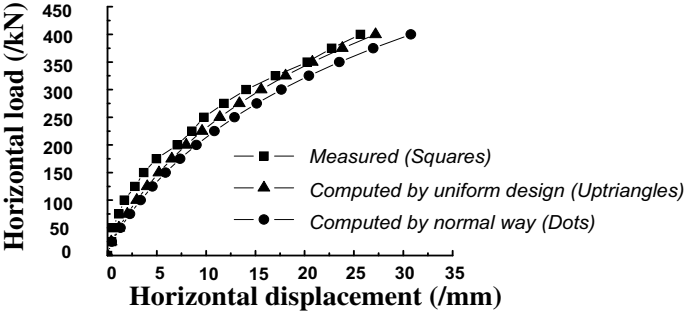

FIG. 2. Calculated results based on different nodes distribution.

The computed results are shown in figure 3 and 4 in order to compare the different nodes distribution. Figure 3 is the curve of the number of nodes and relative error of displacement and figure 4 is the curve of the number of nodes and radius of calculation domain. In the figures, curve **A** represents the meshless method using uniform design, curve **B** represents normal meshless method, **n** is the number of nodes, **r** is the radius of influence domain and $\mathbf{r_u}$ is the relative error of displacement.

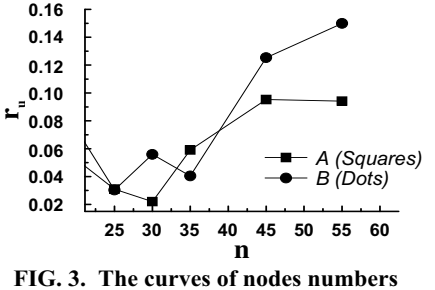

FIG. 3. The curves of nodes numbers and relative error of displacement.

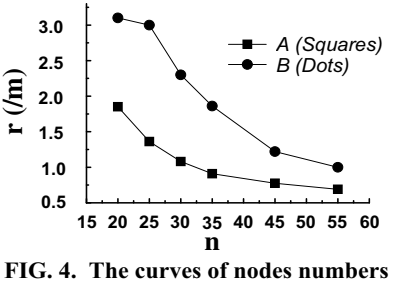

FIG. 4. The curves of nodes numbers and radius of calculation domain.

The curves in figure 3 show that when the number of calculation points is relatively small, the meshless method using uniform design in this paper can produce more accurate computation results. Moreover, due to the fact that the number of calculation

points is reduced, the computing workload is significantly reduced as well. At the same time, different from the finite element method, the calculation accuracy of meshless method does not increase because the number of nodes increases. It shows that the homogeneity of nodes distribution is more important than the number of nodes in meshless method, and uniform design may fit the demand.

In figure 4, the curves show that the radius of influence domain using uniform design is much smaller, and the reason is that the advantages of uniform design are to have the test nodes uniformly distributed in the parameter space, and to have the steady nature towards the model changes. Though the radius of influence domain in this paper is much smaller, it ensures reversibility of the matrix, and reduces computing workload.

CONCLUSIONS

The uniform experiment design has introduced the nodes disposition of meshless method to ensure enough nodes in the definition domain of calculation point. This method is suitable for complicated pile engineering domain and easy to be applied. A load test on pile foundation is introduced and provides engineering background and calculation data. The calculation results obtained by the meshless method based on uniform design show that it's possible that the uniform design may be applied in the nodes distribution of meshless method.

The results show that when the numbers of calculation points are relatively small, the meshless method using uniform design given in this paper can produce more accurate results and the amount of calculation is also significantly reduced. In addition, the radius of influence region selected is smaller than that of influence region of usual meshless method. It ensure that the matrix is reversible and reduces the computing workload.

ACKNOWLEDGMENTS

The authors appreciate the support of Central South University and National Natural Science Foundation of China.

REFERENCES

Fang K.T. (2004). "Theory, method and application of uniform experiment design——historical retrospect" *Chinese Journal of mathematical statistics and management*, Vol. 23 (3): 69-80.

Gu Y T, Liu G R. (2001). "A local point interpolation method for static and dynamic analysis of thin beams" *Computer methods in Applied Mechanics and Engineering*, Vol. 190 (42): 5515-5528.

Fang K.T., Ma C.X. (2001). "Orthogonal and uniform design on experiment" Beijing: *Tsinghua University Press*.

Zhang X., Liu Y. (2004). "Meshless methods" Beijing: *Tsinghua University Press*.

Liu Q.J., Zhao M.H., Li Y. (2004). "In-site load test of the piles in the foundation of Maocaojie bridge" *Journal of Hunan University*(*Natural Sciences*), Vol. 31 (4): 51–54.

Zhao M.H. (2001). "Calculation and test of piles in bridges" Beijing: *China Communications Press*.

Nonlinear Response of Passively Loaded Piles Founded in Soft Bangkok Clay

Sathaporn Pokpong[1]

[1]Lecturer, Faculty of Industrial Technology, Phranakhon Rajabhat University, Bangkok, Thailand; sathap@pnru.ac.th

ABSTRACT: Embankment construction on soft clay can result in the development of significant lateral ground movement. When the pile is installed adjacent to this unstable embankment, it may experience unexpected lateral passive loading along its length and may cause the integrity problem of the superstructure. A lot of numerical and experimental research works have been conducted for better understanding of the behavior of passively loaded pile. However, the nonlinear response of piles subjected to horizontal ground movement is difficult to analyze with two-dimensional technique since the passively loaded piles are truly three-dimensional problem. In order to investigate the complex soil-pile interaction, the three-dimensional finite element analysis was employed in this study. The passive p-δcurves are presented to account for a nonlinear response of piles as the common p-y curves may not properly describe the actual behavior of piles subjected to lateral ground movement. It was found that the generated p-δcurves were dependent on pile spacing; when pile spacing decreased the passive p-δ curves stiffened, whereas the active p-y curves softened. A better understanding of behavior of passively loaded piles adjacent to an embankment constructed on soft Bangkok clay was achieved.

INTRODUCTION

The behavior of piles subjected to lateral ground movement associated with unstable slope is considerably different from the actively loaded piles. In general, the load distribution resulting from horizontal ground movement can be found in pier foundation adjacent to bridge approach embankment, excavation or tunneling operations, piles supporting traffic signs or buildings adjacent to the settling slope. The soil pressures against these piles are nonlinearly induced along the pile shafts. However, the distribution of transmitted lateral forces varies diversely from case to case and no general rules can be specified for practical use (Chen, 1994).

In the analysis of passive single piles by Randolph et al. (1984), it was found that the values of ultimate soil pressure ranges roughly from $9c_u$ to $12c_u$. However, in the back-analysis of piles in unstable slopes conducted by Vigiani (1981), the ultimate soil resistance was somewhat lower, between $2.8c_u$ and $4c_u$. Poulos (1995) found that the

limiting lateral soil pressure increased linearly from $2c_u$ at the ground level to $9c_u$ at a depth of about 3.5D and remained constant below that depth. Based on a two-dimensional numerical analysis adopted by Bransby et al. (1999), it was found that the ultimate soil resistance was equal to $11.75c_u$ and moderately higher than those suggested by others.

A number of laboratory models of coupled piles in soft clay were experimentally performed by Pan et al. (2002b). It was found that the passive soil pressure, measured along the pile shaft, showed small discrepancies between coupled piles in a row at 3D and 5D pile spacing. The horizontal soil pressure at a particular depth tends to increase slightly after lateral displacement was mobilized greater than 3.2 mm. While the soil mass was translated approximately by 0.65D, the ultimate soil pressures p_u were determined to be $7.1c_u$ and $8.6c_u$ for 3D and 5D pile spacing respectively.

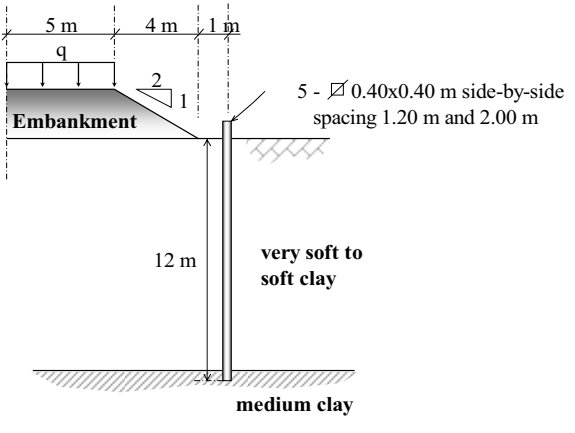

FIG. 1. Passively loaded piles adjacent to an embankment.

In this study, the passive load is imposed on the piles by the down slope ground movement due to the settling embankment constructed on the Soft Bangkok clay, as shown in Fig.1. The three-dimensional finite element analysis is employed to account for the soil-pile-embankment response by using the elasto-plastic continuum approach.

THE RELATIVE SOIL-PILE DISPLACEMENT

As stated by Bransby (1996), the traditional p-y curves may not properly describe the actual soil-pile response of the passively loaded piles subjected to the lateral ground movement. This is because the actively loaded piles are pushed laterally into the surrounding soil and the soil is dragged simultaneously together with the piles while the contact pressures along the passively loaded piles are horizontally induced due to the squeezing soil.

The variation of the ultimate soil resistance p and the relative soil-pile displacement at any depth is presented in term of p-δ curves. The passive p-δ curves adopted by

Bransby et al. (1999) are employed to describe the soil-pile response as the traditional p-y curves show a large displacement for a small incremental soil resistance, i.e., a linear relationship. The magnitude of relative soil-pile displacement $\delta$to mobilize the ultimate soil resistance is approximately 0.015D and 0.025D as proposed by Pan et al. (2002b) and Bransby et al. (1999), respectively.

With an attempt to study the effects of embankment construction on adjacent single pile and pile groups, Stewart (1992) conducted a number of experimental centrifuge models. The prototype square pile, with 0.4 m width and 22.5 m in length, was set up to be freely unrestrained. As a result of centrifuge tests, it was indicated that pile spacing larger than 4.9D is less significant in group effects.

THE NUMERICAL MODELING

Since the actual pile-soil interaction due to lateral ground movement is very complex, the two-dimensional numerical simulation may not properly investigate the real behavior of the passively loaded piles (Pan et al., 2002a). In this study, five unrestrained square piles, with slenderness ratio equal to 30, are simulated in a single row parallel to the embankment toe by using three-dimensional finite element analysis. The 3D and 5D center-to-center pile spacing are examined.

The soil-pile system is constitutively subdivided into a number of 3D eight-node hexahedral elements and analyzed with an iterative technique. The virtual soil-pile interface elements are essentially assigned to investigate the transmitted shear and pressures between two distinct materials. The deformable elements are typically defined as a thin layer, so-called a master-slave or a contact pair concept. The optimized width of contact element is assigned to be 10% of pile diameter. The soil yield criterion is assumed to be governed by an elasto-plastic constitutive relation with a non-associated Drucker-Prager flow rule. The uniform load q is applied vertically and incrementally ranged from 0 to 60 kN/m^2 on the crest of slope in order to trace the nonlinear response of piles and surrounding soil. The material parameters used in the FE analysis are summarized in Table 1.

Table 1. Parameters Used in the Finite Element Analysis

Parameters	Soft Clay	Pile and Pile Cap
Young's modulus (MN/m^2)	4.4	27.0
Poisson's ratio, ν	0.40	0.20
Unit weight (kN/m^3)	14.0	25.0
Undrained shear strength (kN/m^2)	11.3	-
Dilatancy angle (degree)	0	-

LATERAL DISPLACEMENT AND RESISTANCE

When piles are installed near a settling embankment or slope constructed on soft soil, the horizontal ground movement can result in significant bending stresses and displacement along the pile shaft. Even though the vertical movement of embankment can be well estimated, but lateral ground movements are considerably difficult to

predict (Poulos, 1973). A response of the passively loaded piles sustained by the down slope soil movement is described in this section. The normalized pile deflection and the bending moment along the pile shaft are extensively observed. The lateral soil resistance is determined from a contact pressure acting on the face of pile far from the source of the down slope ground movement.

In order to deliberately estimate the relative soil-pile displacement δ the global soil deformation profiles δ_s in the middle of two piles installed at spacing 3D and 5D are observed. The contours of the horizontal ground movement at different pile spacing are explicitly traced in Fig. 2 and 3. The magnitude of the soil displacement between the two piles at larger spacing is slightly greater than those at a smaller spacing. The equivalent uniform soil movement defined as δ_q is calculated from the equally swept areas under an undrained circumstance in which volume change in soil mass is disregarded.

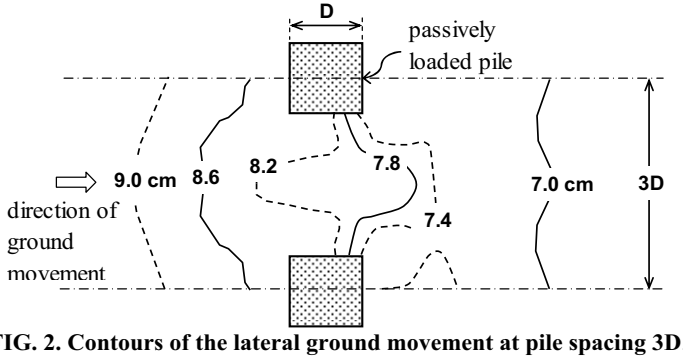

FIG. 2. Contours of the lateral ground movement at pile spacing 3D.

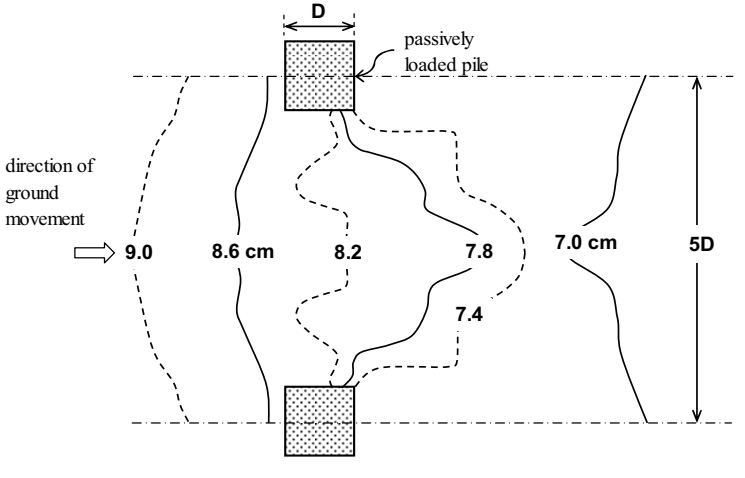

FIG. 3. Contours of the lateral ground movement at pile spacing 5D.

Since the significant difference of the soil and the pile displacement can be noticeably found in the very soft clay layer; therefore, the passive p-δcurves at these depths are presented as a manifold series of p-δcurves as shown in Fig. 4. The ultimate soil resistance per unit length, observed at a mid depth of very soft clay layer, is about 21.0 kN/m and 18.5 kN/m for the passively loaded piles installed at 3D and 5D spacing respectively. At a smaller spacing, the passive p-δcurves are somewhat stiffer than those at a larger spacing.

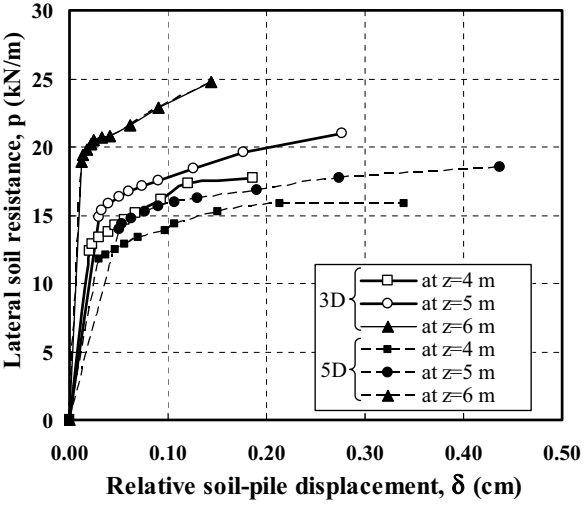

FIG. 4. A series of the passive p-δcurves at pile spacing of 3D and 5D.

CONCLUSIONS

The shape of passive p-δcurves is nonlinear and similar to the conventional active p-y curves. At early stage of lateral soil movement, the relationship between the soil resistance and relative displacement is linearly raised, and thereafter, it perpetually reaches to a critical state and exhibits a convergent trend. It is interesting to note that the generated p-δcurves are dependent on pile spacing. The passive p-δcurves stiffen, whereas the active p-y curves soften when piles spacing is decreased.

The computed ultimate soil pressures remain constant after the relative soil-pile displacements are mobilized at approximately 0.015D for the passively loaded pile founded in soft Bangkok clay. This research finding agrees fairly well with the other previous numerical studies performed by Bransby (1996) and Pan et al. (2002a). However, it should be noted that the lateral contact pressures at any depths are greatly dependent on the local soil deformation and the relative soil-pile stiffness in the analysis.

ACKNOWLEDGMENTS

This research project was completely conducted under the collaborative program between Phranakhon Rajabhat University and Technical University Darmstadt, Germany. The author would like to sincerely thank all scientific staffs of the Institute of Geotechnics, especially the Director of the Institute, Prof. Dr.-Ing. Rolf Katzenbach, who kindly supported and enthusiastically supervised this project during the author's stay in Germany.

REFERENCES

Bransby, M. F. (1996). "Selection of p-y curves for the design of single laterally loaded piles." *International Journal of Numerical and Analytical Methods in Geomechanics*, Vol. 23: 1909-1926.

Bransby, M. F. and Springman, S. (1999). "Selection of load-transfer functions for passive lateral loading of pile groups." *Computers and Geotechnics*, Vol. 24(3): 155-184.

Chen, L. T. (1994). "The effect of lateral soil movements on piles foundation." *Ph.D. Thesis*, University of Sydney, Australia.

Pan, J. L., Goh, A. T. C., Wong, K. S., and Selby, A. R. (2002a). "Three-dimensional analysis of single pile response to lateral soil movements." *International Journal of Numerical and Analytical Methods in Geomechanics*, Vol. 26: 747-758.

Pan, J. L., Goh, A. T. C., Wong, K. S. and Teh, C. I. (2002b). "Ultimate soil pressure for piles subjected to lateral soil movement." *ASCE Journal of Geotechnical and Geoenvironmental Engineering*, Vol. 128(6): 530-535.

Poulos, H. G. (1973). "Analysis of piles in soil undergoing lateral movement." *ASCE Journal of Soil Mechanics and Foundation Engineering*, Vol. 99: 391-406.

Poulos, H. G. (1995). "Design of reinforcing piles to increase slope stability." *The Canadian Geotechnical Journal*, Vol. 32(5): 808-818.

Randolph, M. F. and Houlsby, G. T. (1984). "The limiting pressure on a circular pile loaded laterally in cohesive soil." *Géotechnique*, Thomas Telford, Vol. 34(4): 613-623.

Stewart , D. P. (1992). "Lateral loading of piled bridge abutments due to embankment construction." *Ph.D. dissertation*, University of Western Australia, Perth.

Viggiani, C. (1981). "Ultimate lateral load on piles used to stabilize landslides." Proceedings, *The 10th International Conference of Soil Mechanics and Foundation Engineering*, Stockholm, Vol. 3: 555-560.

Theoretical Analysis and Numerical Simulation of Load-Settlement Relationship of Single Pile

ZHANG Chun-shun [1-2], WANG Yong-he[1], XIAO Hong-bin[3], and FAN Zhen-hui[1]

[1]School of Civil Engineering and Architecture, Central South University, Shaoshan Road, Changsha, 41007, People's Republic of China; email: zhangchunshun@yahoo.com.cn
[2]Geotechnical Engineering Center, Sydney University, Darlington, NSW, 2006, Australia; email: C.Zhang@usyd.edu.au
[3]School of Civil Engineering, Hunan University of Technology, Wenhua Road, Zhuzhou, 410082, People's Republic of China

ABSTRACT: An analytical model is proposed to evaluate the pile skin friction at the pile-soil interface and analyze *P-s* curve of single pile. The model is based on the exponential transfer function technique and allows back-analysis to be carried out easily. The calculated skin friction results is in good agreement with the measured ones and the accuracy of the proposed method has been verified by an example in Xiao *et al.*'s (2002) work. Then the transfer model is implemented into differential equation of pile-soil interaction, and after being iterated by computer simulation, the calculated *P-s* curve is in very good agreement with the results of Xiao *et al.* (2002) and Carrubba (1997). Parameters are initially obtained from lab experiment and subsequently modified by fitting the Carrubba's (1997) pile head displacements to computer simulation.

INTRODUCTION

The most reliable method to determine load-settlement relationship (*P-s* curve) of pile is to conduct the destructive test of the pile (Carrubba, 1997). However, pile tests on site are costly and time consuming, especially for large-diameter pile that requires over thousand tons of test loads, which are sometimes impossible or at least very difficult to be carried (Aschenbrener, 1984; Duncan and Chang, 1970). Therefore, many scholars tried to develop theoretical solution, hoping to find appropriate ways to predict capacity of pile (Wei and Mark, 1998). Uptill now, all kinds load transfer functions could be defined into two sorts: one is linear models including linear, bi-linear, and tri-linear, such as Randolph and Wroth (1978), and Pells, *et al*.(1997); the other is nonlinear models including exponential model (Kezdi, 1957), parabola model (Vijayvergiya, 1977), hyperbolic model (Seed and Reese,1955; Duncan and Chang, 1970; Xiao, *et al.*, 2002). It is to be noted that a number of tests conducted home and abroad have indicated the nonlinear relationship between pile skin friction and pile displacement, which

means over simplification model like linear relation might not be suitable.

An exponential load transfer function to evaluate the pile skin friction at the pile-soil interface is proposed based on reduced scale pile model test and verified by back-analysis of a pile example in Xiao *et al* (2002). The model function is then implemented into differential equation of pile-soil interaction and obtains an analytical equation for calculating *P-s* curve. After automatic iteration in computer program, the equation could be solved and the results are in agreement with the results of Xiao (2005) and Carrubba (1997).

ESTABLISHMENT OF PILE SKIN FRICTION FUNCTION

First of all, a reduced scale pile model test was performed in expansive soils (with constant water content) in our previous work (Zhang C.S. *et al*, 2007) and the results of the skin friction and settlements of the pile are plotted in Figure 1 and the measured and fitted results are listed in Table 1. Note that numbers 1, 2, 3 and 4 are the locations of strain gauges (Zhang C.S. *et al*, 2007).

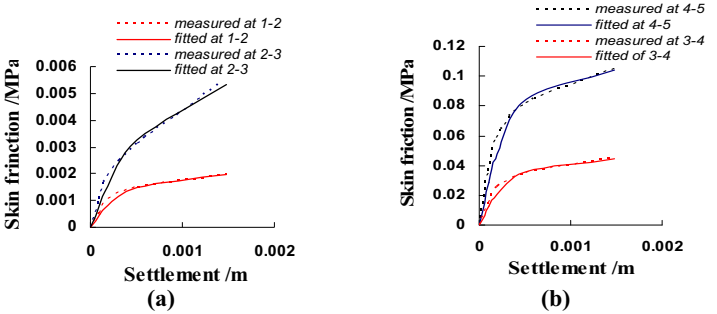

FIG.1. Skin friction and settlement of model pile. (a) presents the skin friction between gauges 1 and 2, 2 and 3; (b) presents the skin friction between gauges 3 and 4, 4 and 5.

Table 1. Fitted Model Pile Skin Friction and Settlement.

	Average Skin Friction between 1 and 2	**Average Skin Friction between 2 and 3**
Fitted curve	$\tau = 0.0059\left(1-e^{-1600S}\right)$	$\tau = 0.002\left(1-e^{-2700S}\right)$
Parameters	$\alpha = 0.0059\,;\beta = 1600$	$\alpha = 0.002\,;\beta = 2700$
Correlating Coefficient	0.981	0.986
	Average skin friction between 3 and 4	Average skin friction between 4 and 5
Fitted curve	$\tau = 0.045\left(1-e^{-3200S}\right)$	$\tau = 0.105\left(1-e^{-3200S}\right)$
Parameters	$\alpha = 0.045\,;\beta = 3200$	$\alpha = 0.105\,;\beta = 3200$
Correlating Coefficient	0.980	0.978

Xiao *et al*. (2002) once adopted a hyperbolic load transfer function in studying the engineering pile mentioned in Carrubba's (1997) work, which resulted in very high accuracy. Based on Xiao's $\tau - s$ curve, the corresponding parameters α and β for the proposed exponential function could be obtained as shown in Table 2 by back-analysis, and the calculated results are compared with Xiao's (2002) results in Fig. 2.

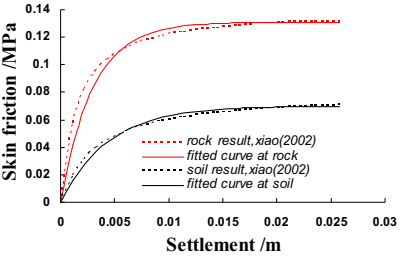

FIG. 2. Comparison between Xiao's result (2002) and proposed function.

From the above two examples, the exponential relation between pile skin friction and settle- ments could be fitted by the proposed exponential function:

$$\tau(z) = \alpha\left(1 - e^{-\beta S(z)}\right) \tag{1}$$

Table 2. Fitted Relationship Between Skin Friction and Settlements

	Average Skin Friction at Soil	**Average Skin Friction at Rock**
Fitting curve	$\tau = 0.07\left(1 - e^{-228S}\right)$	$\tau = 0.131\left(1 - e^{-340S}\right)$
Parameter α , β	$\alpha = 0.07$; $\beta = 228$	$\alpha = 0.131$; $\beta = 340$
Correlating Coefficient	0.982	0.988

where $\tau(z)$ means pile skin friction at z length; α and β are the load transfer parameters of pile skin soil; $s(z)$ is settlement of pile at z depth.

α and β are meaningful in physics where α indicates ultimate friction at the pile-soil interface and β reflects the initial slope in friction-settlement curve.

Hyperbolic relation is widely accepted for pile-end soil resistance, suggested by Seed and Reese (1955):

$$\sigma = \frac{S_b}{a_b + b_s \cdot S_b} \tag{2}$$

where σ is pile-end soil resistance; a_b and b_b are load transfer parameters of pile-end soil.

The interaction between pile and soil when loaded could be illustrated as shown in figure 3. Taking a differential segment of the pile, from the equilibrium condition, one obtains:

$$\frac{dP(z)}{dz} = -u_p \tau\ (z) \tag{3}$$

where u_p is the circumference of pile.

The compression produced in the element is,

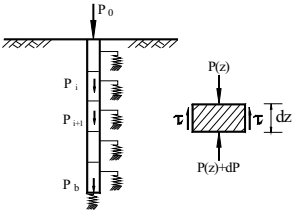

FIG. 3. Interaction model between pile and soil.

Or

$$ds = -\frac{P(z)}{EA}dz \tag{4a}$$

$$\frac{dS}{dz} = -\frac{P(z)}{E \cdot A} \tag{4b}$$

where E is the elastic modulus of the pile, and A is the cross-section area of the pile. By means of

$$\frac{dP(z)}{dz} = \frac{dP(z)}{ds}\frac{ds}{dz} \tag{5}$$

Obtain:

$$\frac{dP(z)}{ds} = \frac{dP(z)}{dz}\frac{dz}{ds} \tag{6}$$

Substituting Equations (3) and (4) into Equation (6), yields:

$$\frac{dP(z)}{ds} = \frac{u_p EA}{P}\tau \tag{7}$$

Substituting the Equation (1) into the Equation (7) and let $\lambda = u_p \cdot E \cdot A$, then obtain:

$$dP = \frac{\lambda}{P}\alpha\left(1 - e^{-\beta s(z)}\right)ds \tag{8}$$

Change Equation (8) into increment form:

$$\Delta P = \frac{\lambda}{P}\alpha\left(1 - e^{-\beta s(z)}\right)\Delta S \tag{9}$$

Equation (9) is just the iteration model for solving the load-settlement relationship of single pile.

ITERATION METHOD

Assume the pile penetrating through two different layers of soil with corresponding length and transfer parameters as shown in Figure 4. The load transfer function parameters of the soil beneath the pile are a_b and b_b. Under the applied load P_0 on the pile top, the settlement of the pile top is S_0. The settlement of the pile end is S_b.

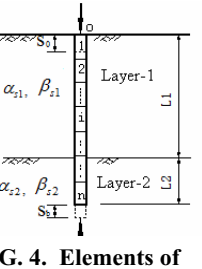

FIG. 4. Elements of assumed pile.

With an assumption of initial settlement of S_b and based on Equation (2), we have:

$$R_b = A \cdot \sigma = \frac{A \cdot S_b}{a_b + b_b \cdot S_b} \tag{10}$$

According to the Equation (1), find the *nth* segment surface resistance of the pile (note that in Figure 4, the *nth* segment is in the second soil layer). That is

$$\tau_n = \alpha_{s2}(1 - e^{-\beta_{s2} S_b}) \tag{11}$$

From Equation (11), obtain:

$$\Delta P_n = u_p \cdot \Delta\, l_n \cdot \tau_n \tag{12}$$

and

$$P_n = R_b + \Delta P_n \tag{13}$$

From Equation (13), we have the average axial force for the segment *nth*,

$$\overline{P_n} = \frac{R_b + P_n}{2} = R_b + \frac{\Delta P_n}{2} \tag{14}$$

and from Equation (14), we find the elastic compression and pile settlement at the top of the *nth*, segment

$$\Delta S_n = \frac{\overline{P_n}}{E \cdot A} \Delta\, l_n \tag{15}$$

and,

$$S_n = S_b + \Delta S_n \tag{16}$$

Then, by substituting the calculated results P_n , S_n and ΔS_n into Equation (9) and conducting iterations on the segment *nth*, we can obtain corresponding results:

$$\Delta P_n^{'} = \frac{\lambda}{P_n} \alpha_{s2}(1 - e^{-\beta_{s2} S_n}) \Delta S_n \tag{17}$$

$$P^{'}_n = R_b + \Delta P^{'}_n \tag{18}$$

$$\overline{P}_n^{'} = R_b + \frac{\Delta P^{'}_n}{2} \tag{19}$$

$$\Delta S^{'}_n = \frac{\overline{P^{'}_n}}{E \cdot A} \Delta\, l_n \tag{20}$$

$$S^{'}_n = S_b + \Delta S^{'}_n \tag{21}$$

The values of $\Delta P^{'}_n, P_n^{'}, \Delta S_n^{'}$ and $S_n^{'}$ obtained from the above equations are different from ΔP_n, P_n , ΔS_n and S_n . Therefore, iterations are taken into account. Every time we substitute the calculated $P_n^{'}$, $\Delta S_n^{'}$ and $S_n^{'}$ for P_n , ΔS_n and S_n , respectively in Equation (17) and find new $P_n^{'}$, $\Delta S_n^{'}$ and $S_n^{'}$. Until the desired accuracy, e.g., within 5% errors, is achieved, and the results are acceptable. Now, the real axial force and settlement of *nth* segment could be obtained by Equations (18–21). These values are also the same as the internal force and settlement at the end of the (*n*-1)*th*. Segment.

Substituting P_n and S_n as the internal force and settlement of the (n-1)*th* segment into Equations (11-21), using the same iteration procedure for the (n-1)*th* segment, we can find P_{n-1} and S_{n-1} , … and so on, until we find P_0 and S_0 . It should be noted that at different soil layers, one should use different α_s and β_s (such as α_{s1}, β_{s1}, α_{s2}, β_{s2}, …… α_{sn}, β_{sn})

Thus, for a given S_b, we can calculate the pile top load P_0 and settlement S_0 and plot the load-settlement P-s curve.

EXAMPLE AND ANALYSIS

The diameter and length of the pile considered by Carrubba is 1.2 m and 18.5 m respectively; pile depth in the soil is 11 m, and in the rock is 7.5 m. The load transfer function parameters: in soil, $\alpha_s = 0.07\,MN/M^3$ $\beta_s = 228MPa$; in rock, $\alpha_r = 0.131\,MN/M^3$ $\beta_r = 340MPa$; at the end of the pile, $1/a_b = 220\,MN/M^3$ $1/b_b = 5.3MPa$; Young's modulus E=31500 MPa. The results calculated by the proposed method and the test data obtained by Carrubba are presented in Fig. 5 for comparison purposes.

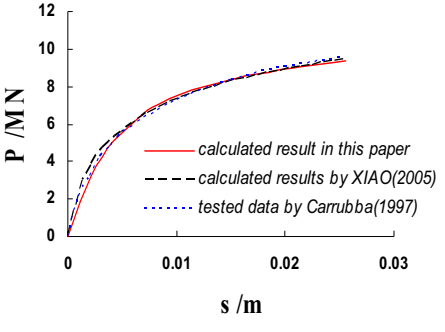

FIG. 5. Load-settlement curve.

From the Fig. 5, it can be seen that the both load-settlement curves for the pile calculated by the proposed method and Xiao's method are very close to those obtained by Carrubba. Therefore, the example verifies the validation and high accuracy of the proposed method. The parameters α and β, could be obtained by shear friction tests of undisturbed soils at different layers, and the load transfer parameters a_b and b_b of pile end soil could be initially referred with compression test results in door and subsequently modified by fitting the Carrubba's (1997) pile head displacements to computer simulation ones. It is noted that the parameters are also related to vertical stress varying at different depth. The present analysis are based on the results data in Paolo and Xiao's research obtained through the corresponding tests of soil samples at middle depth of soil and rock layer (Xiao, 2005).

CONCLUSIONS

A simple exponential load transfer function for evaluating skin friction at pile-soil interface has been established from a reduced scale pile model test and verified by Xiao's example (2002). The function is then implemented into differential equation of pile-soil interaction, obtaining an analytical formula for calculating the *P*-s curve. By

solving the analytical formula, iteration process automatically run by simple computer program is adopted and the results are in good agreement with Xiao H.B.(2005) and Carrubba (1997).

ACKNOWLEDGMENTS

The funding for the research presented in this paper was provided by National Science Foundation of China (No.50378097)

REFERENCES

Carrubba, Paolo. (1997). "Skin friction of large-diameter piles socketed into rock" *J. of Can. Geotech,* Vol. 34, pp. 230-240.

Aschenbrener, T. B. and Olson, R.E. (1984). "Prediction of settlement of single pile in clay. "*Proc. of Symposium by ASCE Geotech.*, edited by J.R. Meyer: 41-58.

Duncan JM, Chang CY. 1970. "Nonlinear analysis of stress and strain in soils. " *Journal of the Soil Mechanics and Foundations Division ASCE*, Vol. 96 (5): 1629–1653.

Wei Dong Guo, Mark F.Randolph. (1998). "Rationality of load transfer approach for pile analysis. " *Computers and Geotechnics*, No.23: 85-112

Randolph, M. F., Wroth, C. P.(1978). "Analysis of deformation of vertically loaded piles. " *J. Geotech. Eng. Div. ASCE*, Vol. 104(12): 1465-1487

Pells,P.J.N and Turner,R.M. (1997). "Elastic solution for the design and analysis of rock-socketed piles. " *J.of Can. Geotech* , No.16: 481-487

Kezdi, A. (1957) "The bearing capacity of piles and pile groups. " *Proceedings, 4th International Conference on Soil Mechanics and Foundation Engineering*, London, Vol. 2: 46 - 51

Vijayvergiya, V. N.(1977). "Load - movement characteristics of piles. " *4th Symposium of Waterway, Port, Coastal and Ocean Division, ASCE* , Long Beach , Calif, Vol.2 : 269-284

Seed H B and Reese L C. (1955). "The Action of Soft Clay Along Friction Piles. " *Trans. ASCE*, Vol.122: 731-754

Xiao H B, and Luo Q Z, et al. (2002). "Prediction of load-settlement relationship for large-diameter piles. " *The Structural Design of Tall Buildings*, Vol 11(4):241-258.

XIAO Hongbin. (2005). "Theoretical and Application Research on Load Transfer of Vertically Loading Large Diameter Piles. " Central South University (in Chinese)

Zhang C.S., XIAO H.B., Zeng Q.G., and Fan Z.H.(2007). "Law of pile in expansive soils with introduction of water". *Proceedings of GEO-CHANGSHA 2007, International Conference on Geotechnical Engineering*, p431-439

The Characteristic of Vertical Stress in the Fill of Piled Embankments

Yu Chuang[1] , Liu Songyu[2] , Pan Linyou[3] and Cai Yuanqiang[4]

[1]Lecturer, College of Architecture and Civil Engineering, Wenzhou University, Zhejiang Wenzhou, China, 325035; geoyuchuang@hotmail.com

[2]Director, Institute of Geotechnical Engineering, Southeast University, Jiangsu Nanjing, China, 210096; liusy@seu.edu.cn

[3]Professor, College of Architecture and Civil Engineering, Wenzhou University, Zhejiang Wenzhou, China, 325035; ply51204@yahoo.com.cn

[4]Professor, College of Architecture and Civil Engineering, Wenzhou University, Zhejiang Wenzhou, China, 325035; caiyq@zju.edu.cn

ABSTRACT: Piled embankments has technical and economical advantages over other soft ground improvement methods. The load transfer mechanism in piled embankments is referred to as arching effect. Piled embankments are generally related to the advantage of soil arching effects of granular soil. Most of present research on piled embankments is focusing on the soil arching effect, but there is lack of investigation on the vertical stress distribution in the inner soil arching under embankments. In this paper a new analytic solution called multi-arching theory is applied to investigate the behavior of soil arching. The solution shows the stress distribution in piled embankments as follows; the vertical stress above the soil arching increased as geostatic state, and inside of the soil arching the vertical stress decreased nonlinearly, which reflects the mechanism of soil arching effect and the vertical stress distribution in piled embankments. The theoretical solutions show good agreements with model test data. The results demonstrate that the distribution of vertical stress in embankments is helpful in understanding the behavior of piled embankments.

INTRODUCTION

The increasing need of infrastructure development has often forced engineers to deal with building on soft soils. Infrastructure constructions such as road and railway embankments, bridge approach and flood protection dam on soft soils have raised several concerns related to excessive total and differential settlements, bearing

capacity failures, lateral pressure and movement and stability of the embankment (Kempfert 2004; Chen 2008; Yu 2006; Liu 2007). These challenges have led to significant development in soil improvement and reinforcement techniques, which show economic solutions for constructions over soft soils. One of the techniques is called piled embankment. Piled embankments are referred to as conventional piles-supported embankment and geosynthetic-reinforced and piles-supported embankment if geosynthetic reinforcement is used in the system (Han 2002).

The design of geosynthetic-reinforced and piles-supported embankment includes the assessment of pile group capacity, embankment load transfer and geosynthetic tensile strength requirement. The mechanism of embankment load transfer to the piles is assumed to occur through the so-called soil arching effect and geosynthetic tension, which will be discussed in detail in this paper.

SOIL ARCHING IN PILED EMBANKMENTS

For conventional piled embankments, piles are required to be closely spaced which is generally around 2 to 5 times the pile diameter in the pile foundation design. Moreover, large pile caps are needed in order to transfer more embankment loads to pile caps and to prevent settlements of the soil between caps being reflected to the embankment surface. On the other hand, to reduce the construction cost, pile spacing needs to be enlarged as wide as possible. Therefore a suitable pile cap size is chosen to ensure that most of the embankment load is transferred to piles.

The embankment fill mass between pile caps, under the influence of its weight, has a tendency to move downward due to the presence of soft foundation soil. Shear resistance from the fill above the pile caps restrains this movement. The shear resistance reduces the pressure acting on the soil between pile caps but increases the load applied on to the pile caps. This load transfer mechanism is referred to as arching effect.

A definition of arching is given by McNulty as “the ability of a material to transfer loads from one location to another in response to a relative displacement between the locations. A system of shear stresses is the mechanism by which the loads are transferred”. When a soil mass is placed on a rigid base, no tendency of differential movement exists so soil arching does not develop. The moment when the soil loses a local support, a true arch or a roof tension arch is formed.

There are several methods for assessing the soil arching effect suggested by researchers such as Terzaghi (1943), Marston and Anderson (1913), Carlsson (1987), and Hewlett and Randolph (1988). Some of them are used in the available design guidelines for piled embankment construction such as BS 8006 in the UK, FHWA in USA and Nordic guidelines in Scandinavian countries. All assessment methods for the soil arching effect consider that the arching is a uniform and simple model. These assumptions will obviously not give a precise solution for the vertical stress in the fill

of embankment. Moreover, the present solution cannot reflect the behavior of vertical stress along the depth of embankments. In this paper, a new modified model is applied to investigate the characteristic of vertical stress in the fill of piled embankments.

MULTI-ARCHING MODEL

Kempfert et al. (1997) adopted the Hewlett and Randolph (1988) approach, with a modification for low-height embankments and for inclusion of subgrade support based on bearing capacity analysis. Like the Hewlett and Randolph Method (1988), Kempfert et al. considered a domed arch spanning between columns or pile caps. The soil arching model is expressed as a function considering the depth z , and the boundary condition of this model is shown as Eq. 1.

$$r_{z=s_d/2} = s_d/2 \quad r_{z\to 0} \to \infty \tag{1}$$

And the function of r_z is given as Eq. 2, (Yu, 2006).

$$r_z = \frac{\lambda_1}{z} + \lambda_2 \cdot z \tag{2}$$

Where $\lambda_1 = \frac{1}{8}(s_d - d)^2$; $\lambda_2 = \frac{s_d^2 + 2d \cdot s_d - d^2}{2 \cdot s_d^2}$, d is the size of piles (caps) ,s_d is the net spacing between piles, the other symbols are shown in Fig. 1.

As shown in Fig. 1, according to the vertical equilibrium, the following governing equation can be obtained.

$$-\sigma_z \cdot dA_u + (\sigma_z + d\sigma_z) \cdot dA_o - 4\sigma_\varphi \cdot dA_s \cdot \sin\left(\frac{\delta\varphi_m}{2}\right) + \gamma dV = 0 \tag{3}$$

Where:

$$dA_u = (r \cdot \delta\varphi)^2 \quad ; \quad dA_O = (r + dr)^2 \cdot (\delta\varphi + d\delta\varphi)^2 \approx 2d\delta\varphi \cdot r^2 \cdot \delta\varphi + 2dr \cdot r \cdot \delta\varphi^2 + r^2 \cdot \delta\varphi^2$$

$$dA_S = (r + \frac{1}{2}dr) \cdot (\delta\varphi + \frac{1}{2}d\delta\varphi) \cdot dz \approx dz \cdot r \cdot \delta\varphi$$

$$dV = (r + \frac{1}{2}dr)^2 \cdot (\delta\varphi + \frac{1}{2}d\delta\varphi)^2 \cdot dz \approx dz \cdot r^2 d\delta\varphi^2$$

$$d\delta\varphi_m = \delta\varphi + \frac{\delta\varphi}{2} \qquad \text{and} \qquad \sigma_\varphi = \xi \cdot K_p \cdot \sigma_z$$

ξ is modified coeffient and the other sybmols are shown in Fig. 1.

The solution of vetical stress of soil between caps is as below:

$$\sigma_z[z] \approx (\lambda_1 + t^2 \cdot \lambda_2)^{-x} \cdot (\lambda_1 + z^2 \cdot \lambda_2)^{-x} \cdot \left\{ \begin{array}{l} (h-t) \cdot \gamma + \dfrac{(t-z) \cdot \gamma \cdot (\lambda_1 + t^2 \cdot \lambda_2)^x \cdot (\lambda_1 + \dfrac{t^2 \cdot \lambda_2}{4})^{-x}}{s_d \cdot (4 \cdot \lambda_1 + t^2 \cdot \lambda_2)} \cdot \\ \dfrac{\left[4 \cdot s_d \cdot \lambda_1 + t \cdot (-2 \cdot d \cdot (\xi \cdot K_p - 1) z) + s_d \cdot t \cdot \lambda_2\right]}{s_d \cdot (4 \cdot \lambda_1 + t^2 \cdot \lambda_2)} \end{array} \right\}$$

(4)

where:

$k_p = \tan^2(45° + \dfrac{\varphi'}{2})$, $t = \begin{cases} h & \text{when } h < s_d/2 \\ s_d/2 & \text{when } h \geq s_d/2 \end{cases}$, γ is unit weight of the embankment fill, h is height of embankment, $\chi = \dfrac{d(k_p - 1)}{\lambda_2 \cdot s_d}$.

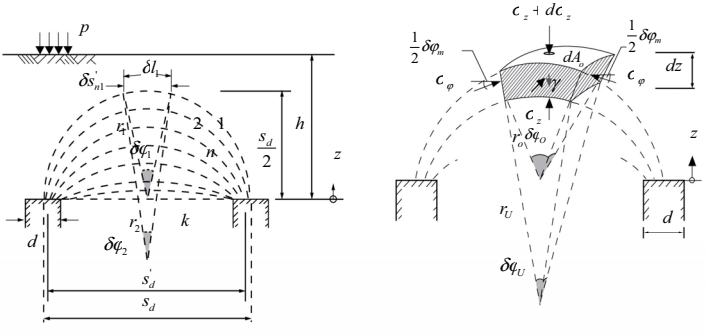

FIG. 1. Multi-arching model.

THE VERIFICATION OF MULTI-ARCHING THEORY

Model Test I

Three-dimensional well-instrumented model tests in a scale of 1:3 were carried out to investigate the stress field of the fill in piled embankments. A group of four piles was placed in a weak soil of peat in a rectangular grid, above which a reinforced or unreinforced sand fill was placed in different heights, which are 0.35 m and 0.70 m. On these two cases with different height, three uniform static loads 20 kPa, 54 kPa and 104 kPa were place at the top of embankments. The stress distribution in the reinforced sand layer was recorded by pressure cells, which are buried along different depth in the center of the embankment. The multi-arching theory is used to compute the vertical stress of the fill under different loads, which are shown in Fig. 2. From the

measured data, we find out that the vertical stress decreases with depth at the soil arching area. The results demonstrate that the comparison between measured and calculated stresses is good at 0.35 m embankment. And the distribution of vertical stress along depth is simulated very well using the soil arching theory. But there is a little difference between measured and computed results due to stress level. The model test results verified the load transfer and the soil arching theory in piled embankments. And the theory presented in this paper simulates the results and reflects the behavior of soil arching very well.

Model Test II

Hewlett et al. (1988) investigated the load ratio carried by piles using model test of piled embankments. The size of model test is as follows: a/s=1/3, *H*/*s*2, where a is the size of piles, H is the height of embankment and s is pile spacing. Fig. 3 gives the ratio changes with the angle of internal friction of the fill. The load ratio carried by piles is found to increase with the increase of K_p, which is passive pressure coefficient. The solution by Hewlett and the multi-arching method are demonstrated in the figure. It could be concluded that the multi-arching's solution is closer to the measured data than the Hewlett's method.

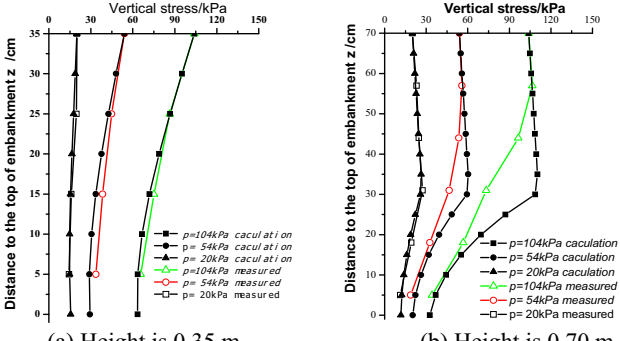

(a) Height is 0.35 m (b) Height is 0.70 m

FIG. 2. Comparisons between measured and calculated results.

CONCLUSIONS

Most of present researches for piled embankments are focusing on the soil arching effect, and there is lack of investigation of the stress distribution in the inner soil arching under embankments. The current analytical procedures for assessing soil arching effect are too simplified in the model. In this paper, a more accurate model called Multi-arching theory is applied to investigate the behavior of soil arching. The computed results show good agreements with measured data. The results demonstrate

that the distribution of vertical stress along the depth in embankment fills, which is helpful to understand the behavior of piled embankments.

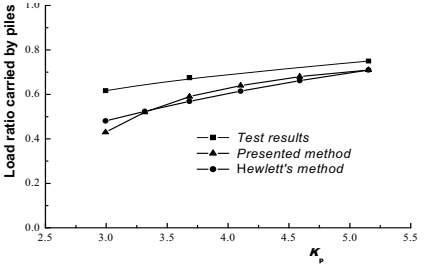

FIG. 3. Comparisons between measured and calculated results.

ACKNOWLEDGMENTS

The authors appreciate the support of the research project of Ministry of Housing and Urban-Rural Development ,China.

REFERENCES

BS8006.(1995). Code of practice for strengthened/reinforced soils and other fills, *British Standard Institution*.

Carlsson, B. (1987). Reinforced soil, principles for calculation. Terratema AB, Linköping.

Chen Yun-min, Cao Wei-ping,Chen Ren-peng. (2008). An experimental investigation of soil arching within basal reinforced and unreinforced piled embankments. *Geotextiles and Geomembranes*, Vol. 26(2),164-174.

Han, J. and Gabr, M.A. (2002) A numerical study of load transfer mechanisms in geosynthetic reinforcedand pile supported embankments over soft soil. *Journal of Geotechnical and Geoenvironmental Engineering, ASCE*, Vol.128(1), 44-53.

Hewlett, W.J. and Randolph, M.F. (1988). Analysis of piled embankments. *Ground Engineering,* Vol.21(3), 12-18.

Kempfert, H.-G., Stadel, M. Zaeske, D. (1997).Design of geosynthetic-reinforced bearing layers over piles. *Bautechnik*, 74(12), 818-825.

Liu, H.L, Ng. Charles W.W, Fei K.(2007). Performance of a geogrid-reinforced and pile-supported highway embankment over soft clay: Case study. *Journal of Geotechnical and Geoenvironmental Engineering*, Vol.133(12),1483-1493.

Marston, A. and Anderson, A.O. (1913). The theory of loads on pipes in ditches and tests of cement and clay drain tile and sewer pip. Bulletin No. 31, Iowa Engineering Experiment Station, Ames, Iowa.

Terzaghi, K. (1943). Theoretical soil mechanics, John Wiley & Sons, New York.

Yu Chuang.(2006).Theory and application of rigid pile composite foundation under embankment loads. A dissertation submitted to Southeast University, Nanjing.

Dynamic Finite Element Analysis of Micropile Foundation in Subgrade

Wang Zhaoyu [1,2], Mei Guoxiong [3], Cai Guojun [4], and Yu Xinbao [5]

[1]PhD student, College of Civil Engineering, Nanjing University of Technology, Nanjing, China; zywang518@yahoo.com
[2]College of Civil Engineering, Yancheng Institute of Technology, Yancheng, China; zywang518@yahoo.com
[3]Professor, College of Civil Engineering, Nanjing University of Technology, Nanjing, China; mgx@163.com
[4]PhD student, College of Civil Engineering, Southeast University, Nanjing, China; focuscai@163.com
[5]PhD student, Civil Engineering Department, Case Western Reserve University, Cleveland, OH 44102, USA; yuxinbao@yahoo.com.cn

ABSTRACT: The effect of micropiles on soil reinforcement under static and dynamic loadings was studied. Embankment on untreated soil and treated soil by micropiles were modeled using the finite element code PLAXIS. The displacement caused by embankment static loading and acceleration of the embankment caused by seismic loading were calculated and compared. It was found that micropiles treated soil can greatly reduce the settlement of the embankment and mitigate seismic response of the embankment. The results of this study provide valuable information about the design and application of micropiles.

INTRODUCTION

Micropiles are small diameter grouted piles that are traditionally used in foundation retrofit. Micropiles can also be installed in almost any ground condition. Experimental evidence has indicated that micropiles behave well under seismic loadings due to their high flexibility. Moreover, observations in the 1995 Kobe Earthquake demonstrated the good performance of friction piles under seismic loading (Wong, J.C.,2004). However, the seismic behavior of micropiles is not fully understood due to limited number of tests both in full and model scale, as well as the limited amount of numerical modeling studies for micropiles. Some researchers such as Yamane,T. et al. (2000), Wong, J.C.(2004), Shanzhi Shu.(2005) and Wang, Liyan et al.(2005) have studied on mechanical characteristics of micropiles. The dynamic analysis of soil-pile-structure interaction is a very complex problem (Nogami,T.et al.,1992; Wu,guoxi et al.,1997; Boulanger, Ross W. et al.,1999; Lok,M.H.,1999; Ousta,R.et al.,2001; and Surendran Balendra, 2005). The Finite Element (FE) method provides a tool to understand the seismic behavior of micropiles. The finite element code PLAXIS with

dynamic analysis function has been used to model the soil and micropiles system, and analyze the dynamic characteristics of unreinforced soil and micropile reinforced foundation.

THE STATIC ANALYSIS OF MICROPILES

The finite element model for insitu four soil layers strata was generated. The soil including fill was treated as perfectly elastic-plastic materials in the simulation. Parameters of soil used in the simulation are listed in the Table 1.

Table 1. Soil Properties for the Micropile Foundation Analysis

Soil Type	Unsaturated Unit Weight (kN/m^3)	Saturated Unit Weight (kN/m^3)	Cohesion (kN/m^2)	Friction Angle (degrees)	Young's Modulus (kN/m^2)	Possi-on's Ratio
Fill	16	20	1	30	8000	0.3
Clay Silt	16	18	5	25	10000	0.35
Soft soil	17	18.5	7	20	5000	0.35
Coarse Sand	17	20	1	34	30000	0.3

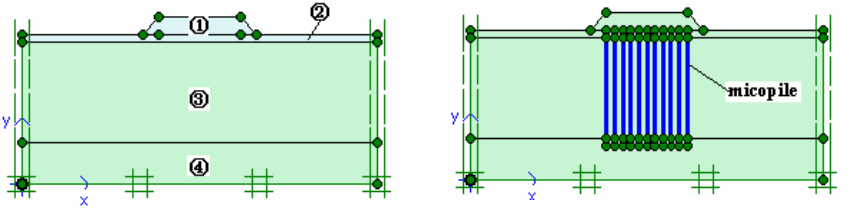

a. Untreated by micropiles **b. Treated by micropiles**

FIG. 1. Problem Setting and the FEM Model.

The micropiles with diameter of 0.2 m and length of 14 m were modeled using the 5-node beam element. The interactions between the soil and the piles were taken into account by setting interface elements between the soil and the pile. In formulating the stress-strain behavior at the soil- pile interface, the thickness of interface was assumed as 0.1 to 0.01 times the length of corresponding interface element. The corresponding strength reduction factors were selected based on both the material properties of the soil and the pile.

The boundary conditions were set as the standard boundary conditions. The displacements in all directions at the bottom boundary were fixed; the boundaries at both sides can only move in the vertical direction. When the geometry and boundary condition setting was complete, the finite element mesh was generated. In order to consider the possible large stress gradient, the meshes are refined at the soil and pile interface.

The total deformation of the embankment is shown in Figure 2. Figure 2(a) shows that the total displacement profile for the whole geometry in the last times step; the maximum displacement at this time step is 33.24 $\times 10^{-3}$ m. Figure 2(b) shows the maximum displacement in the last time step is 10.35 $\times 10^{-3}$ m. The displacement plot shows the maximum displacement at the top of embankment which is untreated is much higher than the displacement at the top of embankment which is reinforced by micropiles. The result shows that micropiles treated soil can greatly reduce the settlement of the embankment.

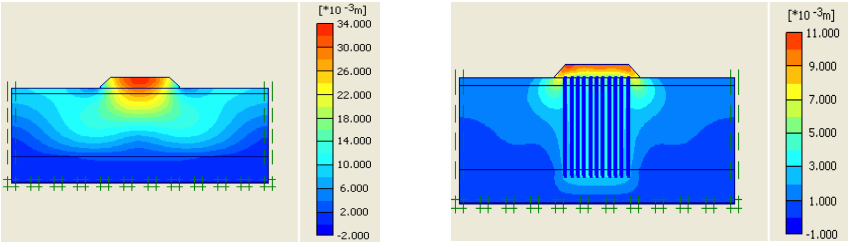

a. Untreated by micropiles **b. Treated by micropiles**

FIG. 2. FEM plot of extreme total displacement.

THE DYNAMIC ANALYSIS OF MICROPILES

The dynamic analysis uses the same geometry as that of the static analysis. The triaxial unloading stiffness E_{ur} is set as 3 times as the triaxial loading stiffness E_{ref} and the oedometer loading stiffness E_{oed} is set the same as the triaxial loading stiffness E_{ref}. The corresponding shear modulus G and p-wave velocity V_p and s-wave velocity V_s are determined based on theories of continuum mechanics and wave propagation:

Table 2. P-wave and S-wave Velocity of Soil

Soil Type	V_p(m/s)	V_s(m/s)
Fill	81.22	43.41
Clay Silt	99.15	47.63
Soft soil	68.01	32.67
Coarse Sand	152.6	81.56

$$V_p = \sqrt{\frac{E_{oed}}{\rho}} \quad \text{where} \quad E_{ode} = \frac{(1-\nu)E}{(1+\nu)(1-2\nu)} \tag{1}$$

$$V_s = \sqrt{\frac{G}{\rho}} \quad \text{where} \quad G = \frac{E}{2(1+\nu)} \tag{2}$$

The boundary conditions were changed to the standard earthquake boundary that was automatically generated as absorbent boundaries (Plaxis, 2002). The left-hand and right-hand boundaries have prescribed displacement u_x = 0.01 m and the bottom boundary has prescribed displacement u_y =0.00 m.

The material damping was considered for the soil. In PLAXIS, a global material damping term (the Rayleigh damping) is assumed, which is proportional to the mass and stiffness of the system. The damping matrix can be written as a combination of the mass matrix and the stiffness matrix:

$$[C] = \alpha[M] + \beta[K] \tag{3}$$

where $[C]$ is damping matrix $[M]$ is mass matrix $[K]$ is stiffness matrix

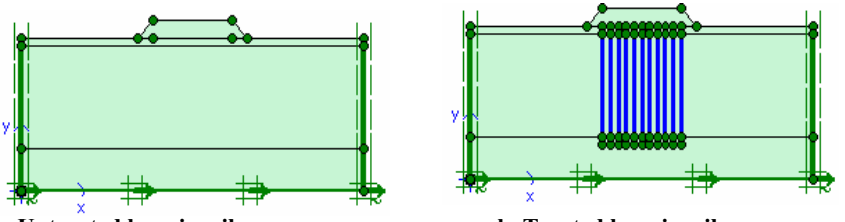

a. Untreated by micopiles **b. Treated by micopiles**

FIG. 3. FEM Dynamic Model.

The Rayleigh coefficients αand βare difficult to determine from soil tests. Based on previous literatures, they can be estimated from the fundamental frequency of the pile-soil system and the hysteretic damping ratio. However, this information was not available for such purpose in this example. The Rayleigh coefficients were assumed as α= 0.01 for mass matrix and β= 0.01 for the stiffness matrix. Since there is lack of recorded strong ground motions, the default ground motion file named 225a.smc (see FIG. 4.) in PLAXIS is set as the rock base ground motion(Plaxis, 2002). The calculation was carried out to 250 time steps with a time interval 10 seconds.

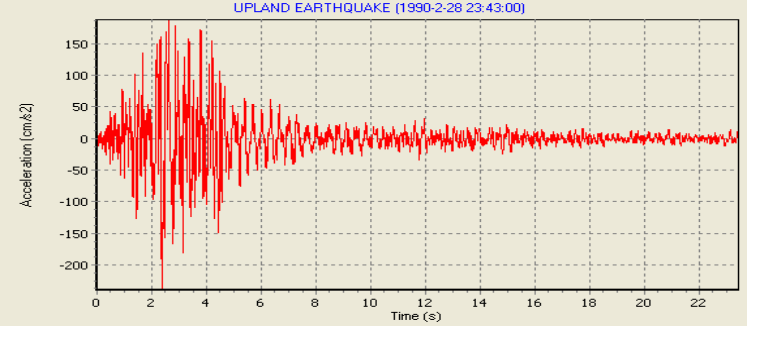

FIG. 4. Record of upland earthquake.

Figure 5 and Figure 6 show time-acceleration curves of point in the middle of the embankment. Figure 5 shows that the maximum acceleration at point E (22, 9) is 1.466 m/s^2 for embankment on untreated soils and 1.065m/s^2 for embankment treated by micropiles.

By comparing Figure 5 and Figure 6, it is found that the acceleration at point E (22, 9) of the untreated embankment is much higher than the treated embankment. The result shows that the piles are effective in increasing the earthquake resistance of soil.

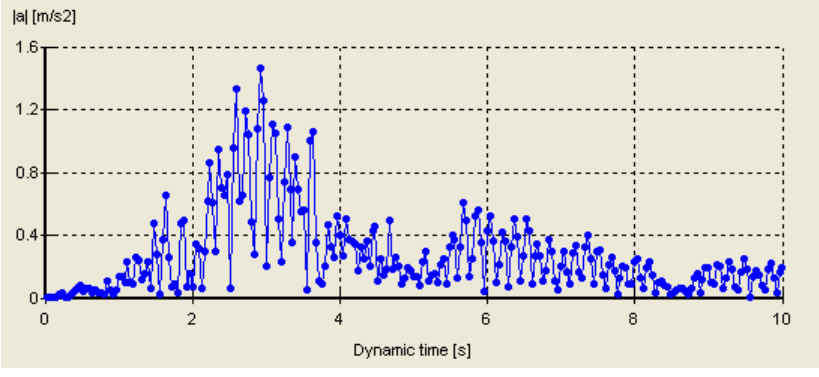

FIG. 5. Time-acceleration curves of E Point before the soil treatment.

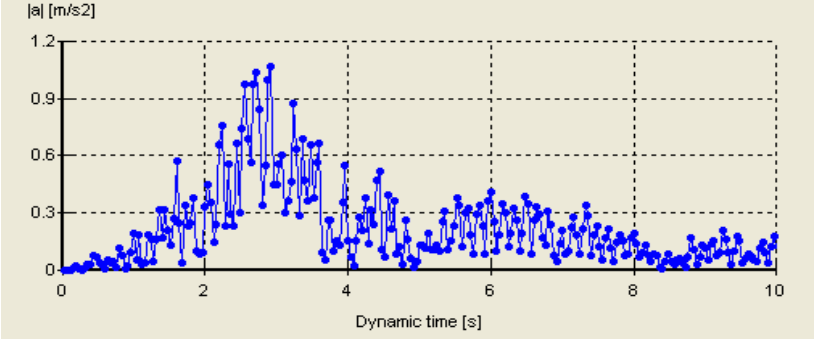

FIG. 6. Time-acceleration curves of E Point after the soil treatment.

CONCLUSIONS

The displacements and dynamic characteristics of pure soil foundation and micropiles reinforced foundation were analyzed using finite element code PLAXIS. The displacement caused by embankment static loading and acceleration of the embankment caused by seismic loading were calculated and compared. It is found that

micropiles treated soil can greatly reduce the settlement of the embankment and mitigate seismic response of the embankment. The results of this study provide valuable information about the design and application of micropiles.

ACKNOWLEDGMENTS

The authors appreciate the support of the National Natural Science Research Foundation of China (50608038).

REFERENCES

Boulanger, Ross W. and Curras, Christina J.(1999). "Seismic soil-pile-structure interaction experiments and analyses."*Journal of Geotechnical and Geoenvironmental Engineering*:750-759.

Lok, M.H. (1999). "Numerical modeling of seismic soil-pile-superstructure-interaction in soft clay." Ph.D. Thesis. University of California, Berkeley.

Nogami, T., Otani, J., Konagai, K., and Chen, H. L. (1992)."Nonlinear soil-pile interaction model for dynamic lateral motion." *Journal of Geotechnical Engineering*, ASCE, 118(1): 89-106.

Ousta,R.,and Shahrour,I. (2001). " Three-dimensional analysis of the seismic behavior of micropiles used in the reinforcement of saturated soil." International Journal for Numerical and Analytical Methods in Geomechanics, Vol. 25: 183-196.

Wu,guoxi and Finn,Liam W.D.(1997). "Dynamic nonlinear analysis of pile foundations using finite element method in the time domain", *Canada Geotech. Journal*, Vol. 34:44-52.

Wong, J.C. (2004). "Seismic behavior of micropiles." M.S. Thesis. Washington State University, Pullman, WA.

Wang,Liyan,Yuan,Xinming.(2005)."Decline and dynamic characteristics of micropiles reinforced foundation. " *Journal of Hydraulic Engineering*,Vol. 12 (9): 1193-1199.

Surendran Balendra(2005)."Numerical modeling of dynamic of dynamic soil-pile-structure interaction." M.S. Thesis. Washington State University, Pullman, WA.

Shanzhi Shu.(2005)."Sand State and Performance Analysis of Micropiles."M.S. Thesis. Washington State University, Pullman, WA.

Yamane, T., Nakata, Y., and Otani, Y. (2000). "Efficiency of micropile for seismic retrofit of foundation system." 12th World Conference on Earthquake Engineering, Auckland, New Zealand:1-8.

Theoretical and Experimental Study on the Vertical Bearing Behavior of Super-Long Filling Piles in Soft Soil Area

ZOU Xin-jun[1] and ZHAO Ming-hua[2]

[1]Professor. College of Civil Engineering, The Hunan University, Changsha, Hunan 410082, P.R. China. xjzouhd@yahoo.com.

[2]Professor. College of Civil Engineering, The Hunan University, Changsha, Hunan 410082, P.R. China. mhzhaohd@yahoo.com.

ABSTRACT: Based on the vertical static load test results on a test pile, located in the soft soil, the load transfer mechanism and bearing behavior of super-long filling piles is first discussed. Then, a method of predicting the axial bearing capacity of super-long piles by the pile top settlement is advised. By introducing the linear elastic-fully plastic model and tri-broken-line model to fit the development of shaft resistance and tip resistance respectively, analytical solutions of axial load capacity is derived under elastic stage of the subsoil. Finally, the present method is applied to analyze the data from the test pile, from which good agreement between the predicted and measured pile top load-settlement curves is found. The results also show that buckling stability analysis and deformation checks are necessary for super-long filling piles, and the axial bearing capacity of super-long piles should be controlled by the allowable settlement on the pile top.

INTRODUCTION

The specific definition of super-long filling piles is not clear so far, but it generally refers to piles whose length is more than 50 m or length to diameter ratio (l/d) is 100 (Lin et al., 1999), and the bearing capacity is mainly due to shaft resistance. Due to the super length, this kind of piles behaves quite differently. Under normal working load, the tip resistance of super-long pile is only a small portion of the total capacity and can be neglected. In addition, studies by Zhu et al (2003) shows that: (i) for a given pile vertical load, if all other factors remain constant, the pile top settlement does not increase with the pile length; (ii) the state of maximum pile shaft resistance or failure of pile shaft structure can be regarded as the ultimate bearing state of the super-long pile. To determine the axial bearing capacity of the super-long pile top settlement is very important (Lu 1981).

In recent years, super-long filling piles are widely used. Nevertheless, due to the complex load transfer mechanism, relevant design methods have not been presented (Poulos 1989; Yang 1998). Therefore, traditional theories have to be adopted in design and calculation. However, for super-long filling piles, the allowable pile top settlement is usually determined by the serviceability criteria of the superstructure and will control the axial load capacity (Zhao 2000; Wang et al. 1999). A large number of pile tests (Shi and Liang 1994) show that, when the *l*/*d* exceeds a certain value, the tip resistance mobilization will decrease or even not mobilize any more. Thus, the validity of calculating the axial load capacity of super-long piles by traditional methods remains to be discussed. Because of these reasons, the piles are generally lengthened to satisfy the bearing capacity in design, but this will lead to unnecessary waste. Fortunately, the load transfer mechanism of super-long piles have already been studied by some researchers (Kraft 1981; Cao 1986).

To discuss the load transfer mechanism and more suitable analysis methods for super-long piles, a field load test was first done on a test pile in the typical soft soil area of Dongting Lakes in China. Then, a method to determine the vertical bearing capacity of super-long piles by the pile top settlement is proposed in this paper.

EXPERIMENTAL STUDY

Test Design

The soil around the test pile is shown in Fig. 1. The test pile with a design diameter of 1.0 m and length of 60 m was formed by stabilized liquid method. A steel pipe of 1.3 m outside diameter, 7 mm wall thickness and 10 m length was used to support the upper unstable segment of the pile bore. The pipe was driven 9.2 m into the ground. The measured thickness of sediment under the pile tip was 50 mm. Anchorage of the counter-force system was provided by a pair of 1.8 m diameter tension piles each with an uplift capacity of about 9 MN (Fig. 2).

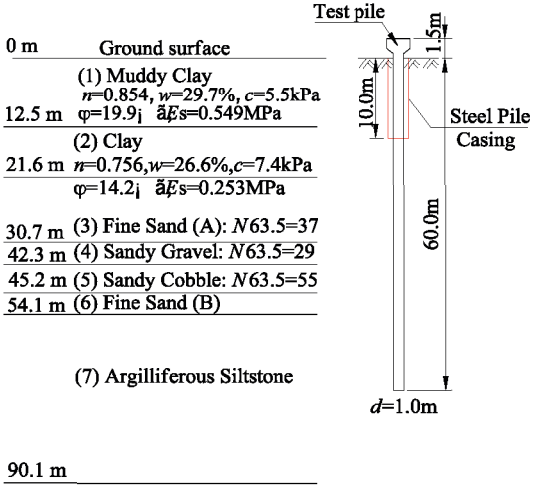

Fig. 1. Soil profile around the test pile.

Four dial gages were placed symmetrically to measure the pile top settlement. Another 2 dial gages are placed around the steel drive pipe on pile top to observe the

settlement of the pipe. In order to determine the distribution of axial force accurately, two kinds of strain gauges, i.e., steel and concrete, were used. In total 34 groups of 136 fully airtight concrete strain gauges were embedded in the test pile.

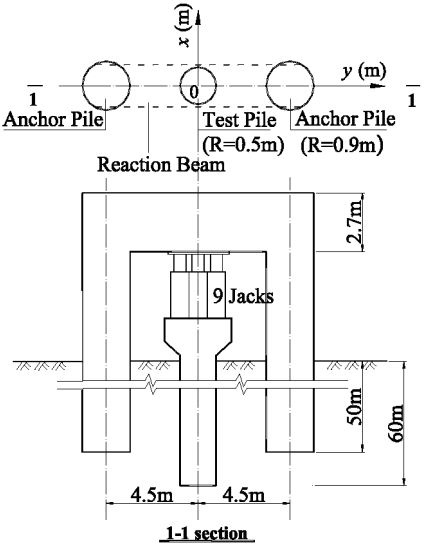

Fig. 2. Sketch of the test equipment.

Test Results

The final steady load on the test pile was 16.72 MN and corresponding top settlement was 35.31 mm. In the loading process, when the load was increased to 17.28 MN, the pile top settlement increased sharply, and exceeded the maximum range of the indicating gauge and could not keep stable. At the same time, the load only kept stable for 3 minutes and then a blare sent out down from the ground. After that, obvious offset of the pile top was observed, and the load decreased from 17.28 MN to 11.00 MN quickly. Furthermore, crack appeared in the ground surface around the pile top. From these, buckling failure of the pile shaft was determined.

The measured pile top load and settlement is shown in Fig. 3. The calculated axial

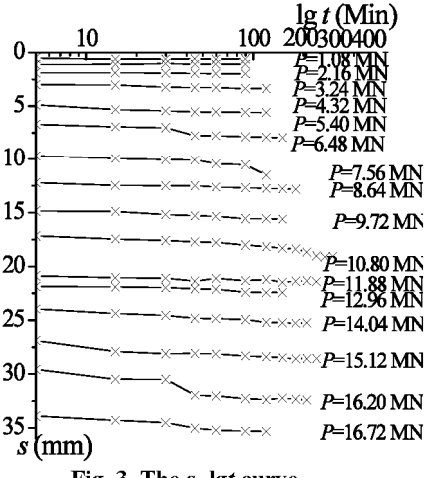

Fig. 3. The *s*~lg*t* curve.

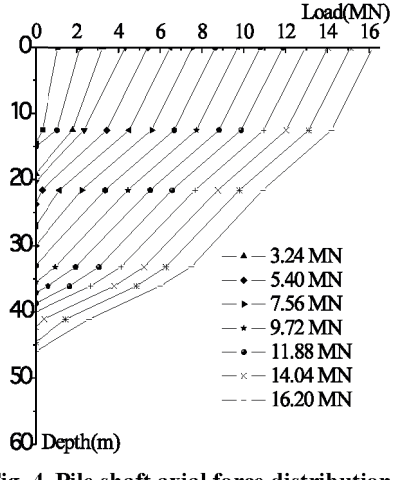

Fig. 4. Pile shaft axial force distribution.

force distribution and shaft resistance τ-relative settlement u curve are shown in Fig. 4 and Fig. 5 respectively. The results indicate that due to the large l/d (=60), the pile was damaged by buckling before any tip resistance developed, and no record was observed from two earth-pressure cells during the test. Even under the failure load, the tip resistance was still almost zero, and it could be neglected.

BEARING CAPACITY OF SUPER-LONG FILLING PILES

Shaft and Tip Resistance Model

In order to fit the development of shaft resistance and tip resistance, the linear elastic-fully plastic model proposed by Kedzi（1965）and tri-broken-line model was adopted with the corresponding constitutive equations defined respectively as:

$$\left.\begin{aligned} \tau_i(z) &= k_{si}u_i & u &< u_{fi} \\ \tau_i(z) &= \tau_{fi} & u &\geq u_{fi} \end{aligned}\right\} \quad (1)$$

Where, k_{si} is the transfer coefficient of shaft resistance in the i^{th} stratum; τ_{fi} is the unit ultimate shaft resistance in the i^{th} stratum; μ_i is the relative settlement in the i^{th} strata; μ_{fi} is the relative settlement strata corresponding to the ultimate shaft resistance.

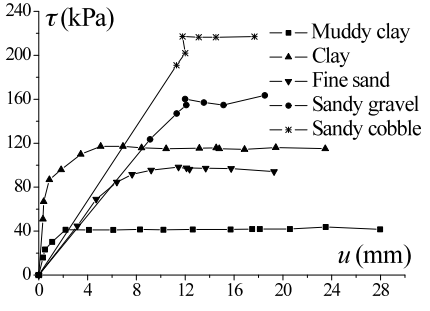

Fig. 5. $\tau \sim u$ curve.

In sedimentary or alluvial plain, shaft resistance is also related to the time of sedimentation and loading on the pile (Sun et al 1984). Time effect of the bearing capacity of super-long pile in soft soil wasn't considered in this paper.

$$\left.\begin{aligned} q_p &= k_{b1}u & u &< \xi_0) \\ q_p &= k_{b1}\xi_0 + k_{b2}(u-\xi_0) & \xi_0 &\leq u < \xi_f \\ q_p &= q_{fp} & u &\geq \xi_f \end{aligned}\right\} \quad (2)$$

Where, k_{b1} is transfer coefficient of toe resistance before the limiting value; k_{b2} is coefficient of bed soil; the ξ_0 is settlement corresponding to the limiting resistance of the sediment under the pile tip; ξ_f is settlement corresponding to the limiting resistance of the bedding soil under the pile tip. These parameters could be obtained by testing or empiric values, generally ξ_0=0.2q_{fp}/k_{b2} (Delpak et al. 2000).

Assumptions and the Control Differential Equation

The following assumptions are made to set up and solve the control differential

equation more easily: 1) The pile shaft material is assumed to be linearly elastic; 2) The buckling failure of the pile shaft should be avoided; 3) Maximum shaft resistance is always reached before tip resistance develops.

Then, based on the load transfer method (Coyle and Reese (1966)), the control differential equation for vertically loaded piles in layered subsoil may be set up as:

$$\frac{d^2u_i}{dz^2} = \frac{k_{si}}{EA}u_i \tag{3}$$

where, E is elastic modulus; A is sectional area; the z is the calculating depth.

As in elastic stage, the tip resistance is not mobilized. The pile shaft was divided into n segments, which equal the number of soil strata around the pile. If the pile top settlement is s_0, the boundary conditions relating to force equilibrium and displacement compatibility between adjacent pile elements were expressed as:

$$\left.\begin{aligned} &u_1\big|_{z=0} = s_0 \\ &EA\frac{du_n}{dz}\bigg|_{z=l_n} = -k_{b1}\,u_n\big|_{z=l_n} \\ &u_i\big|_{z=l_i} = u_{i+1}\big|_{z=l_i}, \qquad (i=1,2,\cdots,n-1) \\ &\frac{du_i}{dz}\bigg|_{z=l_i} = \frac{du_{i+1}}{dz}\bigg|_{z=l_i}, \quad (i=1,2,\cdots,n-1) \end{aligned}\right\} \tag{4}$$

Where the l_i is depth of the i^{th} strata

Then, the solution to Eqn. (3) may be derived as:

$$u_i = c_{1i}\sinh(b_i z) + c_{2i}\cosh(b_i z) \quad (i=1,\ 2,\ \cdots,\ n) \tag{5}$$

Where

$$\left.\begin{aligned} &c_{21} = s_0 \\ &c_{1i}\sinh(b_i l_i) + c_{2i}\cosh(b_i l_i) = c_{1(i+1)}\sinh(b_{i+1}l_i) + c_{2(i+1)}\cosh(b_{i+1}l_i), (i=1,\cdots,n-1) \\ &b_i\left[c_{1i}\cosh(b_i l_i) + c_{2i}\sinh(b_i l_i)\right] = b_{i+1}\left[c_{1(i+1)}\cosh(b_{i+1}l_i) + c_{2(i+1)}\sinh(b_{i+1}l_i)\right] \quad (i=1,\cdots,n) \\ &c_{1n}\sinh(b_n l_n) + c_{2n}\cosh(b_n l_n) = -\beta_1\left[c_{1n}\sinh(b_n l_n) + c_{2n}\cosh(b_n l_n)\right] \end{aligned}\right\} \tag{6}$$

$$b_i = \sqrt{\frac{k_{si}}{EA}}, \quad \beta_i = \frac{k_{bi}}{EAb_n}, \quad (i=1,\ 2) \tag{7}$$

As the soil is in elastic state, $u_i \leqslant u_{f1}$ and the load Q on the pile top is:

$$Q = Q(0) = -EA\frac{du_1}{dz}\bigg|_{z=0} = -EAc_{11} \tag{8}$$

Once the pile top settlement s_0 is known, the load Q on the top may be obtained by Eqn. (8), i.e., to control the bearing capacity by pile top settlement.

APPLICATION

The measured field test data and calculated *Q*-*s* curve by the present method shown in Fig. 6 are in good agreement.

CONCLUSIONS

- The axial bearing capacity of super-long filling piles is mainly supplied by shaft resistance, and should be controlled by the allowable pile top settlement.
- The Kedzi's linear elastic-fully plastic model is more suitable for describing the development of shaft resistance than traditional methods.
- After the *l*/*d* reaches a certain value (50, application results of this paper), the tip resistance is hard to exert and can be neglected. Therefore, to improve the axial bearing capacity by increasing pile length is not advisable.
- For super-long filling piles, the effect of pile shaft material strength on the bearing capacity should be taken into account, and sometimes the deformation and buckling stability check are also necessary.

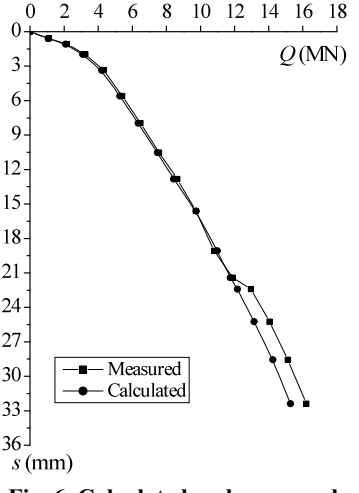

Fig. 6. Calculated and measured load-settlement curves.

REFERENCES

Cao Hanzhi (1986). "The Axial Load transferring of Piles and Numeral Calculating Method for Load- settlement Curve". *Chinese Journal of Geotechnical Engineering*, 8(6): 37-48.

Coyle, H.M.,and Reese, L.C. (1966). "Load transfer for axially loaded piles in clay". *Journal of Geotechnical Engineering*, ASCE, 92(2): 1-26.

Delpak, R.,Omer, J.R.,and Robinson, R.B. (2000). "Load/settlement prediction for large- diameter bored piles in mercia mudstone". *Proc.Instn.Civ.Engrs,Geotech. Engng*, 143, 201-224.

Kedzi. (1965). "Bearing Mechanism of piles". Geotechnics, 20(1), 1-5.

Kraft,L.M., Ray, R.P., and Kagama, T. (1981). "Theoretical τ-z curves". *Journal of Geotechnical Engineering*, ASCE, 107(11), 1543-1561.

Lin Tianjian, Xiong Houjin, and Wang Liqun (1999). Pile foundation design manual. China Architecture & Building Press, Beijing. 115-117.

Lu Shishen (1981). "The discussion on determining the axial load capacity of rock-socketed piles by distortion". *Highway*, (6), 13-19.

Poulos, H. G. (1989). "Pile behavior-theory and Application". *Geotechnique*, 39(3), 365-415.

Shi Peidong, Liang Jinyu (1994). "Vertical Bearing Capacity of Rock-socketed Piles". *Chinese Journal of Geotechnical Engineering*, 6(4): 32-39.

Sun Gengsheng, Zhen Datong (1984). Soft Subsoil and Underground Engineering. China Arthitecture & Building Press, Beijing. 502-526.

Wang Bohui, Shangguan Xing (1999). The Latest Development on Boring Cast-in-situ Piles in China. The People's Communications Press, Beijing. 56-72

Yang Jibao (1998). "Research on load transfer mechanism of super-long pile". *Chinese Journal of Geotechnical Engineering*, 20(6), 108-112.

Zhao Minghua (2000). Calculation and detecting for pile foundations of bridges. The People's Communications Press, Beijing. 32-45.

Zhu Xiangrong, Fang Pengfei, Huang Hongmian (2003). "Research on Super-long Pile in Soft Clay." *Chinesxe Journal of Geotechnical Engineering*, 25(1), 76-79.

Study on Flexural Behavior of Cast-in-Place Concrete Y-shaped Vibro-pile

X. Q. Wang[1], H. L. Liu[2], and Y .H. Chen[3]

[1]Key Laboratory of Ministry of Education for Geomechanics and Embankment Engineering, Hohai University, Nanjing 210098, China；Geotechnical Research Institute of Hohai University, Nanjing, 210098, China; fount352@sina.com
[2]Key Laboratory of Ministry of Education for Geomechanics and Embankment Engineering, Hohai University, Nanjing 210098, China；Geotechnical Research Institute of Hohai University, Nanjing, 210098, China; hliuhhu@163.com
[3]Key Laboratory of Ministry of Education for Geomechanics and Embankment Engineering, Hohai University, Nanjing 210098, China；Geotechnical Research Institute of Hohai University, Nanjing, 210098, China; yonghuich@163.com

ABSTRACT: The influence of four independent variables of Y-shaped cross section configuration on flexural behavior was analyzed by flexural factor of section and area ratio according to actual load on Y-shaped vibro-pile under three conditions, i.e., sharp-angled location of cross section, concave arc position and typical tension point. Flexural behavior under above three conditions is quite different and it changes with variation law of four independent variables of the cross section. The same template radian exists while the other three independent variables are defined, so that flexural behavior under conditions of sharp-angled position and typical tension point reaches the minimum value. Solution of corresponding template radian of the minimum value of flexural behavior has been introduced by utilizing the mathematical analysis software, Mathematica.

INTRODUCTION

The cast-in-place concrete Y-shaped Vibro-pile (referred to as the Y-pile) is a new type of displacement pile with a special Y-shaped perimeter. It is considered as an improvement of the traditional circular bored pile based on special-shaped perimeter enlargement principle of the same cross section area. The configuration of Y-shaped cross section is a curved line triangle consisting of three concave arc lines and three sharp angles as shown in Figure 1 and 2. Shaft friction and lateral bearing performance are increased with the increase of shaft surface area of non-circular pile with the same cross section. Y-pile has larger moment of inertia than circular and square piles with the same section area.

The maximum bending moment of pile is proportional to flexural factor of section, W, therefore cross section with larger W is more reasonable with the same cross

section area. The rationality of the sections with different configuration is studied in terms of the value *W/S*.

At present, there are no published studies on flexural behavior of Y-shaped cross section. As are shown in Figure 2, the cross section of Y-pile is dominated by four independent variables, i.e., radius of envelope circle (R), gap between open arcs (s), radian of steel casing (θ), and internal angle (δ). Expressions of section area, moment of inertia and inscribed circle's radius were educed on basis of symbols. Influence of four independent variables on W_1/S, W_2/S and W_3/S of Y-shaped cross section have been analyzed under conditions of point A at sharp angle (with flexural factor, W_1), point B at concave arc (with flexural factor, W_2) and typical tension point C (with flexural factor, W_3). A certain radian exist such that $\theta_{c\min} = \theta_{1\min} = \theta_{3\min}$, and W_1/S and W_3/S of Y-shaped cross section are the minimum when radius of envelope circle (R), gap between open arc (s) and internal angle (δ) are defined. Solution of $\theta_{c\min}$ is introduced by utilizing mathematical analysis software, Mathematica. Some conclusions were achieved as guiding for cross section design and parameters of Y-shaped cross section in different purposes and configurations.

FIG. 1. Cross section of Y-pile.

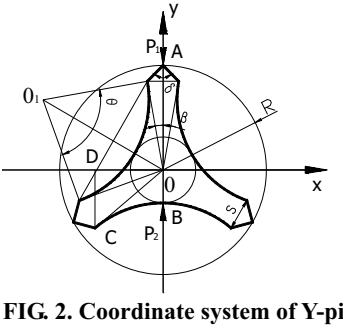

FIG. 2. Coordinate system of Y-pile.

CROSS SECTION AREA, PERFORMANCE OF MOMENT OF INERTIA, AND CALCULATION METHOD OF Y-PILE

The coordinate system and notations are shown in Figure 2. Arbitrary centroid axis of Y-shaped cross section is the principle of centroid axis by axis offset and coordinate transformation. Moment of inertia to any principle centroid axis is the same. Expression of moment of inertia to principle centroid axis of Y-shaped cross section is achieved by integration and moment of inertia of Y-shaped cross section to other axes can be solved by formulas for axis offset.

If

$$\lambda = \sqrt{(R - \frac{s}{2}\cot\frac{\delta}{2})^2 + (\frac{s}{2})^2},\quad \beta = arc\tan(\frac{s}{2R - s\cot\frac{\delta}{2}}),\quad A = -\lambda\sin(\frac{2\pi}{3} - \frac{\theta}{2} + \beta)/\sin(\frac{\theta}{2}),$$

$$B = (\lambda \sin(\frac{\pi}{3} - \beta) / \sin(\frac{\theta}{2}))^2,\ a = \lambda \cos(\frac{\pi}{6} + \beta),\ b = \lambda \cos(\frac{\pi}{6} - \beta),$$

$$H = \lambda \sin(\frac{2\pi}{3} - \frac{\theta}{2} + \beta) / (2 \sin(\frac{\theta}{2})),\ G = \sqrt{3}\lambda \sin(\frac{2\pi}{3} - \frac{\theta}{2} + \beta) / (2 \sin(\frac{\theta}{2})),$$

$$L = -(\lambda \sin(\frac{\pi}{6} + \beta) - \frac{R}{2}) / (\lambda \cos(\frac{\pi}{6} + \beta) - \frac{\sqrt{3}R}{2}),$$

$$M = \lambda R(\frac{\sqrt{3}}{2} \sin(\frac{\pi}{6} + \beta) - \frac{1}{2} \cos(\frac{\pi}{6} + \beta)) / (\lambda \cos(\frac{\pi}{6} + \beta) - \frac{\sqrt{3}R}{2}),$$

$$Q = -(\lambda \sin(\frac{\pi}{6} - \beta) - \frac{R}{2}) / (\lambda \cos(\frac{\pi}{6} - \beta) - \frac{\sqrt{3}R}{2}),$$

$$c = \frac{R\sqrt{3}}{2},\ \beta = arc \tan(\frac{s}{2R - s \cot(\delta / 2)}),\ P = \frac{\lambda R(\frac{\sqrt{3}}{2} \sin(\frac{\pi}{6} - \beta) - \frac{1}{2} \cos(\frac{\pi}{6} - \beta))}{\lambda \cos(\frac{\pi}{6} - \beta) - \frac{\sqrt{3}R}{2}}.$$

The length of line DC is $L = \lambda \sin(\frac{\pi}{3} - \beta)$.

The calculation formula for cross section area of Y-pile is as follows,

$$S = 3(\lambda^2 \sin(\frac{\pi}{3} - \beta) \frac{\sin(\frac{2\pi}{3} - \frac{\theta}{2} + \beta)}{\sin(\frac{\theta}{2})} - \frac{1}{2}\theta\lambda^2 (\frac{\sin(\frac{\pi}{3} - \beta)}{\sin(\frac{\theta}{2})})^2 + \frac{(R - \frac{s}{2}\cot\frac{\delta}{2})s}{2} + \frac{s^2}{4}\cot\frac{\delta}{2}) \quad (1)$$

Radius of inscribed circle of section area of Y-pile is as follows,

$$r = \lambda \csc(\frac{\theta}{2})(\sin(\frac{2\pi}{3} - \frac{\theta}{2} + \beta) - s \sin(\frac{\pi}{3} - \beta)) \quad (2)$$

The moment of inertia to principle centroid axis of Y-shaped cross section can be derived from the following equation 3.

$$I = \frac{1}{12}(-a(8A^3 + 24AB + 12A^2\sqrt{-a^2 + B} + 5B\sqrt{-a^2 + B} - 2a^2(4A + \sqrt{-a^2 + B})) - \frac{2(-(aL + M)^4 + (cL + M)^4)}{L}$$
$$+ \frac{2(-(P + bQ)^4 + (P + cQ)^4)}{Q} - 3B(4A^2 + B) \arctan(\frac{a}{\sqrt{-a^2 + B}}) + \frac{1}{4(b - \frac{s}{2})}((2b - s)(8H(3B + H^2)(2G - s) - 2H(2G - s)^3 \quad (3)$$
$$+ \frac{1}{4}(2G - s)(-10B + 4G^2 - 24H^2 - 4Gs + s^2)\sqrt{4B - (-2G + s)^2} + 2(-8(b - G)^3 H + 8(b - G)H(3B + H^2) +$$
$$(b - G)\sqrt{-b^2 + B + 2bG - G^2}(2b^2 - 5B - 4bG + 2(G^2 - 6H^2)) - 3B(B + 4H^2) \arctan(\frac{b - G}{\sqrt{-b^2 + B + 2bG - G^2}})) +$$
$$6B(B + 4H^2) \arctan(\frac{-2G + s}{\sqrt{4B - (-2G + s)^2}}))) + 2(R^4 - (R - \frac{s}{2}\cot(\frac{\delta}{2}))^4) \tan(\frac{\delta}{2}))$$

ANALYSIS ON FLEXURAL FACTOR OF CROSS SECTION AND AREA RATIO, *W/S* OF Y-PILE

As shown in Figure 2, point A, the sharp angle of Y-shaped cross section has the maximum distance to the neutral axis towards acting direction of all the loads. The maximum distance from edge point A to neutral axis is equal to radius of envelope circle of Y-shaped cross section (R). Since plain concrete has excellent performance

in compression but poor performance in tension, point A is the weak point for loading and corresponding flexural factor is W_1/S. While point B has the minimum distance to the neutral axis, which is equal to radius of inscribed circle of Y-shaped cross section (r) with corresponding flexural factor is W_2/S. The load P_1 and P_2 are in the typical stress direction of Y-pile. Point A has the maximum distance to the neutral axis when load P_1 acts on tensioned cross section; point C has the maximum distance to the neutral axis when load P_2 on tensioned cross section. The distance from point C to the center is $\lambda\sin(\pi/3-\beta)$ and corresponding flexural factor is W_3/S.

Flexural factor of section and area ratio of W_1/S, W_2/S and W_3/S of Y- pile is solved by moment of inertia and area of Y-shaped cross section:

$$\frac{W_1}{S}=\frac{I}{SR},\ \frac{W_2}{S}=\frac{I}{Sr},\frac{W_3}{S}=\frac{I}{S\lambda\sin(\pi/3-\beta)} \tag{4}$$

The influences of four independent variables on W_1/S, W_2/S and W_3/S are analyzed as follows:

Influences of Dominant Variables of Y-pile to W_1/S, W_2/S and W_3/S

(1) Variation law of W_1/S, W_2/S and W_3/S with θ

For the comparison analysis, $\theta\in[50°,90°]$, R is equal to 0.25 m and 0.5 m, δ is 90 and s is 0.12 m. The change of W_1/S, W_2/S and W_3/S with θ is summarised in Table 1.

Table 1. Variation Law of W_1/S, W_2/S and W_3/S with θ

	θ	W_1/S	W_2/S	W_3/S		θ	W_1/S	W_2/S	W_3/S
R= 0.25 m	50°	0.036015	0.076867	0.066920	R= 0.5 m	50°	0.0649951	0.167396	0.0925721
	60°	0.035984	0.081112	0.066863		60°	0.0647657	0.182031	0.0922454
	70°	0.036117	0.086372	0.067110		70°	0.0654463	0.202902	0.0932147
	80°	0.036605	0.093389	0.068017		80°	0.068491	0.237504	0.0975512
	90°	0.037484	0.102718	0.069650		90°	0.0747254	0.295237	0.106431

As shown in Table 1, W_1/S and W_3/S decrease first, then increase with increase of steel casing radian (θ) when R、s、δ are fixed. W_2/S increases with increase of steel casing radian (θ) when R、s、δ are fixed. The extreme point changes for different R of envelope circle. Therefore, minimum of W_1/S and W_3/S can be derived from $\theta_{1\min}$ and $\theta_{3\min}$ when R、s、δ are fixed. Above minimum values must be avoid for determining the configuration of Y-pile according to pile layout and load

direction of Y-shaped cross section. The flexural behavior of Y cross section is remarkably effected by θ.

(2) Variation law of W_1/S, W_2/S and W_3/S with s

$s \in [0.08m, 0.12m]$, R is 0.25 m or 0.5 m, δ is 90° and θ is 60° for comparative analysis. The changes of W_1/S, W_2/S and W_3/S with s are summarised in Table 2.

Table 2. Variation Law of W_1/S, W_2/S and W_3/S With s

	s (m)	W_1/S	W_2/S	W_3/S		s (m)	W_1/S	W_2/S	W_3/S
R= 0.25 m	0.08	0.0340441	0.0884086	0.052581	R= 0.5 m	0.08	0.0594866	0.182187	0.0786086
	0.09	0.0346558	0.0867006	0.0558838		0.09	0.0610665	0.182925	0.0821798
	0.10	0.0351683	0.0848738	0.0593236		0.10	0.0624539	0.183066	0.085621
	0.11	0.0356052	0.0829957	0.0629623		0.11	0.0636789	0.182736	0.0889664
	0.12	0.0359844	0.0811115	0.0668632		0.12	0.0647657	0.182031	0.0922454

As shown in Table 2, W_1/S and W_3/S increase with the increase of gap between open arcs (s) when R、θ、δ are fixed. Variation law of W_2/S is related to radius. It decreases when R is 0.25 m while it increases then decreases when R is 0.5 m.

(3) Variation law of W_1/S, W_2/S and W_3/S toward δ

$\delta \in [50°, 90°]$, R is 0.25 m and 0.5 m, θ is 60° and s is 0.12 m for the analysis. The changed of W_1/S, W_2/S and W_3/S with δ are summarised in Table 3.

Table 3. Variation Law of W_1/S, W_2/S and W_3/S With δ

	δ	W_1/S	W_2/S	W_3/S		δ	W_1/S	W_2/S	W_3/S
R= 0.25 m	50°	0.0293969	0.0794425	0.0978926	R= 0.5 m	50°	0.0579522	0.181671	0.0993759
	60°	0.0314077	0.0791994	0.0813618		60°	0.060222	0.181251	0.0961974
	70°	0.0331503	0.0796676	0.0738002		70°	0.0620285	0.181355	0.0943245
	80°	0.0346603	0.0803604	0.0695537		80°	0.0635121	0.181655	0.0931024
	90°	0.0359844	0.0811115	0.0668632		90°	0.0647657	0.182031	0.0922454

It can be seen from Table 3 that W_1/S increases with increase of internal angle (δ)

when R、θ、s are fixed. W_2/S decreases then increases and extreme point has different positions due to different R of external circle. W_3/S decreases with increase of internal angle (δ) when R、θ、s are fixed.

(4) Variation law of W_1/S, W_2/S and W_3/S with R

δ=90°, θ=60°, s=0.12m. $R \in [0.2m, 0.9m]$ for comparative analysis. The results are summarised in Table 4. As shown in Table 4, W_1/S, W_2/S and W_3/S increase and flexural behavior increase remarkably due to increasing of R of external circle when δ、θ、s are fixed.

Table 4. Variation Law of W_1/S, W_2/S and W_3/S With R

R	W_1/S	W_2/S	W_3/S	R	W_1/S	W_2/S	W_3/S
0.2m	0.029517	0.060539	0.064699	0.6m	0.074945	0.219680	0.102745
0.3m	0.042202	0.101849	0.071188	0.7m	0.084581	0.255766	0.112934
0.4m	0.053906	0.142701	0.081538	0.8m	0.093781	0.290476	0.122819
0.5m	0.064766	0.182031	0.092245	0.9m	0.102628	0.324000	0.132430

Solution of the Minimum Point (θ) for W_1/S, W_2/S and W_3/S of Y-pile

It is apparent that R、s、δ、θ have a certain influence on flexural behavior of cross section of Y-pile from above comparison. In general, radius of envelope circle (R) is determined first, then the other three variables. Due to many factors during design process, the vibration of s、δ are limited and they have been solved according to ideas of extreme minimum point of θ if necessary during the actual design. θ has larger influence to flexural behavior of cross section and it is the key variable in the variation during Y-pile design and $\theta_{1\min}$ and $\theta_{3\min}$ must be avoided.

$$(W_1/S)/(W_3/S) = \sin(\frac{\pi}{3} - \beta)\sqrt{(R-\frac{s}{2})^2 + (\frac{s}{2}\cot\frac{\delta}{2})^2}/R \quad (5)$$

The value of equation (5) is irrelevant to θ so $\theta_{1\min} = \theta_{3\min}$ and it is written as $\theta_{c\min}$.

The introduction to solution of $\theta_{c\min}$ is as follows and the minimum point ($\theta_{c\min}$) of W_1/S and W_3/S of Y-pile can be solved by the first partial derivation of θ by $I/(SR)$ and consider that $\partial(I/(SR))/\partial\theta = 0$. Expression and solution of I/S are very complicated and very easy to make mistake. So it is solved by mathematical analysis software of Mathematica in this study. There are some complicated functions in the equation and they may not be solved by Mathematica. However, they can be solved by FindRoot[] with initial conditions provided.

CONCLUSIONS

R、s、θ、δ have a certain influence on flexural behavior of cross section. As a

special-shaped pile, flexural behavior to marginal points of Y-pile are different due to different distance from the reference point at the cross section to neutral axis. The variation of W_1/S, W_2/S and W_3/S with R、s、θ、δ are apparent. A certain $\theta_{1\min}, \theta_{3\min}$ exist for the minimum values of W_1/S and W_3/S while R、s、δ are fixed and $\theta_{1\min} = \theta_{3\min}$. Optimized design should be carried out according to purpose of Y-piles under actual loading conditions.

It is convenient and accurate to work out extreme value by mathematical analysis software of Mathematica. However, there are some complicated functions in the equation and they may not be solved by Mathematica. However, they can be solved by FindRoot[] with initial conditions provided.

ACKNOWLEDGMENTS

The authors appreciate the support of T. Zhang in format, spelling and grammar.

REFERENCES

Chen Y.H., Wang, X.Q., and Liu H.L., et al. (2008). "Analysis and calculation of additional stress due to skin friction of Y-shaped vibro-pile." *Rock and Soil Mechanics*, Vol.29(11):2905-2911.

Chen Y.H., and Wang, X.Q. (2008). "Research on abnormity characteristic of Y-shaped tube-sinking cast-in-situ pile in highway soft ground." *China Journal of Highway and Transport*, Vol.21(5):19-25.

Fan, Q.S., Wang, B., and Yin Y.J. (2000). "Materials Mechanices." Beijing, Higher Education Press.

Li, Q.Y. Wang, N.C., and Yi, D.Y. (2001). "Numerical Analysis(Version 4)." Beijing, Tsinghua University Pres.

Tongji University Department of Applied Mathematics. "Higher Mathematics (Version5). "Beijing, Higher Education Press.

Wang, X.Q., Chen Y.H., and Liu H.L. (2008). "In-situ study on load transfer mechanism of Y-shaped vibro-pile." *Chinese Journal of Rock Mechanics and Engineering*, Vol.27(3):615-623.

Xu, L.X., Yang, S.H. , and Duan, B. (2007). "Field tests on Y-shaped vibro piles to improve soft clay ground under the expressways." *Chinese Journal of Geotechnical Engineering*, Vol. 29(1):120-124.

Xu, D.Y. Zhu, W. X., and Wang, X. D. (2006). "Materials Mechanices." Nanjing, Hohai University Press.

Calculation of Soil Stresses under Various Pile Sectional Configurations

Y .H. Chen[1], X. Q. Wang[2], and H. L. Liu[3]

[1]Key Laboratory of Ministry of Education for Geomechanics and Embankment Engineering, Hohai University, Nanjing 210098, China Geotechnical Research Institute of Hohai University, Nanjing, 210098, China; fount352@sina.com
[2]Key Laboratory of Ministry of Education for Geomechanics and Embankment Engineering, Hohai University, Nanjing 210098, China Geotechnical Research Institute of Hohai University, Nanjing, 210098, China; hliuhhu@163.com
[3]Key Laboratory of Ministry of Education for Geomechanics and Embankment Engineering, Hohai University, Nanjing 210098, China Geotechnical Research Institute of Hohai University, Nanjing, 210098, China; yonghuich@163.com

ABSTRACT: With development of piling technology, various pile sectional configurations are adopted in the pile industry practice. The soil stresses induced by the piles of various sectional configurations are significantly different. In this paper, the solutions for the induced soil stresses were proposed for Y-shaped pile, closed- and open-ended pipe piles, triangular-shaped pile, rectangular pile, and square pile. The calculation of soil stresses is based on the Mindlin stress solution and Geddes methodology for derivation of soil stresses. It is assumed that the pile end bearing and shaft resistance are uniformly distributed across the pile tip area and shaft perimeter, respectively. The numerical software Mathematica (Nintegrate) was used to provide integrations to the derived theoretical solutions.

INTRODUCTION

In recent years, a number of new ground improvement methods have been developed as results of the high demands for infrastructure construction upon very soft ground. These methods proved to be both effective and economical. In pile engineering, the pile sectional configuration has undergone a revolution against the conventional circular and rectangular pile shape. Based on the principals of making full use of the soil and pile bearing capacity, Y-shaped and X-shaped piles were proposed and used successfully in practice.

For evaluation of foundation settlement, soil stresses are required based on Boussinesq stress solution (Feirolin 1965). However, the Boussinesq stress solution does not take into account the foundation embedment depth and Poisson's ratio. The calculated settlements are therefore largely different from the measured values. Since the solution for soil stress under a point load proposed by Mindlin in 1936

(Mindlin1936), a number of studies have been carried out to obtain solutions under vertical line load, strip load rectangular uniformly distributed load and circular uniformly distributed load, etc. Mindlin solution also has been utilized widely for calculating settlement (Zhang 1999, Ding 2002, Lü 2003, Yan 2007). Base on Mindlin's solution and simplification of pile tip and shaft resistance to point load, Geddes deduced three solutions to soil stress for pile tip load, rectangular and triangular distributed shaft friction (Geddes 1966). Geddes solution is widely used for assessment of pile settlement. However, Geddes solution is not a function of pile diameter since the pile tip resistance is simplified to a point load. Therefore, the soil stresses are not related to the pile sectional configurations.

In this paper, based on the Mindlin solution and Geddes methodology, the solutions for the induced soil stress were proposed for Y-shaped pile, closed- and open-ended pipe piles, triangular-shaped pile, rectangular pile, square pile, H-shaped pile, T-shaped pile, and X-shaped pile. The pile end bearing and shaft resistance are uniformly distributed across the pile tip area and shaft perimeter respectively. The new solution allows more accurate evaluation of single and group pile settlement.

SOIL STRESS DISTRIBUTION UNDER VERTICAL POINT LOAD

Based on Mindlin's solution, as shown on Figure 1, the vertical stress coefficient under point load P acting at point (0, 0, h) in the elastic semi-infinite ground, can be expressed as:

$$I_z = \frac{1}{8\pi(1-\mu)}\left\{\begin{array}{l}\dfrac{(1-2\mu)(z-h)}{R_1^3}-\dfrac{(1-2\mu)(z-h)}{R_2^3}+\dfrac{3(z-h)^3}{R_1^5}+\dfrac{30hz(z+h)^3}{R_2^7}+\\ \dfrac{3(3-4\mu)z(z+h)^2-3h(z+h)(5z-h)}{R_2^5}\end{array}\right\} \quad (1)$$

where,

$R_1 = \sqrt{x^2+y^2+(z-h)^2}$;

$R_2 = \sqrt{x^2+y^2+(z+h)^2}$

r is the horizontal distance from the loading point to the calculation point.

h is depth of the loading point.

μ is Poisson's ratio of soil.

In the rectangular coordination system, the distance from arbitrary stress point (x_j, y_j) to any point (x_i, y_i) at the calculation cross section is calculated as follows,

$$l_i = \sqrt{(x_j - x_i)^2 + (y_j - y_i)^2} \quad (2)$$

I_{zj} can be derived when r in formula (1) is substituted by l_i.

In polar coordinate system, the distance from arbitrary stress point (r_j, α_j) to any point (r, α) can be calculated as,

$$L_i = \sqrt{r^2 + r_1^2 - 2rr_1\cos(\alpha - \alpha_1)} \quad (3)$$

I'_{zj} can be derived when r in formula (1) is substituted by L_i.

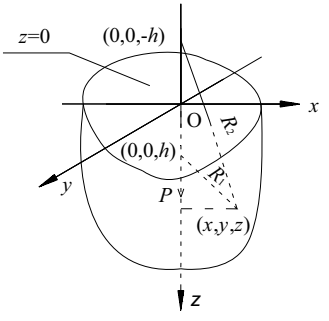

Figure 1. Layout of point load *P* in semi-infinite ground.

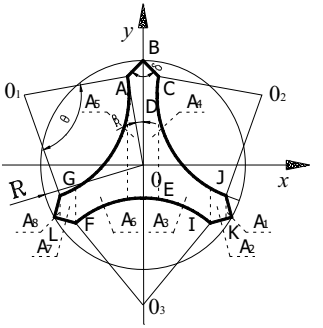

Figure 2. Coordinate system of Y-shaped cross section.

SOIL STRESS DISTRIBUTION UNDER PILED FOUNDATION

Soil Stress under Y-Shaped Pile Foundation

As shown on Figure 2, the cross sectional configuration of the Y-pile is dominated by four independent variables: radius of envelope circle (R), gap between open arcs (s), radian of steel casing (θ), and internal angle (ξ). For comparison with the stress coefficient by Geddes solution, the integration expression is multiplied by L^2 .

For uniform distributed load over Y-shaped pile acting at depth of h in homogenous and isotropic elastic semi-infinite space, the soil stresses can be calculated using formula (1) by integration over the entire Y-shaped cross section at eight integral areas of A_1, A_2, A_3, A_4, A_5, A_6, A_7 and A_8. The integration was performed using NIntegrate, numerical integration function in mathematical software of Mathematica. The integration sequence is y followed by x. The solution of vertical stress coefficient at arbitrary point can be expressed as,

$$I_{YP} = \frac{L^2}{A_Y} \sum_{i=1}^{8} \left(\iint_{A_i} I_{zj} dxdy \right) \tag{4}$$

where, L is pile length; P_d is pile tip resistance; A_Y is cross sectional area of Y-shaped pile.

The shaft resistance is assumed to be uniformly distributed along the pile length. For uniform distributed shaft friction acting at depth of h in homogenous and isotropic elastic semi-infinite ground, the soil stresses at arbitrary point can be calculated using formula (1) by linear integration along the perimeter of Y-shaped pile and then along the pile length. There are 9 integral intervals around the perimeter of Y-pile cross section following the sequence of $\overrightarrow{AB}$, $\overrightarrow{BC}$, $\overrightarrow{CD}$, $\overrightarrow{DE}$, $\overrightarrow{EF}$, $\overrightarrow{FG}$, $\overrightarrow{GH}$, $\overrightarrow{HI}$ and $\overrightarrow{IA}$.

The stress coefficient for shaft resistance uniformly distributed along pile perimeter and rectangular distributed along pile length can be expressed as,

$$I_{Ys1}=\frac{L}{C_Y}\sum_{i=1}^{9}(\int_0^L\int_{\eta_i}I'_{zj}\mathrm{d}s\mathrm{d}h)=\frac{L}{C_Y}\sum_{i=1}^{9}(\int_0^L\int_{\alpha_i}^{\alpha_{i+1}}I'_{zj}\sqrt{(r_i)^2+(\frac{\partial r_i}{\partial\alpha})^2}\,\mathrm{d}\alpha\mathrm{d}h) \tag{5}$$

The stress coefficient for shaft friction uniformly distributed along pile perimeter and triangular distributed along pile length can be expressed as,

$$I_{Ys2}=\frac{1}{C_Y}\sum_{i=1}^{9}(\int_0^L\int_{l}2hI'_{zj}\mathrm{d}s\mathrm{d}h)=\frac{1}{C_Y}\sum_{i=1}^{9}(\int_0^L\int_{\alpha_i}^{\alpha_{i+1}}2hI'_{zj}\sqrt{(r_i)^2+(\frac{\partial r_i}{\partial\alpha})^2}\,\mathrm{d}\alpha\mathrm{d}h) \tag{6}$$

The analytic solutions for formulae (4), (5) and (6) are complicated. The integration can be solved by NIntegrate numerical integration function in mathematical analysis software of Mathematica.

Soil Stress under Closed- and Open-Ended Pipe Pile

Pile radius is designated by "r", shaft resistance by "$P/2\pi r$", pile end bearing resistance "$P/\pi r^2$". For comparison with the stress coefficient by Geddes solution, the integration expression is multiplied by L^2.

The vertical stress coefficient at arbitrary point caused by uniform load under circular cross section can be expressed,

$$I_{\bigcirc P}=\frac{L^2}{A_{\bigcirc}}\iint_{A_{\bigcirc}}I_{zj}dxdy \tag{7}$$

For a special case, the vertical stress coefficient at central point of circular cross section can be expressed as,

$$\begin{aligned}I'_{\bigcirc P}=&\frac{1}{4(1-\mu)}\Big(\frac{2(1-\mu)(h+z)(\sqrt{(h-z)^2}-\sqrt{(h+z)^2})}{\sqrt{(h-z)^2}\sqrt{(h+z)^2}}-\frac{(h-z)(2(h-z)^2(-1+\mu)+R^2(-1+2\mu)}{(R^2+(h-z)^2)^{\frac{3}{2}}}+\\&\frac{1}{(R^2+(h+z)^2)^{\frac{5}{2}}}(-6hz(h+z)^3+(h-z)(R^2+(h+z)^2)^2(-1+2\mu)\\&-(h+z)(R^2+(h+z)^2)(h^2+z^2(3-4\mu)-2hz(1+2\mu))\Big)\Big)\end{aligned} \tag{8}$$

Stress coefficient of shaft friction uniformly distributed along pile perimeter and rectangular distributed along pile length is as follows,

$$I'_{s1}=L^2\int_0^L\oint_l\frac{1}{2\pi rL}I'_{zj}\mathrm{d}s\mathrm{d}h=\frac{L}{2\pi}\int_0^L\int_0^{2\pi}I'_{zj}\mathrm{d}\alpha\mathrm{d}h \tag{9}$$

While stress coefficient of shaft friction uniformly distributed along pile perimeter and triangular distributed along pile length is as follows,

$$I'_{s2}=L^2\int_0^L\oint_l\frac{2h}{2\pi rL^2}I'_{zj}\mathrm{d}s\mathrm{d}h=\frac{1}{\pi}\int_0^L\int_0^{2\pi}hI'_{zj}\mathrm{d}\alpha\mathrm{d}h \tag{10}$$

Same as formulae (4), (5) and (6), the analytic solutions for formulae (8), (9) and (10) are complicated. The integration can be solved by NIntegrate numerical integration function in mathematical analysis software of Mathematica.

For annular cross section, the solution can be obtained by superposing the solutions of two circular areas with different radius.

Soil Stress under Regular-Shaped Pile

As shown on Figure 3, the analytic solution for regular triangle is similar to Y-shaped cross section. The integration sequence is also y followed by x. "L" is side length of regular triangle and integral interval is as follows,

$$x \in [\frac{y}{\sqrt{3}} - \frac{a}{3}, -\frac{y}{\sqrt{3}} + \frac{a}{3}], y \in [-\frac{\sqrt{3}a}{6}, \frac{\sqrt{3}a}{3}]$$

The vertical induced stress coefficient at any arbitrary point caused by uniform distributed load on regular triangle cross section is as follows,

$$I_{\triangle P} = \frac{2L^2}{\sqrt{3}a^2} \iint_{A_\triangle} I_{zj} dx dy \qquad (11)$$

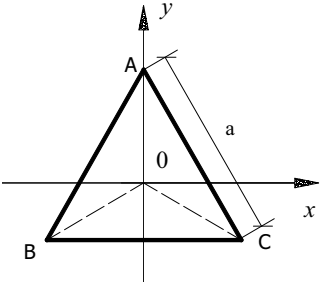

Figure 3. Coordinate system of regular triangle pile.

Polar formula of line $\overrightarrow{CA}$ is

$$r_1 = \frac{\sqrt{3}a}{3(\sin\alpha + \sqrt{3}\cos\alpha)}, \quad \alpha \in [-\frac{\pi}{6}, \frac{\pi}{2}]$$

Polar formula of line $\overrightarrow{AB}$ is

$$r_2 = \frac{\sqrt{3}a}{3(\sin\alpha - \sqrt{3}\cos\alpha)}, \quad \alpha \in [\frac{\pi}{2}, \frac{7\pi}{6}]$$

Polar formula of line $\overrightarrow{BC}$ is $r_3 = -\frac{\sqrt{3}a}{6\sin\alpha}, \quad \alpha \in [\frac{7\pi}{6}, \frac{11\pi}{6}]$

Stress coefficient of shaft friction uniformly distributed along pile perimeter and rectangular distributed along pile length is as follows,

$$I_{\triangle s1} = \frac{L}{3a}\sum_{i=1}^{3}(\int_0^L \int_{r_i}^{} I'_{zj} \mathrm{d}s\mathrm{d}h) = \frac{L}{3a}\sum_{i=1}^{3}(\int_0^L \int_{\alpha_i}^{\alpha_{i+1}} I'_{zj}\sqrt{(r_i)^2 + (\frac{\partial r_i}{\partial \alpha})^2}\,\mathrm{d}\alpha\mathrm{d}h) \qquad (12)$$

While stress coefficient of shaft friction uniformly distributed along pile perimeter and triangular distributed along pile length is as follows,

$$I_{\triangle s2} = \frac{1}{3a}\sum_{i=1}^{3}(\int_0^L \int_{l}^{} 2hI'_{zj} \mathrm{d}s\mathrm{d}h) = \frac{1}{3a}\sum_{i=1}^{3}(\int_0^L \int_{\alpha_i}^{\alpha_{i+1}} 2hI'_{zj}\sqrt{(r_i)^2 + (\frac{\partial r_i}{\partial \alpha})^2}\,\mathrm{d}\alpha\mathrm{d}h) \qquad (13)$$

Same as formulae (4) to (10), formulae (11), (12) and (13) are complicated. The integration can be solved by NIntegrate numerical integration function in mathematical analysis software of Mathematica.

CONCLUSIONS

(1) The soil stresses induced by the piles of various sectional configurations are significantly different. Using NIntegrate numerical integration function of mathematical software of Mathematica, based on Mindlin stress solution and Geddes

derivation, the vertical induced stress coefficient at arbitrary point in the ground are derived for Y-shaped pile, circular pile, pipe pile and regular triangular pile. The pile tip resistance and shaft friction are assumed to be uniformly distributed along cross section and pile body respectively,

(2) Explicit solution can be deduced for the central point of cross sections under uniformly distributed load for circular piles and pipe piles from the formula of vertical induced stress coefficient. The simplified formula can be conveniently used in engineering practice. However, vertical induced stress coefficients at other points need to be calculated by NIntegrate numerical integration function of Mathematica.

(3) The methods described in this paper for induced stress coefficient of pile tip resistance and shaft friction at arbitrary point in the ground are based on the assumption of pile tip resistance is uniformly distributed along cross section of pile and shaft friction is uniformly distributed along pile perimeter. Only special cases of shaft friction rectangular and triangular distributed along pile length are analyzed, which may be different from actual load distribution performance of shaft friction and pile tip resistance. For engineering practice, the settlement of pile foundations can be calculated using the methods presented in this paper combined with real stress distribution of shaft friction and pile tip resistance.

REFERENCES

Ding, J.H., Ma, Y. P., and Yu, Y. F. (2002). “Numerical calculation and analysis of ground settlement based on Mindlin's stress solution.” *Water Resources and Hydropower Engineering*, 33(5):8-11.

Feirolin, B. A. (1965). “Principle of soil mechanics (Chinese Translation).” Beijing: Chinese Building Industry Press.

Geddes, J. D. (1966). “Stress in foundation soils due to vertical subsurface load.” *Geotechnique*, (16):231-255.

Lü, Y. P. (2003). “Study on the design method of pile-raft foundation based on Geddes's stress formula.” *Hangzhou*: Zhejiang University.

Mindlin, R. D. (1936). “Force at a point in the interior of a semi-infinite solid. ” *Physics*, 7(5):195-202.

Yan, B.J., Song, X.G., and Yue, Y. Q. (2007). “Boussinesq-Mindlin united solution method for DJMP composite foundation additional stress.” *Rock and Soil Mechanics*, 28(6):1255-1258.

Zhang, X. P., and Yu, Z. Q. (1999). “Derivation of the formula for induced stress in compound foundation by Mindlin solution.” *JOURNAL OF HOHAI UNIVERSITY*, 27(2):35-39.

Experimental Study on Soft Ground Improvement by Grouted Gravel Pile

Y .H. Chen[1], X. Q. Wang[2], D.H. Cao[3], and W. G. Shen[4]

[1]Key Laboratory of Ministry of Education for Geomechanics and Embankment Engineering, Hohai University, Nanjing 210098, China；Geotechnical Research Institute of Hohai University, Nanjing, 210098, China; yonghuich@163.com

[2] Key Laboratory of Ministry of Education for Geomechanics and Embankment Engineering, Hohai University, Nanjing 210098, China；Geotechnical Research Institute of Hohai University, Nanjing, 210098, China; fount352@sina.com

[3]Zhejiang Zhebei Expressway Manage Co., Ltd, Huzhou 313000, China; dehongcao@126.com

[4]Zhejiang Provincial Transportation Engineering Construction Group Co., Ltd, Huzhou 310013, China; Shenwengang@sina.com

ABSTRACT: Based on field tests on the new developed grouted gravel pile, the bearing performance, working mechanism and improvement effect on the adjacent ground were studied. The variation of pore water pressure, pile-soil stress ratio, ground surface settlement, layered settlement, and lateral displacement of improved zone adjacent to grouted gravel pile were monitored and presented in this paper. It indicates that the properties of adjacent soil surrounding both pile body and pile toe were improved due to the infiltration and cementation of cement grout, therefore both shaft friction and end bearing resistance were remarkably increased and apparently the ultimate bearing capacity was increased.

INTRODUCTION

Grouted gravel pile is a new method of soft ground improvement by using gravel pile (LIU and CHEN 2006) combined with grouting technology. The typical diameter of grouted gravel pile is between 300 mm and 700 mm. Developed from the post grouting technology of conventional pouring pile, grouted gravel pile have many advantages such as convenient construction equipment, fast construction speed, flexible site conditions, less environmental influence, simple operation and high bearing capacity and so on. It is suitable for sandy gravel, clay, silt, silty sand and mud layers, thus it has potentially for wide engineering application. The main

construction processes is as follows: boring, borehole washing, gravel filling, and grouting. Grouted gravel pile after excavation has perfect quality as shown in Figure 1.

FIG. 1. Grouted gravel pile head after excavation.

REINFORCEMENT MECHANISMS

Grouted gravel pile is a small diameter bored pile consisting of crushed stone/ gravel cemented by grout. Similar to other pile types, composite foundation of grouted gravel pile can be formed by adding artificial reinforcement material in the natural soil to bear upper load together. The modulus and strength of pile body are much larger than those of soil between piles and stress on the top of pile head is higher than that of soil between piles and load can be transferred to deeper soil by pile body to reduce load of soil between piles and greatly increase bearing capacity of natural ground and reduce ground settlement effectively. However, grouted gravel pile is remarkably different from conventional pouring pile due to application of post grouting technology; some detailed research on post grouting technology is given in references (ZHANG and RUAN 2002, FU and WANG 1997) and bearing capacity and settlement effected by lateral and bottom grouting are analyzed. Firstly, grouting can guarantee the gravels cemented with grout in the borehole form a solid pile body with high strength similar to concrete pile. Secondly, the grout further infiltrates into adjacent soil around the hole under high grouting pressure, react with natural soil and change soil properties around the pile with compression, consolidation, filling and replacement, etc., and replaced air and water in the ground by cement hydrate and finally form a grout transitional infiltrated zone at the pile-soil interface. Void ratio and compression modulus of soil in transitional zone are less than those of original soil and bulk density is high than that of original soil. Infiltration and cementation of grout can enhance overall density and effective stress of soil between piles and avoid defeat of mud skin on pile body and increase cementation ability of pile body and soil. Pile diameter and surface area are enlarged and shaft friction is increased apparently. Infiltration and cementation can also improve gravel sedimentations at pile toe and grouting pressure can form root type enlarged zone at pile toe to increase the end-bearing resistance of

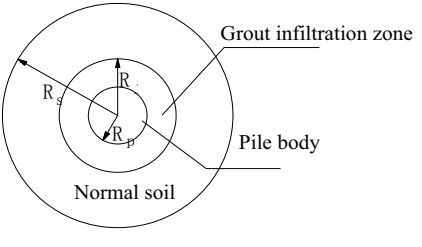

FIG. 2. Schematic diagram of grouted gravel pile composite ground.

the pile (FU and WANG 1997). Figure 2 is schematic diagram of composite foundation of grouted gravel pile; in the Fig. “Rp” is radius of pile body and “Rj” is radius of grout infiltrated zone, and “Rs” is radius of reinforcement zone.

THE EXPERIMENTAL STUDY OF SOFT GROUND IMPROVEMENT BY GROUTED GRAVEL PILE

Settlement in the Reinforcement Zone

Settlement observation of the project at City Ring Expressway in Ningbo includes settlement observation of pile head and ground surface of the soil between piles. Settlement of pile head and soil between piles in deep layer and layered soil between piles for dynamic control of construction speed of expressway embankment are monitored to study settlement of grouted gravel pile and soil between piles under embankment load. One typical monitoring cross section (K25+635) was selected and the settlement curves against time and embankment load are shown in Figure 3. (Note: Ta and Td refer to left and right settlement plates on the soil between piles of the first row of piles on the inner side of shoulder and Tb refers to settlement plate on the soil between piles adjacent to pile tip of central line of embankment. “Tc” refers to settlement plate on the top of pile head at central line of embankment and A refers to settlement plate in deep layer at pile toe at central line of embankment and B refers to settlement plate in deep layer in soil between piles adjacent to pile tip at embankment central line).

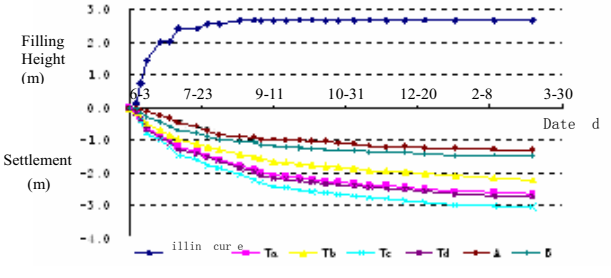

FIG. 3. Settlement curves at cross section of K25+635.

Following variation rules can be observed from Figure 3. Settlement increases with fill height of the embankment and there are several apparent inflection points in the settlement curve. Settlement of pile head and soil between piles are smaller during initial embankment filling period with a slower settlement rate and there is almost no settlement of pile head and the load is mainly taken by soil between the piles. Settlement rates of pile head and soil between piles have the increasing trend when embankment filling height reaches 2.5 m. The settlement rate of soil between piles is

much more than that of pile head and embankment load is adjusted on the top of pile and soil between piles. The grouted gravel piles in the selected cross section are between 28 m and 30 m and they are embedded 0.5 m into the sand gravel layer. Due to infiltration and cementation effect at pile toe, an excellent bearing layer is formed. The soil is effectively reinforced and the settlement is reduced.

Within 6 months after the road pavement is constructed, the monitored settlement is compared with other different ground improvement methods such as vacuum preloading and plain concrete pile listed in Table 1. Settlement observation data of all the sections with different treatment method are shown in Figure 4; the figure show that grouted gravel pile has the best improvement effect. The design settlement of post construction is 7.8 cm however calculated settlement of post construction is between 8 cm and 15 cm according to measured settlement data which is more than design settlement. There are mainly three reasons for that: First, the treatment depth of City Ring Expressway in Ningbo is about 24 m with many construction difficulties and the construction technology need to be improved. Second, insufficient knowledge to live load for design especially for influence on bridge head. Third, insufficient compaction of the fills at the bridge abutment. From settlement observations after construction we can see that pile diameter of 50 cm and gap of 2.7 m and strength of C15 can meet the design requirements completely to define a basic parameter scope for design in the future.

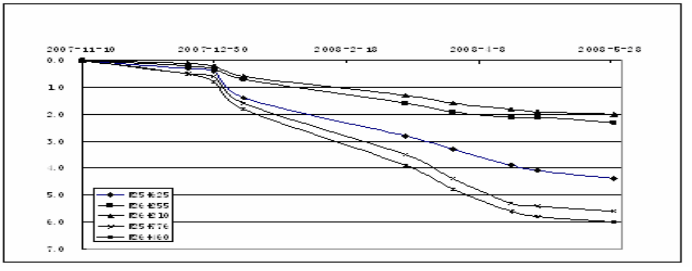

FIG. 4. Settlement observed for all sections with different improvement method.

Table 1. Ground Improvement Methods on Selected Cross Section

Pile No.	K25+625	K26+255	K26+210	K25+776	K26+460
Improv-ement method	Grouted gravel pile			Vacuum preloading	Plain concrete pile
	Diameter: 40 cm Strength: C10 Spacing: 3 m	Diameter: 50 cm Strength: C20 Spacing: 2.4 m	Diameter: 60 cm Strength: C15 Spacing: 2.7 m		

Static Load Test of Pile Foundation

To study the bearing performance, working mechanism and improvement effect on the ground adjacent to composite foundation of grouted gravel pile, some of static

load tests were carried out on grouted gravel piles in western section of City Ring Expressway in Ningbo.

In this paper, the ultimate capacity of the grouted gravel pile is assessed based on the following methods: (1) select the load at which there is a sudden change in Q-s curve, and (2) select the load at 60 mm pile head settlement.

Figure 5 shows the load settlement curve Q-s measured during field testing.

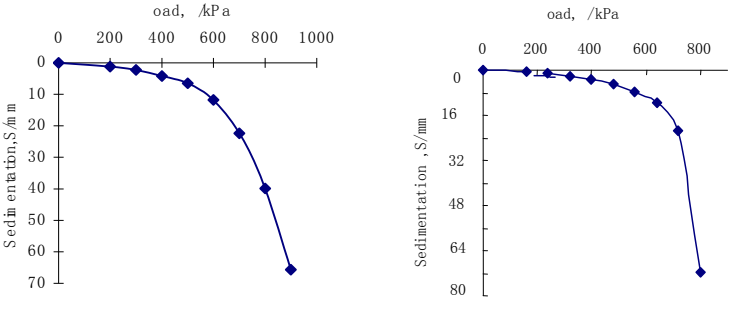

FIG. 5. Typical Q-S curve of single grouted gravel pile (a) smooth variation type, pile 11-12#, and (b) sudden variation type, pile 14-12#.

Table 2. Summary of Ultimate Capacity of Single Pile from Every X-Section

Serial	Position	Pile No.	Q-S Curve Type	Ultimate Bearing Capacity(kN)
1	K25+667	7-6	Smooth variation type	500
2	K26+045	10-12	Smooth variation type	800
3	K26+110	11-12	Smooth variation type	800
4	K26+255	14-12	Sudden variation type	720
5	K26+316	6-5	Sudden variation type	500

The capacity of the composite piled foundation is defined as: (1) half of the extreme load if available, and (2) select the load at certain displacement ratio, i.e., s/b (s is settlement, and b is the width or diameter of the bearing plate) between 0.004 and 0.010 based on the settlement design requirement. If the actual load is less than 1.5 times of selected load, the capacity of the composite piled foundation is then half of the selected loads. Table 3 summarizes the results for the composite piled foundation from every cross section.

Based on the field test results, the grouted gravel pile has a relatively high bearing capacity due to the fact that the shaft friction of the pile is significantly improved compared to other types of pile. The grouted gravel piles can be used as composite piled foundation to reduce settlement and improve the ground condition.

Table 3. Results of Bearing Capacity of Composite Piled Foundation

Position	Pile No. (#)	The Maximum Loading Capacity (kN)	Accumulated Settlement (mm)	Residual Settlement (mm)	Extreme Bearing Capacity of Composite Groundwork (kPa)
K24+600	2-3	1000	320.16	308.38	225
K25+635	Testing pile-9	600	178.54	163.47	240
K25+670	Testing pile-1 Testing pile-2 Testing pile-3 Testing pile-4	2000	448.78	434.63	200
K25+670	Testing pile-5 Testing pile-6 Testing pile-7 Testing pile-8	2100	458.19	447.92	210
K26+110	10-7	1500	281.93	276.69	216
K26+166	6-11	1610	410.42	398.69	199
K26+255	12-16	1350	94.88	78.08	208

CONCLUSIONS

(1) This paper discussed the reinforcement mechanism of the grouted gravel pile. Post grouting technology is applied to inject the grout into the void of gravels for stronger cementation and avoid lateral mud and fragments at pile toe. This simplified technology results in the same effect of reinforcement compared to the lateral and end-bearing post grouting technology.

(2) Field static load tests were performed on single grouted gravel piles and composited piled foundations. The results indicate that the design loads are satisfied using the grouted gravel piles with relatively small settlement.

ACKNOWLEDGMENTS

The authors appreciate the support of T. Zhang in format, spelling and grammar.

REFERENCES

LIU, H.L., and CHEN, Y.H. (2006)."Grouted gravel pile Technology and Application."*Rock and Soil Engineering Interface*,(7):27-30.

ZHANG, W., and RUAN, B. (2002)."Test Research on Bearing Capacity on the Bottom of Pressure Grouting Pile." *Journal of Zhuzhou Institute of Technology*, Vol.16(1):83-85.

GUO, Q.Q., and LI, Z. (2003) "Testing Research and Analysis on Enlarged Toe Post-grouting Pile on the Site ." *Rock and Soil Mechanics*,Vol.24(5):804-80

FU, W.X., and WANG, Q.Y. (1997)."Load Test Research of Pressure Grouting Pile on the Site." *Beijing Water Resources*, (3):47-51.

Pile Samples Classification Method Based on the Self-Organizing Map Neural Network

SiSi Liu[1], MingHua Zhao[2], MingHui Yang[3], and Wei Pan[4]

[1]Research Student (Ph.D), College of Civil Engineering, Hunan University, Changsha, 410082,China; Email: liusi1949@sina.com

[2]Professor, College of Civil Engineering, Hunan University, Changsha, 410082,China; Email: mhzhaohd@21cn.com

[3]Associate Professor, College of Civil Engineering, Hunan University, Changsha, 410082,China; Email: yamih@126.com

[4]Research Student (Ph.D), School of Information Science and Engineering, Central South University, Changsha, 410083,China; Email: viviorange@gmail.com

ABSTRACT: To reduce the noise in learning samples while using BP neural network to predict the bearing capacity of pile foundation, a self-organizing map neural network was adopted to classify the collected pile samples in the paper. Firstly, to maintain the SOM network at a stable situation, pile samples were discriminated into symbol codes and character codes, and a new coding model of pile character was established, by which a SOM neural network's weight formula of reduction was derived. Then, clustering of pile samples were shown by calibrating the maximum response cell of the self-organizing map neural network. Finally, case studies using the clustered samples as input vector to a BP network were presented, and the results showed that it was a good alternative approach for estimating the bearing capacity of pile foundation by using the improved solution with the characters of simplicity.

INTRODUCTION

Neural network technique, for its multivariate analysis decision-making ability and fuzzy judgment ability, is ideally suited for geotechnical problems such as pile capacity prediction. Among all kinds of neural networks, Back-Propagation (BP) neural network, because of its simple structure, fast convergence and easy operation, has proved to be a good method for pile capacity prediction. However, difference of engineering environments, measurement error, device precision, subjective factors of

the engineers and technicians, etc, will make more noise in the sample data. So that, BP network will be harder to converge and lead to the presence of local minima. Furthermore, a large number of training iterations may force a neural network to over train. These are the main problems difficult to be solved when using the BP network in pile capacity engineering calculation.

In fact, larger numbers of the learning samples can not guarantee a better BP network performance. Instead, choosing suitable learning samples would make the BP network more effective and pertinent for the project. In view of this fact, this study uses self-organizing map (SOM) neural network to cluster analyze the pile samples, and obtains better mapping relation between input and output by the way of finding the data which have the same or similar network response in SOM, so as to make the learning samples less interference.

PILE DATA CLASSIFICATION USING SOM NETWORK

Details of SOM Network

Initial value of learning-rate function $\eta(n)$ is set as η_0=0.1, and then decrease gradually, but η_0>0.01; time constant τ_2=1000. The neighborhood function $h_{j,i}(n)$ should initially include almost all neurons in the network centered on the winning neuron i, and then shrink slowly with time. And it is realized by setting the time constant as τ_1=1000/logσ_0. When η<0.01, network get stuck in a metastable state, which belongs to a configuration of the feature map with a topological defect. So, keeping η>0.01 guarantees against the possibility of metastable states. The Neighborhood function $h_{j,i}(n)$ should contain only the nearest neighbors of a winning neuron, which may eventually reduce to 1 or 0 neighboring neurons.

Data Collation

This phase involved gathering the data for use in cluster analysis by SOM network. These data are drawn from actual case records compiled by Feng (1999) for piles in Shanghai area. This consist of results of 40 load tests on precast concrete piles driven into sandy soils. Details of the range of values for the records are summarized in Table 1. These data will also be used in training and testing the BP network. Because the output neuron of BP network is the pile load capacity, the data for use in cluster analysis by SOM network include pile length, pile diameter, embedded depth, side friction weighted mean and bearing capacity of pile tip soil.

Table 1. Summary of Range of Values

Property	Unit	Range of Values
Pile length	m	10.4~61
Pile diameter	mm	300~500
Embedded depth	M	8.4~60.05
Side friction weighted mean	kPa/cm	13~73
Bearing capacity of pile end soil	kPa	800~7800
Pile load capacity	kN	369~8250

Data Normalization

Before presenting the patterns to the SOM network, preprocessing of the data to values between 0-1 was carried out to improve training. The following normalization procedure (Masters 1993) was used. For a variable with maximum and minimum values of V_{max} and V_{min} respectively, each value, V, is scaled to its normalized value, A, using

$$A=(V-V_{min})/(V_{max}-V_{min}) \quad (1)$$

Results

Through SOM network cluster analysis, 40 data are classified into 30 models by the network response values. The data in the same model mean that they have the same network response, and the data in the neighboring models mean that they have the similar network response. The result of data cluster analysis, as shown in Figure 1, shows that some of the spots distributed around model 5 and model 21. The data near model 5 are dispersedly distributed; it shows that these parts of data have the similar network response. The data near model 21 are concentrated in model 20, shows that these parts of data have the same network response.

FIG. 1. SOM network cluster analysis output of piles data.

Training Data Classification

Use the cluster analysis output of SOM network to build training data of BP network. In this study, choose 2 data, No. 5 and No. 35 data, in the model 21~22 and model 1~10 to be the test data. As shown in Table 2, 7 data between model 21~22 are used to be the BP network's training data of No. 5, most of them have the same model type; 14 data between model 1~10 are used to be the BP network's training data of No. 35, and most of these data have similar network response.

PILE CAPACITY PREDICTION USING BP NETWORK

Details of BP Network

In this study, different training data set are used to train 3 BP networks. Initially,

all pile records are used as the training data of the network to calculate the output of No. 5 and No. 35; this network model is denoted as BP1. The second network model uses No. 5 training data set to calculate the output of No. 5 test data; this network model is denoted as BP2. In the third model, No. 35 training data set are used to calculate the output of No. 35 test data. No.5 and No. 35 training data set as in Table 2. In addition, all these three models have the same initial settings. The input data to the BP network consist of the pile length, pile diameter, embedded depth, side friction weighted mean and bearing capacity of pile tip soil. It requires an input layer of 5 neurons. For the problem described herein, a single hidden layer consisting of 12 neurons has been adopted. The output information is pile capacity only, so the out layer consisting of 1 neuron is required.

Table 2 Different Training Data of 2 Test Data

Test Data	Training Data
5	1,3,10,7,9,19,24
35	11,12,15,16,18,21,25,26,27,5,37,38,39,40

BP1-Prediction Using All Training Data

Network model BP1 using 38 training data to calculate outputs of No. 5 and No. 35 test data. The neural network output and the load test results are compared in Fig. 2. For training data, most of the predicted values are lying within ±20% error from the line of perfect agreement with BP1; for test data, output error of No. 5 is about 35% and that No. 35 is 61%.

BP2-Prediction Using No. 5 Training Data Set

Network model BP2 is used to calculate the output of No. 5 test data; 7 training data sets corresponding to No. 5 test data as in Table 2 are used in BP2. The neural network output and the load test results are compared in Fig. 3. It suggests that most of the predicted values are lying within ±10% error from the line of perfect agreement with BP2. Fig 3 also show a computed result and error distribution comparison between BP1and BP2. It is evident that BP2 have better performance than BP1 in the computed output of No. 5 test data and 7 training data sets.

BP3-Prediction Using No. 35 Training Data Set

Network model BP3 is used to compute the output of No. 35 test data. 14 training data sets corresponding to No. 35 test data as in Table 2 are used in BP3. The neural network outputs and the load test results are compared in Fig. 4; it suggests that most of the predicted values are lying within ±10% error from the line of perfect agreement with BP3. Fig. 4 also show computed result and error distribution comparison between BP1and BP3. It is evident that BP3 have a better performance than BP1 in computed the output of No. 35 test data and 14 training data sets. Interestingly, although training data sets used in BP2 and BP3 are all selected from results of cluster analysis of SOM network, BP2 have less error distribution than BP3.

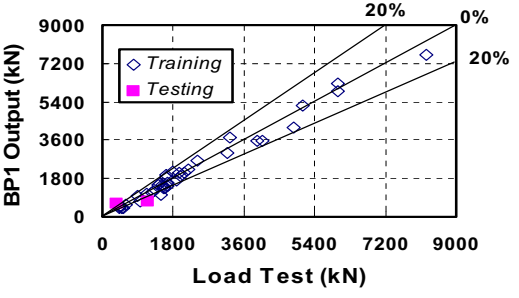

FIG. 2. Comparison of computed (BP1) and load test results.

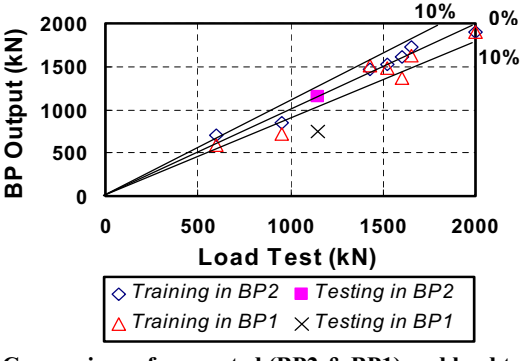

FIG. 3. Comparison of computed (BP2 & BP1) and load test results.

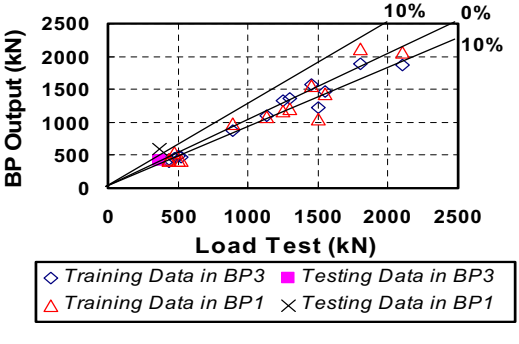

FIG. 4. Comparison of computed (BP3 & BP1) and load test results.

CONCLUSION

This paper investigated the potential of using SOM network to select training data

used in BP network. Building the training data through cluster analysis of SOM network can reduce noise from overabundances training data. The results of 3 BP networks show that compared with using all data from pile load test records, a better performance of network is obtained by using the training data which have the same or similar network responses. A major conclusion from this study is that a better BP network output of pile's bearing capacity can be obtained by using the data processed by SOM network.

REFERENCES

T. Kohonen. (2001). *Self-organizing Maps*, Springer-Verlag, Berlin.

K. Goser. (1997). "Self-organizing map for intelligent process control," in *Proceedings of WSOM'97, Workshop on Self-Organizing Maps, Espoo, Finland, June 4-6,* Helsinki University of Technology, Neural Networks Research Centre, Espoo, Finland, pp. 75-79.

Cigizoglu, H. K. (2005). "Application of generalized regression neural networks to intermittent flow forecasting and estimation." *J. Hydrol. Eng.*, 10(4), 336-341.

Kurup, P. U., and Griffin, E. P. (2006). "Prediction of soil composition from cpt data using general regression neural network." *J. Comput. Civ. Eng.*, 20(4), 281-289.

Lok, T. M. H., and Che, W. F. (2004). "Axial capacity prediction for driven piles using ann: Model comparison." *Geotrans 2004*, Geotechnical Engineering for Transportation Projects (GSP No. 126), M. K. Yegian and E. Kavazanjian, eds.

Middendprop, P. (2004). "Thirty years of experience with the wave equation solution based on the method of characteristics." *7th Int. Conf. on the Application of Stress Wave Theory to Piles*.

Pal, M., and Goel, A. (2006). "Prediction of the end depth ratio and discharge in semicircular and circular shaped channels using support vector machines." *Flow Meas. Instrum.*, 17(1), 50-57.

Pal, M. (2006). "Support vector machines-based modeling of seismic liquefaction potential." *Int. J. Numer. Analyt. Meth. Geomech.*, 30(10), 983-996.

Feng Ziliang, Sun Haitao, and Wang Shujuan. (1999). "Prediction of vertical ultimate bearing capacity of single pile by using artificial neural networks." *Journal of Tongji University*. 27(4), 397-401.

Ahmad I., and Akhtar N. K. (2006). "Kinematic seismic response of piles-importance and modeling." *GeoCongress 2006*, Geotechnical Engineering in the information Technology Age.

Che, W. F. (2003). *"Axial bearing capacity prediction of driven piles using artificial neural network." M.S. Thesis*, FST, University of Macau.

Geotechnical Design of a Bridge Widening Project in a Highly Active Seismic Region of Southern California

Endi Zhai[1], PhD, PE, GE, M. ASCE and Scott Lawson[2], PE

[1]Geotechnical Manager, HDR, Inc., USA; endi.zhai@hdrinc.com
[2]Project Engineer, Kleinfelder, Inc., USA; slawson@kleinfelder.com

ABSTRACT: This paper presents geotechnical issues and our design approaches for the Upper Oso Reservoir Bridge Widening located along State Route 241 in Mission Viejo, California. The total bridge length is approximately 1540 feet (470 m). The foundations of the existing bridge structures consist of 36-inch (0.91 m) diameter cast-in-drilled-hole (CIDH) piles and driven steel H-piles. The subsurface materials at the bridge site were investigated by a field exploration program. Key geotechnical design involved development of new seismic design parameters and acceleration response spectra for an Upper Level Earthquake (ULE) and a Lower Level Earthquake (LLE); evaluation of new fill and liquefaction-induced settlements on the existing and new foundations; pile foundation modeling and capacity assessment; abutment slope seismic stability and deformation.

INTRODUCTION

The existing Upper Oso Reservoir Twin Bridges are to be widened. The bridges are located along State Route 241 in Mission Viejo in Southern California. The site coordinates are approximately N33.6575 degrees and W117.6316 degrees. The total bridge length is approximately 1540 feet (470 m). Both of the existing left and right bridges have six spans and were constructed with cast-in-place pre-stressed concrete box girders. The widened portion of both the left and right bridges will have the same width of 44.7 feet (13.6 m), leaving a gap of varying width between the two widened bridges. The bridge elevation view is shown in Figure 1. The foundations of the existing bridge structures consist of 36-inch (0.91 m) diameter CIDH piles and driven steel H-piles (HP14x89 and HP14x102). The subsurface materials at the bridge site were investigated by drilling borings and CPTs at each support location, and found to be not uniform, but generally consisted of surficial deposits of artificial fill, alluvium, colluvium, and bedrock of different formations. Groundwater was as shallow as 18 feet (5.5 m) below ground surface near Bents 4 and 5. Key geotechnical design involved development of new seismic design parameters and acceleration response spectra for an ULE and a LLE adopted for seismic design of the project; evaluation of new fill and liquefaction-induced settlements on the existing and new foundations; pile

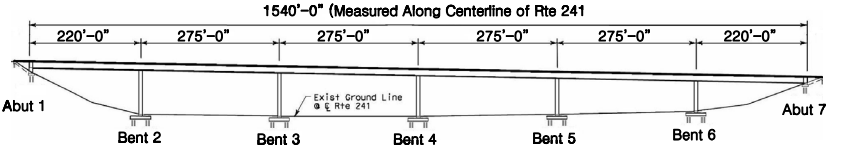

FIG. 1. Elevation view of Upper Oso Reservoir Bridge

foundation modeling and capacity assessment; abutment slope seismic stability and deformation.

SEISMIC DESIGN PARAMETERS AND RESPONSE SPECTRA

A seismic design criterion was established which requires to follow an ULE and a LLE seismic event. The ULE is corresponding to a smoothed envelop of the 975-year average return period probabilistic response spectra and the deterministic Maximum Credible Earthquake (MCE) acceleration response spectra (ARS) using California Department of Transportation (Caltrans) method. Structures are designed not to collapse at this level. The LLE is corresponding to a 72-year average return period probabilistic seismic hazard event. Structures remain elastic subject to this event.

For developing peak ground acceleration and response spectra subject to the ULE, we performed both probabilistic and deterministic seismic hazard analyses. The deterministic seismic hazard analysis followed Caltrans Seismic Design Criteria (Caltrans, 2006). The controlling fault, distance and peak bedrock acceleration (PBA) value are summarized as follows:

- Controlling fault: San Joaquin Hills Blind Thrust Fault (SJHF)
- MCE moment magnitude: 7.0
- Closest rupture distance: 7.8 km
- Soil Profile Type: D
- PBA value: 0.5g

The SJHF was not included in the current Caltrans Seismic Hazard Map. PBA value was calculated using Sadigh et al. (1997) attenuation relationship based on a moment magnitude of 7 and a closest rupture distance of 4.8 miles (7.8 km) from the SJHF to the bridge site. The Caltrans standard ARS curve corresponding to the above seismic parameters was selected and adjusted to account for the near-source rupture directivity effect as follows: 20% increase in spectral values for periods equal to or greater than 1.0 second; no change for periods less than 0.5 seconds; and spectral ordinates for periods between 0.5 and 1 second shall be determined by linear interpolation.

975-year and 72-year return period probabilistic seismic parameters and response spectra were computed using site-specific probabilistic seismic hazard analysis (PSHA) approach with the computer program EZ-Frisk (Risk Engineering, Inc., 2007). The ULE and LLE design ARS curves are presented in Figure 2.

FILL AND LIQUEFACTION INDUCED SETTLEMENTS

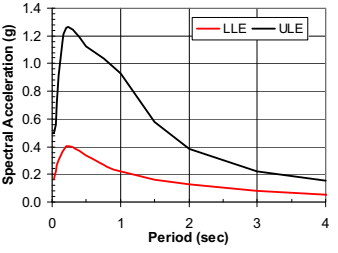

FIG.2. Design ARS Curves

Up to 15 feet (4.6 m) and 22 feet (6.7 m) of new fill was originally proposed for the widening structures at the locations of Bents 4 and 5, respectively. The proposed new fill placement is predicted to result in about 0.8 inch (2 cm) and 1.0 inch (2.5 cm) of settlement at the existing Bents 4L and 5L, respectively, which would cause downdrag on the existing piles. The maximum fill-induced settlement is predicted to be approximately 6½ inches (16.5 cm) and 7½ inches (19.1 cm) at the supports for the widening at Bents 4 and 5, respectively, which would require a long waiting period. We recommended that the maximum fill be reduced at Bents 4 and 5 to limit the settlement at the existing pile locations to not more than 0.4 inch (1 cm) to avoid downdrag loads on the existing piles, yet to allow a maximum compatibility of new and existing column heights. To do so, we performed consolidation settlement analyses repeatedly with varying configuration and thickness of the fill placement until the settlement on the existing piles not greater than 0.4 inch (1 cm), and concluded that the optimal fill thickness is 10 feet (3 m) at Bent 4 and 12 feet (3.7 m) at Bent 5. Our settlement analyses were based on the CPT data recently performed by us for this project using the Schmertmann's method (Schmertmann, 1978).

CPT data was also used to evaluate the liquefaction potential at the site. The calculated liquefaction-induced settlement is approximately 0.6 inches (1.5 cm) at the location of Bent 4 and 1.4 inches (3.6 cm) at the location of Bent 5, and insignificant at other support locations. Downdrag due to liquefaction-induced settlement at Bents 4 and 5 was considered in our pile capacity calculations for the proposed bridge widening.

PILE FOUNDATION MODELING AND CAPACITY ASSESSMENT

Existing Pile Foundation Stiffness Matrices

In general, structural behavior under seismic loading is a function of its dynamic response characteristics which are influenced by the relevant foundation properties. For realistic evaluation of the bridge response, it is necessary to model the force-deformation characteristics of the pile foundations and incorporate them in the analytical model of the bridge structure. We developed equivalent stiffness matrices for single piles and pile group at each bent location. Our analysis approach generally followed FHWA-HRT-06-032 "Seismic Retrofitting Manual for Highway Structures: Part 1 – Bridges" (FHWA, 2006). For a vertical pile group, the stiffness for the translational displacement terms (the two horizontal and the vertical displacement terms) and the cross-coupling terms can be obtained by merely multiplying the corresponding stiffness components of an individual pile by the number of piles.

However, the rotational stiffness terms (the two rocking and the torsional rotations) require consideration of an additional stiffness component. In addition to individual pile-head bending moments at each pile head, a unit rotation at the pile cap will introduce translational displacements and corresponding forces at each pile head (e.g. vertical forces for rocking rotation and lateral pile forces for torsional rotation). These pile-head forces will work together among the piles and will result in an additional moment reaction on the overall pile group. Pile cap passive resistance may be added to the above pile group stiffness. Because of the possibility of soil settlement and the uncertain interaction between the footing and the piles, contributions to soil stiffness and capacity from the footing's base and side shear are neglected; hence the primary source of lateral resistance is the mobilization of passive pressure on the vertical face of the pile cap. Due to space limitation, we only present the results for Bent 4L in Table 1.

Table 1. Pile Foundation Stiffness Matrix

PILE GROUP STIFFNESS MATRIX	Fixed-Head Condition	Pin-Head Condition
Translational Stiffness, K_δ (K11g, Long. Direction)	3.34E+06 LB/inch	1.81E+06 LB/inch
Translational Stiffness, K_δ (K22g, Transv. Direction)	4.58E+06 LB/inch	2.52E+06 LB/inch
Axial Stiffness, K_a (K33g, Vertical Axis)	6.17E+07 LB/inch	6.17E+07 LB/inch
Rotational Stiffness, K_θ (K44g, about Long. Direction)	1.22E+12 Inch-LB/Rad	8.29E+09 Inch-LB/Rad
Rotational Stiffness, K_θ (K55g, about Transv. Direction)	7.28E+11 Inch-LB/Rad	4.98E+09 Inch-LB/Rad
Torsional Stiffness, K_θ (K66g, about Vertical Axis)	1.25E+11 Inch-LB/Rad	4.75E+08 Inch-LB/Rad
Cross-Coupling Stiffness, $K_{\delta\theta}$ (K15g)	1.35E+08 LB	0.0 LB
Cross-Coupling Stiffness, $K_{\delta\theta}$ (K51g)	1.35E+08 LB	0.0 LB
Cross-Coupling Stiffness, $K_{\delta\theta}$ (K24g)	2.39E+08 LB	0.0 LB
Cross-Coupling Stiffness, $K_{\delta\theta}$ (K42g)	2.39E+08 LB	0.0 LB

Widening Foundation Type and Capacity

In order to maintain stiffness and deformation behavior of the new structures similar to the existing structures, use of the same type and same size piles as the existing structures, in particular at the bents, is highly desirable. The foundation types evaluated for support of the proposed widening bridge structures consisted of driven steel H-piles (HP14x89 and HP14x102) and 36-inch diameter CIDH piles. Geotechnical axial capacity includes both skin friction and end bearing for driven steel H-piles and only skin friction for CIDH piles. Skin friction was also ignored in the fill materials. To calculate the tension capacity, a reduction factor of 0.7 was applied to the axial capacity due to skin friction. Downdrag due to liquefaction-induced settlement would occur at Bents 4 and 5 locations and therefore considered in the design. A neutral plane at a depth corresponding to 0.4 inch (1 cm) liquefaction-induced settlement was used to calculate the negative skin friction. Post-liquefaction residual strength based on the mean value from the Seed and Harder (1990) chart was assigned for liquefiable layers. The recommended pile capacity and required penetrations are presented in Table 2. Due to space limitation, Table 2 only shows the results for the left bridge widening.

Table 2. Pile Data Table

Location	Pile Type	Bottom of Pile Cap Elev. (ft, MSL)	Design Loading (Service) (kips)	Nominal Resistance (kips)		Design Tip Elev. (ft, MSL) [1]	Specified Tip Elevation (ft, MSL)
				Compression	Tension		
Abutment 1L	36-inch CIDH	950.46	500	1000	600	887.0 (1) 891.0 (2)	887.0 (1)
Bent 2L	36-inch CIDH	865.59	N/A	1000	600	831.0 (1) 835.0 (2)	831.0 (1)
Bent 3L	HP 14x102	862.59	N/A	400	200	821.0 (1) 813.0 (2)	813.0 (2)
Bent 4L	HP 14x102	857.25	N/A	400	200	821.0 (1) 819.0 (2) 766.0 (3)	766.0 (3)
Bent 5L	HP 14x102	859.59	N/A	400	200	798.0 (1) 812.0 (2) 767.0 (3)	767.0 (3)
Bent 6L	HP 14x89	872.59	N/A	400	200	815.0 (1) 817.0 (2)	815.0 (1)
Abutment 7L	HP 14x89	929.46	200	400	200	834.0 (1) 835.5 (2)	834.0 (1)

Notes:

[1] Design tip elevation is controlled by the following demands:
(1) Compression, (2) Tension, and (3) Downdrag.

The new piles shall be spaced a minimum of 2.5 pile diameters (center-to-center). With this spacing, axial group action may be ignored.

Lateral pile capacity was evaluated using LPILE plus v5.0 (Ensoft, 2006) for pile head deflections at 0.25-inch (0.6 cm) and 1-inch (2.5 cm) which correspond to service and seismic conditions, respectively. The calculated pin-head lateral capacities for Bents 4 and 5 of the left bridge widening were approximately 15 kips (67 kN) and 45 kips (200 kN), respectively. A p-multiplier of 0.6 was used which was developed based on center-to-center spacing of 3 diameters (widths) of the pile.

ABUTMENT SLOPE STABILITY AND DEFORMATION

The embankment slope gradients were planned to match the existing 2H:1V longitudinal slope gradients. Overall (global) slope stability of the slopes at Abutments 1 and 7 was analyzed using the Simplified Bishop's Method for circular slip surfaces and the Modified Janbu Method for slip surfaces of noncircular shape. The design criteria utilized are as follows: permanent abutment slopes are required to have a minimum FOS of 1.5 for the static condition and a minimum FOS of 1.1 for pseudostatic condition using the Caltrans recommended horizontal earthquake loading coefficient equal to 1/3 of the horizontal peak acceleration. A horizontal earthquake loading coefficient of 0.17 g was used, which corresponds to the 0.5g peak horizontal ground acceleration value predicted for the site. Results of the analyses indicated that Abutment 1 slope had a pesudostatic FOS less than 1.1 which would require grading or ground remediation to satisfy the minimum FOS requirement. Re-grading or soil improvement was considered not economical, it was decided to evaluate seismic

deformation and check structural tolerance against the predicted seismic deformation. We performed a seismic deformation evaluation using simplified Bray and Rathje (1998) method and verified with Makdisi and Seed (1978) method. Our evaluation concluded that the abutment deformation subject to the ULE is on the order of 1 inch (2.5 cm). The structural designer performed structural evaluation and concluded that the slope deformation subject to the ULE is tolerable for the bridge structures. Therefore, the owner and the reviewer were satisfied.

CONCLUDING REMARKS

Geotechnical design for a bridge widening project located in a highly active seismic region of southern California was presented in this paper. Two levels of seismic design were adopted which follow an Upper Level Earthquake (975-year probabilistic or Caltrans MCE, whichever is higher) and a Lower Level Earthquake. Bridge structures were designed not to collapse at the ULE level and to behave elastically subject to the LLE event. Probabilistic and deterministic seismic hazard analyses were performed to develop the peak ground acceleration, magnitude, distance to the governing fault, and response spectra for seismic design of the project. New fill placement thickness was optimized so as to avoid a downdrag load on the adjacent existing piles, yet to allow a maximum compatibility on the widening and existing column heights. The stiffness and capacity of the existing and new pile foundations evaluated and provided to the structural designer resulted in a satisfactory evaluation and design of both the existing and widening structures under the service loading and seismic loading conditions.

REFERENCES

Bray, J.D. and Rathje, E.R. (1998) “Earthquake-induced displacements of solid-waste landfills,” *Journal of Geotechnical and Geoenvironmental Engineering*, ASCE, Vol. 124, No. 3, pp. 242-253.

California Department of Transportation, (2006). “Seismic design criteria.”

FHWA-HRT-06-032, (2006). “Seismic retrofit manual for highway structures: part 1 - bridge.”

Makdisi, F.I. and Seed, H.B. (1978). “Simplified procedure for estimating dam and embankment earthquake-induced deformations,” *Journal of the Geotechnical Engineering Division*, ASCE, Vol. 104, No. GT7, July.

Risk Engineering, (2007). “EZ-Frisk Computer Program version 7.24.”

Schmertmann, J.H. (1978) “Guidelines for cone penetration test performance and design,” FHWA-TS-78-209.

Sadigh, K., Chang, C.-Y., Egan, J.A., Makdisi, F., and Youngs, R.R. (1997). “Attenuation relationships for shallow crustal earthquakes based on California strong motion data, *Seismological Research Letters*, Vol. 68, No. 1.

Seed, R.B. and Harder L.F. (1990). “SPT-based analysis of cyclic pore-pressure generation and undrained residual strength.” *Proceedings, H.B. Seed Memorial Symposium*, UC Berkeley, Vol. 2, 351-376.

Time Effect on Bearing Capacity of Composite Foundation with Stone Columns

ZHANG Ling[1], ZHAO Ming-hua[2] and ZHAO Heng[3]

[1]Ph.D candidate, Geotechnical Engineering Institute, Hunan University, Changsha, China, 410082; zhanglhd@163.com

[2]Professor, Geotechnical Engineering Institute, Hunan University, Changsha, China, 410082

[3]Ph.D candidate, Geotechnical Engineering Institute, Hunan University, Changsha, China, 410082

ABSTRACT: Stone column is an economical treatment method in embankment engineering. Controlling potential bearing capacity failure is a challenging problem in this design technique. A modified bearing capacity calculation method which takes the influence of time into account is presented by utilizing two-dimension consolidation theory. Also, a case study to validate the proposed method and to study the time effect on the bearing capacity of stone column foundation system is also presented in this paper. The analytical result shows that the bearing capacity of stone column composite foundation increases with increase in time. It is therefore suggested that the time effect on the bearing capacity of the composite foundation formed by stone columns should be taken into account in embankment engineering for the economical and optimal design.

INTRODUCTION

A composite foundation formed by stone columns (granular piles) is an effective ground improvement technique for increasing bearing capacity, reducing ground settlements, and accelerating consolidation of the soft ground; and it has been extensively used over the last three decades in Europe, Asia, and the United States. Bergado et al. (1990) found from field studies that the installation of granular piles increased the bearing capacity by as much as four times. In recent years, many studies have been carried out to understand the behavior of foundation reinforced by stone columns (Ambily & Gandhi, 2007; J. Liu, 2006; D. Zhang, 1999). How to effectively control potential bearing capacity failure is a challenging problem to the geotechnical engineers. However, the analysis of such composite foundations is complex and challenging (Malek, 2007; Su, 2004; Chen, 2003; Poorooshasb, 1997); despite wide use of stone columns and developments in construction methods/ equipments, present design methods are empirical and only limited information is available on the design of stone columns in codes/ textbooks. Moreover, it should be said that the time effect

on the bearing capacity of composite foundation has not been widely discussed in the geotechnical literature as done by P. Zhao et al. (2002). The purpose of this paper is to present a modified bearing capacity calculation method with consideration of pile arrangement, bulging deformation of stone column and time effect on the bearing capacity.

BEARING CAPACITY OF STONE COLUMN COMPOSITE FOUNDATION

Bearing Capacity Calculation Method

Among various theoretical methods, area ratio method is the most popular method to determine the bearing capacity of composite foundation, and its expression is:

$$f_{ps} = K_1 \lambda_1 m f_p + K_2 \lambda_2 (1-m) f_s \quad (1)$$

where f_p, f_s are the bearing capacities of stone column and the surrounding soil respectively; K_1, K_2 are the modified coefficients, usually $K_1>1$, $K_2>0$; λ_1 is the ratio of the real bearing capacity of stone column to its ultimate bearing capacity, usually $\lambda_1 \leq 1$; λ_2 is the ratio of the real bearing capacity of the soil to its ultimate bearing capacity, usually $0.4 \leq \lambda_2 \leq 1$; m is the replacement ratio of composite foundation.

A New Method to Determine f_p and f_s

(1) **Basic assumptions**. Normally, stone column composite foundations consist of numbers of columns installed in a uniformly and equally spaced pattern. Thus each column acts within a cylindrical cell with a radius of influence denoted by r_e. Balaam and Booker (1981) relate the diameter of the cell, ($2r_e$,) to the actual column spacing by the relation $2r_e=cS$, where S is the actual column spacing and c is a constant having values of 1.05 and 1.13 for triangular and square patterns respectively. To simply the problem, following assumptions have been made: (•a) the stone column with an elastic modulus E_p and a Poisson's ratio μ_p and the soil with an elastic modulus E_s and a Poisson's ratio μ_s are both assumed to possess material linearity; (•b) the vertical stress along the length of column is a constant; (•c) the vertical displacements of the stone column and the surrounding soil under the base are same; (•d) the radial stress distribution of the stone column is symmetrical.

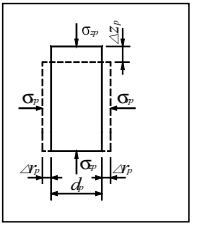

FIG. 1. Stress-strain relationship of stone column.

(2) **Calculation of the vertical vtress of vtone column σ_{zp}.** A homocentric column formed by a single column and the surrounding soil from the composite foundation system is chosen to analyze, as shown in Fig. 1.

According to the theory of elastic mechanics, and substituting K_p=-$\varepsilon_{rp}/\varepsilon_{zp}$ =$\Delta V_{rp}/(2\Delta V_{zp})$ into equations, following equations are obtained:

$$\begin{cases} \sigma_{zp} = \dfrac{E_p}{(1+\mu_p)(1-2\mu_p)}[2\mu_p - \dfrac{(1-\mu_p)}{K_p}]\varepsilon_{rp} \\ \sigma_{rp} = \dfrac{E_p}{(1+\mu_p)(1-2\mu_p)}(1-\dfrac{\mu_p}{K_p})\varepsilon_{rp} \end{cases} \quad (2)$$

where σ_{zp} and σ_{rp} are the vertical and lateral stresses of stone column, respectively; ε_{zp}, ε_{rp} are the vertical and lateral strains, respectively; ΔV_{zp}, ΔV_{rp} are the volume increments in vertical and lateral, respectively; the range of K_p is from 0 to 0.5.

(3) **Calculation of the vertical stress of surrounding soil σ_{zs}.** According to the theory of cavity expansion presented by Vesic (1972), the average lateral stress of the surrounding soil $\overline{\sigma_{rs}}$ is

$$\overline{\sigma_{rs}} = \frac{\int_{r_p}^{r_u}\sigma_{rs}dr}{r_u - r_p} = \frac{\int_{r_p}^{r_u}\left[r_p^2\sigma_{rp}(r,z)\left(1-r_u^2/r^2\right)/\left(r_u^2-r_p^2\right)\right]dr}{r_u - r_p} = -\frac{r_p\sigma_{rp}}{r_u + r_p} \quad (3)$$

where r_p is the radius of stone column; r_u is the effective radius (Zhao M. H.,2006),

$$r_u = r_p \exp\left\{\left[(1-\mu_s)E_p(K_p-\mu_p)\right]/\left[E_s K_p(1+\mu_s)(1+\mu_p)(1-2\mu_p)\right]\right\} \quad (4)$$

If r_u>S/2, the expansive effects of the nearby columns will not overlap. If r_u<S/2, the expansive effects of the nearby columns will be overlapped, as shown in Fig. 2.

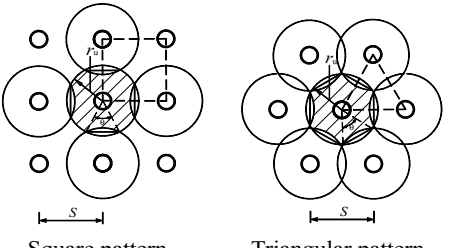

Square pattern Triangular pattern

FIG. 2. Effective area.

According to the assumption (c), the vertical strain of the stone column ε_p is same as that of the soil ε_{zs}. Substituting the following relationships ε_{zs}=ε_{zp} and K_p= -$\varepsilon_{rp}/\varepsilon_{zp}$ into ε_{rs}=(σ_{zs}-2$\mu_s\sigma_{rs}$)/E_s, which is derived from the theory of elastic mechanics, and with consideration of different column span and different column's arrangements, the vertical stress of the surrounding soil σ_{zs} can be expressed as follows.

For square patterns, σ_{zs} is:

$$\sigma_{zs1W} = \frac{2\mu_s A_{1W}\overline{\sigma_{rs}}}{A_s} - \frac{E_s\varepsilon_{rp}}{K_p},\ (r_u \le S/2);\quad \sigma_{zs2W} = \frac{2\mu_s A_{2W}\overline{\sigma_{rs}}}{A_s} - \frac{E_s\varepsilon_{rp}}{K_p},\ (r_u \ge S/2) \quad (5)$$

For triangular patterns, σ_{zs} is:

$$\sigma_{zs1V} = \frac{2\mu_s A_{1V}\overline{\sigma_{rs}}}{A_s} - \frac{E_s\varepsilon_{rp}}{K_p},\ (r_u \le S/2);\quad \sigma_{zs2V} = \frac{2\mu_s A_{2V}\overline{\sigma_{rs}}}{A_s} - \frac{E_s\varepsilon_{rp}}{K_p},\ (r_u \ge S/2) \quad (6)$$

where A_{1v}, A_{2v} are the expansive effect areas without and with consideration of the

overlapped effect for the rectangular form arrangement, $A_{1W}=\pi(r_u^2-r_p^2)$, $A_{2W}=r_u^2(\pi-2\theta)+2r_uS\sin\theta$; A_{1w}, A_{2W} are the expansive effect areas without and with consideration of the overlapped effect for the triangular form arrangement, $A_{1V}=0.5\pi(r_u^2-r_p^2)$, $A_{2V}=0.5r_u^2(\pi-3\theta)+1.5r_uS\sin\theta$; θ=arccos($S/2r_u$).

(4) **Calculation of f_p and f_s.** Then, f_p and f_s can be calculated by following equations

$$f_p=\sigma_{zp|z=0};\ f_s=\sigma_{sp|z=0} \tag{7}$$

In the real project, the surrounding soil is going to deform earlier than the columns, the lateral strain ε_{rp} is determined by Eq.(5) or Eq.(6). Then f_p can be determined Eq. (3). Substituting f_s and f_p into Eq. (1), the bearing capacity of stone columns composite foundation is determined.

Time Effect on The Bearing Capacity of Composite Foundation

Based on the consolidation theory, following relationship exists:

$$s_t = U_t s_u \tag{8}$$

where s_t is the settlement of foundation at t time; s_u is the ultima to settlement; U_t is the consolidation degree of composite foundation, which can be calculated by Carrillo theorem as follow:

$$U_t=1-8\exp(-\beta t)/\pi^2 \tag{9}$$

where $\beta=(1+\kappa F)[\rho_z/(1+F)+\rho_r]$; $\rho_z=\pi^2C_v/(4H^2)$; $\rho_r=2C_h/(F_a+32G/\pi^2)r_u^2$; $\kappa=E_p/E_s$; $F=1/(n^2\text{-}1)$; $F_a=[(\ln n\text{-}0.75)\ n^2+1\text{-}1/(4n^2)]\ /(n^2\text{-}1)$; $n=r_u/r_p$; $G=(k_{rs}\cdot H^2)/(k_{rp}\cdot 4r_p^2)$; k_{rs}, k_{rp} are the lateral penetrative coefficients of soil and stone column respectively; H is the depth of the composite foundation; t is the consolidation time; C_h is the lateral consolidation coefficient of soil, $C_h=k_{rs}E_s/\gamma_w$; C_v is the vertical consolidation coefficient of soil, $C_v=k_vE_s/\gamma_w$; k_v is the vertical penetrative coefficient of soil; γ_w is the unit-weight of water.

Following relationship is derived from Eq. (8):

$$s_t=(U_t/U_{t0})\cdot s_0 \tag{10}$$

where s_0 is the initial settlement and s_t is the settlement at t time, U_{t0} is the initial consolidation degree of the composite foundation.

Let $1+\alpha=U_t/U_{t0}$, then $p_{sp,t}=(1+\alpha)p_{sp,0}$ (12)

where $p_{sp,t}$, $p_{sp,0}$ are the bearing capacities of composite foundation at time t and t_0 respectively; $p_{sp,0}$ can be calculated by Eq. (1).

CASE STUDY

To validate the above bearing capacity calculation method, a composite foundation with stone columns in Jinzhu highway is selected. This section of highway embankment is build over soft proluvial soils. When calculating, the penetrative

coefficients of soil are k_{rs}=1.0×10^{-4} m/d, k_v=1.0×10^{-4} m/d. The elastic modulus of the soil E_s is 4 MPa, and the Poisson's ratio μ is 0.3. The diameter of the stone column is 385 mm and its length is 5.2 m, the actual spacing from center to center of columns is 1.5 m. The columns are arranged in triangular pattern, so the replacement ratio of composite foundation m is 17.5%. The elastic modulus of the stone column E_p is 24 MPa, and Poisson's ratio μ is 0.25. K_p is chosen as 0.385 and the penetration coefficient of the stone column k_{rp} is 0.01m/d. After the columns' construction, the degree of the consolidation foundation has reached 40%.

The bearing capacities of the single stone column, the surrounding soil and the composite foundation are shown in Table 1. The bearing capacities calculated by Eq. (1) and the comparison between the measured bearing capacities and calculated ones are also shown in Table 1. With consideration of the time effect, calculated bearing capacities of the composite foundation are shown in Table 2. The rest periods are chosen as15d, 30d, 60d, 120d, and 240d.

Table 1. Bearing Capacity of Stone Column, Soil and Composite Foundation

Test point	Allowable Bearing Capacity in Situ (kPa)			Calculated Bearing Capacity	calculated value / measured value
	Stone column	Surrounding soil	Composite foundation		
1#	196	137	173	133.30	77.05%
2#	210	146	155.5	142.82	91.85%
3#	220	138	156.9	149.88	95.53%

Table 2. Relationship Between Bearing Capacity of Composite Foundation and Time

Rest period (d)	15	30	60	120	240
Consolidation degree (%)	50.81	58.36	70.15	84.66	95.95
Increase rate of bearing capacity (%)	27.03	45.90	75.38	111.65	139.88
Daily average increase rate (%)	1.80	1.53	1.26	0.93	0.58

As shown in Table 2, the time effect on the bearing capacity of stone column composite foundation is obvious. In addition, the daily average rate of increase is decreased day by day. However, in the real project, the relationship between p and s is un-elastic, and the bearing capacity of foundation may not increase as much as presented in Table 2 when degree of consolidation is high, but it's true that the bearing capacity of foundation is increases with increase in time.

CONCLUSIONS

A modified method to calculate the bearing capacity of stone column foundation system is proposed with consideration of the bulging deformation characteristic and the time effect. Compared with the traditional bearing capacity method, the presented

case study showed that the method is more closer to the real behavior of stone column composite foundation for taking into account the influence of the bulging deformation characteristic, the pile arrangement and the time effect of the bearing capacity. The presented study showed that the calculated bearing capacities of the stone column composite foundation are much closer to the measured ones. The results also indicate that the bearing capacity of composite foundation increased as time increased. Therefore it is suggested that the time effect on the bearing capacity of stone column composite foundation should be taken into account for the optimum design.

ACKNOWLEDGMENTS

Financial support for the work reported here was provided through a project (No. 2006AA11Z104) supported by the High-Tech Research and Development Program of National 863 Project, China.

REFERENCES

Ambily A. P. and Gandhi Shailesh R. (2007). "Behavior of stone columns based on experimental and FEM analysis". ASCE, *Journal of Geotechnical and Geoenviromental Engineering*, Vol. 133(4): 405-415.

Balaam N. P. and Booker J. R. (1981). "Analysis of rigid rafts supported by granular piles". *Int. J. for Num. and Anal. Methods in Geomech.*, Vol.5:379-403.

Chen X. H. (2003). "Discuss on the calculation method of bearing capacity of stone column composite ground". *Soil Engineering And Foundation*, Vol.17(3):58-60.

Liu J. and Zhao M. H. (2006). "Elastoplastic analysis of character for composite foundation with gravel columns". *Rock and Soil Mechanics*, Vol.27(10):1678-1684.

Malek Abdelkrim and Patrickde Buhan (2007). "An elastoplastic homogenization procedure for predicting the settlement of a foundation on a soil reinforced by columns". *European Journal of Mechanics A/Solids*, Vol.26:736-775.

Poorooshasb H. B. and Meyerhof G. G. (1997). "Analysis of behavior of stone columns and lime columns". *Computers and Geotechnics*, Vol.20(1):47-70.

Zhang D. (1999). "Functional mechanism analysis and settlement computation on composite foundation of gravel pile". *Rock and Soil Mechanics*, Vol.20(2):81-86.

Zhao M. H., Yang M. H., Li L. X., et al. (2006). "Study on the calculation of bearing capacity of composite foundation on discrete material pile". *Journal of Shenyang Jianzhu University (Natural Science)*, Vol.22(2):212-216.

Zhao P., Yao Q. Y., Ouyang and X. H. (2002). "The time effect on the bearing capacity of the stone column composite foundation". *Hunan Communication Science and Technology*, Vol.28(4):19-21

Sun J., Liu K. F., Xie X. Y. and Zhu X. R. (2004). "Analysis on bearing capacity of diving dry-vibration compaction stone piles". *Chinese Journal of Rock Mechanics and Engineering*, Vol.23(supp 1):4568-4572.

A Framework for 3D Nonlinear Ground-Foundation Analysis

Jinchi Lu[1], Ahmed Elgamal[2], and Thomas Shantz[3]

[1]Assistant Project Scientist, Department of Structural Engineering, University of California, San Diego, La Jolla, CA 92093-0085; jinlu@ucsd.edu
[2]Professor, Department of Structural Engineering, University of California, San Diego, La Jolla, CA 92093-0085; elgamal@ucsd.edu
[3]Senior Research Engineer, California Department of Transportation, Division of Research and Innovation, 1227 O Street, MS-83, P.O. Box 942873, Sacramento, CA 94273; tom_shantz@dot.ca.gov

ABSTRACT: Three-dimensional nonlinear finite element simulations are becoming increasingly feasible for transportation geotechnical applications. This paper presents a robust and versatile framework that helps streamline the use of finite elements for seismic response of soil-structure systems. In this regard, a Windows-based graphical-user-interface OpenSeesPL is developed for pile-ground interaction analyses. Particularly suited to seismic applications, the open-source computational platform OpenSees is employed throughout. OpenSeesPL allows convenient studies of three-dimensional seismic (earthquake) and/or push-over pile analyses. Various ground modification scenarios may be also addressed by appropriate specification of the material within the pile zone. To illustrate the capabilities of OpenSeesPL, two studies are presented in this paper. Lateral spreading effects on pile foundations are modeled, followed by an investigation of ground remediation in a mildly sloping silt stratum. Along with the insights gained from these studies, the reported effort aims to highlight the analysis framework capabilities and range of potential applications.

INTRODUCTION

Soil-Foundation-Structure Interaction (SFSI) is an important aspect affecting the performance of many pile-supported structures such as bridges, wharves, and so forth. With the development of material modeling techniques and high-speed efficient computers, linear and nonlinear three-dimensional (3D) finite-element (FE) methods become a promising technique for understanding the mechanisms involved in SFSI (Yang 2002). Particularly suited to seismic applications, the open-source computational platform OpenSees (Mazzoni *et al.* 2006**)** provides such 3D simulation capabilities.

On the other hand, in numerical simulations, preparation of the FE data file is a step that requires careful attention to detail. A minor oversight might go undetected, leading to erroneous results. Numerous opportunities for such small errors abound,

and a user-friendly interface can significantly alleviate this problem and allow for high efficiency and much increased confidence.

On this basis, a user-interface "OpenSeesPL" is under development (Figs. 1 and 2), to allow for the execution of push-over and seismic pile-ground simulations (Lu *et al*. 2006, https://neesforge.nees.org/projects/openseespl/). Various ground modification scenarios may be also studied by appropriate specification of the material within the pile zone.

In the following sections, an overview of OpenSeesPL capabilities is first presented, followed by studies of 3D seismic ground simulations (conducted with the aid of OpenSeesPL). Along with the insights gained from these studies, the reported effort aims to highlight the analysis framework capabilities and range of potential applications.

COMPUTATIONAL FRAMEWORK

The open-source platform OpenSees (http://opensees.berkeley.edu, Mazzoni *et al.* 2006) is employed throughout. OpenSees is a software framework for developing applications to simulate the performance of structural and geotechnical systems subjected to earthquakes. OpenSees can be used to study the performance of infrastructure facilities (bridges, buildings, ports, etc) during earthquake events. More importantly, this tool can be used to investigate the propagation of uncertainties in large and complex Soil-Structure Interaction (SSI) systems.

In the OpenSees platform, a wide range of linear and nonlinear soil and structural elements is available. For the nonlinear analyses presented in this paper, the J_2 plasticity soil model (Yang *et al*. 2003) was used. In order to facilitate the reported pre- and post-processing phases, the user interface OpenSeesPL was employed. OpenSeesPL (http://cyclic.ucsd.edu/openseespl) allows for: i) convenient generation of the mesh and associated boundary conditions and loading parameters (FE input file), ii) execution of the computations using the OpenSees platform, and iii) graphical display of the results for the pile and the ground systems.

PRE- & POST-PROCESSING

The OpenSeesPL graphical interface (pre and post-processor) is focused on facilitating a wide class of 3D studies (with additional capabilities yet under development). In the current version, OpenSeesPL may be employed to study a number of geometries and configurations of interest including:

i) Linear and nonlinear (incremental-plasticity based) 3D ground seismic response with capabilities for 3D excitation, and layered soil strata. Multi-yield surface cohesionless (Drucker-Prager cone model), and cohesive (Mises or J_2) soil models are available. The coupled solid-fluid analysis option allows for conducting liquefaction studies.

ii) Inclusion of a pile or pile group in the above-described 3D ground mesh (circular or square pile in a soil island). For the pile response, linear, elastic-perfectly-plastic, or nonlinear fiber elements are available in OpenSees (Mazzoni *et al*. 2006). The pile may extend above ground, and may support a bridge deck or a point mass at the top.

This bridge deck can be specified to only translate longitudinally, or to undergo both lateral translation and transversal rotation. In addition to the seismic excitation option, the pile system may be subjected to monotonic or cyclic lateral push-over loading (in prescribed displacement, or prescribed force modes).

iii) Soil properties within the zone occupied by the pile (as dictated by pile diameter) can be specified independently, allowing for a variety of practical modeling scenarios. For instance, various ground modification scenarios may be studied by appropriate specification of the material within the pile zone. Among other options, liquefaction countermeasures in the form of gravel drains, stone columns, and solidification/cementation may all be analyzed. Of particular importance and significance in these scenarios is the ability to simulate the presence of a mild infinite-slope configuration, allowing estimates of accumulated ground deformation, efficacy of a deployed liquefaction countermeasure, pile-pinning effects, and liquefaction-induced lateral pile loads and resulting moments/stresses.

iv) Slopes and pile embedded in sloping ground can also be simulated within this interface.

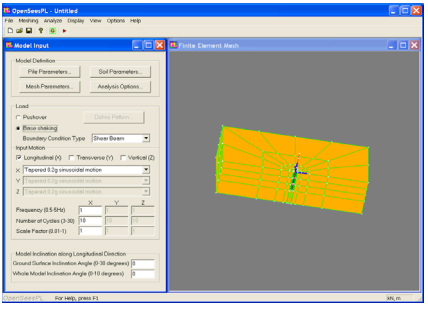

FIG. 1. OpenSeesPL user interface with mesh showing a circular pile in level ground.

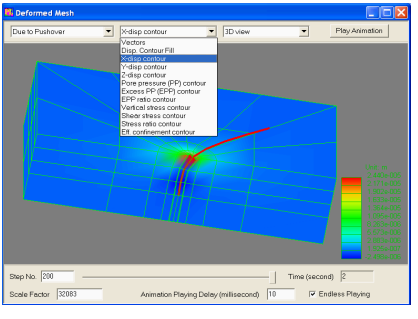

FIG. 2. Push-over analysis and deformed mesh window in OpenSeesPL (Lu *et al*. 2006).

OpenSeesPL also allows convenient post-processing and graphical visualization of the analysis results including the deformed mesh (Fig. 2), ground response time histories, and pile response. As such, OpenSeesPL makes it possible for geotechnical and structural engineers/researchers to rapidly build a model, run the FE analysis, and evaluate performance of the pile-ground system (Lu *et al*. 2006).

To illustrate the capabilities of OpenSeesPL, two studies are presented in the following sections. Lateral spreading effects on pile foundations are addressed first, followed by modeling ground remediation in a mildly sloping silt stratum.

LATERAL SPREADING EFFECTS ON PILE FOUNDATIONS

This section presents an example of 3D seismic ground simulation using OpenSeesPL. A 10 m depth mildly-inclined (4 degrees) saturated medium sand layer was studied (permeability $k = 6.6 \times 10^{-5} m/s$, with Nevada Sand properties at a D_r of

about 40% according to Elgamal *et al.* 2003 and Yang *et al.* 2003). Effect of lateral spreading on pile response was investigated. The pile bending stiffness *EI* was 1.27×10^5 kN·m^2.

Using OpenSeesPL, a half-mesh with 260 elements (Fig. 3) was studied due to symmetry. Length in the longitudinal direction is 42 m, with 21 m transversally (in this half-mesh configuration). The following (solid and fluid) boundary conditions were implemented: (i) excitation was defined along the base in the longitudinal direction (x-axis), (ii) at any spatial locations, displacement degrees of freedom of the left and right boundary nodes were tied together (both longitudinally and vertically using the penalty method) in view of symmetry, (iii) the soil surface was traction free, with zero prescribed pore pressure, and (iv) the base and lateral boundaries were impervious (due to symmetry). For illustration, the Rinaldi Receiving Station record from the 1994 Northridge Earthquake was scaled to one quarter of this motion (top graph of Fig. 4) and employed as the base input acceleration along the x-axis.

Simulation Results

The pile head longitudinal displacement is shown in Fig. 4, reaching 0.75 m at 20 seconds. Figs. 5-7 show representative excess pore pressure histories, shear stress-strain and stress path, and the pile response profiles. The deformed mesh at 20 seconds is shown in Fig. 8.

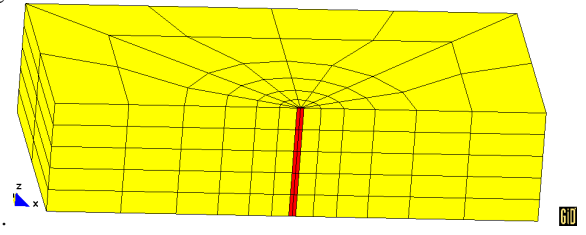

FIG. 3. FE model (½ mesh due to symmetry) for the pile-soil response study (dark zone represents pile).

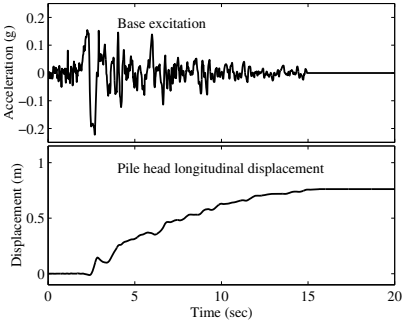

FIG. 4. Base input motion and pile head longitudinal displacement time histories.

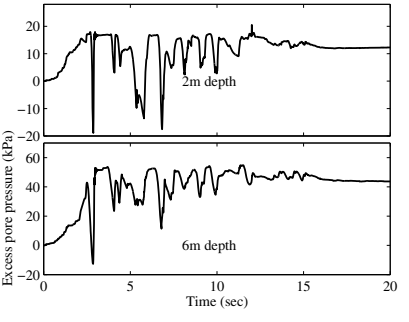

FIG. 5. Excess pore pressure time histories in the free-field.

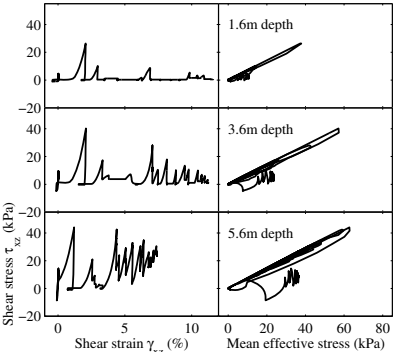

FIG. 6. Shear stress-strain and stress path in the free-field.

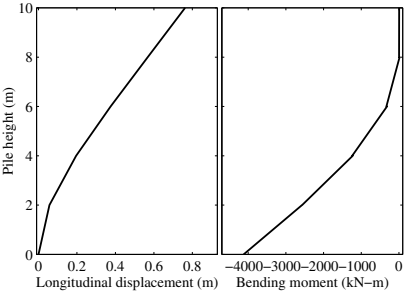

FIG. 7. Pile displacement and bending moment response profiles

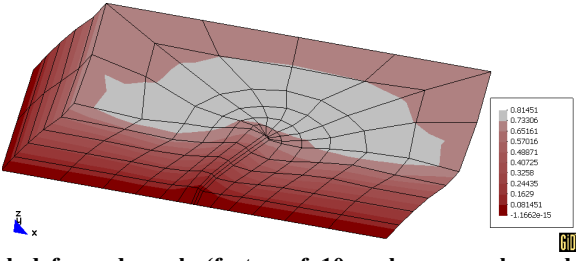

FIG. 8. Final deformed mesh (factor of 10; color map shows longitudinal displacement; unit: m).

REMEDIATION OF A SLOPING SILT STRATUM

This section presents an example of ground remediation simulation using OpenSeesPL. In a remediated area of large spatial extent (Fig. 9), the periodic boundary technique offers an effective approach for conducting 3D analyses (i.e., symmetry allows the investigation of a representative remediated "cell"). On this basis, a half-mesh (100 soil elements in total) in a representative cell within a large remediated ground zone was studied (Fig. 9). The boundary conditions are the same as described in the previous section. In terms of base excitation, the downhole (embedded at a 7.5m depth) NS acceleration record from the Wildlife site during the 1987 Superstition Hills earthquake (Youd and Holzer 1994) was employed along the x-axis (top graph of Fig. 10).

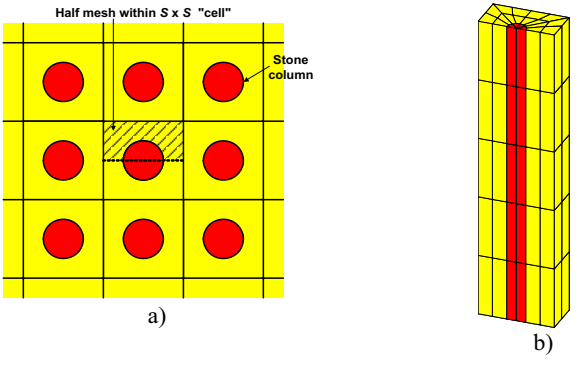

FIG. 9. FE mesh for the ground modification study (dark zone represents remediated domain; replacement ratio area A_{rr} = 20%; stone column diameter *d* = 0.6 m): a) Schematic plan view of stone column or pile layout, b) 3D isometric view (10m thick soil stratum with ½ mesh employed due to symmetry).

A 10 *m* thick mildly-inclined (4 degrees) saturated silt layer was studied (permeability k = 1 x 10^{-7} m/sec, based on Nevada Sand properties at a medium relative density D_r of about 40% (Elgamal *et al*. 2003; Yang *et al*. 2003). The main modeling parameters include standard dynamic soil properties such as low-strain shear modulus and friction angle, as well as parameters to control the dilatancy effects (phase transformation angle, contraction, and dilation), and the level of liquefaction-induced yield strain (γ_y).

A total of 3 simulations were performed. Case **MS** represents the original benchmark **M**edium D_r **S**ilt unremediated situation (essentially a 1D shear wave propagation situation). In order to reduce the extent of liquefaction-induced lateral deformation, remediation by **S**tone **C**olumns (Case **SC**) and by the pile-pinning effect were investigated with an area replacement ratio A_{rr} = 20% (Fig. 9). Diameter of the stone column or pile was set at 0.6 m and the surrounding area was adjusted accordingly. The stone column properties were represented by dense sand properties (Lu *et al*. 2006) and a representative gravel permeability of $k = 1.0 \times 10^{-2}\, m/s$. The pile has a bending stiffness $EI = 1.27 \times 10^5\ kN{\cdot}m^2$.

Simulation Results

Fig. 10 shows the lateral displacement time histories at the model surface center for the 3 cases. The mild 4 degrees inclination imposes a static driving shear stress component (due to gravity), causing the accumulated longitudinal downslope deformation (Fig. 10). For Case SC, the final lateral displacement was reduced to 0.5 m, compared to 1.7 m in Case MS, which can serve as a reference of free-field response. There is essentially no lateral displacement in the pile-pinning case, showing this approach to be highly viable for remediation.

Fig. 11 displays the excess pore pressure time histories at the mesh center for cases MS and SC. Upon liquefaction, 15 seconds into the shaking event, asymmetric

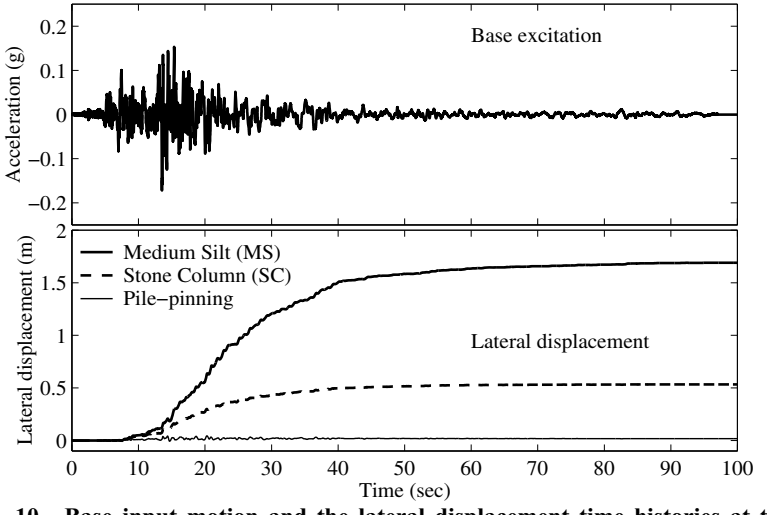

FIG. 10. Base input motion and the lateral displacement time histories at the model surface center.

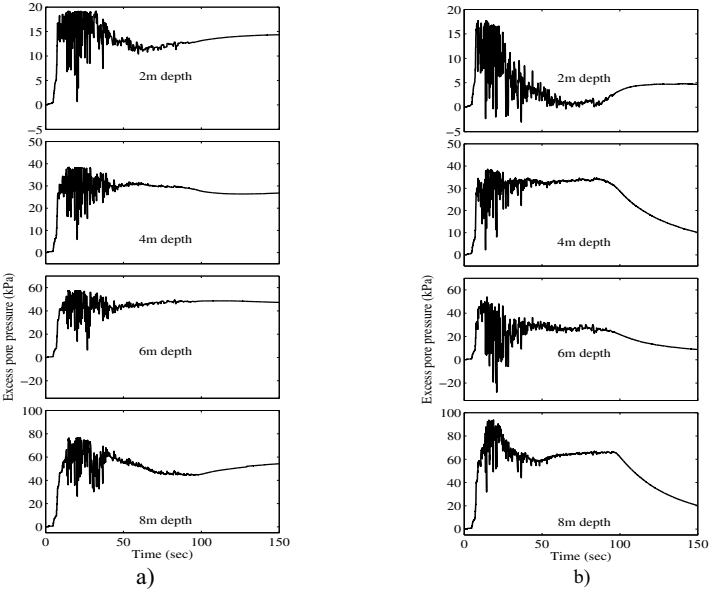

FIG. 11. Excess pore pressure time histories at the model center for a) Case MS; b) Case SC.

acceleration response with lower positive values (Fig. 11) signifies the downslope low shear resistance and associated accumulation of permanent deformation (Fig. 10). This response prevails throughout the strong phases of seismic excitation up to about 40 seconds for cases MS and SC (Fig. 11). At the end of shaking (about 100 seconds), pore pressure starts to dissipate in case SC while staying high in case MS due to the low silt permeability. At the relatively shallow 2m depth, the stone column is also able to start dissipating excess pore pressure shortly after the strong shaking phase.

SUMMARY AND CONCLUSIONS

A robust and versatile framework for computational analysis of pile-ground systems was presented. The open-source platform OpenSees was employed throughout the framework. Scenarios of lateral spreading effects on a pile foundation as well as ground remediation were studies using this tool. The conducted investigations aim to highlight the analysis framework capabilities and range of potential applications.

ACKNOWLEDGMENTS

The authors are grateful for the funding provided by the Pacific Earthquake Engineering Research (PEER) Center under NSF Award Number EEC-9701568, and the PEER Lifelines program.

REFERENCES

Elgamal, A., Yang, Z., Parra, E., and Ragheb, A. (2003). "Modeling of cyclic mobility in saturated cohesionless soils." *International Journal of Plasticity*, 19(6), 883-905.

Lu, J., Yang, Z., and Elgamal, A. (2006). *Openseespl three-dimensional lateral pile-ground interaction version 1.00 user's manual. Report No. SSRP-06/03*, Department of Structural Engineering, University of California, San Diego.

Mazzoni, S., McKenna, F., and Fenves, G. L. (2006). *Open system for earthquake engineering simulation user manual*, Pacific Earthquake Engineering Research Center, University of California, Berkeley (http://opensees.berkeley.edu/).

Yang, Z. (2002). "Development of geotechnical capabilities into OpenSees platform and their applications in soil-foundation-structure interaction analyses," PhD Thesis, Department of Civil Engineering, University of California, Davis, CA.

Yang, Z., Elgamal, A., and Parra, E. (2003). "A computational model for cyclic mobility and associated shear deformation." *Journal of Geotechnical and Geoenvironmental Engineering*, 129(12), 1119-1127.

Youd, T. L., and Holzer, T. L. (1994). "Piezometer performance at Wildlife liquefaction site, California." Journal of Geotechnical Engineering Division, ASCE, Vol. 120, No. 6, 975-995.

Research about the Regularization of Ground Surface Movement and Deformation Caused by Mountain Tunnel Excavation

He Yue Guang[1] Yang Lei[2] and Liu Li Lin[3]

School of Communication and Transportation Engineering, Changsha University of Science and Technology, Changsha Hunan, 410076; hyg@csust.edu.cn

ABSTRACT: Through analyzing the process of tunnel construction using the finite element method, we conclude the regularization of ground surface movement, and take a contrastive analysis with the analysis result of ground surface movement and deformation by using the stochastic medium theory. The research shows that stochastic medium theory is adopt to predict the ground surface movement and deformation of crushed surrounding rock tunnel; the value of subsidence on the tunnel axis is maximal, and far away from the axis direction the value of subsidence decreases; the ground surface horizontal displacement on the cross section of mountain tunnel increases with the increase of distance from the central axis of tunnel, the value arrives the maximum at the point of inflection, after that decreases; when the mountain tunnel depth increases, the area of influence of ground surface movement and deformation enlarges and the strength of influence weakens. The actual ground surface movement of this tunnel by monitoring proves the reliability of this research.

INTRODUCTION

The excavation of high-grade road tunnel in mountainous/hilly area is carried out inside the rock. It unavoidably disturbs the rock body, which will cause redistribution of the internal stress field and displacement field inside the rock and cause movement and deformation of the ground. For the purpose of reducing the harmful effect on buildings on the ground, underground facilities and around environment, which results from the ground's movement and deformation caused by the excavation of tunnel, the ground's movement and deformation must be correctly forecasted (Yang Jun sheng and Liu Baochen, 2002 and Liu Haiyan and Jiang Yusong, 2005). The finite element numerical analysis is used in this paper to study law of ground movement and deformation caused by tunnel construction.

THREE DIMENSIONAL FINITE ELEMENT CALCULATION MODEL

A numerical analysis, by means of finite element numerical software MIDAS/GTS, is performed on the construction process at the K1+935, K1+875 shallowly-buried section at the entrance of Dayan tunnel, with the model size 100 m in dip direction, 60 m in excavating direction, and the actual buried depth as the model depth. See figure 1 for the tunnel's 3-D model. It is separated into 30064 elements with Drucker Prager ideal elastoplastic model adopted. Constraint condition for horizontal displacement is set around the tunnel model to constraint the displacement in normal direction, model top as the free boundary and bottom as the fixed vertical boundary. For numerical analysis, the influence of underground water is negligible and the initial equilibrium state is calculated under the self-weight condition to simulate the prime stratum stress.

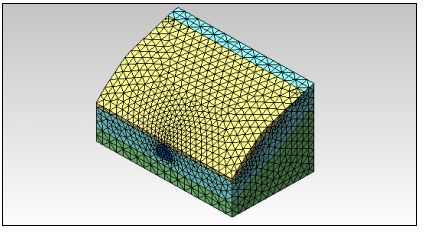

FIG. 1. Three-dimensional numerical analysis of the tunnel network model.

Among the ground's movement and deformation parameters, the movement parameters mainly include the settlement of earth surface and horizontal displacement and the deformation parameters mainly include the earth surface's inclination $T(X)$ and the curvature $K(X)$ or curvature radius $R(X)$ both caused by the uneven settlement of earth surface as well as the horizontal deformation $E(X)$ resulted from the uneven horizontal displacement of the earth surface.

Settlement Law of Ground Surface

Because the tunnel at mountainous area features great surface relief, correspondingly, the buried depth of the tunnel varies greatly and the change of geological conditions of surrounding rock manifestly affects the settlement law of ground surface. See figure 2 for the process that the tunnel construction affects the settlement of ground surface. It is shown that along the excavating direction of tunnel and with the increase the tunnel's buried depth, the affecting range of the settlement of ground surface is expanding forward like a sector with transverse affecting area on the rise. The ground settlement caused by tunnel excavation is mainly within the range of ground settlement trough's radius.

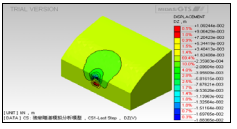

(a) CS1 settlement isoclines figure of the ground surface

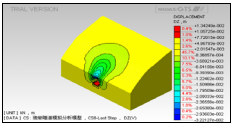

(b) CS8 settlement isoclines figure of the ground surface

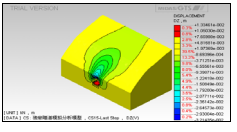

(c) CS15 settlement isoclines figure of the ground surface

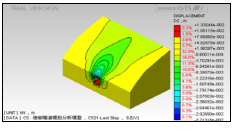

(d) CS21 settlement isoclines figure of the ground surface

FIG. 2. Settlement isoclines figure of the ground surface by tunnel excavation.

The settlement distribution curve that is drafted according to the analysis results distributes symmetrically with single peak value. See figure 3 for ground settlement distribution curves of five transverse cross sections—station K1+925, K1+913.5, K1+905, K1+896, and K1+886.5 with the maximum settlement values 12.3 mm, 6.7 mm, 4.9 mm, 4.2 mm, and 3.8 mm,respectively, presenting that the ground settlement value is inclined to decrease with the increasing buried depth, and the ground settlement's maximum value of the cross section occurs at the axis location, which is decreasing away from the axis to two sides.

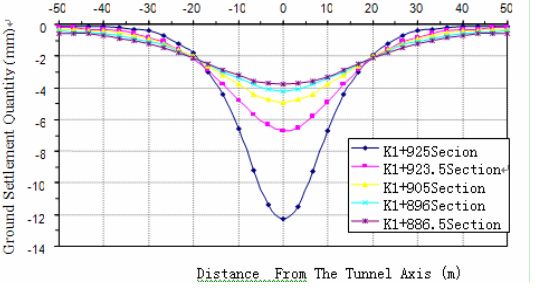

FIG. 3. Ground settlement distribution curve of the tunnel's cross section.

Horizontal Displacement Law of Ground Surface

Figure 4 shows the distribution curve of lateral horizontal displacement of ground surface of the tunnel's cross section; it shows that the curve is symmetrical about the origin, and no lateral horizontal displacements occur at the central point of tunnel's each cross section. From the central point to two sides, the lateral horizontal displacement values of points of cross section are increasing, reaching maximum at the inflection point and then decreasing gradually. In the figure 4, the maximum values of five curves occur at different locations, so the location of inflection point of each ground cross section is different. The greater the tunnel's buried depth is, the farther the inflection point is from the central point. According to the distribution condition of curve, the lateral horizontal displacement of ground surface with great buried depth varies gently, which is affected slightly.

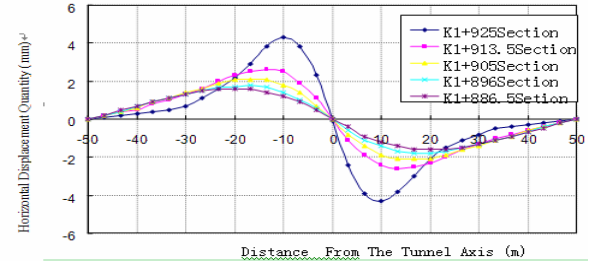

FIG. 4. Distribution curve of lateral horizontal displacement of ground surface of the tunnel's cross section.

Deformation Law of Ground Surface

Figure 5 and 6 are the distribution curves of ground surface's inclination deformation and curvature deformation respectively. For example, four cross sections—K1+925, K1+913.5, K1+905, and K1+896 presents that the varying degree of ground deformation distribution curve is declining with the increasing buried depth of tunnel, the excavating effect on which is decreasing gradually.

- **Inclination deformation of ground surface.** As shown in figure 5, inclination deformation occurs at the ground surface at two sides of tunnel's central line, pointing to the axis. Because the ground settlement curve is a smooth and continuous curve obtaining the maximum value when X=0 at which $dW(X)/dX = 0$ is satisfied, i.e., the ground surface inclination $T(0) = 0$, so, at the locations X=0 and $X = \pm\infty$, the ground surface inclination value is zero. From the distribution curve of ground surface inclination, with the increase of distance X between the ground surface point and tunnel axis, the inclination value of ground surface is growing gradually. After the inclination value reaches the maximum, it decreases gradually until tending to zero.

The ground inclination deformation curve has a similar character as the horizontal displacement curve.

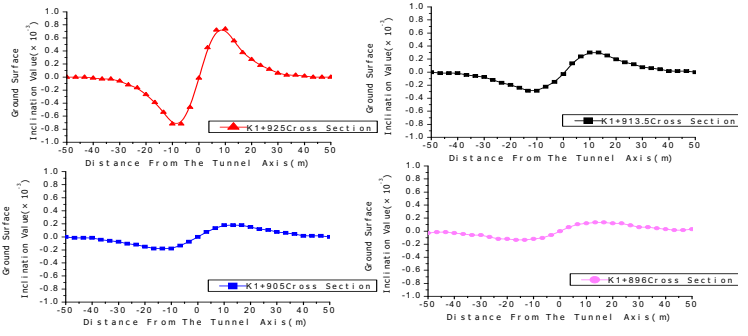

FIG. 5. Inclination deformation law of the mountain tunnel's ground surface.

- **Curvature deformation of ground surface.** The ground inclination distribution curve is a smooth and continuous curve obtaining the maximum at the inflexion point and satisfying $dT(X)/dX=0$, i.e., $K=0$, so the curvature deformation value at the ground surface of inflexion point is zero and the curvature value at the ground surface above the tunnel's centre, i.e., $X=0$, reaches the maximum. The figure 6 indicates the curvature deformation distribution of ground surface of tunnels in mountainous area. That is, within the range between two inflexion points of tunnel's cross section, the curvature deformation value of ground surface is positive, the ground settlement curve within this range presenting concave. Beyond this range, the curvature deformation value of ground surface is negative, the ground settlement curve within this range presenting convex relatively.

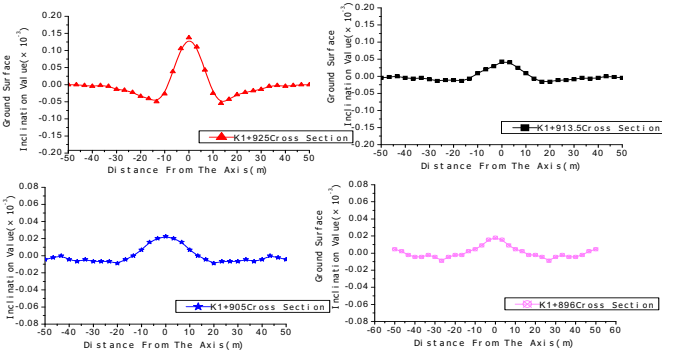

FIG. 6. Curvature deformation law of the mountain tunnel's ground surface.

- **Horizontal deformation of ground surface.** The horizontal displacement distribution curve of ground surface is a smooth and continuous curve; because the

horizontal displacement of ground surface obtains the extreme value at the inflexion points, $dU(X)/dX = 0$ so the horizontal deformation values of ground surface at these two inflexion points are zero. At this, the horizontal deformation distribution curve is similar in shape to the curvature deformation curve with the maximum compression deformation occurring at the ground surface above the tunnel centre. Within the range between two inflexion points, compression deformation exists on ground surface and the horizontal deformation value of ground surface is negative. Beyond this range, stretching deformation exists on ground surface and the horizontal deformation value of ground surface is positive.

ON-SITE MONITORING RESULTS

During construction, the monitoring work on ground settlement is carried out according to the requirement of documents (Chen Jianxun and Ma Jianqin 2004) for the purpose of construction guidance and guaranteeing safety at the shallowly-buried section of the tunnel's opening. The actually-measured settlement distribution curve of ground surface at the station K1+925 of tunnel exit. The maximum value of ground settlement at the station K1+925 of tunnel exit is 22.5 mm and simulated result is 12.3 mm, the difference between which is 10.2 mm. This difference is related to the assumptions done during simulation analysis, so the model constructed fails to completely present the actual status of construction. In addition, the collapse on the arch crown at the entrance that was not immediately handled is not a negligible reason. Although there is certain difference between the values of simulated results and actually measured results, the dynamic process of monitoring points of the ground surface and the distribution law of ground settlement troughs are consistent.

CONCLUSIONS

By means of numerical analysis method to study the law of displacement and deformation of ground surface resulted from the tunnel construction at mountainous area, the obtained characteristic of deformation and displacement of ground surface is to some extent consistent with the monitored results on site. The distribution curves concerning displacement and deformation of ground surface caused by tunnel construction at mountainous area are both smooth and continuous curve, which are symmetrical about the tunnel axis. Its affecting range distributes like a sector, gradually expanding with the increase of buried depth but the maximum movement and deformation declining and the affecting degree reducing relatively. To understand the laws of displacement and deformation of ground surface during tunnel construction at mountainous area is of guidance meaning to protect the buildings on ground in safe.

REFERENCES

Yang Jun sheng and Liu Baochen. (2002). "Ground surface movement and deformation caused by city tunnel excavation. " China Railway Publishing House ,Beijing.

He Yueguang. (2003). "Modeling and Monitoring of Ground Surface Movements due to Excavation." Central South University, Changsha.

Liu Haiyan and Jiang Yusong. (2005). "Research and Analysis about the Effecting of the Ground and Buildings Caused by Tunnel Excavation" *Western Prospecting Project.* Vol.17 (3):108-109.

Yan Ronggui. (1995). "Surface Mining Subsidence and Fecundating Construction" Metallurgical Industry Press, Beijing.

Chen Jianxun and Ma Jianqin. (2004). "Tunnel Project Test Technology" The Traffic Press. Beijing.

Failure Mechanisms and Corresponding Stability Charts of Homogenous Rock Slopes

X.L. Yang[1], F. Huang[2], L.H. Zhao[3] and H.W. Wei[4]

[1]Doctor, School of Civil Engineering and Architecture, Central South University, Changsha 410075, China; yxnc@yahoo.com.cn
[2]Doctoral candidate, School of Civil Engineering and Architecture, Central South University, Changsha 410075, China
[2]Doctoral candidate, School of Civil Engineering and Architecture, Central South University, Changsha 410075, China
[4]Doctor, School of Civil Engineering and Architecture, Central South University, Changsha 410075, China; whw.edu@163.com

ABSTRACT: Failure mechanisms of homogenous rock slopes were investigated within the upper bound theorem of limit analysis. In rich water zone, the effective stress analysis of saturated slopes is considered. The corresponding charts for different types of rocks are presented for practical use. From the results, it is found that the stability factors increase with the increasing rock strength, and that the nonlinear parameter and rock types have important effects on failure mechanisms. According to the results, new equations for determining the stability factors are proposed.

INTRODUCTION

As well known, most of computer codes and designs in rock engineering, which are currently employed for evaluating the slope stability factors, are formulated in terms of a linear Mohr-Coulomb failure criterion. A linear failure criterion is also commonly used among the extensive literature concerned with slope stability problems. However, experiment data have shown that the strength envelopes of almost all types of soils and rocks have the nature of nonlinearity (Agar et al. 1985; Hoek 1983). Consequently, a question, which frequently arises in practice, is how to determine the stability factors with a nonlinear failure criterion. In order to analyze the influences of a nonlinear failure criterion on bearing capacity of a strip footing on the upper surface of a flat-sided slope, Baker and Frydam (1983) applied the variational calculus technique to formulate the bearing capacity, and governing expressions were presented in their work. Zhang and Chen (1987) converted the complex differential expressions to an initial value problem, and presented an effective numerical procedure, called the inverse method, for solving plane strain stability limit analysis problem with a general nonlinear failure criterion. Yang (2007) presented the numerical results of critical earthquake force and seismic displacement of an infinite,

homogenous and free surcharge slope. Based on the upper bound theorem, Collins et al. (1988) proposed a tangential technique to evaluate the stability factors of an infinite and homogenous slope without surcharge.

In the past, the effects of underground water pressure had been considered in some literature focusing on upper bound solutions to slope stability problems. In general, underground water pressures are obtained from ground water conditions, which are simulated by a flow net or a water pressure ratio. Water pressure was considered as internal forces, and used two kinds of failure mechanism to estimate the slope stability. Water pressure was assumed to be hydrostatic below a free water surface (Miller and Hamilton 1989). However, the water pressure was regarded as external force, and employed a log-spiral rotation failure mechanism to analyze the effects of water pressure on slope stability (Kim et al. 1999). The distribution of water pressure is described by a coefficient. Therefore, effective stress should be adopted for the slopes subjected water pressure.

In the present study, the kinematical theorem of limit analysis is applied to calculate the stability factors of rock slopes with the nonlinear failure criterion since the strength envelops of almost all types of rocks had the nature of nonlinearity. The stability factors of rock slopes with this kind of rock masses are formulated within the upper bound theorem of limit analysis. The tangential technique is employed to formulate the stability problems as the optimization problems. The effective stress is adopted in the analysis. In this approach, herein the work using a linear MC failure criterion is extended to that using the nonlinear failure criterion Numerical results are presented for practical use in rock engineering.

NONLINEAR FAILURE CRITERION

Due to the fact that the rock masses of the slopes have intrinsic characteristics such as joints, faults and weak bedding plane, which makes the media express anisotropy, the stability of rock slopes was commonly developed using block theory in conjunction with finite element method in previous literature. Block theory is theoretically accepted by researchers, which can determine potentially unstable rock block. However, with the increase of joint number, which leads to block elements increase within the range of considered slope, this kind of analysis is becoming complex, and its applications may meet some inconvenience in practice. An alternative approach, homogenized approach, attempts to regard the behavior of the jointed rock masses as homogenous and isotropic material. This approach was employed to evaluate the stability of jointed rock structures (Maghous et al. 1998). This approach was also employed to estimate the stability factors of jointed rock slopes in the absence of water pressures and surcharge loads (Collins et al. 1988). Characteristics technique was employed to evaluate the ultimate bearing capacity of a strip footing resting on homogenous and isotropic rock masses using the original and modified failure criteria (Serrano and Olalla 1994). Therefore, we can consider the jointed rock mass exhibits an isotropic and homogeneous behaviour if the following two conditions are satisfied. First, none of faults or bedding planes exists in the jointed rock masses. The directions of discontinuity surfaces are sufficient randomly distributed. The joint separation is small compared with the magnitude of rock structures. Second, the

discontinuity surfaces must be sufficiently dense in the sense that the spacing between the two adjacent discontinuity surfaces is small enough when compared with the overall dimension of rock structures. In practice, there are times when the rock masses are so weak that its behaviour exerts greater effects than discontinuity factor. Under these cases, the weak rock masses also express the property of homogenous and isotropic material. At the present analysis, the basic idea of isotropic and homogenization is adopted for computing the magnitude of stability factors of jointed rock slopes subjected to water pressures with the tangential line technique. The failure of rock masses obeys the nonlinear failure criterion, which can be described by the following form (Hoek 1980):

$$\sigma_1 - \sigma_3 = \sigma_c \left[m\sigma_3 / \sigma_c + s \right]^{0.5} \tag{1}$$

where σ_c is the uniaxial compressive stress of the rock at failure, σ_1 is the major principal stress at failure, and σ_3 is the minor principal stress or confining pressure at failure. The magnitude of m and s depends on the geological strength index which characterizes the quality of the rock masses. For a given rock type, the two parameters are not independent. Based on the experimental data, Hoek gave a log-log plot of the values of the two parameters. The relationship between m and s can be approximated by the expression (Hoek 1980):

$$m = m_i \exp[8.27(1 - s^{-0.043})] \tag{2}$$

where the parameter m_i is the value of intact rock and can, in principle, be obtained from the measured inclination of the fracture planes in compression experiments. The parameter value of m_i can be obtained from the measured inclination of the fracture planes in compression experiments. If there are no test data available, Hoek presented the approximate values for five types of rocks (Hoek 1990), which is

(a) $m_i \approx 7$ for carbonate rocks with well developed crystal cleavage; (b) $m_i \approx 10$ for lithified argillaceous rocks; (c) $m_i \approx 15$ for arenaceous rocks with strong crystals and poorly developed crystal cleavage; (d) $m_i \approx 17$ for fine-grained polyminerallic igneous crystalline rocks; and (e) $m_i \approx 25$ for coarse-grained polyminerallic igneous and metamorphic rocks. Thus, for a given rock type, if the values of parameters σ_c and s are known, the nonlinear failure criterion can be expressed as a function with a single variable s.

By introducing a mobilized internal friction angle, a tangential line to the curve at the location of tangency point is described by the following expression of $\tau = c_t + \sigma_n \tan\varphi_t$, where φ_t and c_t are the tangential friction angle and the intercept of the straight line to τ - axes, respectively.

In rock engineering, although the nonlinear failure criterion of Equation (1) has been updated, many engineers still accepted the old criterion for their convention. Meanwhile, most of old designs in engineering are still adopted the Equation (1). In order to check the safety of rock structures, Equation (1) is still used in calculation and analysis. Therefore, the nonlinear failure criterion is adopted for the present analysis. The nonlinear failure criterion can be applied to the intact rocks, or the rock masses where there are a sufficient number of closely spaced discontinuities that isotropic behaviour involving failure on discontinuities can be assumed. The nonlinear failure

criterion cannot generally be applied to the rock masses containing only a few discontinuities or its behaviour is basically anisotropy.

LIMIT ANALYSIS THEORY

The method of slices of limit equilibrium, the most commonly employed numerical method for rock slope stability, assumes that the failure occurs by sliding along slip surface. However, failure involves stability factors in critical state rather than slip surface, because the safety problem is more important issue than the slip location. In practice, engineers must resort to limit analysis method to estimate the stability factor.

Limit analysis has been widely used to stability problems of earth structures such as shallow foundations, slopes and retaining pressure of walls in the last 20 years or so. By using the upper and lower bound theorems of plasticity, the range, in which true solution falls, can be found. The kinematical approach of limit analysis has been used here to arrive at the critical height for rock slopes, and the results are presented in the form of tables and charts. The technique of calculations is based on the kinematical theorem of limit analysis. This theorem states that the rate of work done by traction and body forces is less than or equal to the rate of energy dissipation in any kinematically admissible failure mechanism

$$\int_V F_i v_i^* dV + \int_S p_i^0 v_i^* dS \le \int_V \sigma_{ij}^0 \dot{\varepsilon}_{ij} dV \tag{3}$$

where $\dot{\varepsilon}_{ij}$ is the strain rate in a kinematically admissible velocity field, σ_{ij}^0 is the stress tensor associated with $\dot{\varepsilon}_{ij}$, v_i^* is the jumps velocity on boundary S which is given kinematical boundary condition, F_i and p_i^0 are the vector of outside loads, and S and V are the loaded boundary and the volume, respectively. A more comprehensive description of this method can be found in Chen (1975).

UPPER BOUND SOLUTIONS

Stability Factor Formulation

Without considering the effects of water pressure on rock slope stability, a tangential technique was proposed to evaluate the stability factors with a nonlinear failure criterion. Using the linear Mohr-Coulomb failure criterion for slopes, Chen (1975) presented the stability factors by pertain to 5-degree intervals of friction angle. The slope stability factor for the nonlinear failure criterion is defined as

$$N_n = H_c \gamma / (s^{0.5} \sigma_c) \tag{4}$$

where N_n is the stability factor for the nonlinear failure criterion, γ is the unit weight, and H_c is the critical height of slopes.

A homogenous and isotropic rock slope with a certain angle is considered in the present study. If the slope is subjected to water pressure, effective stress analysis are adopted, else the total stress are used for the analysis. The tangential technique can be employed to calculate the stability factors of rock slopes with the nonlinear failure criterion. In Equation (4), H_c is a function of the variable of c_t. However, the c_t is

a function of the φ_t . The solutions are minimized Equation (4) with respect to the φ_t .

The difference between the present analysis and the work by Collins et al. (199) is that the former employs the nonlinear failure criterion controlled by one parameter s which did not employed the linear stability factors given by Chen (1975); while the later must employ the linear stability factors of Chen (1975).

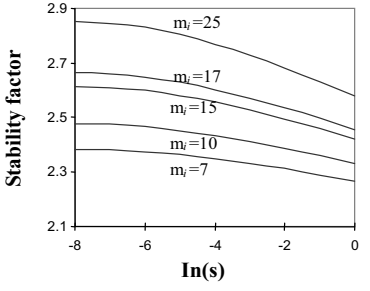

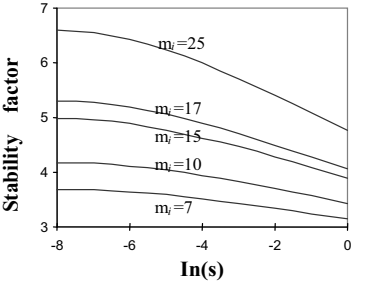

FIG. 1. The stability factors for $\beta = 85°$

FIG. 2. The stability factors for $\beta = 75°$

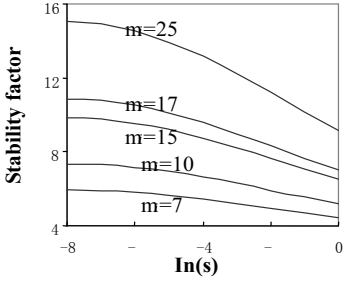

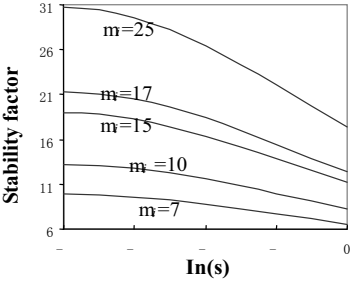

FIG. 3. The stability factors for $\beta = 65°$

FIG. 4. The stability factors for $\beta = 55°$

Design Tables

The problem considered here is the stability factor of slopes with the nonlinear failure criterion. The numerical results to this problem have been obtained by the

optimization. Using the tangential technique, the stability factor is obtained by minimizing Equation (4) with respect to φ_t. Figs.1-4 illustrate the stability factors for five types of rocks corresponding to $\alpha = 0°$, and the slope angle β being equal to $85°$, $75°$, $65°$ and $55°$. These stability factors are given for practical use in rock engineering. According to the numerical results, simulation equation for determining the stability factors for rock slopes is presented. The simulation equation of stability factor is expressed as the function of variable $\ln(s)$. For example, the function is $0.0034[\ln(s)]^2 - 0.062\ln(s) + 2.58$ for case of $\beta = 85°$ and $m_i = 25$, and the function is $-0.02[\ln(s)]^2 - 0.4\ln(s) + 4.72$ corresponding to $\beta = 75°$ and $m_i = 25$.

Effects of Nonlinear Parameter

Fig.5 illustrates the stability factors for highly jointed rocks corresponding to $\beta = 75°$ and $m_i = 15$, with the nonlinear parameter $\ln(s)$ ranging from 0 to -8. From Fig.5, it is found that the nonlinear parameter has an important influence on the failure mechanisms. The collapse area decreases with the decreasing value of $\ln(s)$. However, the failure surface of $\ln(s) = -6$ is very close to that of $\ln(s) = -8$. This is contributed to the fact that the stability factor for $\ln(s) = -6$ approximates to the stability factor for $\ln(s) = -8$.

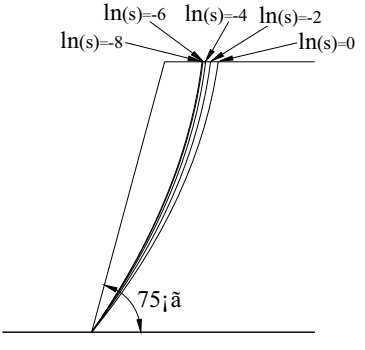

FIG. 5. Effects of nonlinear parameter on failure surfaces.

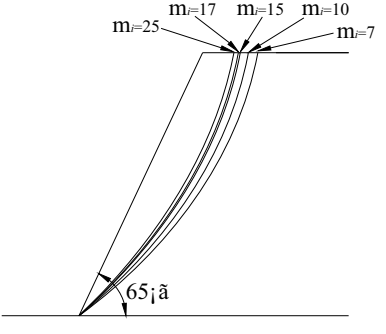

FIG. 6. Effects of rock types on failure surfaces.

Effects of Rock Types

Fig.6 shows the effects of different rock types on the failure mechanisms with the failure surface passing through the slope toe, corresponding to $\beta = 65°$ and $\ln(s) = -3$. From Fig.6, it is found that the collapse area decreases with the m_i increasing.

CONCLUSIONS

With the nonlinear failure criterion, the stability factors of rock slopes are developed within framework of limit analysis, not utilizing the linear stability factors given by Chen (1975). Due to the use of Equation (1), the stability factors of rock slope are calculated for given rock parameter s. Numerical results are presented and drawn into charts for five types of rocks, which benefits to the practical use in rock engineering. According to the numerical results, the effects of nonlinear parameter and rock types on the failure mechanisms are discussed, and new equations for determining the stability factors are proposed.

REFERENCES

Agar, J. G., Morgenstern, N. R., and Scott J. (1985). "Shear strength and stress-strain behaviour of Athabasca oil sand at elevated temperatures and pressure." *Canadian Geotechnical Journal*, Vol. 24(1):1–10.

Baker, R., and Frydman, S. (1983). "Upper bound limit analysis of soil with nonlinear failure criterion." *Soil and Foundations*, Vol. 23(4): 34–42.

Chen, W. F. (1975). *Limit analysis and soil plasticity*. Elsevier Scientific Publishing Company, Amsterdam.

Collins, I. F., Gunn, C., Pender, M.J., and Wang, Y. (1988). "Slope stability analyses for materials with a nonlinear failure envelope." *International Journal for Numerical and Analytical Methods in Geomechanics*, Vol. 12(5): 533–550.

Hoek, E. (1983). "Strength of jointed rock masses." *Geotechnique*, Vol. 33(2): 187–223.

Hoek, E. (1990). "Estimating Mohr-Coulomb friction and cohesion values from Hoek-Brown failure criterion." *International Journal of Rock Mechanics and Mining Sciences*, Vol. 27(3): 227–229.

Kim, J., Salgado, R., and Yu, H. S. (1999). "Limit analysis of slopes subjected to pore-water pressures." *Journal of Geotechnical and Geoenvironmental Engineering*, Vol. 125(1): 49–58.

Maghous, S., Buhan, P., and Bekaert, A. (1998). "Failure design of jointed rock structure by means of a homogenization approach." *Mechanics of Cohesive-Frictional Material*, Vol. 3(2): 207–228.

Miller, T. W., and Hamilton, J. M. (1989). "A new analysis procedure to explain a slope failure at the Martin Lake Mine." *Geotechnique*, Vol. 39(1): 107–123.

Serrano, A., and Olalla, C. (1994). "Ultimate bearing capacity of rock masses." *International Journal of Rock Mechanics and Mining Sciences*, Vol. 31(2): 93–106.

Yang, X. L. (2007). "Seismic displacement of rock slopes with nonlinear Hoek-Brown failure criterion." *International Journal of Rock Mechanics and Mining Sciences*, Vol. 44(6): 948–953.

Zhang, X. J., and Chen, W. F. (1987). "Stability analysis of slopes with general nonlinear failure criterion." *International Journal for Numerical and Analytical Methods in Geomechanics*, Vol. 11(1): 33–50.

A Model of Tunnel Safety Risk Quantitative Identification

CHEN Jiejin, YANG Junsheng, WANG Honggui, LIU Baochen, and YANG Xiaoli

School of Civil Engineering and Architecture, Central South University, Changsha, Hunan, China ,410075.
email:chenjjin1975@163.com

ABSTRACT: As in urban areas, construction of tunnel inevitably leads to ground movements. These must be carefully predicted if there is a risk of settlement damage to nearby structures. How to identify the real danger is the basis of quantitative risk analysis of buildings. Due to various conditions, it is impossible to undertake a risk assessment of each building. In the process of excavation, the mechanism of interaction of the tunnel and adjacent structures is very complicated because ground movements are affected by a lot of factors, such as the formation conditions, the tunnel section depth and size, foundation type and geometric characteristics of adjacent building, and relative position, etc. So, a practical and reliable quantitative model with concise, clear physical meaning of the parameters is in need. Referencing the quantitative risk assessment methodology of petrochemical plant, tunnel safety risk identification model could be established and it can be quickly and reliably identify the high-risk buildings.

INTRODUCTION

In 1863 the first underground railway line was opened in London. Since then over 100 cities worldwide have implemented underground transport systems and over 50% of them are undergoing development or expansion (Hellawell et al, 2001). New tunnel projects have to be constructed beneath high density urban areas. The construction and operation of these systems can cause a restriction of services, and damage to surface or other subsurface structures.

In urban areas ground subsidence can affect existing surface and subsurface structures. Predicting tunnel induced deformation of such structures and assessing the risk of damage is an essential part of planning, design and construction of tunnels in an urban environment (Mair et al., 1996).The three-stage risk assessment method concluded preliminary assessment, second stage assessment and detailed evaluation (Burland, 1995). This approach can be highly conservative as it assumes that any structure follows the Greenfield settlement profile (Standing, J. R. 2001). However, the structure's stiffness is likely to alter ground induced soil movement and, hence, to reduce the building's deformation. In 1997 Potts & Addenbrooke presented an approach which considers the building's stiffness when predicting

tunnel induced building deformation. In the second stage of the evaluation methods, parameters of access are very difficult. This paper presents a qualitative method to determine a building-damage-risk index (BDRI) as one possible method to assess the buildings damage hazards associated with tunnel excavation.

TECHNIQUE TO DETERMINE A BUILDING-DAMAGE-RISK INDEX (BDRI)

The purpose of this paper is to present a qualitative method for determining the BDRI. The response of existing constructor to tunnelling induced ground movements depends on a num-ber of factors including (1) geological, hydro-geological and geotechnical conditions, (2) tunnel geometry and depth, (3) excavation methods and the quality of workmanship and management and (4) surface buildings conditions. According these factors, a model of building-damage-risk index could be set up as shown in Figure 1.

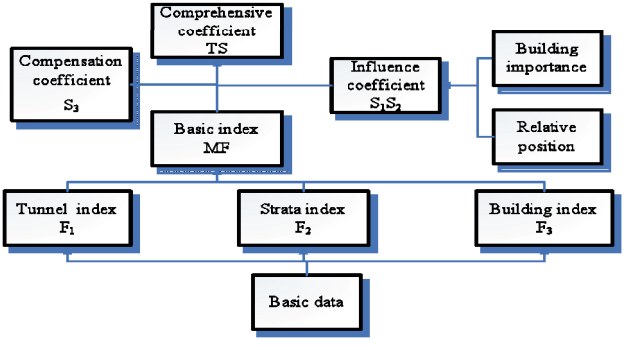

FIG. 1. The model of building-damage-risk index.

Surrounding Rock Properties

The ground and groundwater condition along the route are one of the main factors controlling ground movements. They are also the fundamental parameters controlling the volume loss. If the geological conditions are good, some positive results could be produced, such as the simple excavation method, excavation section convergence, small Stratigraphy losses, small surface subsidence, and the small influenced range also. However, bad geotechnical condition means that complicated excavation method, large strata loss and surface subsidence because it is difficult to control the strata section convergence. Construction of the tunnel in the city, the strata encountered general are IV level or even worse. The assessment values "1", "3", "5." were assigned to “IV”, ‘V”, “VI”-class surrounding rock correspondingly. It means that the greater is the value, the greater the hazard is.

Underground Water

The underground water condition has important impact on the long-term settlement trough. Where the initial pore pressures are high, significant time-dependent settlements can take place due to consolidation and drainage. The underground water is also the important factor influencing the stability of the surrounding rock. The higher is the water table and the greater is water volume, and then the greater the risk is.

Ratio of Depth/Width

Fig. 2 shows the maximum ground settlement and lateral displacement caused by the single-arch tunnel excavation in different buried depth when the ground loss is 1.5%. As can be seen from the figure, when the ground loss rate is constant, the greater the tunnel buried depth is, the smaller the ground settlement and lateral displacement is. When the tunnel is shallow buried, the ground settlement and lateral displacement decreases rapidly with the increase of tunnel buried depth. Otherwise when tunnel is deeply buried, the ground settlement and lateral displacement decreases slowly with the increase of tunnel buried depth.

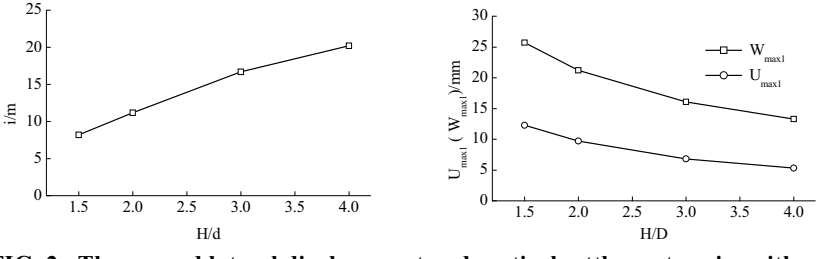

FIG. 2. The ground lateral displacement and vertical settlement varies with buried depth-diameter ratio in tunnelling.

Tunnel Width

Tunnel width is also a major factor that influences the transverse settlement troughs. Different shape and size of tunnel section has different influence on the movement and deformation of ground surface. Research shows that with other conditions unchanged, the settlement of ground surface and the width of settling trough increase with the increasing excavation size of tunnel. Detailed assessment values were shown in table 1.

The Tunnelling Method

The comprehensive influence of different Construction Method and construction level to the ground surface movement and deformation can be reflected by radial constringency of tunnel excavation; it also can be determined on the change of surface subsidence caused by tunnel radial constringency when using different construction condition and other things being equal. The results show that the

ground surface movement and deformation increased with the tunnel radial constringency.

Skills

Through the contractor's credibility, experience and technology, the construction technology and management level will be assessed. The smaller is the assessment value indicates that the construction level is the better.

Building Foundation

The displacement formation caused by tunnel excavation is carried to the building through the foundation, so the foundation of the building is an important factor of surface building damage. Especially independent basis that is very sensitive for displacement and easily damaged foe buildings. The sensitivity of the basis for the displacement is generally ranking for the pile foundation, an independent foundation, strip foundation, raft foundation and box foundation. They are assigned correspondingly by the assessment value “5”, “4”, “3” , “2” , “1” as shown in Table 1.

Building Geometry

The geometry shape of building is also sensitive factor that could damage the earth’s surface building. If the geometry size become bigger, the shape become more anomalistic, the sensitivity of building towards displacement become stronger, the building should be easy to destroy. A careful review of the reported damage shows that much of it occurred at connections between adjacent structures; particularly where are differences in foundation type or structure type (Burland, J.B 2001).The assessment values are given in table 1.

Relative Stiffness

Several detailed case records have been assembled that show that building stiffness can substantially reduce the Greenfield site relative deflections (Mari, 2001). The building has greater rigidity, relative to stratum, the sensitivity of building towards displacement become weaker. The larger the relative rigidity of buildings is, the smaller the impact buildings affected by ground deformation are. Detailed assignment method is shown in table 1.

Current Situation

Current situation of building has an import influence on the anti-deformation capacity of building. The better is the anti-deformation capacity, the smaller the assessment value. The buildings damaged state is divided into five categories, such as good, basic good, in general, damage and serious damage. Detailed assignment method is shown in table 1.

Adjustment Coefficient

The total of the adjustment factor is divided into three parts. One part of the building is the importance of building. The more important is, the greater the risk is, and the greater the adjustment factor is. The second part of the building is the relative location to the tunnel. The closer to the tunnel, the greater the impact is and the greater the adjustment factor is. The third part is the construction of the remedial measures taken, according to the compensation effect of the adjustment factor to determine the value, as shown in table 1.

Table 1. Hazard Category for Determining the BDRI

Category	Parameter	Assessment Value	Weight	Category Value
Geologic Factors				
1. Surrounding rock properties	surrounding rock level is IV, surrounding rock level is V, surrounding rock level is VI Soft soil unknown	1 3 4 5 3	5	
2. Ground water	Poor relatively development development rich a large number of water gushing unknown	1 2 3 4 5 3	3	
Tunnel Factors				
3. Tunnel width	<5m 5~9m 9~15m 15~20m >20m	1 2 3 4 5	5	
4. Ratio of depth /width	>4 3~4 2~3 1.5~2 <1.5	1 2 3 4 5	5	
5. The tunnelling met-hod	two-side wall drift heading method CRD CD bench method entire section method	1 2 3 4 5	5	
6. Skills	very good good general poorer Poor	1 2 3 4 5	3	
Buildings Factors				

7. Building foundation	Box foundation Raft foundation Strip foundation Independent foundation pile foundation	1 2 3 4 5	4	
8. Relative stiffness	>10 layers 5~10 layers 3~5 layers 2~3 layers 1 layer	1 2 3 4 5	4	
9. Building geometry.	Very regular regular general irregular very irregular	1 2 3 4 5	3	
10. Current situation	Intact or date of construction <5years basic intact or 5~10 years general or 10~20 years damage or 20~30 years serious damage or date >30years	1 2 3 4 5	3	
Adjustment Coefficient				
Building importance S_1	neglected Not important general important Very important	0.1 0.4 0.6 0.8 1		
Relative position S_2	e>3 z_0 2 z_0~3 z_0 1.5 z_0~2 z_0 1. z_0~1.5 z_0 e<z_0	0.1 0.4 0.6 0.8 1		
Compensation coefficient S_3	foundation underpinning structure reinforcement foundation reinforcement surrounding rock reinforcement	0.1~0.5 0.4~0.8 0.4~0.8 0.4~0.8		
Assessment Calculation				
$MF = F_1F_2F_3$ =				
$TS_1 = S_1S_2(MF)$ =				
$BDRI = (TS_1)S_3$ =				

Note. z_0 is the tunnel depth.

RISK ACCEPTANCE CRITERIA

Based on the above analysis, the building of the risk index of the surface buildings damage induced by the tunnel excavation could be acquired and classified, as shown in table 2. Risk is divided into grades 4, to meet the risk assessment of the building damage caused by tunnel excavation works.

Table 2. Tunnel Construction Environmental Risk Rating

BDRI	Risk Rank	Acceptance Criteria
<50	low	negligible
50~100	medium	acceptable
100~150	high	unwanted
>150	Very high	unacceptable

CONCLUSIONS

1. This study proposes a building-damage-hazard-assessment method for the tunnel excavation that can be used to help the engineer to reduce the buildings potential damage by taking proper measures.
2. The proposed building-damage-hazard-assessment technique is comprised of 10 hazards categories that cover a range of geological factors, tunnel factors and buildings factors. Each category has a set of parameters that allow for the estimation of an assessment value between "1" and "5." These parameters are based on experience gained from visiting more than 60 different operating tunnels and from an investigation of relevant topics in the literature.
3. The technique involves calculating a BDRI. Very good conditions produce BDRI values approaching 0, while the poorest conditions produce BDRI values approaching 200. In some cases, where significant adjustments are made, the BDRI may be exchanged.

REFERENCES

Burland, J. B. 1995. “Assessment of risk of damage to buildings due to tunneling and excavation. Invited Special Lecture.” *In: 1st Int. Conf. on Earthquake Geotech. Engineering IS Tokyo '95*.

Burland, J. B., Standing, J.R. & Jardine, F.M. 2001 “Building response to tunneling.” London. *Proc. Instn. Civ. Engrs.*, (1), 342-343.

Cooper, M. L., & Chapman, D. N. 2000. “Settlement, rotation and distortion of Piccadilly Linetunnels at Heathrow.” *In: Proc. of the International Symposium on Geotechnical Aspectsof Underground Construction in Soft Ground*. Balkema, Rotterdam.

Grant, R.J., & Taylor, R.N. 2000 “Tunneling-induced ground movements in clay.” *Proc. Instn.Civ. Engrs. Geotech. Engineering*, 143, 43-55.

Hellawell, E. E., Hawley, A. J., Pooley, S. D., Garrod, B., & Legett, M. 2001. “Metros under Construction around the world.” *Proc. Instn. Civ. Engrs. Geotech. Engineering,* 149, 29-39.

Jardine, R. J., Symes, M. J. & Burland, J. B. 1984. “The measurement of soil stiffness in the tri-axial apparatus.” *Geotechnique*, 34(3), 323-340.

Mair, R. J., & Taylor, R. N. 2001. “Elizabeth House: settlement predictions.” *Chap. 14 of:* Burland, J. B., Standing, J. R., & Jardine, F. M. (Eds), *Building response to tunnelling*, vol. 1.

Standing, J. R. 2001. Elizabeth House, Waterloo. Chap. 30 of: Burland, J. B., Standing, J. R., & Jardine, F. M. ( ), *Building response to tunnelling, vol. 2.*

Monitoring and Numerical Analysis of Soil Displacements due to Excavation of the Exit of Liuyang River Tunnel

Ruihua Jia[1], Junsheng Yang[2], and Jiansheng Li[3]

[1]Doctoral Candidate, School of Civil Engineering and Architecture, Central South University, Changsha, 410075; rhjia@yahoo.cn
[2]Professor, School of Civil Engineering and Architecture, Central South University, Changsha, 410075; jsyang@yahoo.cn
[3]Master, School of Civil Engineering and Architecture, Central South University, Changsha, 410075;

ABSTRACT: Liuyang River tunnel, one of the longest tunnels in Wuhan-Guangzhou railway passenger dedicated line, encountered low overburden, weak rock and crowded surface buildings in exit. If incorrect excavation method was tacked, it will cause serious damages to the environment and buildings.

As it belongs to large-section excavation, for which cross section area surpasses 150 m^2. In order to avoid oversize subsidence by excavation of the large cross section, field monitoring including stratum displacement and three dimensional deformations were carried out. Combined field monitoring with numerical analysis, stratum displacement distributed rule in large cross section tunnel excavation process was observed, which showed that the construction process is safe.

INTRODUCTION

Liuyang River Tunnel, which underpass the Liuyang River in Changsha, China, nearly has a length of 10km, and it mostly encountered complex geological conditions, such as weak rocks, shallow overburden and watery strata. When tunnel face in exit was driven, it needs to control the ground settlement because of adjacent or overlying structures. Although many scholars have studied similar problem at present, further investigation needs to take into considerations. Huang Jun (2004) obtained stratum movement basic rule of soft rock under rich water condition in Shenzhen by field measurement and regression analysis, Park (2005) proposed the analytic solution of stratum displacement distribution in the clay. Potts and Addenbrookea (1997) proposed a new approach, based on the relative stiffness of a building and the underlying soil, to account for the deformation and potential damage of buildings. However, ground deformation caused by such large cross section excavation was little reported up to present.

As surface buildings of Liuyang River tunnel exit are crowded, if it's driven incorrectly it may cause severe destruction. Stratum displacement pattern was investigated by field monitoring and numerical calculation, and the research finally indicated that the construction satisfied the safety control requirements.

BACKGROUND

The section, from DIIK1569+680 to DIIK1569+028 of Liuyang River tunnel exit, frequently underpasses adjacent structures, which also has an excavation section area surpasses 150 m^2. As there exists weak surrounding rocks, so it maybe easily encountered collapses, burst mud and water inrush.

To protect the surface structures, bench method, along with grouting reinforcement with pipe shed and small pipe as pre-supporting technology, was selected. Primary support consists of sprayed steel fiber concrete and entire link I20a steel frame with 0.5m spacing. In addition, anchor rods combined with shortcrete were used to strengthen weak rocks, which has 4.0 m in length and 1.0 m ×1.0 m in spacing. Pipe shed adopts ϕ 108 hot rolling seamless steel tube with 6mm in thickness, 18 m in length and 0.4 m in ring spacing. Small pipe adopts ϕ 42 hot rolling seamless steel tube, which has 3.5 m in length and 0.4 m in ring spacing.

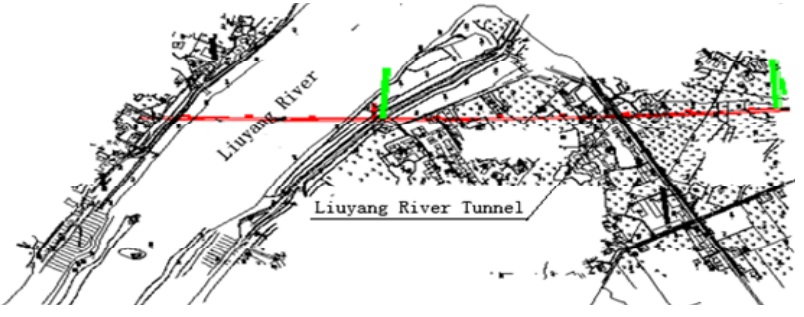

FIG. 1 Planar graph of Liuyanghe River Tunnel.

FIELD MEASUREMENT ARRANGEMENT

To observe the settlement of surface and subsurface, multi-point extensometers are lay out in situ. Multi-point extensometers are arranged in DIIK1569+261, which are replaced by rebar from DIIK1569+200 to DIIK1569+260. These fixed rebar are used to observe the settlement of middle stake. Representative section of settlement is selected for DIIK1569+230.

3D deformation of surrounding rock is observed by arbitrary station with universal thodolite, and non-contact observation system under condition of clearance, consisted of high precision total station, portable microcomputer and reflection diaphragm, obtain 3D deformation by precise angle measurement and ranging (Yang Songlin, Liu Weining, 2006). This data is used to study the development of 3D deformation.

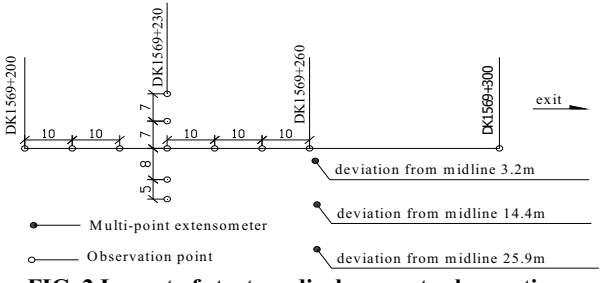

FIG. 2 Layout of stratum displacements observation.

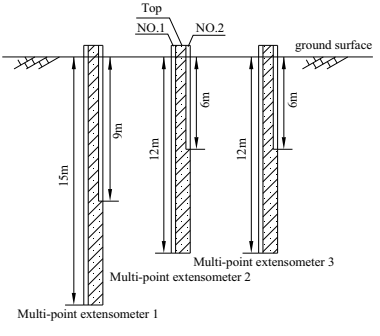

FIG. 3 Layout of extensometers.

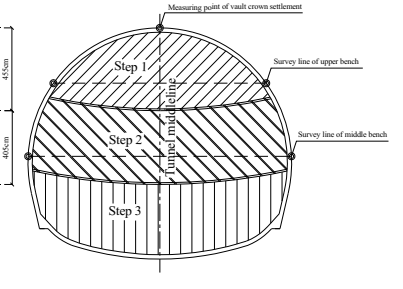

FIG. 4. Benching tunneling method and test points of 3 D deformation.

FIELD MONITORING

Observation and Analysis of Stratum Displacement

- **Ground settlement**

Transverse settlement curves of ground surface along with upper bench excavation are shown in Figure 5, of which cylindrical represent the distance of tunnel face apart from the DIIK1569+261 section, the negative value represents tunnel face which has not yet arrived at DIIK1569+261, by contrast the positive value represents tunnel face which has passed this section. The ground surface settlement gradually increases along with excavation of working face of upper bench. When tunnel face arrives at DIIK1569+190 , namely upper bench has crossed measuring point 5L, of which L is the largest tunnel excavation span. Invert locates at DIIK1569+257, at this time ground settlement has been already basically stable.

Vertical settlement on top of multi-point extensometer No.1 is given in Fig. 6. When the time passes away 20 days, upper bench just passes DIIK1560+261 and the rate of ground settlement increases obviously. When time passes away 42 days, bottom bench arrives at DIIK1560+258.1, which means that bottom bench has passed away DIIK1560+261, and the rate of ground settlement starts to reduce. When time passes away 57 days, invert arrives at DIIK1560+257, at this time whole primary support has

been close, and ground settlement varies very little, so ground settlement can be regarded as basically stable.

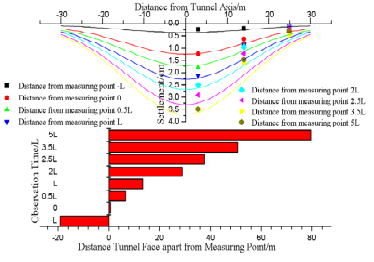

FIG. 5. Ground Settlement in DIIK1569+261 during upper step tunneling process.

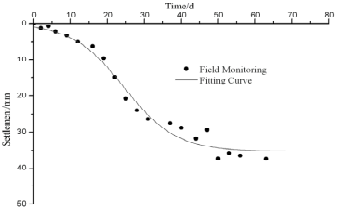

FIG. 6. Vertical settlement on top of multi-point extensometer No. 1.

- **Subsurface settlement**

Final settlements of multi-point extensometer are listed in table 1. Multi-point extensometer No.1, most close the tunnel axis, is influenced by excavation, so its settlement is also the biggest. Multi-point extensometer No.3, farthest from the tunnel axis , has very small settlement.

Table 1. Various Settlement (in mm) of Multi-Point Extensometer

	No. 1	No. 2	No. 3
Top	34.9	14.8	3.1
Hore NO.1	37.38	16.52	3.09
Hore NO.2	35.12	16.32	3.08

- **3 D Deformation in tunnel**

3D deformation in tunnel is observed with free stationing. Through coordinate transformation, vault crown settlement and peripheral displacements are given in Fig. 7. From the field monitoring result, we know that vault crown settlement is bigger than peripheral displacement, and the displacement of survey line 2 is obviously smaller than the survey line 1.

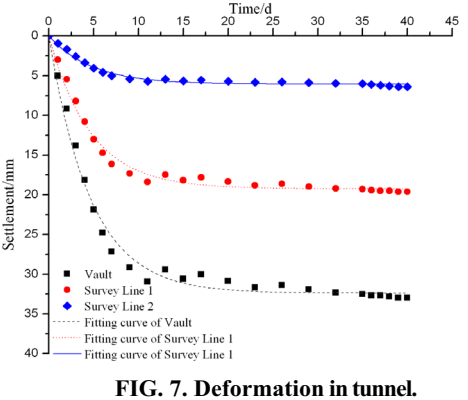

FIG. 7. Deformation in tunnel.

NUMERICAL ANALYSIS

Numerical analysis is completed by ABAQUS, which is a suite of powerful engineering simulation programs, based on the finite element method (ABAQUS, 2003). ABAQUS contains an extensive library of elements that can model virtually any geometry, offers a wide range of capabilities for simulation of linear and nonlinear applications. It has an equally extensive list of material models that can simulate the behavior of most typical engineering materials such as soils, rock and reinforced concrete. As, it has got Ultra-intense nonlinear calculation ability, so it's applied in geotechnical engineering more and more.

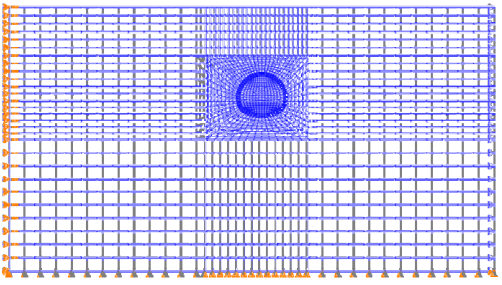

Fig. 8. FEM Model.

Finite element method (FEM) model, for which left and right boundary are determined 5 times the largest excavation span apart from tunnel axis and the lower boundary takes outside 4 times excavation span, has a size of 150 m x 80 m. Tunnel depth takes 20 m. Left and right boundary are fixed in x direction, and the lower boundary is fixed in y direction. Model calculation parameters are shown in table 2.

Table 2. Model Calculation Parameters

Material	Density (kg/m^3)	Elastic Modulus (GPa)	Poisson ratio	Cohesion (kPa)	Internal Friction Angle(^{0})
Soil	1600	0.062	0.40	10	20
Reinforced Soil	1600	0.2	0.4	20	20
Shotcrete	2300	35.82	0.2		
Invert backfill	2300	28	0.2		
Lining, invert	2300	22	0.2		

Displacement Analysis

FEM calculation results, along the depth 0.0 m, 6.0 m, 9.0 m, 12.0 m and 15.0 m, are shown with the field monitoring result in Fig. 9. It's shown that the largest ground settlement is 36.19 mm in surface above tunnel axis and settlement deviation from

tunnel axis 3.2 m is 35.81 mm, which agrees well with settlement on the top of multi-point extensometer No.1. Ground settlements, outside deviation from tunnel axis 43 m, are less than 5 mm, but field monitoring data show that settlement deviation from tunnel axis 25.9 m is 3.08 mm. Ground settlements, outside deviation from tunnel axis 58 m, are less than 1 mm, which means that tunnel excavation has little influence on ground settlement.

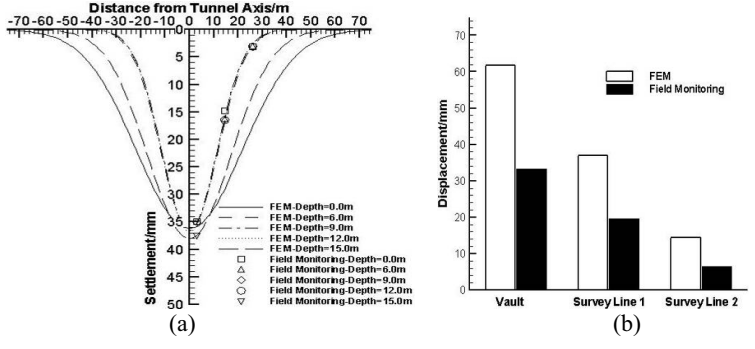

FIG. 9. Comparison of FEM and field monitoring: (a) settlements and (b) relative convergence.

The in-site peripheral convergence of survey line 1 is 19.6 mm, but the numerical calculation result is 61.2 mm. There is great difference for survey line 1, which is same between field monitoring and numerical calculation. It may be that during the tunnel excavation field monitoring is influenced by excavation, especially the survey lines can't be arranged immediately after excavation (Kong Heng, 2003). The numerical analysis simulated the entire excavation process, so the numerical calculation result is the final convergence. Although, field monitoring are started after the tunnel face is excavated forward certain distance, so there is inevitably difference for them. However, the in-site observation indicates that the excavation section, after lower bench excavation, is in stable, and there is not partial collapses or distortion oversized region.

Stress and Strain Analysis

Plastic strain near excavating boundary contour map, after tunnel construction, is shown in Fig. 10. The plastic region mainly concentrates nearby the side wall and the haunch. The maximum plastic region appears foothold of upper bench, which is also the stress concentration area. The arch, adopting pipe shed and small pipe, has small plastic area than side wall.

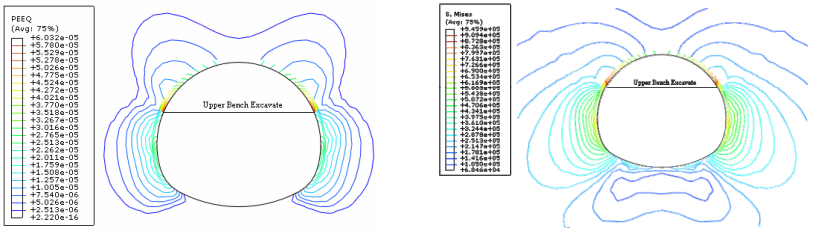

(a) (b)

FIG. 10. Close view of contour of: (a) plastic strain and (b) stress.

CONCLUSIONS

Because of the crowded surface buildings in tunnel exit, multi-point extensometers are lay out in-situ to gain ground settlement of surface and subsurface. In addition, 3D deformation of surrounding rock is also observed. Through field monitoring and numerical calculation, the stratum displacement pattern was obtained finally, at the same time we can also find some useful conclusions as follow:

1. 3D deformation in tunnel, observed by arbitrary station with universal thodolite, is less disturbed by excavation and has high automaticity, which may reduce measuring error in large section excavation under complex geology conditions.
2. The numerical calculation results agree well with the field monitoring data. Field monitoring, compared by numerical analysis, indicates that the construction process satisfies the safety control requirements, but we still pay enough attention to the field construction.

REFERENCES

Huang Jun, Zhang Dingli. (2004). "Analysis of large deformation regularity in stratum above metro tunnel ". *Rock and Soil Mechanics*, 25(8): 1288-1293.

Kyung-Ho Park. (2005). "Analytical solution for tunnelling-induced ground movement in clays ". *Tunnelling and Underground Space*, 20: 249-261.

D.M.Potts, T.I.Addenbrooke. (1997). " A structural's influence on tunnelling-induced ground movement. " *Proc. Instn Civ. Engrs Geotech. Engng*, 125:109-125

Yang Songlin, Liu Weining, Shi Hongyun,etc. (2006) " A study on the theory and method of non-contact monitoring for tunnel rock deformation based on free stationing of a total station ". China Civil Engineering Journal, 39(4):100-104.

ABAQUS. (2003) "ABAQUS Users Manuals Version 5.8"

Kong Heng. (2003) "Study on Mechanism of Stratum Pre-reinforced and Its Application for Shallow Tunnels Construction Method in Urban Subway ". Beijing: Beijing Jiaotong University, 2004

Study on Construction Methods for Tunnels of Large Cross-Section Excavated in Weak Rocks

Lichuan Wang[1], Haibo Hu[2], Shibin Wang[3], and Ruihua Jia[4]

[1]Doctoral Candidate, School of Civil Engineering and Architecture, Central South University, Changsha, 410075; Chief Engineer, Jingsui Construction Corporation of China Railway Tunnel Group, Beijing, 100022 China; wlc773747@126.com

[2]Master, School of Civil Engineering and Architecture, Central South University, Changsha, 410075; huhaibo1982@yahoo.com.cn

[3, 4]School of Civil Engineering and Architecture, Central South University, Changsha, 410075.

ABSTRACT: The double side drift method, CRD and CD method are widely adopted for super large cross-section excavation for tunnel in weak rock in China. Further, it is shown good adaptability because of the extensive application in highway, railway, especially in urban underground facilities.

However, there are also some problems in work efficiency, structure safety and engineering management and so on. It is necessary to make optimization of construction methods under these conditions. In this paper these shortcomings for double side drift, CRD and CD methods are detailed. The work efficiency, load conversion mechanism and the influence on tunnel structure, and construction management are discussed. Then suggestions for tunnel excavation determination in such conditions are put forward. It is shown that if auxiliary measures are adopted first, partial excavation could be abandoned. Even full-face excavation may be feasible. The principle proposed in this paper has been used in practice, which is proved once more for tunnel excavation in soft and weak surrounding ground.

INTRODUCTION

The tunnels, with a speed exceed 350 kilometer per hour in China, often have an excavation area 140~170 m^2, which belong to super large section tunnel. Tunnel construction and design in weak surrounding rocks adopt double side drift method, CRD method and CD method, namely three methods. Although the application of three methods has obtained good effects and successful experience (Wang Mengshu, 2004), it is still necessary to optimize the construction process for the limitation in work efficiency, management level and operation techniques.

NUMERICAL ANALYSIS

Shallow tunnel driven by double side drift method was selected typical example.

Because of weak surrounding rock and adjacent structures, it needs to control ground settlement strictly. To ensure the safety, partial excavation was adopted. In addition, grouting reinforcement with pipe shed and small pipe was used as pre-supporting technology. Primary support consists of sprayed steel fiber concrete and entire link I20a steel frame with 0.5 m spacing. In addition, anchor rods combined with shortcrete were used to strengthen weak rocks, which has 4.0 m in length and 1.0 m ×1.0 m spacing. Pipe shed adopts ϕ 108 hot rolling seamless steel tube with 6mm in thickness, 18 m in length and 0.4 m in ring spacing. Small pipe adopts ϕ 42 hot rolling seamless steel tube, which has 3.5 m in length and 0.4 m in ring spacing.

Numerical analysis is completed by ABAQUS, which is a suite of powerful engineering simulation programs (ABAQUS, 2003). ABAQUS contains an extensive library of elements that can model virtually any geometry, offers a wide range of capabilities for simulation of linear and nonlinear applications. It has an equally extensive list of material models that can simulate the behavior of most typical engineering materials such as soils, rock and reinforced concrete. As its Ultra-intense nonlinear calculation ability, so it's applied in geotechnical engineering more and more.

Finite element method (FEM) model, left and right boundary are determined 5 times the largest excavation span apart from tunnel axis and the lower boundary takes outside 4 times excavation span, has a size of 150mx80m. Buried depth is 20m, and horizontal and vertical boundaries are fixed. Numerical calculations include five cases, namely the three methods, bench method and full section method. The mechanical parameters of rock in the vicinity of tunnel face are improved as a simplified approach for systematic bolts, grouting pipe shed and small pipe.

Table 1. Physico-Mechanical Parameters

Material	Density (kg/m^3)	Elastic Modulus (GPa)	Poisson Ratio	Cohesion (kPa)	Internal Friction Angle(^{0})
Soil	1600	0.062	0.40	10	20
Reinforced Soil	1600	0.2	0.4	20	20
Shotcrete	2300	35.82	0.2		
Invert backfill	2300	28	0.2		
Lining, invert	2300	22	0.2		

Stratum Displacement

Stratum displacements under different construction conditions are shown in Fig.1, of which the largest ground settlement and crown settlement are listed respectively as follows: 27.20 mm and 53.69 mm for CRD, 28.58 mm and 56.78 mm for double side drift method, 33.66 mm and 64.87 mm for CD, 37.41 mm and 65.32 mm for bench method, 54.40 mm and 90.09 mm for full section method. Although the working procedures for full section method are the least, both numerical calculation and field experience indicate that the application of full section method for large section excavation under weak geotechnical conditions may be infeasible.

If construction adopts three methods, namely double side drift method, CRD method

and CD method, ground settlements under these methods are better controlled than bench method, but such divisional excavation mode will greatly reduce the work efficiency, even cause some mechanical injuries accident. Although ground settlements for bench method construction exceed over three methods, the method, if combined with certain auxiliary procedure, can still satisfy the safety requirements.

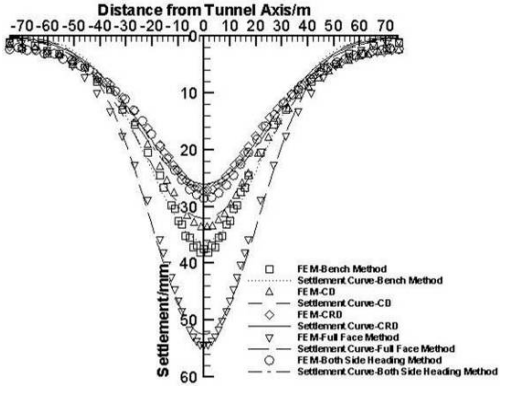

Fig. 1. Ground settlement under different construction methods.

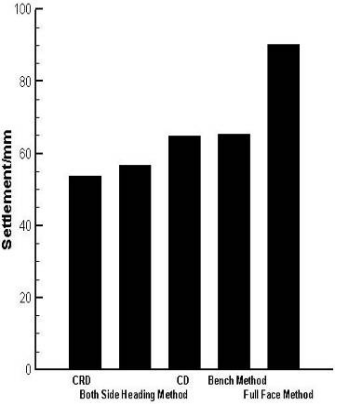

Fig. 2. Crown settlement under different construction methods.

Plastic Zone

Plastic zones under different construction methods are shown in Fig. 3. Distribution range of plastic zone for full section method is the most widely. The plastic zone,

excerpt for invert, even have developed to form a connected domain, which shows that full section method must be considered cautiously for weak surrounding rock. Plastic region for bench method and CD method take second place, and it's the smallest for double side drift method and CRD method, of which plastic zone in arch scope distribute dispersedly. When tunnel construction adopts bench method, most regions along excavation boundary turn into plasticity, especially plastic zone in side wall and haunch extends toward surrounding rock inner, so these regions should be selected carefully.

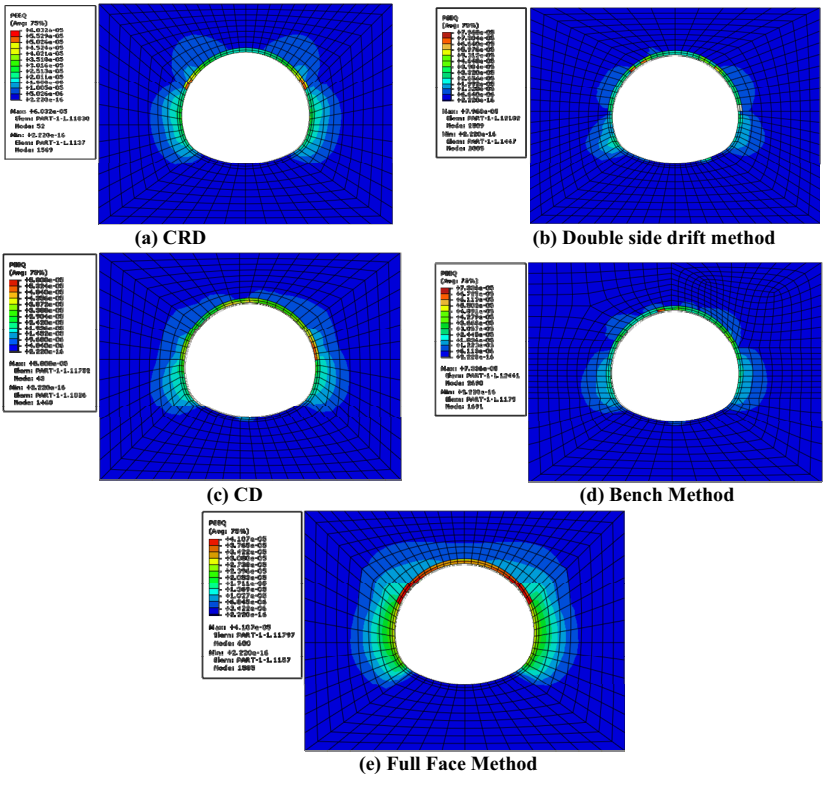

Fig. 3. Plastic zone for different construction methods.

Structural Internal Force

As mentioned in previous section, stability for primary support system, surrounding rock and lining needs to be considered for each excavation method. Calculated results of internal force under different construction methods are listed in table 2.

Table 2. Calculated Results of Internal Forces

		CRD	Double side drift Method	CD	Bench Method	Full Face Method
Bending Moment	Tension/kN•m	43.75	25.10	44.31	26.67	28.86
	Compression/kN•m	41.52	30.55	30.17	16.49	16.32
Maximum Axial Force	Tension/kN	275.7	213.4	203.4	66.74	29.93
	Compression/kN	217.9	143.5	289.5	118.7	147.6
Maximum Shear	Tension/kN	54.81	66.59	46.51	18.14	23.47
	Compression/kN	54.82	93.08	45.90	12.08	23.47

Internal forces for bench method are shown in Fig. 4, of which maximum tensile axial force, locating on left arch foot of lining, is 66.74 kN, and maximum compression axial force, locating on right arch foot of lining, is 118.7 kN. Maximum tensile bending moment, locating on the vicinity of haunch, is 26.67 $kN \cdot m$, and maximum compression bending moment, locating on vault, is 16.49 $kN \cdot m$.

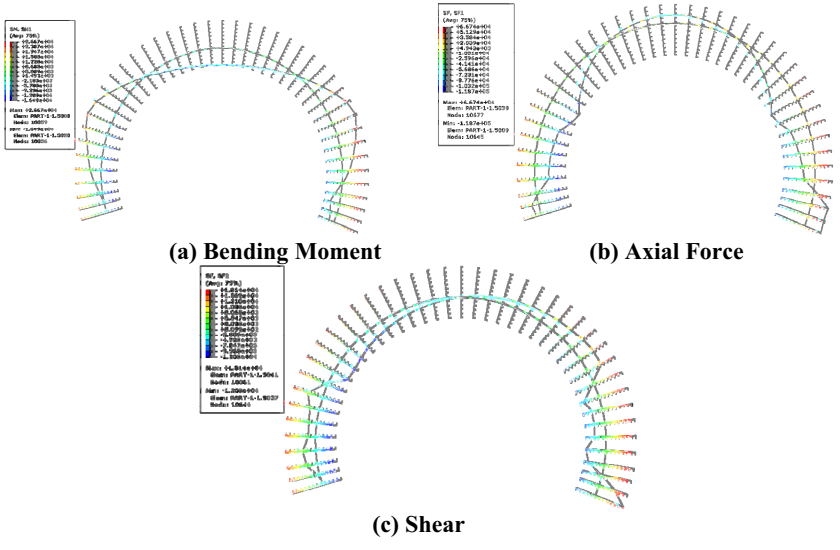

(a) Bending Moment **(b) Axial Force**

(c) Shear

Fig. 4. Internal force caused by bench method.

As there are many conversion procedures for three methods, so the supports joints often become the key points because of stress concentration. Therefore, three methods, compared with bench method, are easy to cause larger internal force, which will become the potential security trouble for later period.

NEW CHOICE FOR LARGE SECTION EXCAVATION

At present there are many choices for tunnel construction under weak surrounding rock, and safety can also be guaranteed for them. With experiences accumulation for successful erection of long tunnel and large underground engineering and improvement for mechanized operation, construction method for tunnel remains to be innovated and raised.

As three methods have some disadvantages in practical application, so these new choices, namely less divisional excavation or no divisional excavation for large section excavation, are put forward on the basis of literatures published in home and abroad and tunnel construction practice (Li Shihui, 1999; Wang Mengshu, 2005; Zhao Dongping, 2005). The paper, based on actual geological and construction conditions, proposes four kinds of method as follows:

- **Reinforcement from side hole or ground.** First, we can excavate some small holes, which are close to tunnel face or located on ground surface, then the surrounding rock in the vicinity of tunnel face will be grouting reinforced ahead, the mechanic characteristics of rock mass will be enhanced, thus entirety and stability of strata will be also improved, which can provide guarantee for large section excavation.
- **Reinforcement from advancing middle drift.** Firstly a small section hole is excavated at upper part of excavation section, which will be used to grout surrounding rock in the vicinity of tunnel face. If grouting reinforced region are enough, then we can selected bench method or full section method under weak rock.
- **Advancing strong support.** The method means that large pipe shed will be inserted into ground before excavation to form a closed annual space, meanwhile limited range strata will be grouting reinforced, and then pipe sheds combine with strengthening stratum to form supporting system.
- **Advancing improvement with small pipe.** Firstly hollow grouting anchor or small pipes are inserted into ground, then sufficient grouting will be used to strengthen surrounding rock, which forms strengthening arch ring, thus large section excavation can be carried on underneath the strengthening arch ring. However, the above four methods have their application scope, in actual local conditions, tunnel length, construction condition and time requirement will be taken into account for the excavation method choice.

APPLICATION AND DISCUSSION

Original design constructions for some tunnels in Zhejiang-Jiangxi line are double side drift method and CRD method, of which fractured weak zones account for 60% of full length. According to local conditions, firstly the surrounding rock would be reinforced with small pipe and grouting, and then construction methods actually turn into bench method. Although there are collapse zones for tunnel exit, entire construction safety can be guaranteed because of these treatments, even the construction period can be shorten more than a year than the approved time.

Original design construction for some railway tunnel inlet is CRD method, actually the method turns into bench method with small pipe and grouting, of which temporary

invert isn't considered. Surrounding rock in exit, which cannot be grouting effectively, is grade of V. Construction method for the first 30 m in exit turn into bench method with large pipe shed, of which temporary transverse support is set partially, and method for the second approximately 80 m in exit also turns into bench method with small pipe, of which upper section excavation area is 62 m^2. During the entire process construction is safe, except for ground settlement of approximately 6~10 m in exit is a little abnormal. The main monitoring data are listed as follows: average settlement in inlet is 18mm, and the maximum is 27 mm. Average settlements in exit are 85 mm, and the maximum is 96 mm.

CONCLUSIONS

The application of three methods is feasible in practice, but there are still many limitations in structure safety and quality, process, construction period and engineering economy, so it's necessary to explore scientific economic construction method. Based on the deficiency of three method application, new choice for large section excavation is put forward, namely large section excavation should turn into less divisional excavation or no divisional excavation, which has achieved success and shows good performance, broad prospect in application.

REFERENCES

China Railway Publishing House. (2005). "Technology guide for construction of passenger dedicated line in China (TZ214-2005)."

China Railway Publishing House. (2002). "Code for construction on tunnel of railway (TB10204-2002). "

China Communications Press. (2004). "Code for Design of road tunnel (JTG D70-2004)."

Wang Mengshu. (2004). "Overall discussion on shallow mining method of underground engineering." ISBN: 9787533642358.

ABAQUS. (2003). "ABAQUS Users Manuals Version 5.8"

Li Shihui. (1999). "New discussion on support and design of tunnel." ISBN: 7030070534.

Wang Mengshu. (2005) "Discussion on design and construction of large tunnel on passenger dedicated line." *Journal of Railway Engineering Society*, 1:10-16.

Zhao Dongping, Wang Minnian.(2005) "Study on construction method of large-span tunnels by numerical simulation." *Chinese Journal of Underground Space and Engineering,* 1(6):844-847

Interaction of Pipe-roof Reinforcement and Tunnel Construction under Existing Highway

ZHANG Ge[1] and KANG Shilei[2]

[1]School of Civil and Architectural Engineering, Central South University, Changsha, Hunan 410075, China; Lecturer of School of Water Conservancy, Changsha University of Science & Technology, Changsha , Hunan 410076,China

[2]Associate Professor of School of Civil Engineering, Changsha University of Science & Technology, Changsha , Hunan 410076,China

ABSTRACT: Pipe-roof has been adopted extensively as pre-support in tunnel construction. The vertical deformations of the pipe-roofs in the entrance of Liuyanghe Tunnel are monitored by installation of a series of strain gauges to investigate the mechanical behavior of the pipe-roofs during the tunnel excavation. Based on the monitoring results, the mechanical characteristics and the evaluation of the reinforced effect of pipe-roof in the construction process were analyzed.

INTRODUCTION

The tunnel project of under-crossing surface buildings is adopted increasingly in the new highway design and construction. During the excavation of shallow tunnel, the disturbance for surrounding rock will cause ground settlement and deformation or even tunnel collapse. Therefore, pre-supporting method should be used to enhance ground stiffness and strength. One of the pre-supporting methods is pipe-roof reinforcement, which has been applied extensively in the tunneling practice.

In tunnel engineering design, pipe-roof is generally simulated to be a beam, which cannot completely reflect the process of its deformation and bearing load during the tunnel excavation. The pipe-roofing mechanics changes are resulted from different construction methods and construction periods. In this paper, the mechanical characteristics and the evaluation of the reinforced effect of pipe-roof in the construction process were analyzed based on the field monitoring results.

TUNNEL CONSTRUCTION AND PIPE-ROOF MONITORING

Liuyanghe Tunnel, which is a high-speed railway tunnel of Wuhan to Guangzhou, passes across the Changsha Airport Highway. The tunnel is buried 8 meters under the ground and covered with incompact clay and weathering rock. For guaranteeing the safety of the highway and tunnel construction, pipe-roof reinforcement was used as pre-support. The tunnel design adopts the steel pipe with diameter of Φ325mm, and filling with cement slurry to improve stiffness and strength. The tunnel construction adopted the method of two side and step excavation.

In order to acquire the changes of pipe-roof deformation during the tunnel construction, 3 strain gauges, with interval of 5 meters, were installed inside each pipe of No. 30, No. 40 and No. 50 to monitor strain, as can be seen in FIG.. 1. The monitored pipes are in the outer layer, and its numbers are shown in FIG. 1(a). FIG. 1(b) shows the construction of the upper part of pipe-roof in the field.

The ground surface settlement, tunnel vault subsidence and constringency were also monitored during tunnel construction. The observations show that the pipe-roof construction has a great effect to reduce the ground settlement. The largest settlement is about 30 mm, which occurs on the upper step excavation. The rate of subsidence is obviously large in the early days of tunnel construction while reduce gradually along with time. The largest constringency is 7.05 mm. During the whole construction process, the stress and transmutation of reinforcement structure do not exceed the limits of material strength.

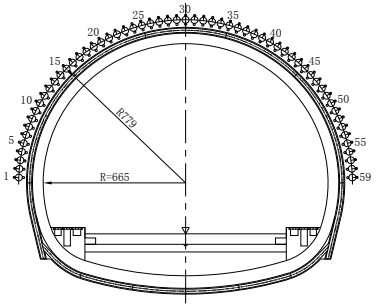

(a) **(b)**

FIG.1. Layout of pipe-roof and monitored steel pipes.

FIG. .2 and FIG. .3 shows the relation curves of $\Delta\varepsilon_i$-t for steel pipe No.30 and No.50. It can be seen that the deformation of pipes were increasing gradually as the excavation cross section approaching to monitor gauges. The largest deformation appeared when the excavation cross section was exactly under the gauges. The change rate of pipe deformation was reducing obviously and the strain was minishing. After

the completion of early support, the strain of steel pipe keeps invariability with the passing time. For upper step excavation had a greatest influence to the pipe strain, which was with its strength, conclusion can be drawn that pipe-roof is in the elasticity state and the pre-support effect has exerted. That is, earth pressure was sharing by the pipe when tunnel excavated.

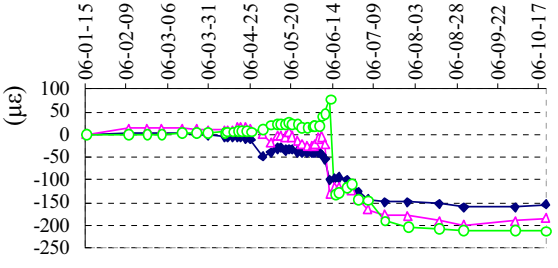

FIG. 2. Relation curves of $\Delta\varepsilon_i$ and t for steel pipe No. 30.

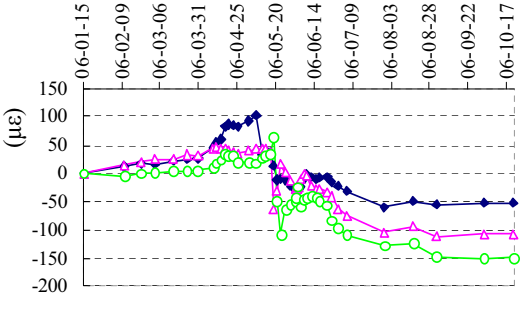

FIG. 3. Relation curves of $\Delta\varepsilon_i$ and t for steel pipe No.50.

According to the relationship between the $\Delta\varepsilon_i$-t curve and the tunnel construction schedule, the vertical curves of the pipe No.30 and No.50 along its longitude were obtained, which are shown in FIG. 4 and FIG. 5.

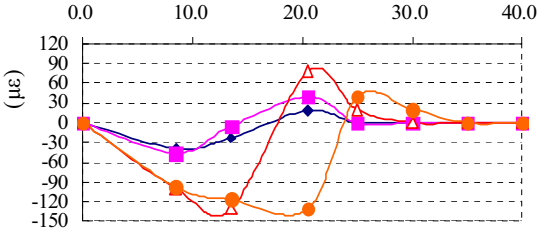

FIG. 4. Relation curves of strain and tunnel longitudinal position for pipe No. 30.

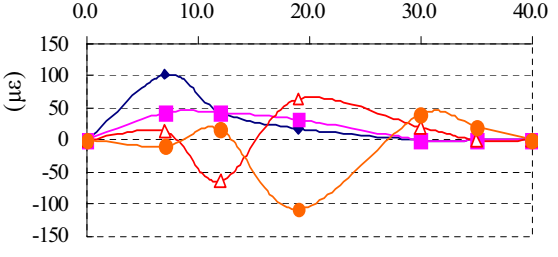

FIG. 5. Relation curves of strain and tunnel longitudinal position for pipe No.50.

It can be seen that the pipe vertical deformations are concave as a whole and move forward and downward according to tunnel excavation advancement. When the excavation cross section is under gauge A (x=5m), the reading rate of gauge B (x=10m) increase obviously, but the rate of gauge C (x=15m) increase hardly. It seems that the excavation incidence is about 10 m. When the excavation cross section is under gauge B, the reading rate of gauge C increase obviously, but the rate of gauge A (x=15m) reduced. It is considered that pipe-roof is exerting the pre-support effect and adjusting rock pressure.

When the excavation cross section is under gauge C, the reading rate of gauge A change hardly and the rate of gauge B reduced. It is shown that pipe-roof and early support has burden the rock pressure together.

CONCLUSIONS

Based on the monitoring data and analyzing, the following conclusions can be obtained:

1. Pipe-roof was within the elasticity state and exerting the pre-support effect well. It maintains the stability of tunnel together with early support.
2. Pipe-roof has reduced the earth surface displacement, the vault subsidence and the constringency effectively. Therefore, good engineering result and economic

performance were obtained when pipe-roof is adopted.
3. The stress and strain of pipe-roof are changing fluctuant in the course of tunnel construction. The largest stress and strain occurs when the excavation cross section just under the monitoring section, which can be regard as the most disadvantageous condition in pipe-roof design.

REFERENCES

GOU Deming, YANG Junsheng, ZHANG Ge. (2007). "Deformation monitoring and mechanical behaviors of pipe-roof in shallow tunnels." *Chinese Journal of Rock Mechanics and Engineering*, VOL.26(6):1258-1264

GOU De-ming, YANG Jun-sheng, GAO Shi-ju. (2008). "Numerical analysis of pre-reinforcement action about double-layer pipe roof in multi-arch tunnel under the existing highway." *JOURNAL OF CHANGSHA COMMUNICATIONS UNIVERSITY*, VOL. 24(2):16-22.

CHEN Hao, JIANG Jingshan, YAO Haibo. (2006). "Construction and distortion analysis of pipe-roof installed in Chongwenmen metro station underneath existing metro line". *Tunnel Construction*, VOL.26(1): 78-80

XING Houjun, XU Zhenxiang. (1999). "Application of big pipe-roof in large-span shallow buried tunnel engineering". *Chinese Journal of Rock Mechanics and Engineering*, VOL.18(Supp.):1059-1061

CHUNGSIK Y, HYUN-KANG S. (2003). "Deformation behavior of tunnel face reinforced with longitudinal pipes-laboratory and numerical investigation". *Tunneling and Underground Space Technology*, VOL.18(4):303-319

Stability Analysis of Tunnel Driven in Stratified Anisotropic Rockmass

ZHANG Xuemin, YANG Junsheng, and CHEN Jiejin

School of Civil Engineering and Architecture, Central South University, Changsha, China, 410075, zhangxm@mail.csu.edu.cn

ABSTRACT: In present engineering design, rock mass is simply treated as an isotropic material and their strength parameters are given by decreasing those of intact rock through joint connectivity, which is introduced to reflect the integrity of rock mass separated by joints. This method may be acceptable for most jointed rockmass. But for some sedimentary or metamorphic rocks, such as shales, sandstones, slates, phyllites and schists, are characterized by inherent anisotropy due to the existence of the preferentially oriented weakness plane. In this study, the influences of the anisotropic properties of rockmass on the deformation and stability of tunnel are analyzed by the site monitoring and numerical calculation. A detailed investigation on the engineering geological conditions of the horizontal stratified strata in Queerxi Highway Tunnel was carried out. The deformation and the surrounding rock pressure are monitored, and then field measuring results and distributing law are summarized. The results show that anisotropy of rockmass has remarkable influence on the deformation properties and stability of tunnel in stratified jointed rockmass.

INTRODUCTION

Sedimentary rock mass with stratified structures, such as sedimentary sandstone, mudstone, shale, etc, is approximately seventy-five percentage of lithosphere area. There are more and more underground facilities constructed in stratified rock masses, in which the stratification is generally characterized by its planar geometry and persistence. For example, there deposited typical horizontal stratified strata in the west of Hunan Province, China, and 33 highway tunnels of about 40 km in length were constructed in this stratified strata. The Construction of these tunnels was an important part of the Highway from Changde to Jishou City in Hunan Province of China.

The behavior of layered rock mass is predominantly a reflection of the behavior of the discontinuities presented by joints and bedding planes, which is a key factor of stability of tunnel excavations. There are two distinctive features concerning stratified rockmass. Firstly, low or zero tensile strength in the direction perpendicular to the stratification; and secondly, relatively low joint shear strength in comparison to that of the intact rock. The stability of underground excavations in layered rock masses has been analyzed by different approaches, such as pressure arch theory (Sansone et al.

1998) and voussoir beam theory (Mottahed, et al., 1995), etc. Based on finite element analyses and laboratory experiment results, Wright (1974) created a design procedure for the control of layered, bolted or unbolted, underground undermined roofs when tunnelling in stratified strata. The approach for determination of deformation properties for stratified rocks is given by Vlasov et al. (1995).

GEOLOGICAL CONDITIONS AND FIELD MEASUREMENTS

A detailed geological and engineering geological study was carried out in the construction sites. In order to constitute the geological model and determine the engineering geological properties of surrounding rock mass, site investigations were carried out. It was shown that the main deposits in tunnel sites included bedding calcareous sandstone and claystone, banded alternate layers of these units (HPCPSDI, 2004).

The length of Queerxi Tunnel is 1417 m and located in typical horizontally stratified rock mass. The main lithological sequences along the tunnel were found to be at upper Cretaceous Age, Jinjiang River Group. Close to the stratum surface Quaternary Holocene silty clay and soil aggregate with 0.3 m to 1.2 m in thickness were widely distributed. This tunnel was excavated in rock mass with a monoclinal structure and alternation of calcareous sandstone to clayey stone. The sandstone and the claystone are all weathered in varying degrees along the depth direction. The strata might be divided into three types from youngest to oldest, i.e., intense weathering, moderate weathering and weak weathering.

Laboratory tests have also been conducted on rock samples collected from drilling rock cores in the field site of Queerxi Tunnel, to evaluate their mechanical properties. Especially, testing results indicate that the water content largely influences the engineering properties of claystone, inducing deterioration of claystone properties. Strength of claystone decreases along with the increase of water content, and its deformation increases. When the claystone was exposed in air, and particularly during rainy season, it gradually developed a fissile appearance, and the fresh claystone disintegrates to a silty-muddy loose mass after a few months. Its deterioration phenomenon may heavily influence the stability of tunnel.

When tunneling in horizontally stratified strata, there encountered some geotechnical problems such as excessive overbreak, rock falls, instability of the face, collapse, etc. This is synthetically influenced by some factors. Because the excavation of a tunnel results in a general unloading of the tunnel environment and the shear strength of bedding planes is often greatly reduced. Therefore, the spalling condition is quite common, and bedding planes often participate in forming rock blocks. Furthermore, blasting has a prominent impact on the stability of tunnel in stratified strata, even though by smooth blasting and short delay blasting because of the dynamical mechanical effect of the blasting; especially the vertical joints are largely distributed in perpendicular direction. A tunnel that would have been stable during construction could require ground pre-support, such as advance supports of anchor bolts or grouting pipe-roof, etc.

Field measurements were conducted in Queerxi Tunnel. The measuring items consisted of settlements at the crown, horizontal convergences of the tunnel, axial

forces of rock bolts, pressures between lining and surrounding rock, stresses of shotcrete and linings, stresses of steel arches and lining, etc. Distribution law of the measured pressures between support of shotcrete and reinforced concrete lining, and the calculated axial forces and bending moments of the concrete lining of Queerxi Tunnel in YK193+732 section based on the field observations of stresses are also shown in Figure 1 and 2.

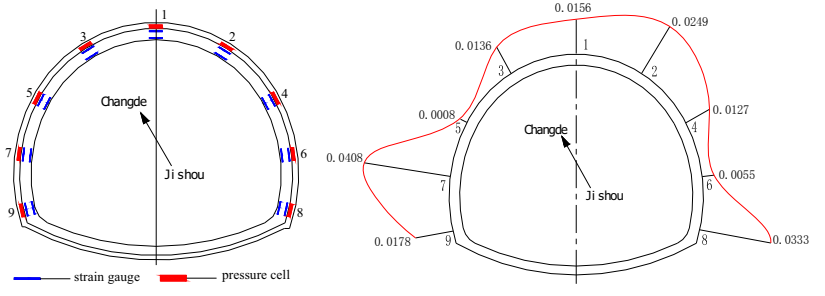

FIG. 1. Instrumentation of YK193+732 section and pressures between primary shotcrete and concrete lining (MPa).

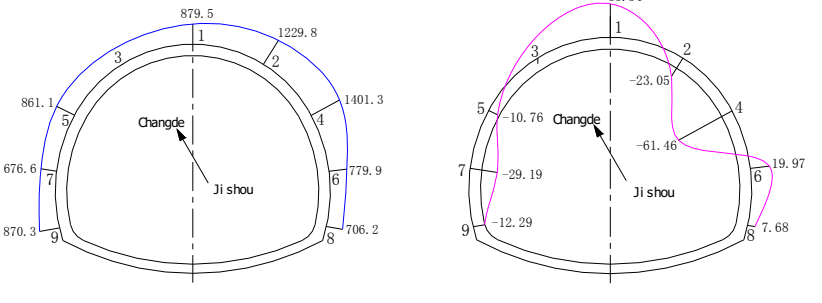

(a) Axial forces (kN) (b) Bending moments (kN.m)

FIG. 2. Distribution of axial forces (kN) and bending moments (kN.m) of the concrete lining.

NUMERICAL MODEL

Modeling

Numerical model studies were achieved using a 2-dimensional, finite difference numerical modeling code (FLAC). Figure 3 shows the selective numerical model in stratified rock mass with an alternation of sandstone and claystone 0.3 m in thickness. Numerical models are constructed based on assumption of isotropic elasto-plastic plane strain model using quadrilateral isoparameter elements. Deformation between

alternation of sandstone and claystone layers is assumed to be continuous according to site investigating conditions.

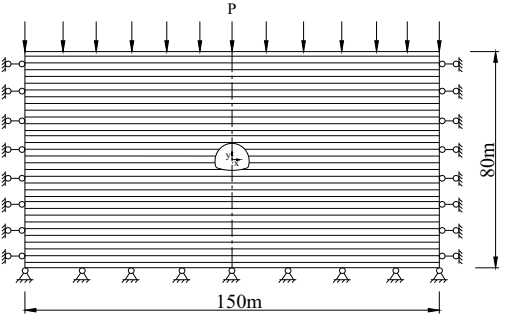

FIG. 3. Numerical model of tunnel in the stratified rockmass.

Input parameters

The mechanical properties of surrounding rock mass as input parameters are listed in table 1. Deformation modulus of primary shotcrete lining is 21 GPa. For secondary concrete lining, corresponding parameters are 29.5 GPa.

Table 1. Material Properties in Numerical Modeling

Material	ρ (kg/m^3)	E (GPa)	K (GPa)	G (GPa)	ν	c (MPa)	ϕ (°)	σ_t (MPa)
Sandstone	2400	13	9.85	5.08	0.28	1.1	45	1.2
Claystone	2000	1.5	2.50	0.54	0.4	0.1	23	0.3

Notes: ρ= density; E=deformation modulus; K= bulk modulus; G= shear modulus; ν=Poisson's ratio; c=cohesion; ϕ=internal friction angle; σ_t=tensile strength.

RESULTS AND ANALYSIS

Displacement Analysis

The distributions of stresses and deformations of surrounding rocks and lining of tunnel, as well as internal forces in support system in each excavation stage were obtained from numerical analysis. When lower benching excavation is finished, the total subsidence displacement of tunnel crown is 10.03 mm, and the total horizontal convergent displacement is 10.47 mm, and the corresponding floor heave is 8.76 mm. For top heading a maximum displacement in vertical and horizontal direction respectively is 7.93 mm and 4.33 mm.

Roof subsidence of tunnel mainly occurs and increases significantly in the stage of the upper bench excavation, which is 79% of total deformation. For horizontal

convergence of tunnel, most deformation takes place in lower bench mining about 60% of total horizontal convergent displacement because of decrease of clamping action at the side walls. Compared to the unsupported excavation in each benching, the displacements have been slightly reduced by only application of rockbolts for section in the top benching and lower benching, but the combination of rockbolts and shotcrete has reduced the maximum displacement, especially a reduction of deformation at the roof and at the left and right sidewalls of tunnel.

Plastic Zone and Internal Force

The distributions of plastic zones in surrounding rock of tunnel during top heading and benching excavation stages were shown in Figure 4. The yielded elements are mainly concentrated at the left and right sidewalls and at the two bottom corners of the tunnel sections. But the extent of the yield zone at the tunnel crown is smaller. Cracking initiates as a result of the removal of the confining stress and the loading by tangential stress concentration. The cracks then tend to grow parallel to the excavation surfaces forming slabs of rock (Cai, et al. 2004).

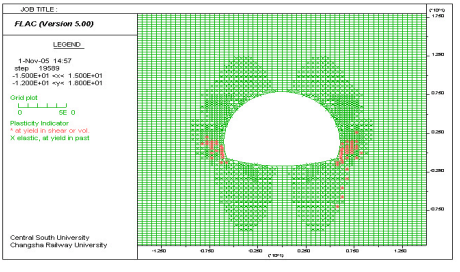

FIG. 4. Distribution of plastic zones after top heading and bench excavation.

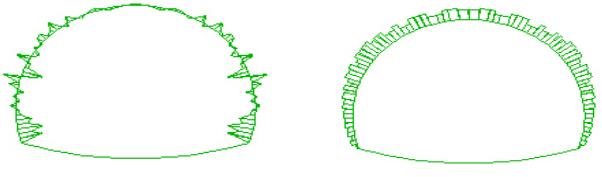

FIG. 5. Moments and axial forces in the shotcrete lining.

In the region of the sidewalls and floor, propagation of tensile cracks parallels to the major principal stress plotted in figure 4. These tensile failures mainly occur and extend along the alternation layers of sandstone and claystone. But they can be arrested by features such as bedding planes. This suggests that the separation of the layers of sandstone and claystone will actually take place. From distribution of maximum principle stress in surrounding rock, it is also seen that in both the roof and the floor region, delamination of the layers occurs. The value of major principal stress

on the interface of layers is equal to zero or close to zero because different strains occur between layers of sandstone and claystone. Influence of alternation of sandstone and claystone layers can be reflected by the fluctuation of the axial forces and moments in shotcrete shown in figures 5.

CONCLUTIONS

Queerxi Tunnel was excavated in typical horizontally stratified sedimentary rock mass with alternation of sandstone and claystone layers. A detailed engineering geological study was carried out. The main deposits include bedding calcareous sandstone and claystone, banded alternating layers of these units. Especially, Laboratory testing results indicate that the water content largely influences the engineering properties of claystone, which strength of claystone decreases along with the increase of water content. Its deterioration phenomenon can heavily influence the stability of tunnel. In order to decrease the deterioration of claystone, the protecting measures such as 5 cm thickness shotcrete coating should be taken as soon as possible to all exposed surrounding rock surface, especially in the toping range of the tunnel. The field measurements and the results obtained by numerical analysis indicated that alternation layers of sandstone and claystone is very significant influence on the deformation properties and stability of surrounding rock in stratified strata.

ACKNOWLEDGMENTS

The authors appreciate the support of the National Natural Science Foundation of China (No. 50808178).

REFERENCES

Cai, M., Kaisera, P.K., Tasakab, Y., Maejimac, T. Moriokac, H. and Minami, M., 2004. “Generalized crack initiation and crack damage stress thresholds of brittle rock masses near underground excavations.” *International Journal of Rock Mechanics & Mining Sciences*, 41, 833-847

Hunan Provincial Communications Planning, Survey and Design Institute (HPCPSDI), 2004. “The survey and design of the Highway Tunnels from Changde to Jishou of Hunan Province.” Changsha. (In Chinese)

Mottahed, P. and Ran, J., 1995. “Design of the jointed roof in stratified rock based on the voussoir beam mechanism.” *CIM Bulletin*, 88(994), pp 56-62.

Sansone, E.C. and Ayres Da Silva, L.A., 1998. “Numerical modeling of the pressure arch in Hoek, E. and Brown, E. T., 1980. *Underground Excavations in Rock. London*: Institution of Mining and Metallurgy.

Vlasov, A. N. and Merzlyakov, V. P., 1995. “Deformability parameters of stratified and jointed rock.” in: Eurock93. *Safety and environmental issues in rock engineering. Proc. symposium, Lisboa*. Vol. 2, L. Ribeiro, E. Sousa & N.F. Grossmann(Ed), pp. 975-981.

Wright, F.D., 1974. “Design of roof bolt patterns for jointed rock. Bureau of Mines.” N.T.I.S., U.S. Department of Commerce.

Dynamical Response of Qifeng-Lake Dam during Earthquake

YANG Xiuzhu[1] and LEI Jinshan[1]

[1]Institute of Tunnel and Underground Engineering, Central South University, 22# South Shaoshan Road, Changsha 410075, P R China;xzyang1661@126.com

ABSTRACT: Two dimensional dynamical finite element and effective stress method were used to analyze dynamical response of Qifenghu Lake earth-rock dam during earthquake. During analysis, the floodwater level in the upriver is 198.5 meter and 180 meter in the downriver. Peak acceleration of earthquake was 0.275g and it lasted 10s. Calculation results showed that pore water pressure after earthquake was as near twice as that before earthquake. Some region in the central clay wall and the silt groundsill where pore water pressure is equal to lateral consolidation pressure was found. This will endanger the stability of the dam. Through analyzing dynamical response of nodes on the dam surface, we find that absolute peak acceleration and peak displacement of D and E node in the middle of the dam is greater than others.

INTRODUCTION

The dam made up of soil and stone is used widely because these materials are easy to get and the construction is relatively simple. But during earthquake, especially with the higher water level of the reservoir, the excess pore water pressure will produce and result in the reduction of the effective stress in the dam and may cause the dam slipping and other dangers. There are many famous shake disaster, for example, during the earthquake in Tangshan of China, the inclined wall of main dam of Miyun reservoir collapsed and the dam groundsill of Douhe reservoir liquefied and lead to serious crack in the dam. So, if the change of stress in the dam can be learned ahead of schedule during earthquake through numerical simulation, we can take measures to strengthen the dam and avoid some disaster.

ENGINEERING BACKGROUND

The dam located in Hunan province of China includes the main dam, assistant dam and overfall dam. The drainage area is 246.7 km^2 on the upper river of the dam. The design flood standard is 50 years and the check standard is 500 years. The main dam is moraine dam with clay central wall. It is 190.0 meters long and 54.0 meters high. The elevation of its top is 207.9 meters. From FIG.1, we can see the typical section of the

dam. A represents clay central wall, B represents moraine filler, C represents silt groundsill, and D represents gravel stratum. Their permeability coefficients are 10^{-7} cm/s, 10^{-2} cm/s, 10^{-7} cm/s, 10^{-2} cm/s respectively.

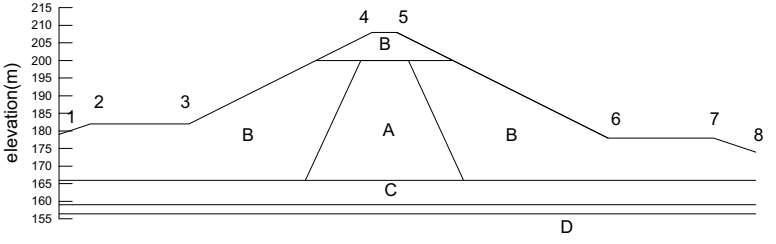

FIG. 1. Representative section of the dam.

THEORETICAL MODEL

Control Equation

The control equation for dynamic response of the system of the dam and its groundsill can be expressed in finite element formulation as:

$$[M]\{\ddot{\delta}\}+[C]\{\dot{\delta}\}+[K]\{\delta\}=\{F_{(t)}\} \tag{1}$$

Where:

[M]=mass matrix
[C]=damping matrix
[K]=stiffness matrix
$\{\ddot{\delta}\}$=vector of nodal accelerations
$\{\dot{\delta}\}$=vector of nodal velocities
$\{\delta\}$=vector of nodal displacements
$\{F_{(t)}\}$=vector of loads

The value of $G/G_{\max}$

$G_{\max}$ is got according the formula as follows:

$$G_{\max}=k(\sigma_0')^n \tag{2}$$

Where σ_0' is the mean principal effective confining stress. k and n are constants, which can be obtained by tests .

Model of Excess Pore Water Pressure

A relationship has been developed between the excess pore water pressure U_g and the cyclic number ratio as follows:

$$U_g = f(B) \tag{3}$$

The function *f* can be obtained by statistics of the experimental data, where B=N/ N_L, N is the stress cycles and N_L is the stress cycles required to produce liquefaction.

CALCULATING PARAMETERS

Soil Parameters

The value of maximum shear modulus and dynamic Possion's ratio is listed in Table 1. And Table 2 shows the relationship between dynamic shear modulus, damping ratio and shear strain, where A, B, C, and D represent clay, moraine, silt, gravel and scree respectively.

Table 1. The Value of Maximum Shear Modulus and Possion's Ratio

Parameter	Clay	Moraine	Silt	Gravel and Scree
k	467	2010	429	1415
n	0.5	0.5	0.439	0.5
μ	0.47	0.43	0.33	0.42

Table 2. The Relationship between Dynamic Shear Modulus, Damping Ratio and Shear Strain

Shear	Strain	1×10^{-5}	5×10^{-5}	1×10^{-4}	5×10^{-4}	1×10^{-3}	5×10^{-3}	1×10^{-2}
A	*G/Gmax*	0.951	0.891	0.851	0.542	0.397	0.177	0.075
	$\lambda(\%)$	3.42	3.96	4.2	5.3	6.4	11.3	15.7
B	*G/Gmax*	0.98	0.915	0.831	0.581	0.447	0.156	0.077
	$\lambda(\%)$	1.96	3.41	3.94	6.31	7.75	8.1	20.3
C	*G/Gmax*	0.934	0.901	0.859	0.602	0.473	0.141	0.04
	$\lambda(\%)$	1.39	1.78	2.16	4.37	6.2	17.3	23.2
D	*G/Gmax*	0.97	0.89	0.8	0.525	0.4	0.22	0.155
	$\lambda(\%)$	1.98	1.98	2.43	3.97	4.92	8.4	10.9

Earthquake Acceleration

The acceleration of earthquake is shown in Fig. 2. Its peak value is 0.275g and it lasts 10s.

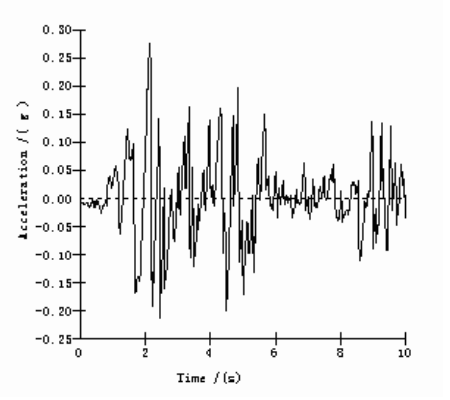

FIG. 2. Earthquake acceleration.

RESULTS

The dynamical response of the dam is analyzed with finite element method. The section is divided into 255 elements including 8-noded quadrilateral and 6-noded triangle elements and 824 nodes in all. The stress, strain, displacement and other dynamical response are obtained.

Acceleration and Displacement on the Dam Surface

From FIG. 3, we can see that the peak acceleration values of the nodes on the dam surface, whose position is shown in FIG. 1. The acceleration of node 4 and 5 in the middle of the dam is greater than the others. From FIG. 4 we can see that their displacement. The displacement of node 4 and 5 in the middle of the dam is greater than others.

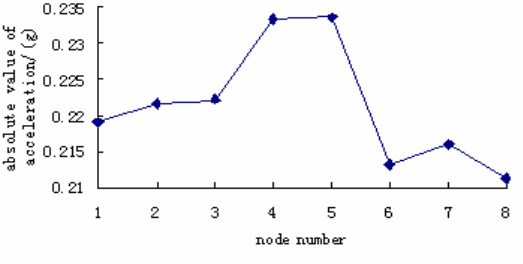

FIG. 3. Acceleration of nodes on the dam surface.

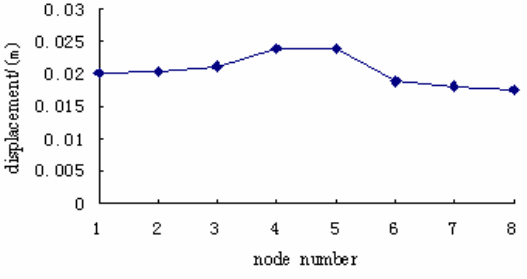

FIG. 4. Displacement of nodes on the dam surface.

Dynamical Response in the Dam

In analysis, we used the check flood level. It is 198.5 meters high in the upriver and 180 meters in the downriver. The isoline of the pore water pressure before earthquake is shown in FIG. 5. and that after earthquake is shown in FIG. 6. By comparison we can find that the latter is as near twice as the former. And when the earthquake finished, some region in the central clay wall and the silt groundsill where pore water pressure is equal to literal consolidation pressure was found (shown in FIG. 7).

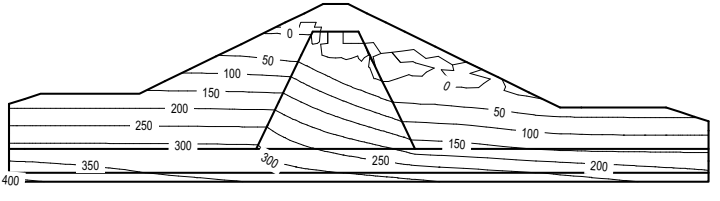

FIG. 5. Isoline of pore water pressure before earthquake.

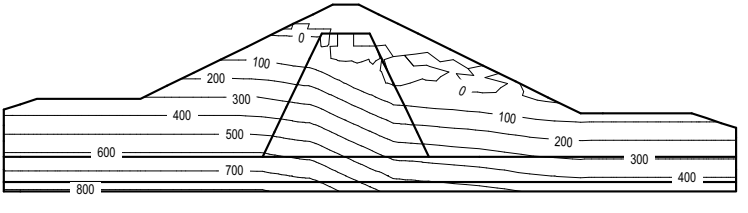

FIG. 6. Isoline of pore water pressure after earthquake.

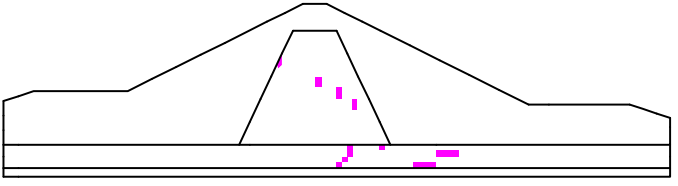

FIG. 7. The region where pore water pressure is equal to lateral consolidation pressure after earthquake

CONCLUSIONS

The dynamical response during earthquake is a big problem for the design and construction of the dam. It is significant to study the problem for dam safety .During analysis, the floodwater level in the upriver is 198.5 meter and 180 meter in the downriver. Peak acceleration of earthquake was 0.275g and it lasted 10s. Calculation results showed that pore water pressure after earthquake was as near twice as that before earthquake. Some region in the central clay wall and the silt groundsill where pore water pressure is equal to lateral consolidation pressure was found. This will endanger the stability of the dam.

ACKNOWLEDGEMENTS

The work was supported by Hunan Provincial Natural Science Foundation of China. The support is gratefully acknowledged.

REFERENCES

Ni hangen, Jin chongpan. (1994). The anti-seismic characteristics and calculation of dam. Publishing company of Dalian Science and Technology University,:482-527

Pan shu,Shen fengsheng ect (1994). Analysis of earthquake reaction in xiaolangdi declined core earth and rockfill Dam. *The people's Yellow River*, (8):36-39

Qian jiahuan,Yinzongze. (1996) Principle and calculation of civil engineering. Publishing company of water conservancy and hydroelectricity of China,:596-605

The Japanese institution of electricity and civil engineering technology. Engineering of earth and rockfill dam up to the minute. (1981). Publishing company of water conservancy and hydroelectricity :386-459

Woodward,P.K. Griffiths,D.V. (1996) Influence of viscous damping in the dynamic analysis of earth dam using simple constitutive model. *Computers and geotechnics.* 19(3):245-263

Yener Ozkan. M. (1998). A review of considerations on the seismic safety of embankment and earth and rock-fill dams. *Soil dynamics and earthquake engineering*, 17(7-8):439-458.

Rigid Blocks Failure Mechanism for Stability of Shallow Tunnel Using Upper Bound Solution

F. Yang[1] and J. S. Yang[2]

[1]Doctor, School of Civil Engineering and Architecture, Central South University, Changsha 410075, China; yf5754@126.com
[2]Professor, School of Civil Engineering and Architecture, Central South University, Changsha 410075, China; jsyang@yahoo.cn

ABSTRACT: A rigid block failure mechanism of shallow rectangular tunnel is proposed to calculate the needed support pressure σ_T for tunnel stability using upper bound solution. The velocity discontinuities in the side wall of the shallow rectangular tunnel of the failure mechanism occur in both radial and tangent directions. Formula for calculating support pressure σ_T using upper bound solution are deduced based on the presented failure mechanism, and the calculation program is compiled. It is shown that the proposed rigid block failure mechanism can be used effectively to analyze the stability problems of shallow rectangular tunnel using upper bound solution.

INTRODUCTION

Excavating shallow tunnels in the soft ground, the collapse would happen, if no sufficient support pressure or additional measures was adopted. The stability of shallow tunnel has been investigated by several authors. Atkinson *et al*. (1977) has studied the shallow circular tunnels in frictional material with limit analysis. Davis *et al*. (1980) employ kinematic upper bounds and statically lower bounds for plane strain circular tunnels and tunnel heading in clays with method of limit analysis. Leca *et al*. (1990) used upper and lower bound solutions to investigate the face stability of shallow circular tunnels in frictional material, and three three-dimensional failure mechanism were proposed for upper bound solution. Sloan *et al*. (2003) used finite element limit analysis to investigate the stability of undrained plane strain heading with soils, and the undrained strength varies with depth. Osman *et al*. (2006) has developed a kinematic solutions for ground movements around a shallow unlined tunnel in undrained clay. Klar *et al*. (2007) presented 2D and 3D failure mechanisms for tunnels in soft ground. In his study, incompressible flow fields for upper bound solutions were derived from the theory of elasticity. In this paper, the stability of shallow rectangular tunnel in cohesive-frictional soil ground was investigated based on the upper bound solution with a proposed failure mechanism. The needed support

pressure σ_T for tunnel stability was obtained using upper bound solution. And the influence factors were also investigated by parameter study.

FAILURE MECHANISM OF SHALLOW RECTANGULAR TUNNEL

FIG.1 shows the model of plane strain unlined rectangle tunnel. The tunnel has the height D, half width b, and cover C. The soil around tunnel has gravity γ, cohesion c and internal friction angle ϕ On the ground surface, surcharge σ_S was employed. Inside the tunnel, support pressure σ_T was employed for stability.

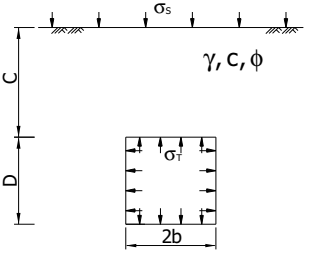

FIG. 1. The plane strain unlined rectangle tunnel.

The upper bound theorem assumes a perfectly plastic soil model with an associated flow rule. It states that the internal energy dissipated by admissible velocity field, which is equal to the work done by the external loads.

A failure mechanism should be assumed before hand, and its corresponding velocity field should satisfy associated flow rule, velocity boundary conditions and compatibility requirements (Chen, 1975), when upper bound solution was employed. Energy dissipation can only occurs on velocity discontinuities, for the assumed failure mechanism is composed of rigid blocks.

A rigid blocks failure mechanism for shallow rectangle tunnel in cohesive frictional soil ground is proposed here. The geometry of the failure mechanism and corresponding velocity field are described for preparation of upper bound solution.

The failure mechanism and its corresponding velocity field with variables are shown in FIG. 2. and FIG. 3. The failure zone above the tunnel is a whole non-plastic block with the absolute velocity of v_0 as a unit, with the vertical direction. The angle between velocity discontinuity L_r and vertical direction is ϕ. The failure zone of tunnel side wall are composed of m triangular rigid blocks in the upper part and $m\times$ (n-1) quadrangular rigid blocks in the outer part as shown in FIG. 2. The velocity discontinuities are $L_{j,i}$ (j=1,...,n; i=1,...,m) in the radial directions and $M_{j,i}$ (j=1,...,n; i=1,...,m) in the tangential directions. The angles between each pair of $L_{j,i}$ and $M_{j,i}$ in counter-clockwise are assumed equal to $\pi/2+\phi$. It is noted that dashed lines N_j (j=1,...,n-2) and b_j (j=1,...,n-1) are not velocity discontinuities, and lines N_j (j=1,...,n-1) are all parallel.

The failure mechanism is determined by a series of angles of β_i (i=1,...,m), $\alpha_{j,i}$ (j=1,...,n-1; i=1,...,m) and the length of $L_{1,1}$ and b_j (j=1,...,n-1), as shown in FIG. 2.

Once these variables are known, the values of N_j (j=1,…,n-1), $L_{j,i}$ (j=1,…,n; i=1,…,m), $M_{j,i}$ (j=1,…,n; i=1,…,m) as well as all the areas of rigid blocks, S_i (j=1,…,n) and $S_{j,i}$ (j=1,…,n; i=1,…,m), can be calculated. As shown in the right part of FIG.. 2, the angles of $\alpha_{j,i}$ (j=1,…,n-1; i=1,…,m) are expressed as an increment, i.e. $\alpha_{j,i}$ is the acute angle between each pair of $L_{j-1,i}$ and $L_{j,i}$.

The non-plastic block above the tunnel and the entire triangular and quadrangular rigid blocks in the side wall all move as the velocity field requires (see FIG.3), when the initial failure of plastic flow occurs. The velocity of non-plastic block above the tunnel is v_0. The velocities $v_{j,i}$ (j=1,…,n; i=1,…,m) are absolute velocities corresponding to the rigid blocks shown in the right part of FIG.. 3, and velocities $v'_{j,i}$ (j=1,…,n; i=1,…,m) and $v''_{j,i}$ (j=1,…,n-1; i=1,…,m) shown in the left part of FIG.. 3 are relative velocities on the discontinuities $L_{j,i}$ (j=1,…,n; i=1,…,m) and $M_{j,i}$ (j=1,…,n-1; i=1,…,m), respectively. All the absolute and relative velocity vectors are closed, so as to meet the velocity compatibility requirement. The geometric relations of velocity vectors are expressed as the functions of β_i (i=1,…,m), $\alpha_{j,i}$ (j=1,…,n-1; i=1,…,m).

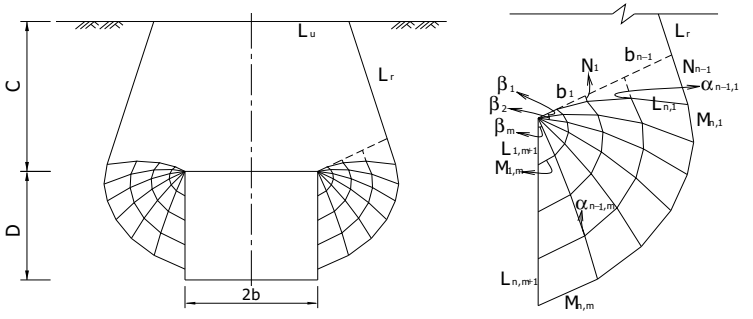

FIG. 2. Failure mechanism of shallow rectangle tunnel.

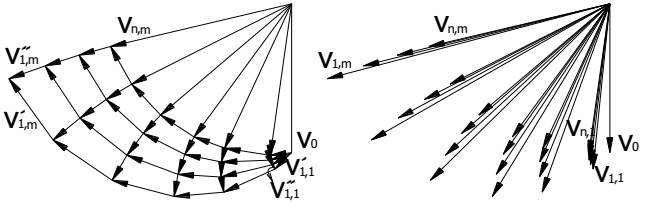

FIG. 3. Velocity field of the failure mechanism.

CALCULATING PROCEDURE

It is assumed that the soils surround the tunnel is cohesive frictional Mohr-Coulomb material, which obeys associated flow rule, with surcharge σs on the

soil surface, and support pressure σ_T on the tunnel outline. The external work of P_γ contributed by gravity in the failure zone is calculated as following:

$$P_\gamma = \gamma\left(v_0 \sum_{j=1}^{n} s_j + \sum_{j=1}^{n}\sum_{i=1}^{m} s_{j,i} v_{j,i}^{y} \right) \tag{1}$$

Where $v_{j,i}^{y}$ is the vertical compound of absolute velocity $v_{j,i}$.

The internal energy dissipation of P_c in the failure zone can be calculated as the following:

$$P_c = c\cos\phi\left(L_r v_0 + \sum_{j=1}^{n}\sum_{i=1}^{m} L_{j,i} v'_{j,i} + \sum_{j=1}^{n-1}\sum_{i=1}^{m} M_{j,i} v''_{j,i} + \sum_{i=1}^{m} M_{n,i} v_{n,i} \right) \tag{2}$$

The external work of P_s contributed by surcharge σs on the soil surface is calculated as following:

$$P_s = v_0 \sigma_S L_u \tag{3}$$

The external work of P_T contributed by support pressure σ_T on the tunnel outline is calculated as following:

$$P_T = \sigma_T\left(b v_0 + \sum_{j=1}^{n} L_{j,m+1} v_{j,m+1}^{x} \right) \tag{4}$$

Support pressure σ_T can be calculated by following expression, when the incremental external work is made to be equal to the internal energy dissipation:

$$\sigma_T = \left(P_\gamma + P_S - P_c\right) \Big/ \left(b v_0 + \sum_{j=1}^{n} L_{j,m+1} v_{j,m+1}^{x} \right) \tag{5}$$

The above expression is the object function of support pressure σ_T, and can be obtained by maximizing σ_T with variables of β_i (i=1,...,m), $\alpha_{j,i}$ (j=1,...,n-1; i=1,...,m), $L_{1,1}$ and b_j (j=1,...,n-1), subject to constraints the failure mechanism and velocity field requires. As shown in FIG. 2 and FIG.. 3, the constraints of variables of β_i (i=1,...,m), $\alpha_{j,i}$ (j=1,...,n-1; i=1,...,m), $L_{1,1}$ and b_j (j=1,...,n-1) should assure the geometric conditions of failure mechanism and velocity field. The maximization procedure can be performed by using present optimization software.

CALCULATION EXAMPLES AND DISCUSSIONS

In order to investigate the parameter influences of the results of support pressure σ_T, we simply take the soil unit weight γ=20 KPa, tunnel height D=10m, half of tunnel width b=5m and γD/c=3.0 as invariable. And take the depth of cover C, soil internal frictional angle ϕ and surcharge σs as variable. The results of support pressure σ_T for various variables are shown in Table 1. For convenience to compare with the results of cohesive soil materials, the results of (σs-σ_T)/c are also shown in the Table.

As shown in Table 1, for soils materials with ϕ=0º, the values of Support pressure σ_T increased linearly with the increase of C/D and surcharge σs. Also, for various surcharge σs, the values of (σs-σ_T)/c are equal to the same C/D which is presented in FIG.. 5(a). The results are consistent with those of Davis, who follows that the stability ratio $N = [\sigma_S - \sigma_T + \gamma(C + D/2)]/c$ can be used for tunnel in undrained condition.

Table 1. Support Pressure σ_T for Various Variables

ϕ (°)	σs (KPa)	C/D=1.0	C/D=2.0	C/D=3.0	C/D=4.0	C/D=5.0
		σ_T (KPa)	σ_T (KPa)	σ_T (KPa)	σ_T (KPa)	σ_T (KPa)
		(σs-σ_T)/c	(σs-σ_T)/c	(σs-σ_T)/c	(σs-σ_T)/c	(σs-σ_T)/c
0	0	104.0	258.31	419.65	586.53	757.15
		-1.56	-3.87	-6.29	-8.80	-11.36
	200	304.07	458.30	619.66	786.48	957.38
		-1.56	-3.87	-6.29	-8.80	-11.36
	400	504.06	658.29	819.67	986.37	1157.2
		-1.56	-3.87	-6.30	-8.80	-11.36
5	0	72.40	182.47	287.91	389.27	487.13
		-1.09	-2.74	-4.32	-5.84	-7.31
	200	233.62	331.45	427.04	520.27	611.31
		-0.50	-1.97	-3.41	-4.80	-6.17
	400	394.90	480.44	566.20	651.37	735.68
		0.08	-1.21	-2.49	-3.77	-5.04
10	0	45.23	118.25	178.66	229.65	273.47
		-0.68	-1.77	-2.68	-3.44	-4.10
	200	171.89	222.87	266.51	304.59	338.35
		0.42	-0.34	-1.00	-1.57	-2.08
	400	289.60	327.57	354.74	380.26	404.23
		1.66	1.09	0.68	0.30	-0.06

For soil internal frictional angle ϕ= 0º, the values of support pressure σ_T increased with the increase of C/D, with nonlinear relation. For various surcharge σs, the values of (σs-σ_T)/c are not equal at this time for the same C/D, but increased with the increase of surcharge σs. That is to say, for frictional materials, the stability ratio $N = [\sigma_S - \sigma_T + \gamma(C + D/2)]/c$ can not be a single parameter to evaluate the stability of shallow tunnels. And the soil internal frictional angle ϕ has significantly influences the results of support pressure σ_T when its values increased.

FIG. 4 shows the results of support pressure σ_T for various variables without surcharge σs. It is seen that σ_T and C/D has the linear relation when ϕ=0º, well nonlinear relation when ϕ>0º. With the increase of soil internal frictional angle ϕ the value of σ_T needed for keeping tunnel stable decreased.

FIG. 5(a) shows the values of (σs-σ_T)/c for various variables with soil internal frictional angle ϕ=0º. As mentioned above, the values of (σs-σ_T)/c are equal to each other with the same C/D and various ground surface surcharge σs. And (σs-σ_T)/c decreased when C/D increased. It is found that if the values of (σs-σ_T)/c are below the curved line, the shallow tunnel is in the stable condition, otherwise, when the values above the curved line, the shallow tunnel is in the unstable condition.

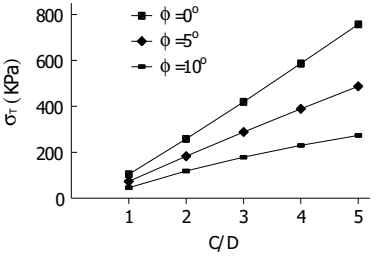

FIG. 4. Support pressure σ_T for various variables (σs=0 kPa).

FIG.. 5(b) and (c) shows the values of $(\sigma s-\sigma_T)/c$ for various variables with soil internal frictional angle ϕ=5º and ϕ=10º. The values of $(\sigma s-\sigma_T)/c$ are not equal to each other with the same C/D and various ground surface surcharge σs in cohesive frictional materials. However, the values of $(\sigma s-\sigma_T)/c$ decreased with the decrease of ground surface surcharge σs and increase of C/D. It can also be found that the values of $(\sigma s-\sigma_T)/c$ increased when the soil internal frictional angle ϕ increased. The stability ratio $N=[\sigma_S-\sigma_T+\gamma(C+D/2)]/c$ can be influenced and can not be a single parameter when the tunnel is excavated in the cohesive frictional materials to evaluate the stability of shallow tunnels.

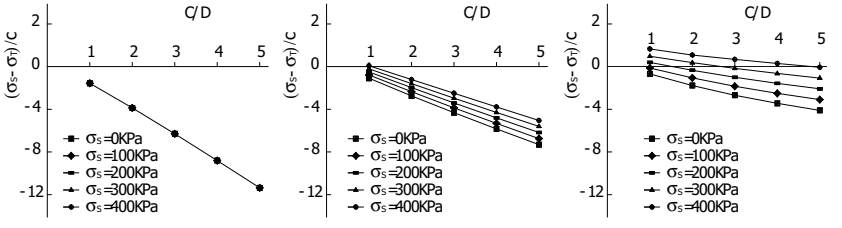

FIG. 5. Values of $(\sigma s-\sigma_T)/c$ for various variables.

FIG.. 6 shows the optimized failure mechanisms and corresponding velocity fields for σs=200 kPa and soil internal frictional angle 0º, 5º and 10º. The whole non-plastic block is above the tunnel with the unit velocity of v_0=1, and the absolute velocity vectors in the side wall of the shallow tunnel are all shown in the right part. As can be seen, the directions of velocity vectors turns from vertical to near horizontal gradually, and its value also increased gradually. Shown in the left part of the tunnel side wall, the optimized failure mechanisms are composed of a series of rigid blocks. It can be seen that the velocity discontinuities in the bottom are all intersect to the lower corner of the rectangular tunnel. With the increase of the soil internal frictional angle, the

areas of the failure zone decreased, while the absolute velocities in the side wall are increased. That is the reason that the shallow tunnel will be more stable when the soil internal frictional angles increased.

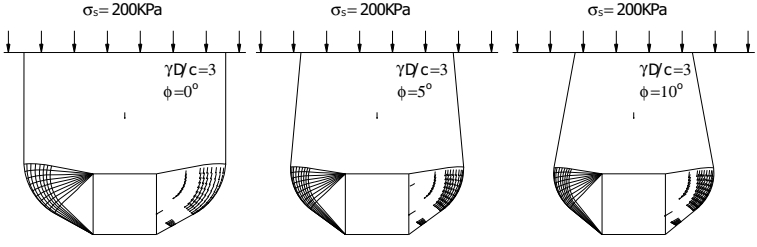

FIG. 6. Optimized failure mechanisms and corresponding velocity fields.

CONCLUSIONS

This paper proposed a rigid block failure mechanism for shallow rectangular tunnel in cohesive frictional soil, which can be used to obtain the needed support pressure σ_T for tunnel stability using upper bound solution. The obtained results shown that the stability ratio N, follows by Davis, which can be used to evaluate tunnel stability in cohesive soil materials, can not be a single parameter to evaluate the stability of shallow tunnels in cohesive frictional soil materials. The parameter study shows that the value of σ_T needed for keeping tunnel stable deceased with the increase of soil internal frictional angle ϕ This is properly caused by the decrease of the areas of failure zone and the increase of absolute velocities.

REFERENCES

Atkinson, J.H. and Potts, D.M. (1977). "Stability of shallow tunnel in cohesionless soil." *Géotechnique*, Vol.27(2): 203-215

Davis, E.H., Gunn M.J. and Mair R.J. etc. (1980). "The stability of shallow tunnel and underground openings in cohesive material." *Géotechnique*, Vol. 30(4): 397-416

Leca, E. and Dormieux, L. (1990). "Upper and lower bound solutions for the face stability of shallow circular tunnels in frictional material." *Géotechnique*, Vol. 40(4): 581-606

Augarde, C.E., Lyamin, A.V. and Sloan, S.W. (2003). "Stability of an undrained plane strain heading revisited."*Computers and Geotechnics*, Vol.30: 419-430

Osman, A.S., Mair, R.J. and Bolton, M.D. (2006). "On the kinematics of 2D tunnel collapse in undrained clay." *Géotechnique*, Vol.56(9): 585-595

Klar, A., Osman, A.S. and Bolton, M. (2007). "2D and 3D upper bound solutions for tunnel excavation using elastic flow fields." *Int. J. Numer. Anal. Meth. Geomech.*, Vol.31: 1367-1374

Chen W.F. (1975). "Limit analysis and soil plasticity." Elsevier: Amsterdam.

Simulation of a New Construction Method in a Shallow-buried Weak Tunnel

AN Yonglin[1] and PENG Limin[2]

[1] Doctor, Hu'nan University of Science and Technology, Xiangtan, Hu'nan Province,China 411201; anyongling@yahoo.com.cn
[2] Professor, Central South University, Changsha, Hu'nan Province,China 410075; lmpeng@mail.csu.edu.cn

ABSTRACT: The double down-side drifts construction method was put forward in a shallow-buried weak tunnel. Its construction behavior was studied by numerical simulation using MIDAS. Results show: (1) this method can improve tunnel load, the key construction step is arch ring excavation and core soil is good to tunnel steady; (2) weak parts mainly locate wall foot and crown foot of drifts, crown foot of tunnel and the connections; (3) reinforcement of soil under the drifts has no apparent effect on improving rock deformation and support load. From an economical and safety point of view, main parts to be reinforced are drifts (its foot depth, connection parts with tunnel, and its corners); core soil should be kept if rock is unsteady and needs reinforcing.

INTRODUCTION

The prominent character of shallow-buried weak tunnel is its serious influence on the surrounding environment due to its stratum losses during excavation. Naturally, how to effectively control ground surface deformation has become a hot issue during tunnel design or tunnel construction. Researchers have made much progress through studying the problem from these aspects: in-site monitoring, laboratory experiments, numerical simulation and theoretical study (Dalgic, et al, 2000; Jeng Fushu, et al, 2002). However, excavation methods of weak tunnel are always traditional such as short bench stage method, side drifts method, CD (Cross Diaphragms) method, CRD (Center Cross Diaphragms) method, etc. A new construction method, double down-sides drifts, is presented in this paper (Shi Shengli, 2007). Also its construction behavior is studied by numerical simulation and some advice on tunnel construction is given. Conclusions drawn from the paper can be used as guidance for similar weak rock tunnel projects.

CONSTRUCTION STEPS AND LOAD ANALYSIS

The traditional excavation principle in shallow buried-weak tunnels is to divide a large span into several small spans under preliminary strengthening measures, such as

fractional excavation method, CRD and so on. The measures including advanced pipe roof and ground grouting are adopted mainly to strengthen the rock around the crown.

Nevertheless, to some special shallow-buried weak tunnels, weak rock locates not only in the above of the tunnel but in the below of the arch foundation and the invert. Then there will be subsidence and cracks in the ground surface to different degree as well as cracks in the arch foundation even under preliminary support of the pipe roof in the arch, seeing Fig. 1. Why? Just because foundation beam can not be formed into an effective bearing structure due to special weak foundation and special low bearing capacity. The double side-down drifts method has some similarities to the CRD method. For example, both of them are to firstly excavate the two sides of the tunnel. But the double side-down drifts method lays emphasis on the treatment and reinforcement of the below parts of the tunnel. Geometry conditions can be detected and foundation can be reinforced in advance through utilizing advancing double side-down drifts. Then tunnel construction will be safe.

Construction steps of the double side-down drifts are given as follows, seeing Fig.1a: (1) excavation of double side-down drifts; (2) excavation of the crown ring part; (3) excavation of the core part; (4) excavation of the below part and backfill of the double side-down drifts; (5) casting of the secondary lining.

Force transiting mechanism of the double side-down drifts is also given as follows, seeing Fig.1b: (1) vertical surrounding rock pressure transits to the strip foundations of the drifts through steel girders and this will greatly reduce the subsidence of ground surface and the steel girders; (2) horizontal surrounding rock pressure transits to the undisturbed rock through one strip foundation and then transits to the other strip foundation of the drifts.

NUMERICAL SIMULATION AND ANALASIS

To reduce influence of boundary confinement on calculation results, the left boundary is 30 m away from the tunnel center, the right boundary is 30 m, the bottom boundary is 30 m, and the top boundary is in the ground surface. Horizontal degree of the left boundary is fixed as well as the right boundary. Vertical degree of the bottom boundary is fixed and the top boundary is free.

Rock is supposed to be isotropic and satisfy Mohr-Column yield criterion. Beam elements are used to simulate shotcrete and secondary lining. Table 1 gives properties of rock and support structures.

Fig. 2 shows settlements of crown and center of the ground surface vs. construction steps without foundation reinforcement of double side-down drifts. From the Fig. 4, we can see: (1) the total settlement is about 1.7 mm and it is good to rock steady; (2) settlement during casting secondary lining is the maximum, 1.3 mm. This is just because rock belongs to VI classification and is very weak. The main bearing structure is the secondary lining. In this paper, it undertakes 70% load; (3) settlement

during arch ring excavation is also very big. Therefore, in weak rock region, particularly in the rock where steady time is very short or steady time is zero, secondary lining should be cast as soon as possible.

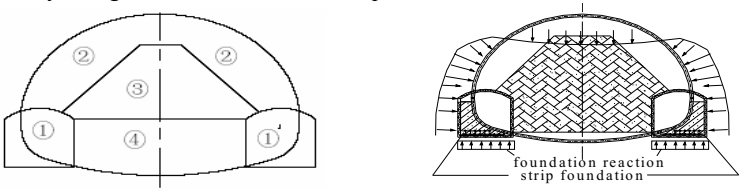

(a) Construction steps **(b) Load analysis**

Fig. 1. Construction steps and load analysis

Table 1. Properties of Mechanical Parameter

Materials	*E*/GPa	γ/kN. m^{-3}	*μ*	*c*/MPa	*φ* /°
VI rock	0.8	17.00	0.4	0.05	18
Preliminary support	28.98	22	0.2	-	-
Secondary lining	31	25	0.2	-	-
Support of side drifts	31	25	0.2	-	-
Foundation reinforcement of side drifts	1.16	18	0.44	0.18	23

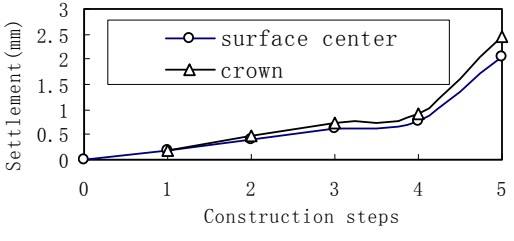

Fig. 2. Settlements vs. construction steps

Fig. 3 shows distribution of the maximum principle stress (supposed pressure positive '+'), the minimum principle stress and shear stress during every construction steps. We can know from the figure: (1) distributions of the maximum and minimum principle stress are similar and symmetrical to the tunnel center. Stress concentration mainly locates around the arch foot and foot corners of the double side-down drifts where compressive failure may occur, so a great emphasis should be laid on these parts during construction. The influence of the excavation on the maximum principle stress is more serious than on the minimum principle stress due to its more curved degree. (2) shear stress is anti-symmetrical to the tunnel center with its concentration in arch foots and foot corners of the double side-down drifts too where shear failure is

easy to happen. These parts should also be paid attention to during construction.

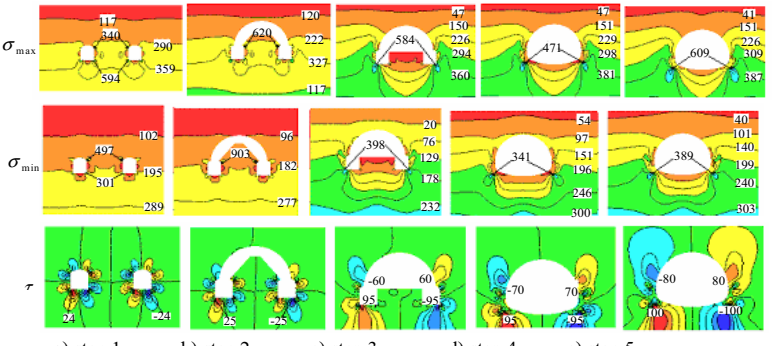

a) step 1 b) step 2 c) step 3 d) step 4 e) step 5

Fig. 3. Stress distribution (unit kPa).

Due to symmetry of the structure and construction, internal forces of the left side-down drift are studied in Fig. 4. It is supposed that moment is positive ('+') if the outer side of the drifts is tensile, axis force is negative ('-') if it is tensile. From the figure, we can see:

(1) On the whole, moments increases as excavation area enlarges, but its increasing gradient varies in different excavation steps. For instance, moment is -8 kN.m in step 1, -9 kN.m in step 2, -17 kN.m in step 3, -18 kN.m in step 4. Oppositely, axial forces decrease as excavation area enlarges. The maximum gradient of moment occurs in step 3, so is axial force. Therefore, core soil, as a side confinement, is good to side drifts. If the tunnel is unsteady and has some risks, it is better to keep core soil as soon as possible before emergent measures are taken.

(2) As excavation area enlarges, moment of the left side wall of the drift increases a little, but axial force increase greatly due to rock pressure above the tunnel crown transiting to the side wall through the drift crown. Generally, axial force is much larger than moment in accordance with the character that the wall bears pressure.

(3) For the pressure near the right arch foot is undertaken by double side-down drifts, moment of the right foot is smaller while moment of the left arch foot, left wall foot and right wall foot is bigger. For the connection between the tunnel crown and the left side drift is near to the left sidewall, most rock pressure is undertaken by the left wall. Axial force of the left side wall is hence much larger than the right wall. During step 3, the left side wall should be paid attention to for its axial force is tensile (20 kN).

(4) Moments of the connection between the tunnel crown and the left side drift varies sharply during construction. For example, moment is very small (-13 kN.m) in step 1 and step 2; then is very large (189 kN.m) and changes direction in step 3; then is

small (-30 kN.m) and changes direction once more in step 4. Therefore, the connection should be reinforced during step 3 for the safety sake.

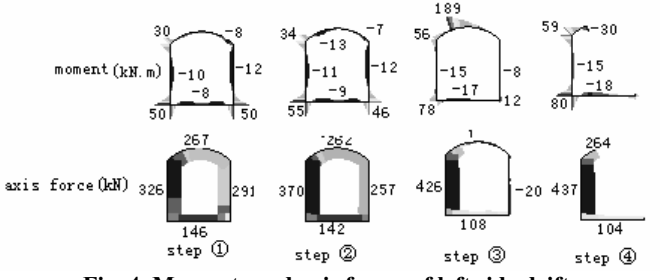

Fig. 4. Moments and axis forces of left side drift.

Fig. 5 shows internal forces of preliminary support structures. By analyzing the figure, we can see:

(1) Moment is very small (2 kN.m) in step 2; then is very large (-189kN.m) and changes direction in step 3; then is very small in step 4 and step 5. Why? Because after step 3 (core soil excavation), the confinement of the side drifts and the excavation face decreases; but after step 4, double side-down drifts is backfilled to increase the drifts' stiffness.

(2) Moment of the crown, wall foot and invert is very small and axial force of the below parts is smaller than in the above. This is different from internal forces using the traditional excavation methods such as the whole excavation and bench excavation method. Why? Just because most pressure transits through the tunnel crown, then through the double side-down drifts, and finally transits to the foundation under the drifts. Therefore, double side-down drift method can improve tunnel mechanism.

(3) During step 4, the connection between the tunnel and the drifts should be paid attention to for its axial force is tensile.

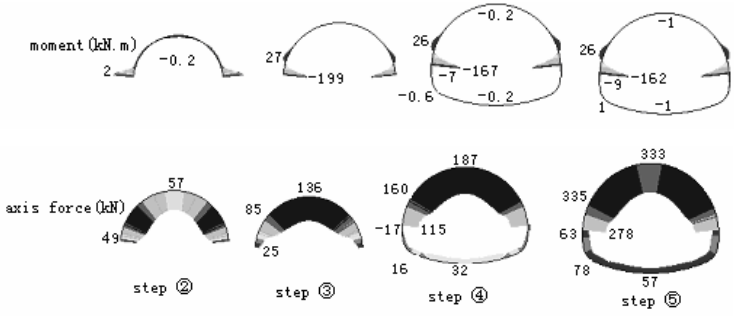

Fig. 5. Moments and axis forces of initial support.

Fig. 6. Forces without reinforcement.

Fig. 7. Forces with reinforcement.

Fig. 6 and Fig. 7 show internal forces of the secondary lining with considering foundation reinforcement or not. By analyzing the figure, we can see:

(1) Moment of the crown, wall foot, invert and the connections is larger and axial force of the below parts is also smaller than in the above. The reason is the same to the preliminary support structures' analysis.

(2) Internal forces changes a little after foundation reinforcement except axial force of the invert decrease from 94 kN to 76 kN. Therefore, to partly reinforce foundation under the drifts has no apparent part in improving tunnel mechanism

CONCLUSIONS

1. To some shallow-buried weak tunnels, double side-down drifts can be used to detect geometry conditions and reinforce the foundations in advance. Then ground surface subsidence will be well controlled and tunnel construction will be safe.
2. The key construction step is core soil excavation which is good to tunnel mechanism. The vulnerable parts locate wall foot of the drifts, wall foot and arch foot of the tunnel, and the connections. So a great emphasis should be attached to these parts.
3. From an economical and safety point of view, main parts to be reinforced are drifts (its foot depth, connection parts with tunnel and its corners).

ACKNOWLEDGEMENT

It is a Project supported by the Graduate Students Innovation Foundation of Hunan Province (3340-74236000004). The authors would like to thank the authorities concerned.

REFERENCES

Dalgic, Suleyman (2000). "Influence of weak rocks on excavation and support of the Beykoz Tunnel, Turkey". *Engineering Geology*, 58(2):137-148.

Jeng Fushu, Weng Mengcha, Huang TsanHwei et al (2002)."Deformational characteristics of weak sandstone and impact to tunnel deformation". *Tunnelling and Underground Space Technology*, 17(3):263-274.

Shi Shengli (2007). "Study on tunnel construction technology with weak foundation and shallow cover"[J]. *Journal of Changsha Railway College*(Social Science), 8(1),141-142. (in Chinese)

Study on the Stratum Deformation Caused by Tunnel Excavation with Different Division of Cross-Section

Shi Chenghua, Peng Limin, and Li Jun

School of Civil Engineering and Architecture, Center South University, Changsha, China, 410075; csusch@163.com

ABSTRACT: Sequential excavation method is often used in urban tunnel construction. Based on the stochastic medium theory and according to the stratum deformation caused by element excavation, the stratum deformation united calculating equation under this excavation method is studied, which can take into account the development course of the deformation with the different tunnel section excavation. Then the time-space rules of the stratum deformation caused by tunnel excavation with different division of cross-section are discussed. The maximum of stratum deformation and curvature arise after some part of the whole tunnel, rather than the whole tunnel section has been excavated. Double-sidewalls heading excavation method has more control effect on stratum deformation than central departure excavation method. The study achievement can provide scientific basis for controlling the stratum deformation caused by tunnel construction, and protecting the safety of the buildings and pipelines around the tunnel.

INTRODUCTION

With the development of the industry and the expansion of the city in China, urban tunnel and metro are built to improve the traffic condition. When tunnel is excavated under busy roads in the majority cities, sequential excavation method is used to reduce the disturbance to surrounding stratum and ground surface. In this method, the whole cross-section of tunnel is divided into several smaller sections to excavate, and each section has some distance in longitude. Under this method the movement and deformation of the stratum around tunnel is far more complicated than full cross section excavation, and the stratum deformation caused by each small cross section will interact and superpose with each other. Many project cases show that the reciprocal influence on different section's excavation can not be ignored especially when the longitude distance of sections are not very far away from each other.

As to the stratum deformation caused by tunnel excavation, many scholars have studied, but most of them focused on the surface subsidence, and the stratum inclination, horizontal strain are not calculated. Numerical computation methods such as FEM seldom discuss the time effect of stratum deformation, although space effects are considered. In this paper, which based on the stochastic medium theory, such

problems are further discussed, calculated formulas are deduced and some revenant laws are extracted.

STRATUM DEFORMATION CAUSED BY TUNNEL CONSTRUCTION

According to statistics, an underground excavation can be divided into infinitesimal excavation elements. The effect due to the total excavation is then equal to the sum of the effects caused by the infinitesimal excavations. An excavation with an infinitesimal unit width, length and thickness ($d\xi$, $d\varsigma$ and $d\eta$, respectively) is called the elementary excavation. Assuming that the excavation depth of tunnel is H and the excavation speed is v (m/d) from a starting point $t=0$ to the right (Figure 1), at any moment (τ) in the time interval (0, t), the excavation length of tunnel is $d\tau$ and $\varsigma = v\tau$. According to the stochastic medium theory, the stratum subsidence caused by elementary excavation $d\xi d\varsigma d\eta$ at any place (X, Y, Z)and at any moment t is (Yang and Liu 2002).

$$W_e(X,Y,Z,t)=\frac{\tan^2\beta}{(Z-\eta)^2}\{1-\exp[-C(t-\tau)]\}\exp\left\{-\frac{\pi\tan^2\beta}{(Z-\eta)^2}\left[(X-\xi)^2+(Y-v\tau)^2\right]\right\}d\xi d\varsigma d\eta \quad (1)$$

Where C is the speed coefficient of stratum subsidence, β is the main influence angle of the stratum.

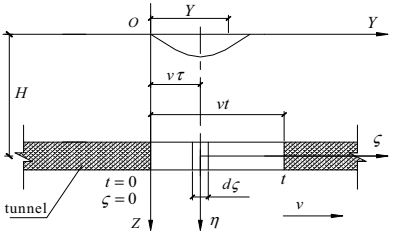

FIG. 1. Diagram of vertical section.

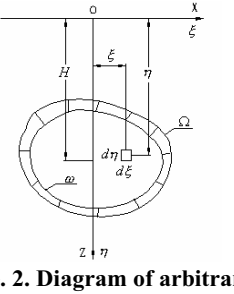

FIG. 2. Diagram of arbitrary cross section

Assuming the area of the excavating cross-section of tunnel is Ω, when tunnel is excavated, such space begins to distort, and the final area is a (Figure 2). According to superposition principle, when the excavation time of tunnel is t, the horizontal displacements along the X,Y axis are (Shi 2007).

$$W(X,Y,Z,t)=\iint_{\Omega-\omega}d\xi d\eta\int_0^t\frac{v\tan^2\beta}{(Z-\eta)^2}\{1-\exp[-C(t-\tau)]\}\exp\left\{-\frac{\pi\tan^2\beta}{(Z-\eta)^2}\left[(X-\xi)^2+(Y-v\tau)^2\right]\right\}d\tau \quad (2)$$

$$U_X(X,Y,Z,t)=\iint_{\Omega-\omega}d\xi d\eta\int_0^t\frac{v\tan^2\beta(X-\xi)}{(Z-\eta)^3}\{1-\exp[-C(t-\tau)]\}\exp\left\{-\frac{\pi\tan^2\beta}{(Z-\eta)^2}\left[(X-\xi)^2+(Y-v\tau)^2\right]\right\}d\tau \quad (3)$$

$$U_Y(X,Y,Z,t)=\iint_{\Omega-\omega}d\xi d\eta\int_0^t\frac{v\tan^2\beta(Y-v\tau)}{(Z-\eta)^3}\{1-\exp[-C(t-\tau)]\}\exp\left\{-\frac{\pi\tan^2\beta}{(Z-\eta)^2}\left[(X-\xi)^2+(Y-v\tau)^2\right]\right\}d\tau \quad (4)$$

The subsidence and horizontal displacement caused by tunnel excavation are no

uniform, and thus will certainly cause the stratum inclination and horizontal strain. The inclination T_X, T_Y, horizontal strain E_X, E_Y, and curvature ratio K_X, K_Y of stratum along the X, Y axis can be calculated as follows :

$$T_X = \partial W/\partial X,\ T_Y = \partial W/\partial Y \tag{5}$$

$$E_X = \partial U_X/\partial X,\ E_Y = \partial U_Y/\partial Y \tag{6}$$

$$K_X = \partial^2 W/\partial X^2,\ K_Y = \partial^2 W/\partial Y^2 \tag{7}$$

THE CALCULATION OF THE STRATUM DEFORMATION DURING THE SEQUENTIAL EXCAVATION

Figure 3 shows the CD excavation method which is prevalently used in urban metros. The whole cross-section is divided into 4 smaller excavation parts (part 1, 2, 3, 4 in the figure). A coordinate system is established which is shown in figure 4. Part 1 is excavated from the moment $t=0$, the excavation speed is v_1; after time Δt_1, the excavation of part 2 begins, the speed is v_2; then after time Δt_2, the part 3 begins with the speed v_3; finally after Δt_3, the part 4, and the speed is v_4. Assuming the four parts are all excavated continuously, and the excavation time of part 1 is t_1, then the excavation time of part 2 is $t_2 = t_1 - \Delta t_1$, while part3 is $t_3 = t_2 - \Delta t_2 = t_1 - \Delta t_1 - \Delta t_2$, and part 4 is $t_4 = t_3 - \Delta t_3 = t_1 - \Delta t_1 - \Delta t_2 - \Delta t_3$. Assuming the areas of the four parts are Ω_1, Ω_2, Ω_3, Ω_4 after excavation, the areas of them converge to a_1, a_2, a_3, a_4 respectively. The horizontal distances from the centers of the four parts to the origin of coordinates system are l_1, l_2, l_3 l_4 and the vertical distances are h_1, h_2, h_3 h_4. According to superposition principle:

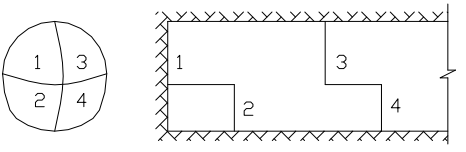

FIG.3. Diagram of CD excavation method.

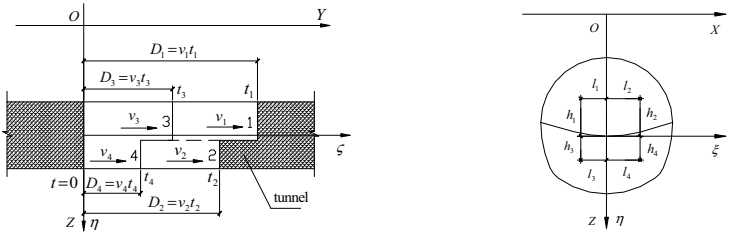

FIG. 4. The coordinate system of CD excavation.

$$W(X,Y,Z) = \iint_{\Omega_1-\omega_1} d\xi d\eta \int_0^{t_1} \frac{v_1 \tan^2\beta}{(Z+h_1-\eta)^2} \{1-\exp[-C(t_1-\tau)]\} \exp\left\{-\frac{\pi \tan^2\beta}{(Z+h_1-\eta)^2}\left[(X+l_1-\xi)^2+(Y-v_1\tau)^2\right]\right\} d\tau$$

$$+ \iint_{\Omega_2-\omega_2} d\xi d\eta \int_0^{t_2} \frac{v_2 \tan^2\beta}{(Z+h_2-\eta)^2} \{1-\exp[-C(t_2-\tau)]\} \exp\left\{-\frac{\pi \tan^2\beta}{(Z+h_2-\eta)^2}\left[(X-l_2-\xi)^2+(Y-v_2\tau)^2\right]\right\} d\tau$$

$$+\iint_{\Omega_3-\omega_3} d\xi d\eta \int_0^{t_3} \frac{v_3 \tan^2\beta}{(Z-h_3-\eta)^2}\{1-\exp[-C(t_3-\tau)]\}\exp\left\{-\frac{\pi\tan^2\beta}{(Z-h_3-\eta)^2}\left[(X+l_3-\xi)^2+(Y-v_3\tau)^2\right]\right\}d\tau$$

$$+\iint_{\Omega_4-\omega_4} d\xi d\eta \int_0^{t_4} \frac{v_4 \tan^2\beta}{(Z-h_4-\eta)^2}\{1-\exp[-C(t_4-\tau)]\}\exp\left\{-\frac{\pi\tan^2\beta}{(Z-h_4-\eta)^2}\left[(X-l_4-\xi)^2+(Y-v_4\tau)^2\right]\right\}d\tau \quad (8)$$

The horizontal displacement, inclination, horizontal strain, curvature ratio of stratum caused by sequential excavation can also be deduced through the same method, and the detailed realization is ignored here.

When the tunnel is excavated by other methods (such as CRD excavation method, sidewalls heading excavation method, bench method, etc.), the calculating formula can be deduced according to the similar method.

ANALYSIS OF CASE HISTORY

General Introduction of the Case

Tongyoushan tunnel is located on South Nanerhuan Road in Liuzhou city in China. Double arch structure is used for tunnel and NATM method is adopted to excavate. There are 180 meters shallow cover part at the entrance of the tunnel, and the tunnel depth is about 18 meters. The layer of Qml is 3~5m depth from the ground surface, and below the Qml is marlite which has developed joint fissure. The cross section and excavation steps of Tongyoushan tunnel are shown in figure 5.

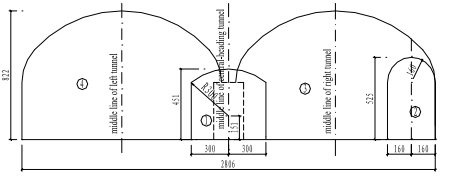

FIG. 5. Excavation steps of the tunnel.

On the ground surface of the shallow tunnel, there are several residential buildings. The excavation steps of tunnel are that firstly excavating the central -heading tunnel, then right pilot-tunnel and right tunnel, finally excavating the left tunnel. The excavating speed of the central-heading tunnel is 3.0 m/d, and 2.5 m/d to right pilot-tunnels, 1.5 m/d to the right and left tunnels. At each step of the construction, distort will occur around the tunnel after excavation. And the deformation of the stratum can be calculated through the formula which is deduced in this paper.

According to the monitoring data, the basic calculation parameters can be obtained. The stratum deformation parameter $\tan\beta$ is 0.969; the average subsidence of central-heading tunnel S_m is 21.28 mm, of right pilot tunnel S_r 20.30 mm, and the left and right tunnels S_z is 32.13 mm. The time coefficient of subsidence C is 0.2231 (1/d).

The Calculation Results and Analysis

The results of ground surface subsidence observations of two cross-section after central-heading tunnel excavated are compared in Figure 6 and 7 with the theoretical

curve calculated from equation (8).

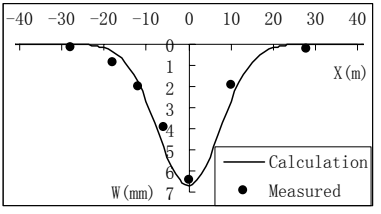

FIG. 6. Comparison between observe subsidence and calculation results on K2+330.

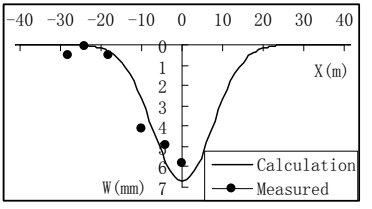

FIG. 7. Comparison between observe subsidence and calculation results on K2+370.

In order to study the development law of the stratum deformation at different stages of excavation, the stratum horizontal displacement, inclination, horizontal strain, curvature along the X-axis and subsidence are shown in figure 8 to12. In which, Curve a is the result when central-heading tunnel excavates to the cross-section; Curve b is the result when right pilot-tunnel excavates to the cross-section; Curve c is the result when right tunnel excavates to the cross-section; Curve d is the result when left tunnel excavates to the cross-section; Curve e presents the results when the whole tunnel is finished.

From the calculation results we can see that:

(1) With the gradual excavation of different steps of Tongyoushan tunnel, the stratum subsidence, horizontal displacement and inclination are all increasing, and reach the peak at the end when the whole tunnel is finished. The location of the

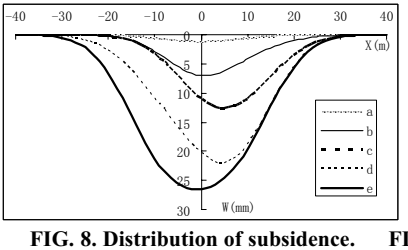

FIG. 8. Distribution of subsidence.

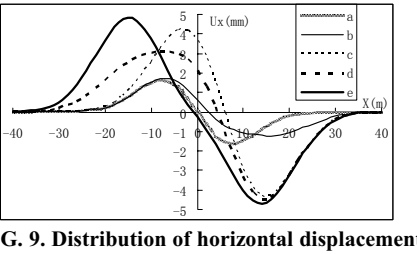

FIG. 9. Distribution of horizontal displacement.

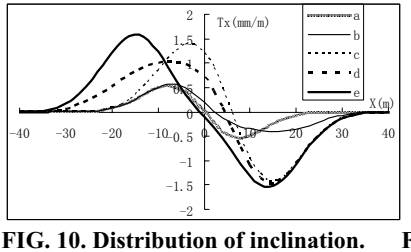

FIG. 10. Distribution of inclination.

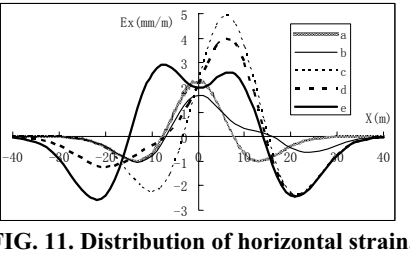

FIG. 11. Distribution of horizontal strain.

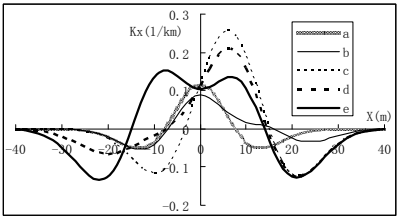

FIG. 12. Distribution of curvature.

maximum value varies according to the excavation steps of tunnel.

(2) The maximum value of the stratum horizontal strain and curvature ratio does not emerge when the whole tunnel is finished, but when the only one part of tunnel (right tunnel) is finished. The stratum horizontal strain and curvature ratio when the whole tunnel is finished are only a little larger than the one when the central-heading tunnel is excavated. This means that to the tunnel which uses the method of sequential excavation, if the final deformation is only considered, the precise judgment can not be made on the safety of the buildings around the tunnel.

(3) The final distribution of the stratum deformation is symmetrical. But after the different excavation steps of the tunnel, the distribution of stratum deformation is not symmetrical because of the influence on the sequential excavation.

THE INFLUENCE OF DIFFERENT CROSS-SECTION DIVISION TO THE STRATUM DEFORMATION

In order to study the influence on the stratum deformation by different cross-section division excavation method, assuming that the excavated section is horseshoe shaped. The span of which is 16 m, and the average value of constringency is 30 mm, the depth from the tunnel vault to the ground surface is 10.0 m, the tangent of main influence angle of the stratum is 1.0 and the influence radius R is 10m, the speed coefficient of the subsidence is $0.2d^{-1}$, and all parts of the tunnel is excavated at the speed of 2.0 m/d ($1.0CR$). In the calculation, the central departure excavation method (divided into left and right parts and each part's span is 8.0 m), the double-sidewalls heading excavation method (divided into left and right pilot-pits and central pit, the span of the left and right pilot-pits is 4 m, and the central part is 8 m), the sidewalls heading excavation method (the span of the side pilot-pit is 6.0 m, and the other part is 10.0 m) are all studied. The distribution of ground surface deformation under different excavating methods are shown in figure 13 - 17, in which curve A, B, C is the calculating results of central departure excavation method, double-sidewalls heading excavation method and sidewalls heading excavation method respectively, while D is the calculating results after the whole tunnel is excavated.

Figure 13 - 17 illustrate that:

(1) Although the final stratum deformations are the same under different methods and same execution conditionare, but during the excavation process the deformation varies when different parts are excavated. The deformation caused by

double-sidewalls heading excavation method is the smallest while the deformation caused by one-sidewalls heading excavation method is larger, and the largest arises when applies the central departure excavation method.

(2) When applying the three excavation methods, the stratum horizontal strain and curvature ratio are larger than the final value when the whole tunnel is finished. The maximum deformation (stretch strain and positive curvature) arises on the middle of the excavation parts, which is harmful to the surrounding buildings. Thus in practical projects, when there are important buildings which is sensible to stretch strain, the side near the building should be excavated first to minimize the harmful influence.

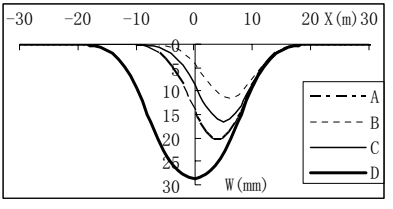

FIG. 13. Distribution of subsidence.

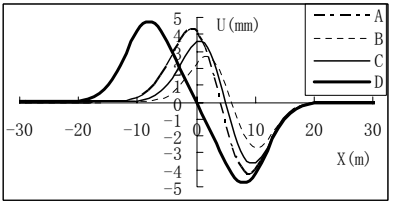

FIG. 14. Distribution of horizontal displacement.

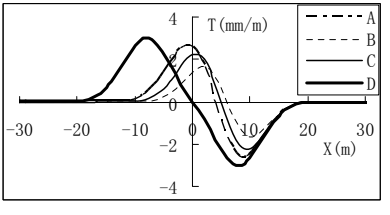

FIG. 15. Distribution of inclination.

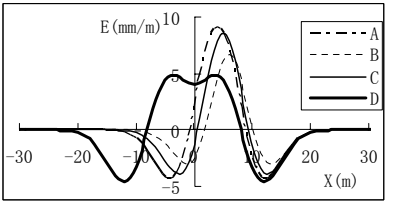

FIG. 16. Distribution of horizontal strain.

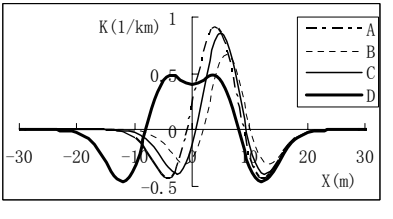

FIG. 17. Distribution of curvature.

Because there are a lot of reasons which caused the stratum deformation, constringency under different excavation methods and supports varies from each other. Such conclusions are based on the condition that constringency in the tunnel are the same under different excavation method. So in practical projects the comprehensive influence should be taken into consideration so as to control stratum deformation.

CONCLUSION

Based on the stochastic medium theory, and take the time effect of stratum deformation into consideration, the uniform calculation formula of the stratum deformation during the tunnel excavation is deduced, and the time-space effect of stratum deformation when different parts of tunnel are excavating is studied. All these give support to the deformation control and building protection.

(1) The horizontal stratum deformation and curvature ratio are larger than the final values when the tunnel is finished. The maximum deformation (stretch strain and curvature) arises when the excavation is near the middle of the divided parts, which is harmful to the surrounding buildings. Thus in practical projects, when there are important buildings which is sensible to stretch deformation nearby, the side near the building should be excavated first to minimize the harmful influence.

(2) Different divisions of the cross-section of tunnel have certain influence on the stratum deformation, and compared with the central departure excavation method, double-sidewalls heading excavation method has better effect on the stratum deformation control around tunnel.

REFERENCE

Peck R. B(1969). “Deep excavation and tunneling in soft ground.” State of the Art Report. Proc. 7Int. Conf. *On Soil Mechanics and Foundation Engineering*, Mexico City：225-290

T. Nomoto, H. Mori, M. Matsumoto (1995). “Overview of ground movement during shield tunneling: A survey on Japanese shield tunneling.” in: Fujita & Kusakabe eds. Proc. *Underground Construction in Soft Ground*, Balkema, Rotterdam: 345-351

Wei-I. Chou, Antonio Bobet (2002). “Predictions of ground deformation in shallow tunnels in clay.” T*unnelling and Underground Space Technology*. (17): 3-19

LIAO Shao-ming, YU Yan, BAI Ting-hui (2006). “Distribution of ground displacement field owing to two overlapped shield tunneling interaction.” *Chinese Journal of Geotechnical Engineering*, Vol. 28(4): 485-490

WU Bo, GAO Bo, SUO Xiao-ming (2004). “Study on influence of metro tunnel excavation on buried pipelines.” *Rock and Soil Mechanics*, Vol. 25(4): 657-662

AN Hong-gang, HU Xiang-dong (2004). “Prediction of Ground Deformation in Cross-over MetroTunnelling Using Evolutionary Intelligent Method.” *Journal of Tongji University*, Vol. 32(12): 1573-1577

YANG Junsheng, LIU Baochen (2002). “Ground Surface Movement and Deformation Caused by Urban Tunnel Construction.” Beijing: *China Railway Publishing House*

SHI Chenghua (2007). “Study on time-space united calculating theory of stratum deformation for urban tunnel excavation and its application” [D]. changsha, Centre South University

SHI Chenghua, PENG Limin, LIU Baochen (2003). “Stratum Movement and Deformation in Longitude due to Shallow Tunnel Construction.” *China Railway Science*, Vol. 8(4), 87-91

Method of Ground Settlement Prediction in Urban Tunnel Construction Based on ARMA

YANG Wei-chao[1], PENG Li-min[2], and Wang Li-chuan[3]

[1]Doctoral candidate, School of Civil Engineering and Architecture, Central South University Changsha 410075, China; weic_yang@163.com

[2]Vice-President, School of Civil Engineering and Architecture, Central South University Changsha 410075, China; lm_peng@mail.csu.edu.cn

[3]Beijing China Tunnel Group Construction Co.; Ltd.; Beijing 100022; wlc7737477@126.com

ABSTRACT: Deformation of surrounding rock during tunnel excavation could be regarded as a time sequence. In this paper, the auto regressive moving average (ARMA) process of tunnel deformation prediction during construction, which can, to some extent, modulate model parameters according to the input and output data, adjust them to its optimal values in some statistical conditions through the iterative algorithm. Firstly, the raw monitoring data is dealt with by difference operation (d=1) and the stationary error time series is obtained. Secondly, the randomicity and the stabilization of the error series have been analyzed to confirm the feasibility of ARMA model. Both the autocorrelation function (ACF) and partial autocorrelation function (PACF) of the error series are tested, and the order of model ARMA is obtained based on the AIC criterion. Finally, the method of least square is adopted for parameter estimation. As a test, this modeling is used to predict the surface settlement of a Shenzhen metro line 2 of China. The results of engineering case indicate that ARMA is reliable in deformation prediction. In addition, the new-information model idea has been put into the model to achieve the real-time forecast of settlement.

INTRODUCTION

As an important part of NATM, the processes of monitoring and measurement are important and indispensable in the tunnel construction, which effectively reflect the rock deformation and its mechanical behavior, and provide a suitable installation time for tunnel lining structure. Scientific analysis and forecast real-timely on monitoring data provide a precondition for supporting the strategic decisions of construction

organization, as well as dynamic design. Several methods – both causal and non-causal – have been proposed to forecast such measurement data. The former includes the widely studied classification problem. The later, on the other hand, study the historic values of a variable in order to forecast its future value. Many forecast models have been proposed and implemented in this field including linear regression (LR), supporting vector machines (SVM) and neuro-fuzzy models (NFM). LR, usually adopting multivariate linear or exponential function model, is too simple to reflect the real impact from the construction progress, while SVR could not get satisfactory results for the trouble choosing appropriate kernel function. By comparison, Time series methods are generally used when there is not much information about the generation process of the underlying variable and when other variables provide no clear explanation of the studied variable. In this paper, the in-suit monitoring and measurement data of surrounding rock is regarded as a time sequence, and the rock deformation and its mechanical behavior is modeled by an ARMA process and secondly on a accuracy comparison of different model parameter.

ARMA MODELING TECHNIQUE

ARMA modeling belongs to a class of modern spectral analysis techniques, which is more generally known as autoregressive (AR) time series modeling. The ARMA method is the preferred method for this class since it is the best compromise between temporal resolution and speed, efficiency and simplicity of algorithms. Consider $\{y_t, t \in Z\}$, Z the set of integers, autoregressive-moving average (ARMA) process of order (p, q) in dimension n, which satisfies the vector difference equation

$$\sum_{i=0}^{p} \alpha_i X_{t-i} = \sum_{j=0}^{q} \beta_j \varepsilon_{t-j}, t \in Z \tag{1}$$

where $\{\varepsilon_t, t \in Z\}$ is the innovation process, a sequence of independent zero-mean n-dimensional random variables each having positive definite covariance matrix $\sum$, and where $\alpha_j, \beta_j \in R^{n \times n}$,are the parameter matrices, and $\alpha_0 \equiv \beta_0 \equiv I_n$.
We use L to denote the backward shift operator on Z, for example $Ly_t = y_{t-1}$; then (1) can be written as
$\alpha(L) y_t = \beta y_t \varepsilon$, where

$$\alpha(z) = 1 - \sum_{j=1}^{p} \alpha_j z^j \neq 0, |z| \leq 1 \qquad \beta(z) = 1 - \sum_{j=0}^{q} \beta_j z^j \neq 0, |z| < 1 \tag{2}$$

are the associated matrix polynomials. We further assume the eigenvalues of the matrix polynomials $\alpha(z)$ and $\beta(z)$ to be outside the unit circle so the elements of $\alpha^{-1}(z)$ and $\beta^{-1}(z)$ can be written as power series in z. These eigenvalues are obtained by solving the scalar polynomials $\mathrm{dat(a(z))} = 0$ and $\mathrm{dat(b(z))} = 0$, where dat(x) is the determinant of x. We assume that the matrix polynomials $\alpha(z)$ and $\beta(z)$ have no

common eigenvalues.

Let $\{y_t, t=1,\cdots N\}$ be a time series generated by the ARMA process (2) and let the set of parameters $\vartheta=(\vartheta_1,\cdots,\vartheta_l)$, where denotes transposition and $l=n^2(p+q)$. The following definition of the parameter vector ϑ is introduced $\vartheta=\mathrm{vec}(\alpha_1,\alpha_2\cdots,\alpha_p,\beta_1,\beta_2\cdots,\beta_q)$, where vec X as usual stands for the vector resulting from stacking the columns of a matrix X on top of each other. We assume, as usual, that the nuisance parameters included in Σ are functionally independent from the parameters of interest included ϑ.

ENGINEERING SURVEY AND DATA ACQUISITION

In order to ease the traffic pressure of Shenzhen, Guangdong of China, in 2007, the government decided to increase a 17.2 km-long subway-Shenzhen metro line 2, from the tourist attractions-Window of World of Nanshan District, to South Dongmen of Luohu Dist. It is worth noting that there are Multi-residential buildings and a variety of floor office building near the Window of World, the monitoring and prediction were indispensable for construction security.

The actual data used in this work according to the ground settlement in YDK15+238, being a time series that contains the daily ground settlement covering the period from November 10, 2007 to June 6, 2008 (Fig. 1). The total displacement had an obvious increasing trend. The first necessary step that must be done is to remove this feature. This is achieved as following:

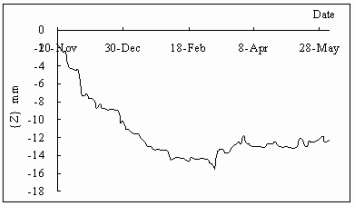

FIG. 1. Ground Settlement in YDK15+238.

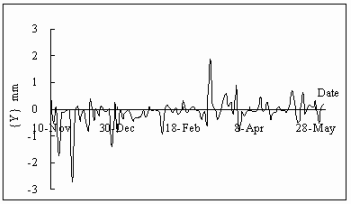

FIG. 2. Ground Settlement in YDK15+238 after Removal of Trend.

- Assume a vector of daily loads: $\{z_1,\cdots,z_n\}$
- First-order difference of the total settlement $x_t=z_t-z_{t-1}$, got the settlement rate series $\{X_t\}$, if the $Var[\overline{X}]\le 2.0\times S.E.[\overline{X}]=\sqrt{Var[\overline{X}]}$, then, $\{X_t\}$ can be regarded as zero mean series, otherwise:
- Zero mean normalization $Y_t=X_t-\overline{X}$, where $\overline{X}=1/N\sum_{i=1}^{N}x_i$, got series $\{Y_t\}$

The resulting time series (Figs. 2) show no apparent trend. It can be considered as a realization of a stationary process.

MODELING WITH ARMA PROCESSES

In addition to that, both the Auto Correlation Function (ACF) and Partial Auto Correlation Function (PACF), obtained as formula (3) and (4), tend very fast to zero (Figs. 3 and 4) showing that series $\{Y_t\}$ can be modeled by an AR or an ARMA model. An m-variate ARMA model of order (p, q) [ARMA (p, q)] for a stationary time series of vectors $\mathbf{y}$ observed at equally spaced instants $k = 1, \cdots, n$ is defined as equation (1), and the following task is the estimation of the predictor's matrix coefficients $\{A_i, B_j\}$ Determining the order of the ARMA process is usually the most important part of the problem. Over the past years, substantial literature has been produced for this problem and various different criteria, such as Akaike's, Rissanen's, have been proposed to implement the order selection process. Using the real data provided ARMA model order ϑ identification and parameter estimation was accomplished by the Akaike's AIC (A-Information Criterion).

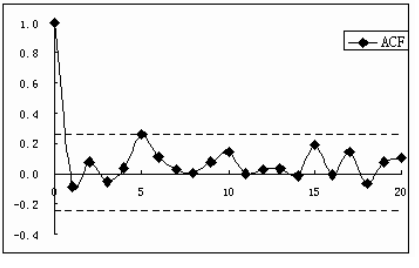

FIG. 3. The ACF for the Mean Stationary Series. Dashed Lines Represent the Bounds of Confidence Intervals.

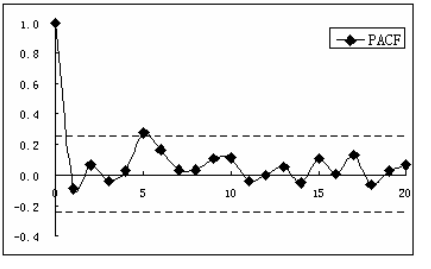

FIG. 4. The PACF for the Mean Stationary Series. Dashed Lines Represent the Bounds of Confidence Intervals.

$$AIC(n) = \ln \sigma_a^2(n) + 2n / N \tag{3}$$

The optimization procedure led us to the following ARMA (p, q) model, their parameters listed in Table 1.

From Table 1, one can see that the loss function of ARMA (2,1) is less than ARMA (2,0) but more than ARMA (4,5), which show that $\{Y_t\}$ is likely to be modeled by ARMA. Furthermore, the loss function difference between ARMA (4,5) and ARMA (2,1) is too be small to be ignored. Then the optimization model is ARMA (2, 1).

Table 1. Modeling Results of the Comparison

ϑ	ARMA(p,q)		
	(4,3)	**(2,1)**	**(2,0)**
α_1	1.613	0.9069	0.02949
α_2	-0.9425	0.05186	0.05485
α_3	0.2017		
α_4	0.0664		
β_1	1.635	0.9168	
β_2	-0.9754		
β_3	0.2269		
Loss function	0.2347	0.2359	0.2477

NEW-INFORMATION PREDICTION

It is necessary to continuously measure the deformation along with the development of the construction, update the new monitoring data real-timely. Adding new samples to the training set, replacing the old ones, and regenerating the prediction model is called the equal-dimension new-information model method. Put the equal-dimension new-information model idea into model ARMA (2,1), and forecast real-timely the settlement in the next 10 days (Table 2).

Table 2 Comparisons between the Prediction and Monitoring Data

Time M-D	**Monitoring /mm**	**Prediction /mm**	**Relative Error %**	**Absolute Error /mm**
6- June	2.07	1.90	8.0%	0.17
7- June	2.98	2.94	1.4%	0.04
8- June	3.16	3.28	-3.9%	-0.12
9- June	2.56	2.82	-10.2%	-0.26
10- June	2.36	2.53	-7.2%	-0.17
11- June	1.80	2.32	-29.1%	-0.52

All the monitoring data and its prediction value are shown in Table 2, the maximum of absolute error is 0.26 mm, the minimum is 0.04 mm, and the average relative error of this model is only 6.8 %, as indicates that it is feasible to forecast the deformation during the tunnel construction based on ARMA(p,q).

CONCLUSION

According to monitoring data of tunnel by NATM method, the data was regarded as a time series. The stationary process would be obtained after first-order difference operation and zero mean normalization of the raw monitoring data. The analysis by Auto Correlation Function (ACF) and Partial Auto Correlation Function (PACF) show that the series could be modeled by ARMA. Using the real data provided ARMA model order ϑ identification and parameter estimation was accomplished by the Akaike's AIC (A-Information Criterion). As a test, this modeling is used to predict the surface settlement of Shenzhen metro line 2 during excavation. The results of engineering case indicate that ARMA is reliable in deformation prediction. In addition, the new-information model idea has been put into the model to achieve the real-timely forecast of settlement during urban tunnel construction. The requirements of urban tunnel construction are stricter on the environmental requirements. ARMA model can provide a short-term prediction on the surface subsidence.

ACKNOWLEDGMENTS

This paper is funded by the Science-technology Developing Item of the Ministry of Railways of China, 2005K002-A-1-1.

REFERENCES

ZHANG Jun-yan, FENG Shou-zhong, LIU Dong-ha, (2005).A Forecasting Method for *Tunnel Surrounding Rock Deformation Using RBF Neural Network[J], Engineering Science*, 7(10):87-90 (in Chinese);

TIAN Zhi-xiang, QIAO Chun-sheng, TENG Wen-yan, LIU Kai-yun, (2004). Method of Predicting Tunnel Deformation Based on Support Vector Machines [J]. *China Railway Science*,， 25(1): 86-90 (in Chinese);

ZHAO Hong-bo. (2005). Predicting the Surrounding Deformations of Tunnel Using Support Vector Machine[J]. *Chinese Journal of Rock Mechanics and Engineering*, , 24 (4):649-652 (in Chinese).

Andrés Ubierna, Santiago Velilla, (2007), A goodness-of-fit process for ARMA(p,q) models based on a modified residual autocorrelation sequence[J*]. Journal of Statistical Planning and Inference* 1372903–2919.

Makridakis, S., Wheel wrigth, S. C., & Hyndman, R. J., (1998). Forecasting: Methods and Applications. Prentice Hall.

Research on Mechanic Characteristic of Waterproof Membrane for Highway Tunnel

Wei Hu[1] and Yinsheng Zou[2]

[1]Doctor, College of Civil Engineering, Hunan University, Changsha, Hunan, 410082, China
[2]Professor, College of Civil Engineering, Hunan University, Changsha, Hunan, 410082, China

ABSTRACT: Multi-waterproof measures are adopted to highway tunnel, where waterproof membrane is the most vital link between initial lining and final lining during waterproof system. In light of plenty of field monitoring data by compress sensors, the article presents phase and position of the maximal compress stress of waterproof membrane during pouring final lining, and different calculation formula of analyzing self-weight stress and temperature stress of concrete. The article also presents tensile stress condition under surrounding rock bad extra-excavation and stress calculation by finite element method (FEM) of nonlinear hardening constitutive model. The mechanic characteristic contributes to applied value for simplifying reliability assessment parameters and conducting safety construction for waterproof membrane.

INTRODUCTION

It is well known that highway tunnels give birth to many quality problems: such as tunnel seepage, lining fracture and limit infraction, which tunnel seepage comes to the chief problem for its emergence frequency. According to field investigation, ninety percent of highway tunnels at home give birth to seepage in different seepage flow, even if waterfall.

New Austrian Tunneling Method (NATM) is adopted to design and construct current highway tunnel. On tunnel drainage, comprehensive principle for surrounding rock inflow water dispose is adopted by combining drainage, intercept and caulking joint. Waterproof membrane is the most vital link between initial anchor-shotcrete support and final lining.

Although multi-waterproof measures are adopted to highway tunnel, many factors, such as bad surrounding rock (e.g., layer slate local collapse), blasting skill and constructor quality, conduce to final lining seepage. Final lining seepage must be provided with two conditions. One is that waterproof membrane is destroyed during construction or by convexity during final lining pouring concrete or that bonding leads to fracture. The other is that water pressure accumulates to a certain value. Once final lining hydraulic pressure trolley (HPT) is positioned, waterproof membrane becomes concealment structure without doubt. The aim of paper is to investigate mechanic characteristic of waterproof membrane during concrete pouring and consolidation to

resolve reliability of waterproof membrane because of convexity or extra-excavation of surrounding rock.

WATERPROOF MEMBRANE MECHANIC IN-SITU MONITORING

Reliability of field data depends on reasonable installation of compress sensors. Researchers such as Zhao and Gao (2002), Li (2002),Wang and Hu (2003), Zhao and Xie (2004) published different solution for installing compress sensor to monitor and survey compress stress between initial lining and final lining by man-made drilling or initial anchor-shotcrete support surface fixup. The author offers a new and reasonable solution for installing compress tensor on base of long-term field monitoring and surveying work during tunnel construction (fig. 1). Compress sensor is put into a bag by two different area waterproof membrane bonding together on the side of final lining. Certainly pay attention to selecting flat position of surrounding rock. This solution could posses the following benefits:

(1) It is for the first time to monitor and survey stress of waterproof membrane. Even if there is a gap between initial lining and final lining, the compress sensor on the top of tunnel could offer compress stress value, which avoids wasting sensor.

(2) Waterproof membrane possesses a certain flexibility to regulate position of sensor, which avoids bearing point load only at two side-points position.

(3) Waterproof membrane possesses certain strength and compress sensor is sealed in bag, which avoids confined stress from concrete of final lining;

(4) This solution for installing compress sensor is simple and shortcut, without disturbing normal tunnel construction.

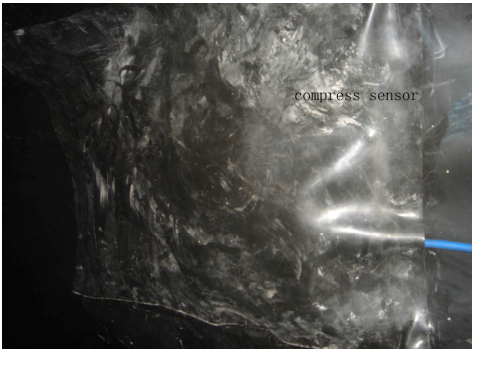

FIG. 1. Compress sensor with sealed installation.

MECHANIC CHARACTERISTIC OF WATERPROOF MEMBRANE

Introduction

XueFeng mountain tunnel is the third lengthy highway tunnel at home. In order to resolve subject on key technology research of extra-length XueFeng mountain highway tunnel, many monitoring sections were installed. Figure 2 shows a long-term

monitoring result from a typical section where seven compress sensors were installed along with waterproof membrane circumference.

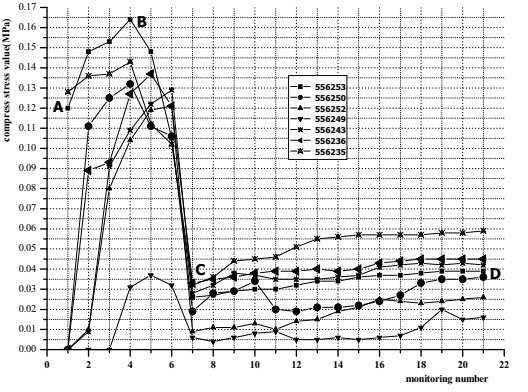

FIG. 2. σ - t curve at different point in typical measuring section.

Compress Mechanic Characteristic

Figure 2 illustrates the following compress stress mechanic characteristic of waterproof membrane:

(1) All compress sensors possess a similar mechanic characteristic that waterproof membrane compress stress comes to the maximum during concrete pouring (Point B, fig. 2), and compress stress decreases with concrete consolidation. when final lining HPT is dismantled, waterproof membrane compress stress suddenly decreases because of concrete elastic deformation (Point C, fig. 2).

(2) The maximal compress stress appears in side-wall position, while the minimal compress stress appears in the top of tunnel.

(3) Final lining HPT is dismantled under the condition of concrete consolidation to 80 percent of total compress strength. Comparing to final lining pouring, the compress stress from surrounding rock deformation toward waterproof membrane is little. The compress stress from surrounding rock deformation is equal to 3 to 10 percent of maximum compress stress from final lining pouring.

(4) Researchers such as Zhao and Gao (2002), Wang and Hu (2003), Zhao and Xie (2004) regard the minimal compress stress (Point C, fig. 2) as the compress stress from surrounding rock deformation toward waterproof membrane. In fact, the compress stress(Point C, fig. 2) only is produced by self-weight stress and temperature stress of concrete.

(5) The phase for reliability assessment of waterproof membrane should consider pouring final lining phase, not surrounding rock deformation phase after dismantling final lining hydraulic pressure trolley.

(6) Self-weight stress of concrete and temperature stress of concrete commonly result in compress stress of waterproof membrane. The former stress is far lager than the latter stress.

Tensile Stress Condition

During final lining concrete pouring, waterproof membrane may produce tensile stress, which depend effective surrounding rock wall perimeter L_1,design surrounding rock wall perimeter L_0 and waterproof membrane margin value L_2 .The relationship may be expressed by

$$L_1 \Big/ (L_0 + L_2) \geq 1 \qquad (1)$$

Usually there is a decided relation between design surrounding rock wall perimeter and waterproof membrane margin value. The relationship is defined by

$$L_2 = 0.15 L_0 \qquad (2)$$

Substituting Equation (2) into Equation (1), we have

$$L_1 \Big/ L_0 \geq 1.15 \qquad (3)$$

WATERPROOF MEMBRANE MECHANIC ANALYSIS

Waterproof Membrane Tensile Analysis

Waterproof membrane quality inspection provides with tensile strength and a relation curve between tensile power and elongation, which could be transformed into stress-strain relation curve of waterproof membrane. Waterproof membrane possesses stress hardening mechanic characteristic. When tensile analysis is taken into account under the condition of gap between waterproof membrane and initial lining, FEM is the optimal choice by adopting shell cell (shell51), stress harden and nonlinear elastic-plastic constitutive model and two side fixed, central pressure and plain strain physical model.

Waterproof Membrane Compress Analysis

Under the condition of continuous pouring concrete and dense condition, self-weight stress of concrete can be calculated by the following formula

$$\sigma_p = \gamma h \qquad (4)$$

where γ refers to specific gravity of concrete, h refers to height apart monitoring point.

Because of constraint from surrounding rock and final lining HPT, temperature stress of concrete can be calculated by the following formula

$$\sigma_T = E(t)\alpha\Delta T(t) \quad (5)$$

Where α refers to linear delate coefficient, $\Delta T(t)$ refers to a time function, which can be measured by thermometer easily. $E(t)$ refers to a time function ,which can be calculated (Zhu,1998)

$$E(t) = (1 - \exp(-0.28t\text{^}0.52)) * 3e10 \quad (6)$$

Where t refers to time.

Combining Equation (4) and Equation (5) total compress stress σ of waterproof membrane can be calculated:

$$\sigma = \sigma_P + \sigma_T \qquad (7)$$

CONCLUSIONS

Here we may draw the following conclusion:

1. It is for the first time that the author has implemented monitoring and surveying stress of waterproof membrane during construction, and has applied for reliability assessment of waterproof membrane successfully.

2. The author offers a new and reasonable solution for installing compress tensor in the form of bag, which has many benefits.

3. It is emphasized that the minimal compress stress (Point C, fig. 2) is not produced by surrounding rock deformation toward waterproof membrane, but by self-weight stress and temperature stress of concrete commonly.

4. The paper has pointed out that reliability assessment of waterproof membrane should consider pouring period of final lining during pouring period. The maximum compress stress of waterproof membrane produce by self-weight stress and temperature stress of concrete commonly and provide with calculation formula respectively. Total monitoring curve shows that compress from initial lining toward final lining begin with B point the total compress value is equal to ($\sigma_{t\infty} - \sigma_{tB}$), which usually is less than that from pouring period.

5. During final lining concrete pouring, waterproof membrane may produce tensile stress, which depend effective surrounding rock wall perimeter L_1, design surrounding rock wall perimeter L_0 and waterproof membrane margin value L_2. FEM is the optimal choice by adopting shell cell (shell51), stress harden and nonlinear elastic-plastic constitutive model and two side fixed, central pressure and plain strain physical model.

REFERENCES

Zhanchang Z. and Yongli X., et al. (2004). Observation research on mechanical characteristic of highway tunnel lining in loess. *China Journal of Highway and transport*,17(1): 66-69.

Yuguang, Z. and Bo g., et al. (2002). Field monitor measuring and geological disaster forecast at the mouth of tunnel near the rocky steep side slope under unsymmetrical loading. *Journal of Geological Hazards and Environment Preservation*, 13(3): 32-35.

Lizhong, W. and Yayuan H., et al. (2000). Stability analysis and monitoring for tunnel in loose soils during construction. *Chinese Journal of Rock Mechanics and Engineering*,22(4): 589-595.

Li Xiaohong. (2003). *Tunnel NATM and its Technology of Monitoring and Survey*. Beijing Science Press.

Zhu Baifang. (1998). *Temperature Stress and Temperature Control in Large Scale Concrete. Beijing*: China electric power Press.

Effect of Mechanics and Optimum Process in Excavating Multi-Arch Tunnel

Wu Congshi[1], and Ding Zude[2]

[1]Professor, Changsha University of Science and Technology, Changsha, Hunan Province, China 410012; wucosh@163.com
[2]Ph.D candidate, Central South University, Changsha, Hunan Province,China 410012; dzdvsdt@126.com

ABSTRACT: Based on the Chenjiaqiao tunnel project, the construction process of tunnel under different surrounding rock conditions and with various construction methods is analyzed with MIDAS program. The mechanical behavior under complex process of construction and the optimization of the construction process of multi-arch tunnel are studied by the analysis of the monitoring measured data and the numerical analysis results. The main contents of the research contain: The 3D elastoplastic model of multi-arch tunnel is set up, which contains Grade III, IV and V surrounding rock. The stress of the surrounding rock and the supporting structure at typical excavation stage under above three excavation methods are simulated and analyzed. The monitoring data is analyzed and compared with the simulated data. The reasonable distance between the working faces of the right and left tunnel is obtained.

INTRODUCTION

Because of the multi-arch tunnel's big span and small ratio of rise to span, it has various construction procedures. If the excavating method and the time for supporting are unreasonable, these are inclined to cause tunnel damages such as collapses and lining cracks. Therefore, it is necessary to study the excavating and supporting processes of multi-arch tunnel, so as to provide basis and guidance for the design and construction of multi-arch tunnel.

PROJECT INTRODUCTION

Located on a hilly area, Chenjiaqiao tunnel is a two-way-and-six-lane multi-arch tunnel of Wenzhou Ring Expressway, with 282 m in full length, 10.86 m in maximum excavation height, and 35.24 m in maximum excavation span width. The surrounding rock of the tunnel's entrance and exit section is Grade V, and the rock inward from the two ends is Grade IV and Grade III in sequence, according to the Chinese Code for Design of Road Tunnel. See table 1 for the surrounding rock parameters.

Table 1. Surrounding Rock Parameters of Chenjiaqiao Tunnel

Grade of Rock	Bulk Density (kN/m3)	Young's Modulus (GPa)	Poisson's Ratio	Cohesion (MPa)	Friction Angle (°)
III	25	6.0	0.28	0.80	40
IV	22	1.5	0.33	0.35	28
V	20	0.8	0.38	0.15	22

The middle wall of multi-arch tunnel is in a curve profile, which is made of C25 reinforced concrete. With the three-centered inner profile as the combined lining structure, the tunnel's primary supporting measures include anchor rod, double-layer rebar mesh, and shotcreting, etc. The integral moulded concrete structure is adopted for the second lining. See table 2 for the supporting parameters.

Table 2. Supporting Parameters of Chenjiaqiao Tunnel

Grade of Rock	Shotcreting C20 (m)	Anchor Rod Φ25 (m)	Rebar Mesh (m)	Steel Arch (m)	Second Lining (m)
III	0.15	3.5@1.2×1.5	0.15×0.15	-	0.45
IV	0.25	4.5@1.2×1.0	0.15×0.15	@1.0	0.50
V	0.30	4.5@1.2×0.5	0.15×0.15	@0.5	0.60

Chenjiaqiao tunnel is excavated from the exit in one direction. The excavation of the left tunnel is lagging behind that of the right tunnel. Because of the poor rock conditions at the Grade V and Grade IV section of the tunnel exit, three-pilot-tunnel measure is taken. For the better rock condition at the Grade III section, by comparing the middle-pilot-and-half-section method with the middle-pilot-and-full-section method, the middle-pilot-and-full-section measure is adopted.

NUMERICAL SIMULATION OF CONSTRUCTION

The finite element method is applied to the numerical simulation of construction process which mainly includes the partial excavation of rock-soil body and the layering arrangement of supporting structure. The finite element equation describing the mechanics properties at different construction stages can be written as follows:

$$\{[K_0]+[\Delta K_i]\}\{\Delta\delta_i\}=\{\Delta F_{ir}\}+\{\Delta F_{ig}\}+\{\Delta F_{ia}\} \quad (i=1,...,L) \qquad (1)$$

Where: L is the number of construction stages; $[K_0]$ is the initial total rigidity matrix of the rock-soil body before excavation; $[\Delta K_i]$ is the increment and decrement of the rigidity of rock-soil body and supporting structure; $\{\Delta F_{ir}\}$ is the equivalent node force of the released load at the excavation boundary during the No. i construction stage; $\{\Delta F_{ig}\}$ is the equivalent node force of the newly added self-weight during the No. i construction stage; $\{\Delta F_{ia}\}$ is the equivalent node force of the increment load during the No. i construction stage; $\{\Delta\delta_i\}$ is the increment of node displacement during the No. i construction stage. When the rock-soil body is under the non-linear

flexible conditions or the elastoplastic conditions, by taking constant stiffness increment iteration, the calculating equation of each construction stage can be illustrated as:

$$[K_{i0}]\{\Delta\delta_i\}^k = \{\Delta F_i\}^k \quad (i = 1,...,L; k = 1,...,N) \tag{2}$$

Where: N is the non-linear iterative step.

Four calculating models are established, i.e., simulating the middle-pilot-and-half-section construction process and the middle-pilot-and-full-section construction process at the Grade III rock section, the three-pilot construction process at the Grade IV and at the Grade V rock section.

For the three dimensional effect simulation, 6D~7D is used for the transverse width and 2D~3D for the longitudinal length for this calculation of which D is the diameter of single tunnel. The single tunnels' average diameter of Chenjiaqiao tunnel is 16.5 m.

During calculation, hexahedron unit simulates the surrounding rock, second lining and middle wall; plate unit simulates the shotcreting and truss unit simulates the anchor rod.

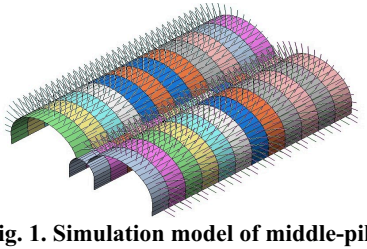

Fig. 1. Simulation model of middle-pilot -and-full-section construction process.

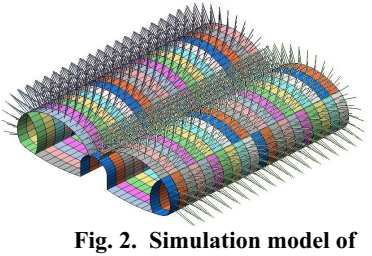

Fig. 2. Simulation model of three-pilot construction process.

MECHANICS PROPERTIES ANALYSIS DURING CONSTRUCTION

The analysis of simulating calculation indicates that during construction the stress variation of surrounding rock concentrates at the perimeter of tunnel structure, including the affecting area of anchor rod, the top and bottom of middle wall, which should be emphasized during construction and stress analysis of surrounding rock.

The affecting area of stress that the main tunnel construction acts on the surrounding rock mainly concentrates within 12 m-16 m at the back from the working force of the main tunnel at the same side. The main tunnel construction of one side affects slightly on the surrounding rock stress of the other side tunnel at Grade III rock section. But at Grade IV and Grade V rock sections, the influence that the main tunnel construction of one side acts on the surrounding rock stress of the other side tunnel is greater.

During the whole construction, the middle wall is basically under the condition of eccentric compression. The anti-overturning and deflection of the middle wall should be considered during construction. The surrounding rock at the top of middle wall is disturbed greatly for many times, of which the stress value and the fluctuation degree are obviously greater than those of the side surrounding rock of main tunnel. Therefore, the influence that the excavating space of the right and left tunnel exerts on the middle wall and top rock should be considered during design and construction.

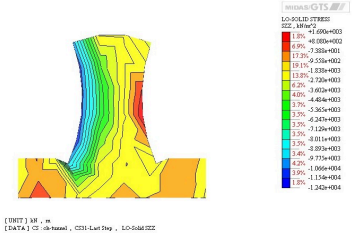

Fig. 3. Vertical stress of middle wall after excavation of right tunnel.

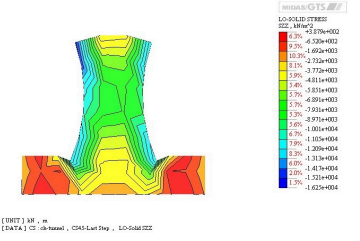

Fig. 4. Vertical stress of middle wall after excavation of left tunnel.

The tension of shotconcrete at some locations of Grade III rock exceeds its ultimate tensile strength, so the supporting should be strengthened or the second lining is timely constructed. The anchor rods with great stress are mainly located between the hance and arched crown of two main tunnels, and with small stress at the side wall and between the arch foots, the force applied is becoming bigger with the increase of surrounding rock's grade, so the length and space of the anchor rods in this area can be considered to be optimized during design.

By comparing the stress between the full-section method and half-section method, it is shown that the variation laws of internal forces by means of two methods are basically the same. The stress of half-section method is slightly bigger than that of the full-section method, so after the middle wall and neighboring rock is well protected, the full-section excavation method can be adopted for reducing working procedures and accelerating construction process.

The global stress of the second lining at Grade IV and Grade V rock section is significantly greater than that of the Grade III rock section, which is becoming bigger with the increase of surrounding rock's grade. This indicates that the second lining, primary support and surrounding rock are together bearing the perimeter loads, and the second lining at Grade IV and Grade V rock section not only to be the long-time safety reservation.

REASONABLE SPACE BETWEEN TUNNELING FACES OF TWO HOLES

For further study on the influence that the left tunnel construction acts on the arch crown of the right tunnel, the excavating spaces are set as 24 m, 32 m, and 48 m by using the middle-pilot-and-full-section calculation model at the Grade III rock section. 24 m means that the left tunnel excavation begins after the right tunnel is excavated 24 m, and so do the 32 m and the 48 m.

For the convenience of analysis, the arch crown of the right tunnel opening is chosen as the characteristic points. See Fig. 5 for the varying curve of the characteristic points' settlement of arch crown with the advancing of main tunnel's working face under conditions of different spaces.

From the settlement-varying curve, it is shown that if the excavating face space of the right and left tunnel is too close, it has a great influence on the settlement of the right tunnel. At this, the space between excavating faces more than 32 m will affect

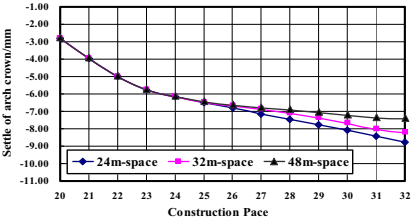

Fig. 5. Settlement varying curve of right tunnel's arch crown.

less on the settlement of the right tunnel.

By the same method, it can be calculated and analyzed that the space about 40m is comparatively suitable at the Grade IV rock section and if the space is more than 40m at the Grade V rock section, the left tunnel excavation will affect less on the settlement of the right tunnel's arch crown.

By taking average excavating span of single tunnel D=16.5m, the spaces between the excavating faces of the right and left tunnel under conditions of Grade III, IV and V rock condition are respectively 1.9D, 2.5D and 2.5D~3D.

CONSTRUCTION MONITORING OF TUNNEL

The monitoring settlement of arch crown is performed during construction. See Fig. 6 for the simulated results of the settlement at the right tunnel's arch crown of YK25+160 section, and Fig. 7 for the on-site measured results of the arch crown's settlement of this section.

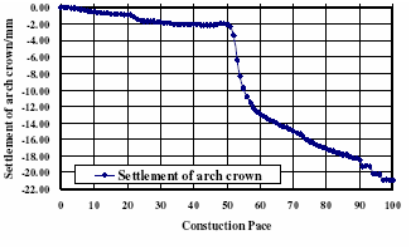

Fig. 6. Simulation of arch crown Settlement of YK25+160 section crown.

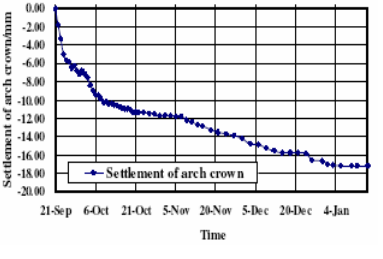

Fig. 7. Settlement-time curve of actual accumulated settlement of arch.

In the Fig. 6, the pace 1 to pace 46 represent the settlement that the pilot excavation affects the rock of this section; and pace 46 to pace 47, the settlement of this section during the excavation of right tunnel; pace 50 to pace 60 are the 10 paces before and after the excavating faces passing the objective section YK25+160; pace 68 to pace 88 show the settlement during the excavation of left tunnel; pace 89 to pace 100 indicate the settlement during invert excavation and the supporting process of the second lining.

The Fig. 7 is the varying curve of accumulated settlement of arch crown of the right tunnel of YK25+160 section with the date from September 2006 to January 2007, in

which the time from the last ten-day of September 2006 to the middle ten-day of January 2006 is the stage of right tunnel excavation while the left tunnel is not started; the time from the middle ten-day of November 2006 to the middle ten-day of December 2006 is the stage the left tunnel excavation starts and passes the corresponding location to this section; the time in and after the last twenty-day of December is the stage of invert excavation and supporting of the right tunnel opening.

By comparing the simulated results with on-site measured results of the arch crown settlement of YK25+160 section, the varying process and trend of two are basically the same. Actual measurement or numerical simulation, both indicate that the left tunnel (lagging tunnel) excavation and invert construction will affect the stress and deformation of the right tunnel (preceding tunnel). When the excavating face of left tunnel passes the objective section, this will have a great influence on the surrounding stress of right tunnel.

CONCLUSIONS

By making 3-D numerical simulation, combined with the monitoring measurement data on site of Chenjiaqiao tunnel, the optimum analysis is performed for the construction process. The conclusions are made as follows:

(1) The global stressing of the second lining is growing with the increase of rock grades. For the Grade IV and V rock sections, the second lining is not only for the long-time safety reservation, and it bears the perimeter loads together with primary supporting and surrounding rock.

(2) The reasonable spaces between the excavating faces of the right and left tunnel should be controlled about 1.9D for the grade III rock section; 2.5D for the grade IV rock section; 2.5D ~ 3D for the grade V rock section.

(3) When the middle-pilot is constructed, the middle-pilot's top and bottom rock should be strengthened and the concreting quality of middle wall should be ensured.

(4) The numerical simulation and the practice show that the middle-pilot-and-full-section method is feasible at the Grade III rock section of Chenjiaqiao tunnel. The whole construction goes smoothly in safety without any accidents and so far the tunnel has been gone through.

ACKNOWLEDGEMENT

It is a project supported by Provincial Natural Science Foundation of Hunan (08JJ3102) and by Scientific Research Fund of Zejiang Provincial Communications Department (2005H003). The authors would like to thank the authorities concerned.

REFERENCES

G.Galli, A.Grimaldi, and A.lenoardi(2004).“Three-dimentional modeling of tunnel excavation and lining.” *Tunneling and underground space technology*,31(2),171-183.

Liu Tao, Shen Mingrong, and Tao Lubin(2006). “Model test and 3D numerical simulation study on excavation of double-arch tunnel.” *Chinese Journal of Rock Mechanics and Engineering*,25(9),1802-1808.

Wu Congshi, Deng Jisheng, and Ye Yong(2008). “Stability of the shot concrete lining of multi-arch tunnel with large span and flat section.” *Journal of Changsha University of Science and Technology*, 5(2),34-42.

Author Index

Page number refers to the first page of paper

Subject Index

Page number refers to the first page of paper